NOTICE

The quality of this microform is heavily dependent upon the quality of the original thesis submitted for microfilming. Every effort has been made to ensure the highest quality of reproduction possible.

If pages are missing, contact the university which granted the degree.

Some pages may have indistinct print especially if the original pages were typed with a poor typewriter ribbon or if the university sent us an inferior photocopy.

Reproduction in full or in part of this microform is governed by the Canadian Copyright Act, R.S.C. 1970, c. C-30, and subsequent amendments.

AVIS

La qualité de cette microforme dépend grandement de la qualité de la thèse soumise au microfilmage. Nous avons tout fait pour assurer une qualité supérieure de reproduction.

S'il manque des pages, veuillez communiquer avec l'université qui a conféré le grade.

La qualité d'impression de certaines pages peut laisser à désirer, surtout si les pages originales ont été dactylographiées à l'aide d'un ruban usé ou si l'université nous a fait parvenir une photocopie de qualité inférieure.

La reproduction, même partielle, de cette microforme est soumise à la Loi canadienne sur le droit d'auteur, SRC 1970, c. C-30, et ses amendements subséquents.

Canada

UNIVERSITY OF ALBERTA

Experimental and Analytical Investigation of Flow Pressure Transients in Left Ventricular Ejection With Applications to Hypertrophic Cardiomyopathy

BY

ANDREW STUART HAY ©

A thesis submitted to the Faculty of Graduate Studies and Research in partial fulfillment of the requirements for the degree of Doctor of Philosophy.

DEPARTMENT OF MECHANICAL ENGINEERING

Edmonton, Alberta

Spring 1995

THE AUTHOR HAS GRANTED AN
IRREVOCABLE NON-EXCLUSIVE
LICENCE ALLOWING THE NATIONAL
LIBRARY OF CANADA TO
REPRODUCE, LOAN, DISTRIBUTE OR
SELL COPIES OF HIS/HER THESIS BY
ANY MEANS AND IN ANY FORM OR
FORMAT, MAKING THIS THESIS
AVAILABLE TO INTERESTED
PERSONS.

L'AUTEUR A ACCORDE UNE LICENCE
IRREVOCABLE ET NON EXCLUSIVE
PERMETTANT A LA BIBLIOTHEQUE
NATIONALE DU CANADA DE
REPRODUIRE, PRETER, DISTRIBUER
OU VENDRE DES COPIES DE SA
THESE DE QUELQUE MANIERE ET
SOUS QUELQUE FORME QUE CE SOIT
POUR METTRE DES EXEMPLAIRES DE
CETTE THESE A LA DISPOSITION DES
PERSONNE INTERESSEES.

THE AUTHOR RETAINS OWNERSHIP
OF THE COPYRIGHT IN HIS/HER
THESIS. NEITHER THE THESIS NOR
SUBSTANTIAL EXTRACTS FROM IT
MAY BE PRINTED OR OTHERWISE
REPRODUCED WITHOUT HIS/HER
PERMISSION.

L'AUTEUR CONSERVE LA PROPRIETE
DU DROIT D'AUTEUR QUI PROTEGE
SA THESE. NI LA THESE NI DES
EXTRAITS SUBSTANTIELS DE CELLE-
CI NE DOIVENT ETRE IMPRIMES OU
AUTREMENT REPRODUITS SANS SON
AUTORISATION.

ISBN   0-612-01700-1

UNIVERSITY OF ALBERTA

RELEASE FORM

NAME OF AUTHOR: Andrew S. Hay

TITLE OF THESIS: Experimental and Analytical Investigation of Flow Pressure
Transients in Left Ventricle Heart Ejection With Applications to
Hypertrophic Cardiomyopathy

DEGREE: Doctor of Philosophy

YEAR THIS DEGREE GRANTED: 1995

Andrew S. Hay
#606 5210 122 Street
Edmonton, Alberta
T6H 3S4

January 3, 1995
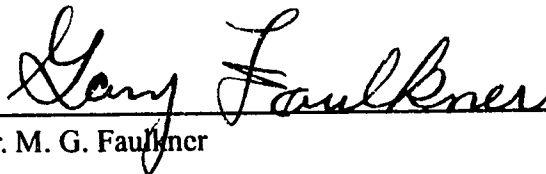
UNIVERSITY OF ALBERTA

FACULTY OF GRADUATE STUDIES AND RESEARCH
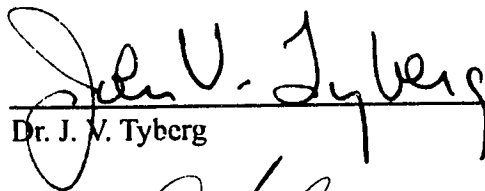
The undersigned certify that they have read, and recommend to the Faculty of Graduate Studies and Research for acceptance, a thesis entitled **Experimental and Analytical Investigation of Flow Pressure Transients in Left Ventricular Ejection With Applications to Hypertrophic Cardiomyopathy** submitted by Andrew S. Hay in partial fulfillment of the requirements for the degree of Doctor of Philosophy.

_____

Dr. D. J. Wilson

_____

Dr. M. G. Faulkner

_____

Dr. J. V. Tyberg

_____

Dr. D. Weaver

_____

Dr. W. H. Finlay

_____

Dr. K. K. Teo

ABSTRACT

The objective of this research was to look for fluid mechanical explanations of the abnormal pressure - flow patterns seen in hypertrophic cardiomyopathy. Two conflicting theories currently exist: one which proposes that the high pressure difference between the left ventricle and aorta is due to a flow obstruction, and another which 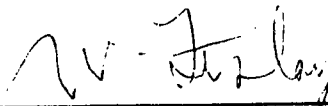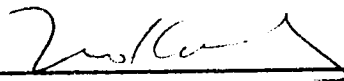suggests that this pressure difference is caused by inertial acceleration due to the unusually vigorous contraction of the left ventricle.

To test these different theories, the present study used theoretical flow modelling and laboratory modelling. The theoretical flow analysis allowed quantification of the geometry and flow rate variables that contribute to the pressure differences, while laboratory models gave valuable insight into the nature of the flow. The techniques utilized were:

- one-dimensional order of magnitude analysis;
- one-dimensional inviscid mathematical analysis;
- two-dimensional quasi-steady computational fluid dynamics modelling;
- two-dimensional transient planar piston laboratory modelling;
- two-dimensional steady flow laboratory modelling.

A new method of presenting the *in vivo* pressure-flow data was developed. This separates left ventricle ejection into unrestricted, progressively restricted and severely restricted cases. This method uses ejection volume and time to define a normalizing "stroke" pressure, which is successful in collapsing the large variability of *in vivo* data to a few single curves, with characteristic shapes depending on the degree of obstruction. Hypertrophic cardiomyopathy is shown to fall into both unrestricted and progressively restricted categories. Normal hearts match the unrestricted case, while a severe aortic valvular stenosis is characteristic of the severely restricted case.

Using this method of normalizing the pressure-flow data. it was found that although the unobstructed transient planar piston laboratory model was tested with ejection rates far exceeding those possible by a human heart, it was incapable of producing the magnitude of stroke normalized pressure noted for the severe hypertrophic cardiomyopathy case. However, when operated in a progressively restricted mode, the laboratory model easily produced large stroke normalized pressures, which suggests that severe cases of hypertrophic cardiomyopathy are progressively restric

ACKNOWLEDGMENTS

TABLE OF CONTENTS

LIST OF FIGURES

LIST OF TABLES

LIST OF NOMENCLATURE, ABBREVIATIONS AND SYMBOLS

NOMENCLATURE

Angina: chest pain combined with a choking feeling due to lack of oxygen to the heart.

Aorta: the main artery of the heart, originating at the left ventricle.

Aortic Valve: a three-leaved valve separating the left ventricle and aorta.

Apical: referring to the top or apex.

Atrium: one of the two upper chambers where blood first enters the heart.

Cardiomyopathy: any disease affecting the heart muscle.

Diastole: referring to the period of time between contraction of the ventricles.

Dyspnea: Difficulty in breathing or a shortness of breath.

Echocardiography: a method of diagnosis that studies heart structure and motion using ultrasonic waves directed towards the heart. Waves are reflected backward as they pass from one type of tissue to another.

Ejection Fraction: ratio of the volume of blood ejected from the left ventricle to the total end diastolic left ventricular volume.

Haematocrit: the volume percentage of cells in blood.

Hypertrophy: a significant increase in the normal size of an organ or tissue.

Intraventricular: occurring within the ventricle.

in vivo: occurring within a living organism.

Mitral Valve: a bicuspid valve between the left atrium and left ventricle.

Myectomy: the removal of muscle tissue.

Myofibrillar: slender strands of muscle tissue.

Myotomy: the cutting away of muscle tissue.

Palpitation: the feeling of a racing or pounding of the heart by the subject.

Plasma: the part of blood which is fluid.

Septal: associated with the wall separating the ventricles of the heart.

Stenosis: a narrowing of a passageway.

Stroke Volume: the volume of blood ejected during systole.

Stroke Time: the time of systole.

Supernormal: greater than the normal condition.

Syncope: light-headedness or a fainting spell.

Systole: the contraction of the ventricles, driving blood out of the heart.

Tricuspid Valve: the valve separating the right atrium and right ventricle.

Ventricle: (left or right) a small cavity surrounded by muscle which ejects blood from the heart.

ABBREVIATIONS

CFD: computational fluid dynamics.

HCM: hypertrophic cardiomyopathy.

L.V.D.T.: linear variable differential transformer.

LVOT: left ventricular outflow tract.

SAM: systolic anterior motion (of the anterior leaflet of the mitral valve).

PVC: premature ventricular contraction.

SYMBOLS

A: cross sectional flow area at an outlet boundary, used by FLOW3D (m^2).

A_p: cross sectional area of the piston region (m^2).

A_{surf}: surface area for use in determining viscous drag force (m^2).

A_{in}: area at upstream end of section under consideration (m^2).

A_{out}: area at downstream end of section under consideration (m^2).

B: height of planar model (m).

$\vec{B}$: body force used by FLOW3D (N).

C_μ: constant used by FLOW3D for determining μ_T (default value of 0.09).

C_1: empirical constants used by FLOW3D in transport equations (default value of 1.44).

C_2: empirical constant used by FLOW3D in transport equations (default value of 1.92).

D_c: diameter in constriction region of axisymmetric model (m).

D_e: diameter in exit region of axisymmetric model (m).

D_p: diameter in piston region of axisymmetric model (m).

$D_{p_{initial}}$: initial diameter in piston region of axisymmetric model (m).

$D_{p_{final}}$: final diameter in piston region of axisymmetric model (m).

$F_{inertial}$: inertial force (N).

$F_{quasi-steady}$: total quasi-steady force (does not include inertial acceleration terms) (N).

$F_{spatial}$: spatial force (N).

F_{total}: total force acting on fluid (N).

$F_{viscous}$: viscous drag force (N).

$f_{effective}$: effective low pass filter frequency (Hz).

f_{res}: resonant frequency (Hz).

H_p: distance between piston faces of planar model (m).

$H_{p_{initial}}$: initial distance between piston faces of planar model (m).

H_c: distance between constriction region walls of planar model (m).

H_e: distance between expansion region walls of planar model (m).

H_i: cross-stream distance between walls at inlet of flow section (m).

H_{local}: cross-stream channel width at any location (m).

H_o: cross-stream distance between walls at outlet of flow section (m).

i: integer counter used in integration.

L: length of model section (m).

L_c: length of constriction region (m).

L_e: length of expansion region (m).

L_{eff} = effective length of tube used to mount pressure transducer (m).

L_p: length of piston region (m).

M: desired mass flow rate out of computational domain, used by FLOW3D (kg).

M^i: actual mass flow rate out of computational domain, used by FLOW3D (kg).

m: mass of fluid (kg).

m_{ave}: average mass of fluid contained in flow section (kg).

$\dot{m}$: rate of change of mass (kg/s).

$m_{initial}$: mass of fluid contained in flow section at start of piston closure (kg).

N: number of points filtered.

n: direction normal to the boundary, used by FLOW3D.

P: shear production, used by FLOW3D.

p: pressure (Pa).

p_c: pressure at minimum constriction (Pa).

p_e: pressure at expansion region exit (Pa).

p_{i_c}: pressure at inlet of constriction region (Pa).

p_{i}: pressure at fixed wall (v=0) in piston region (Pa).

P_{inlet}: pressure at inlet of section (Pa).

p_p: pressure in piston region (Pa).

Re_D: Reynolds number based on aorta diameter D.

Re_H: Reynolds number based on planar piston exit region width H.

St_D: Strouhal number based on diameter D.

St_H: Strouhal number based on diameter H.

t: time (seconds).

t_{stroke}: time duration of flow occurring between left ventricle and aorta (seconds).

U: velocity in the cross-stream (x) direction (m/s).

U^i: velocity at the boundary, used by FLOW3D (m/s).

u: velocity in the cross-stream (x) direction (m/s).

u_c: constriction wall velocity at point of maximum restriction (m/s).

u_i: wall velocity at flow section inlet (m/s).

u_o: wall velocity at flow section outlet (m/s).

u_p: piston wall velocity (m/s).

V: velocity in the y-direction (m/s).

V_c: stream-wise velocity in the constriction region (m/s).

V_e: stream-wise velocity in the expansion region (m/s).

V_i: stream-wise velocity at inlet of flow section (m/s).

V_{max}: stream-wise maximum velocity at any cross-section (m/s).

V_p: stream-wise velocity in the piston region (m/s).

V_{stroke}: average aortic (exit) velocity during systole (m/s).

Vol: volume inside pressure transducer (m^3).

Vol_{tube}: volume inside pressure transducer tube (m^3).

v: velocity in the y-direction (m/s).

x: cross-stream coordinate (m).

y: stream-wise coordinate (m).

y_c: stream-wise coordinate in the constriction region (m).

y_e: stream-wise coordinate in the expansion region (m).

y_p: stream-wise coordinate in the piston region (m).

GREEK SYMBOLS

α_D: Womersley Parameter based on diameter D, see equation 2.48.

α_H: Womersley Parameter based on channel width H, see equation 2.54.

β_D: geometry factor in axisymmetric model based on diameter, see equation 2.48.

β_H: geometry factor in planar model based on channel width. see equation 2.54.

ΔP_{stroke}: pressure difference based on stroke velocity, used for normalizing (Pa), see equation 3.22.

Δt: time between points for filtering (seconds).

Δy: incremental stream-wise distance, used in integration (m).

δ_{ave}: average boundary layer thickness (m), see equation 2.22.

ε: turbulence dissipation rate (m^2/s^3).

η_D: restriction factor in axisymmetric model based on diameter, see equation 2.50.

η_H: restriction factor planar model based on channel width, see equation 2.54.

η_{area}: restriction factor based on an area basis, see equation 2.54.

κ: turbulence kinetic energy (m^2/s^2).

μ: dynamic viscosity (Pa-s).

μ_{eff}: effective viscosity, used by FLOW3D (Pa-s).

μ_T: eddy (turbulent) viscosity, used by FLOW3D (Pa-s).

v: kinematic viscosity (m^2/s).

Φ: stroke normalized pressure difference between any point along the mid-line and the expansion region exit, see equation 3.21.

Φ_{mid}: stroke normalized pressure difference between center of piston region and expansion exit, see Figure 3.8.

ρ: fluid density (kg/m^3).

σ: stress tensor, used by FLOW3D (Pa).

σ_r: standard deviation in the normalized piston to constriction pressure difference.

σ_p: standard deviation in the piston region pressure (Pa).

σ_c: standard deviation in c constriction exit pressure (Pa).

σ_e: standard deviation in the expansion exit pressure (Pa).

τ_w: wall shear stress (Pa).

ξ: stream-wise direction normalized by distance to point of maximum restriction, see equation 3.25.

Υ: stroke normalized central piston region to constriction region exit pressure difference, see equation 3.24.

$\Upsilon_{laminar}$: stroke-normalized piston to constriction region exit pressure difference for FLOW3D laminar flow solution.

$\Upsilon_{turbulent}$: stroke-normalized piston to constriction region exit pressure difference for FLOW3D turbulent flow solution.

CHAPTER 1 • INTRODUCTION

This thesis examines the fluid mechanics of a medical problem in the blood flow from the human heart. The research focuses on the transient pressure/flow relationships of blood being ejected from a diseased left ventricle. The disease, known as hypertrophic cardiomyopathy, causes an abnormal pressure difference between the left ventricle and outflow region (aorta) during the ejection period. Two differing viewpoints exist among cardiologists as to the cause and significance of this pressure difference. This research uses a variety of techniques to analyze this problem:

- one-dimensional order of magnitude analysis;
- one-dimensional inviscid mathematical analysis;
- two-dimensional quasi-steady computational fluid dynamics modelling;
- two-dimensional transient planar piston laboratory modelling;
- two-dimensional steady flow laboratory modelling.

Both the medical or engineering equivalent terms will also be used to assist the reader when encountering terminology which is distinct to either the medical or engineering profession.

1.1 HYPERTROPHIC CARDIOMYOPATHY

The heart muscle disease now referred to as hypertrophic cardiomyopathy (HCM) was first reported over thirty years ago by Brock (1957, 1958) and Teare (1958). Since then, numerous investigations have defined the characteristics of HCM. It is a heart muscle disorder of unknown cause, with a high degree of myofibrillar (strands of muscle tissue) disarray in the left ventricle, see Goodwin (1982). Figure 1.1 shows the relevant anatomy.

A heartbeat is divided into two separate phases. The first part of the beat is diastole, in which the left and right ventricles relax and fill with blood. The other phase

Figure 1.1: Anatomy of a Normal Human Heart
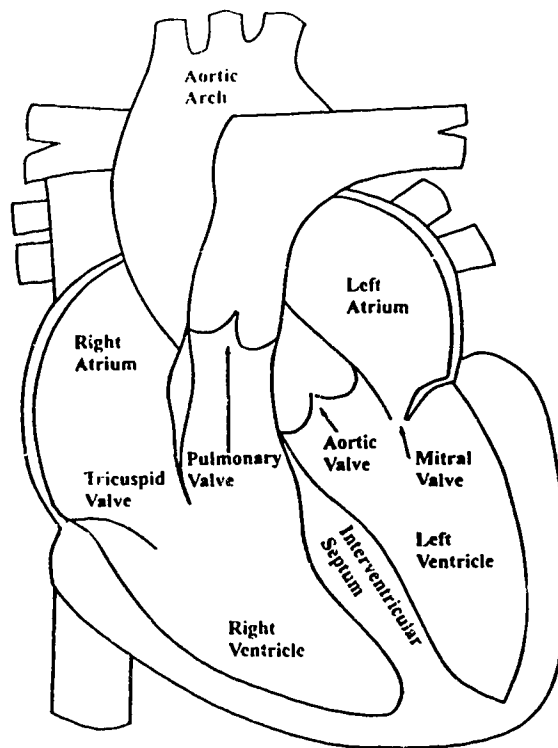
The human heart is approximately the size of a clenched fist.
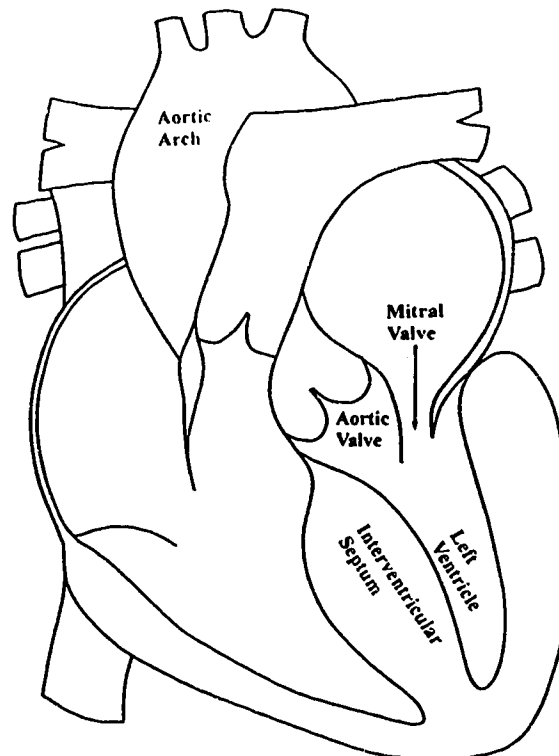
Figure 1.2: Anatomy of an HCM Heart

follows, which is known as systole, in which the ventricles contract, ejecting most of their volume. With HCM, there is supernormal systolic function (the left ventricle contracts at a higher than normal rate), abnormal diastolic relaxation and compliance, along with rhythm disturbances, see Canedo and Frank (1981). The heart muscle is hypertrophied (enlarged). The heart is larger than normal, but the ventricular volume is reduced as shown in Figure 1.2. An abnormally large pressure difference between the left ventricle and aorta is often observed during systole. Patients afflicted with HCM often experience angina (chest pain), dyspnea (shortness of breath), palpitations (racing heartbeat), and syncope (light-headedness). In addition, sudden unexpected death is quite common, as noted by Criley and Siegel (1993).

The pressures for a normal left ventricle and aorta along with the aortic flow velocity are compared to a typical HCM case in Figure 1.3, based on data from Murgo, Alter, Dorethy, Altobelli, McGranahan & Dunne (1980). Pressure pulses such as this are measured *in vivo* using miniature pressure transducers mounted near the tip of a catheter (catheter sizes as small as 1.67 mm diameter are common), Millar and Baker (1973). The pressures are referenced to the pressure at the tricuspid valve to provide consistency between patients, Guyton (1971, page 227). The pressures measured are static pressures and the accuracy of these measurements is rarely reported; the standard deviation of the values for a group of patients is usually listed. For example, Murgo *et al* (1980), in a study of a group of 30 HCM patients, give the peak left ventricular pressure as 140 mm Hg with a standard deviation of 28 mm Hg. This standard deviation of 20% is common for this type of measurement. Flow measurements are made invasively with catheter flow velocity probes, during heart operations with flow probes which encircle the aorta, and noninvasively using pulsed Doppler ultrasound techniques. These methods give results which are all qualitatively consistent. However, the accuracy of such measurements is typically not cited; the variation between patients appears to be of greater interest.
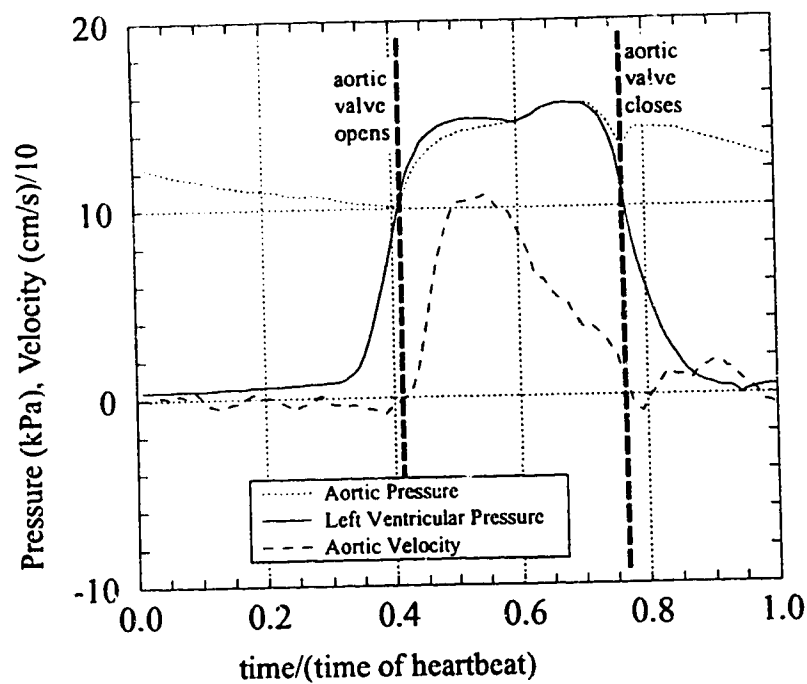
(a) Normal Heart
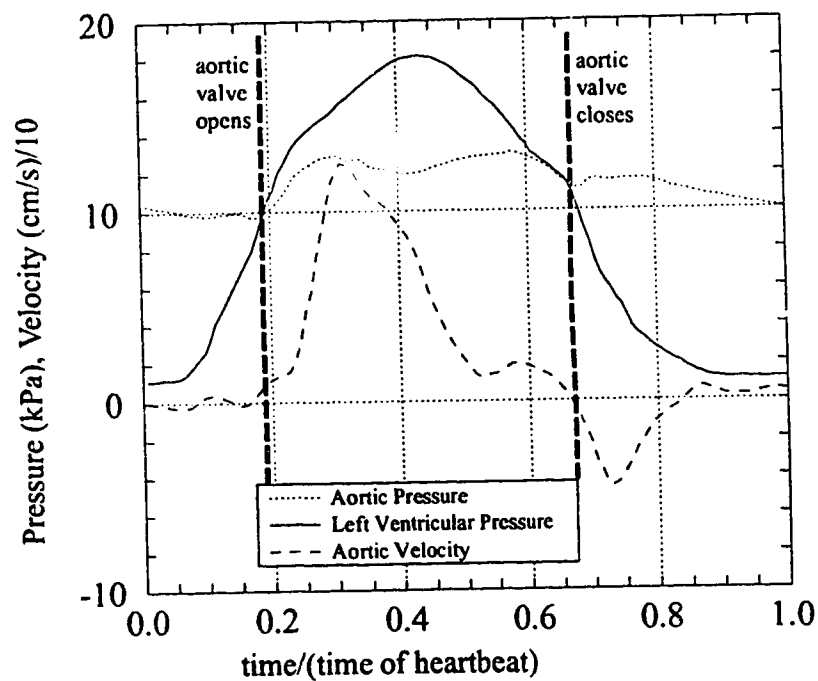
(b) Hypertrophic Cardiomyopathy Heart

Figure 1.3: *In Vivo* **Pressure Pulses and Flow Velocity**
Values obtained from data of Murgo *et al* (1980).

The usual sequence of events for systole (ejection) in the normal heart begins immediately following diastole (filling). The left ventricle begins to contract, causing the left ventricular pressure to rise. The mitral valve immediately closes, preventing blood from flowing back into the left atrium. Pressure in the left ventricle continues to rise until it exceeds the pressure in the aorta, at which time the aortic valve opens. This is the point at which flow commences. Aortic pressure now begins to rise, lagging only slightly behind that of the left ventricle. As the left ventricle reaches its maximum contraction, the pressure in the left ventricle falls, causing a corresponding decline in the flow rate. Aortic pressure also falls, but not as quickly as that in the left ventricle. This causes the aortic pressure to exceed the left ventricle pressure, which leads to a brief period of back flow prior to closing of the aortic valve. The back flow is marked by a sudden decrease in the aortic pressure, followed by a rebound: this feature is known as the dicrotic notch. The flow from the left ventricle ceases as the left ventricle relaxes, marking the end of systole.

The sequence of events in the HCM case is similar. Unlike the normal heart, the pressure in the left ventricle continues to rise well beyond that in the aorta during systole. Significant flow from the left ventricle takes place only during the first third of systole. The final part of systole is again similar to the normal heart, with relaxation of the left ventricle allowing the pressure to fall and the aortic valve to close. Criley and Siegel (1986) divide systole into three separate periods: (1) the initial period during which peak flow is achieved as left ventricular pressure and aortic pressure rise together; (2) a middle period in which flow decreases while the left ventricular pressure continues to increase while the aortic pressure decreases; and (3) a period of no flow while the left ventricular pressure continues to exceed the aortic pressure.

1.2 THE HCM CONTROVERSY

It is the origin and physiologic significance of the intraventricular pressure

difference that have been the source of a continuing controversy. This pressure difference is currently explained by a variety of causes. One possible cause suggested by researchers such as Pollick, Rakowski & Wigle (1984) and Maron, Gottdiener, Arce, Rosing, Wesley, and Epstein (1985) is an abnormal displacement of the anterior leaflet of the mitral valve during systole, commonly referred to as systolic anterior motion or SAM. It is postulated that as this leaflet becomes progressively displaced during systole, it blocks the flow from the left ventricle into the aorta, causing the pressure in the left ventricle to exceed that in the aorta. This abnormal displacement has been observed using echocardiography to detect contact between the mitral leaflet and the septum. It has been suggested that the cause of SAM-septal contact was a venturi effect due to rapid early systolic ejection.

Another variation of this mechanism is systolic anterior motion of the posterior leaflet of the mitral valve during systole, as suggested by Maron, Harding, Spirito, Roberts & Waller (1982). This is similar to the SAM concept, except that the posterior mitral leaflet is involved rather than the anterior leaflet. This has been detected using echocardiography. The suspected cause was a congenital elongation of a segment of the posterior mitral valve leaflet. This is less common than the aforementioned systolic motion of the anterior leaflet.

A second, more controversial theory, is that the abnormal pressure difference between the left ventricle and aorta are inertial in nature, due to a much higher rate of ejection and not caused by an obstruction, see Criley and Siegel (1985a). Since the pressure difference is proportional to the fluid acceleration, the pressure difference will be significantly enhanced if the rate of ejection is increased. One of the key points reinforcing this argument is that a left ventricle in HCM has a higher ejection fraction (ratio of the volume of blood ejected from the left ventricle to the total end-diastolic left ventricle volume) and ejects most of the volume during the first half of systole as shown in Figure

1.4. For example, Sugrue, McKenna, Dickie, Myers, Lavender, Oakley, and Goodwin

(1984) determined that a range of 59% to 95% of the stroke volume was ejected in the first

half of systole. This is significantly different than the normal left ventricle, where a range

of 59 to 76% was found during the first half of systole. In general, the normal left ventricle

ejects blood at a slower rate throughout the entire systolic period (see velocity plotted in

Figure 1.3). The basic premise of this theory is that if the left ventricle is emptying more

completely and at a faster rate than a normal heart, how could there possibly be an

obstruction? This theory is commonly referred to as a "non-obstructive" approach, while

the preceding two theories are denoted as "obstructive".

These differing viewpoints have created a controversy among cardiologists. This

controversy is quite serious, as treatments for HCM depend on the perceived cause. Until

recently, if the obstructive mechanism is favoured, a surgical technique was employed to

remove the obstruction, usually in the form of a septal myotomy-myectomy (a removal of

heart wall muscle tissue in the area of the suspected obstruction), to provide an

unobstructed path for the ejection from the left ventricle, Borer, Bacharach, Green, Kent,

Rosing, Seides, Morrow & Epstein (1979). A more recent procedure is to use left

ventricular pacing, Fananapazir, Cannon, Tripodi, and Panza (1992). This technique pre-

excites the interventricular septum using external electrical signals (pacing). This causes

the septum to move away from the left ventricular wall during systole, increasing the

outflow area and reducing the suspected obstruction. If a non-obstructive cause for HCM

is suspected, drug therapy is used to treat the disease, Criley and Siegel (1986). These are

very different treatments and thus it is of utmost importance to resolve the controversy

surrounding HCM.

1.3 CURRENT HCM RESEARCH

The basic question HCM research has attempted to answer is: can a progressive
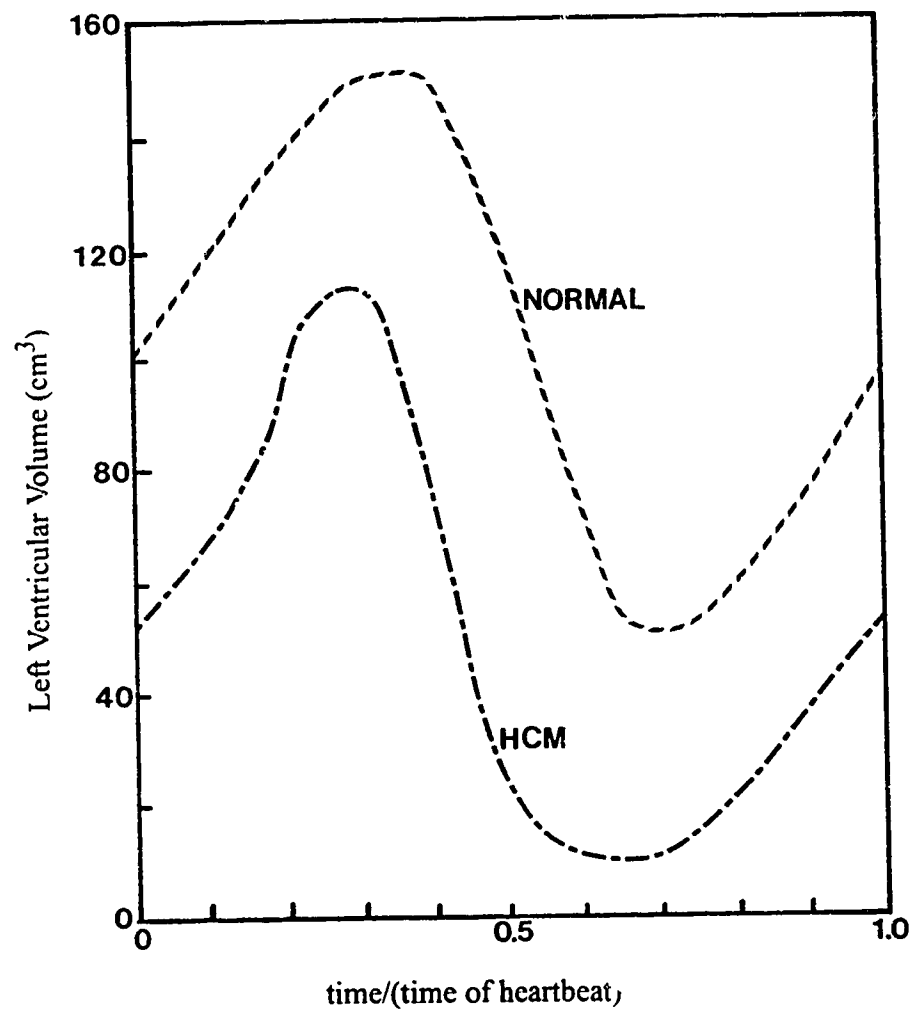
Figure 1.4: Left Ventricle Volume for Normal and HCM Patients.
Based on data from Criley and Siegel (1985b)

obstruction produce the pressure difference between the left ventricle and aorta during systole, and still permit the high rate of left ventricle emptying seen in HCM, or can this be produced without a physical obstruction? Several basic approaches have been used.

1.3.1 *In Vivo* Measurements

The first has been to make measurements of pressure and velocity *in vivo*, along with measurements of the physical positions of the relevant anatomy. Velocities have been measured with special catheters by Murgo *et al* (1980), but unfortunately the results have proved inconclusive. One of the problems has been that the *in vivo* measurements are invasive and thus disturb the flow. Another associated problem is that the left ventricle moves slightly with respect to the chest cavity during systole and thus there may be motion of the heart relative to the catheter. The flow into the aorta has also been measured intraoperatively with encircling flow probes (a "C" shaped electromagnetic flowmeter placed over an artery), and noninvasively by ultrasonic Doppler flowmeters. Physical positions have been measured using both radiographic techniques and echo-cardiography in an attempt to determine the relative positions of the heart walls and mitral leaflets. These techniques determined that some contact between the mitral leaflets and septum occurs for some patients, but the measurements only provide a two-dimensional picture of a complex three-dimensional shape. This observed leaflet-septum contact has not dispelled the controversy, as both the obstructive and non-obstructive theories can account for distortion of the mitral leaflets and subsequent septal contact.

1.3.2 Scale Modelling

Another approach has been to analyze the problem using laboratory scale modelling. Only two model tests have been reported, with mixed results. A model developed by White, Criley, Lewis and Ross (1967) was a latex replica of the left ventricle, complete with aortic and mitral valves. The entire model was contained within a

plastic box that could be pneumatically pressurized, causing the latex model to collapse, ejecting the fluid (water) from the left ventricle into an aortic outflow region. This outflow region was reinforced with plastic to prevent it from collapsing. Pressures were measured using catheters connected to pressure transducers. This model was capable of producing a difference in pressure between the aorta and left ventricle during systole without an obstruction. However, the model did not have a progressive obstruction to simulate the SAM mechanism, making comparisons between the unobstructed and obstructed theories inconclusive.

A second model, tested by Criley and Siegel (1986), consisted of a water-filled, conical latex sleeve, pinched off at its apex and emptying into a larger cavity at the open end. Similar to White's model, the sleeve was contained within a plastic box and contractions to simulate systole were achieved by injecting air pressure into the cavity surrounding the latex sleeve. Pressures were recorded using catheters while velocities were measured simultaneously using pulsed Doppler ultrasound techniques. Again, HCM-type pressure differences between the left ventricle and aorta were produced without an obstruction, but a progressive obstruction could not be simulated.

1.3.3 Computer Modelling

The third logical approach would be to apply numerical analysis, using computational fluid dynamics techniques. No work has been reported in this area, perhaps due to the complexity of the problem. There has been some computational fluid dynamics analysis performed for the *in vivo* left ventricle, but this was limited to normal left ventricles for low Reynolds numbers and laminar flow. Due to the irregular, moving boundaries involved, only a few researchers have ever attempted to model the normal left ventricle.

Peskin (1972, 1977, 1982) devised a numerical method to solve the Navier-Stokes equations (non-linear equations describing the fluid flow) for flow around heart valves in two dimensions. He was able to represent solid boundaries at mesh points within a periodic box, thus incorporating a model for the dynamics of the muscle itself. Peskin and Greenburg (1986) and Peskin and McQueen (1989) extended this method to three-dimensions. Their work was limited to laminar flow with very low Reynolds numbers (1/25 of the actual *in vivo* Reynolds numbers), and required the use of major computing facilities. The two-dimensional work was completed using a CDC 6600 computer; the three-dimensional work was done using a Cray X- MP/SSD computer (personal communication with Peskin, 1987).

In the area of arterial flows with moving boundaries interacting with the flow, there has also been very little research. Robertson, Clark and Cheng (1982) used a nonorthogonal geometric transformation to obtain numerical solutions for laminar viscous flow in a channel with an oscillating obstruction. By using boundary fitted coordinates, the physical domain was mapped onto a fixed computation grid. This work was limited to a 50% obstruction with Reynold numbers of up to 240, 20 times less than a normal human heart.

Ralph and Pedley (1988) extended this technique using multigrid methods to solve viscous laminar flow in a channel with a single periodic obstruction. This was a two-dimensional asymmetric case, with the obstruction forming on one wall only. Flows for Reynolds numbers of up to 670 were solved (still only 15% of the actual *in vivo* values associated with HCM).

Recently, Kiris, Rogers, Kwak and Chang (1993) used a computational approach to evaluate the flow in three-dimensions through an artificial heart. The approach utilized

artificial compressibility to model the internal flow and incorporated an algebraic turbulence model. The technique accounted for moving walls with prescribed wall motion, and gave flow predictions which compared well to experimental results for predicting velocity profiles and pressure losses.

1.4 PRESENT STUDY

The research described in this thesis approaches the problem from two directions: theoretical flow modelling and laboratory modelling. It was felt that the theoretical flow analy... would allow quantification of the geometry and flow rate components contributing to the pressure differences, while laboratory models could give valuable insight into the nature of the flow.

The theoretical analysis modelled the portion of systole in HCM when flow was occurring from the left ventricle into the aorta. This period is characterized by a pulsatile flow with pressure difference between the left ventricle and the aorta increasing as time progresses. It is this period of increasing pressure difference with decreasing flow rate that has caused most of the HCM debate on obstructionist vs. non-obstructionist mechanisms.

An analysis was undertaken to develop a parameter capable of characterizing the flow from the left ventricle into the aorta. This work is detailed in section 2.2, where a new parameter is developed that contains the Womersley paramet.· (a dimensionless parameter used to characterize pulsatile flow), a flow restriction factor and a geometry (heart shape) factor. This new parameter will be used to match the laboratory and mathematical models to the in vivo situation.

Another issue that must be addressed is the fluid - solid wall interaction. If the flow involved in HCM were to be modelled exactly, a model for the heart wall muscle

compliance would have to be included. However, Mirsky and Pasipoularides (1980) noted that heart muscle which has become hypertrophied is much stiffer than normal heart muscle. Thus selecting a non-compliant solid model for the moving walls seems reasonable and greatly simplifies the problem. As a result, most of the modelling done here used rigid walls. Some exploratory laboratory studies were carried out with compliant walls to explore these effects.

1.4.1 Laboratory Modelling Approach

In general, there have been very few flow models of the left ventricle and only two reported attempts to experimentally model HCM. While Bellhouse (1972) developed models to evaluate both mitral valve and aortic valve flows, he did not include the left ventricle as part of the model. The aorta has been modelled by researchers such as Clark (1976a and 1976b), Nerem and Seed (1972), Rodkiewicz (1975), and Walburn & Stein (1981), without the left ventricle. Models of artificial hearts have been developed, see Tarbel, Gunshinan, and Geselowitz (1986), but these are too dissimilar to a real heart to be useful for comparisons.

1.4.1.1 Transient Planar Piston Laboratory Model (Two-dimensional)

A deficiency of the previous models was the inability to directly control the motion of wall surfaces modelling the left ventricle. The approach taken here was to develop a laboratory model that had walls with controllable motion and position. This configuration allowed testing of both unobstructed and progressively obstructed theories.

The laboratory model is a simple, two-dimensional shape, illustrated in Figure 1.5. Two opposing rectangular pistons are forced together, driving the fluid into an outflow tract. Independent constriction wall control allowed for mild fixed restriction and progressively restricted configurations, shown in Figure 1.6. In addition, a severe fixed
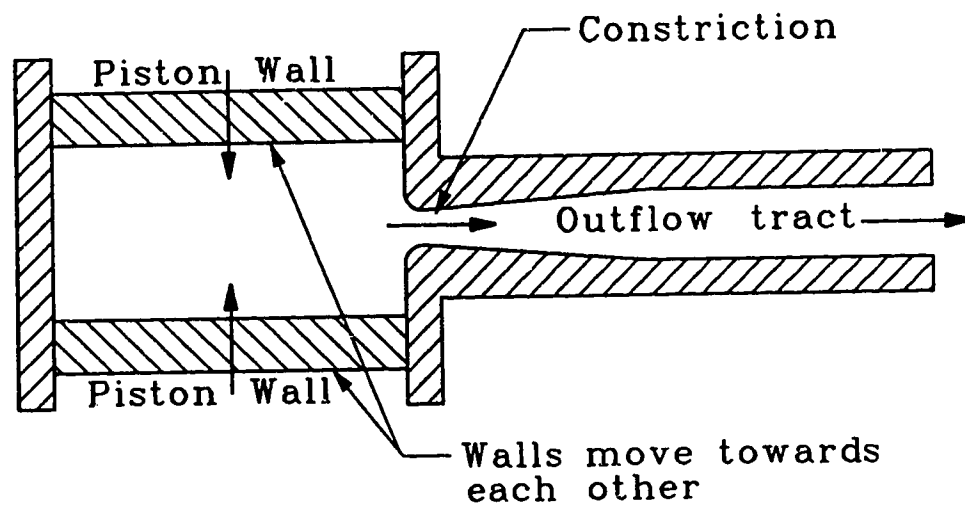
(a) Wall positions at the onset of motion
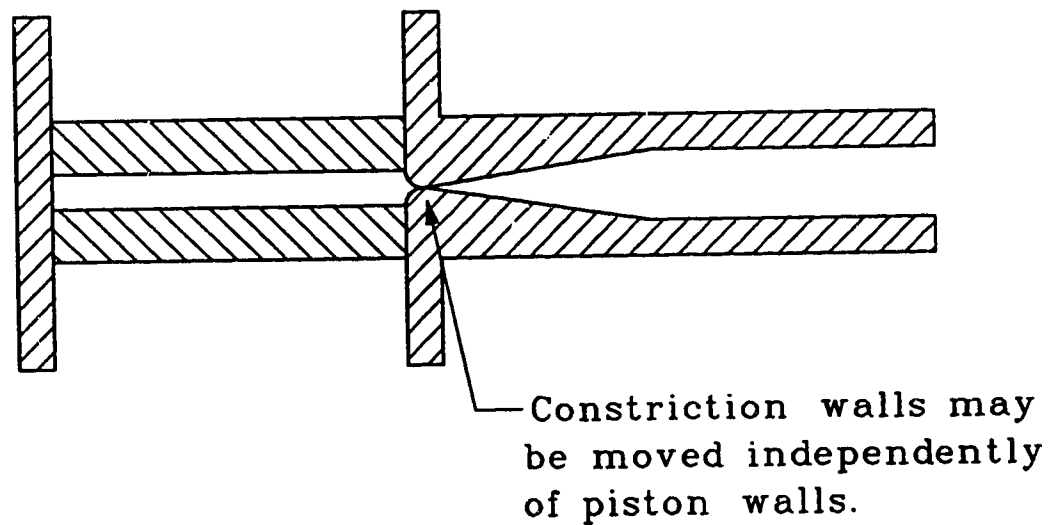
(b) Wall positions at the end of motion (progressive restriction shown)

Figure 1.5: General Model Configuration

Final Position

u_p

Restriction is minor and does not change throughout the contraction

u_p

Initial Position

(a) mild fixed restriction

Final Position

u_p

Restriction becomes progressively more severe

u_p

Initial Position

(b) progressive restriction

Final Position

u_p

Restriction is severe and does not change throughout the contraction

u_p
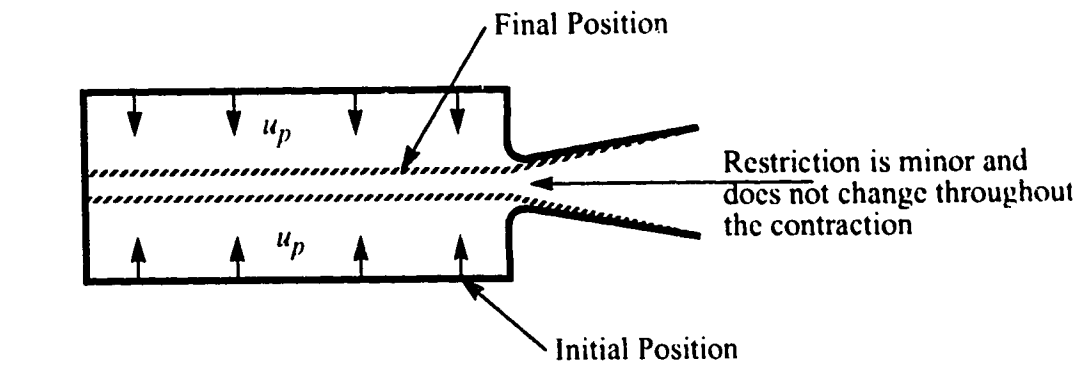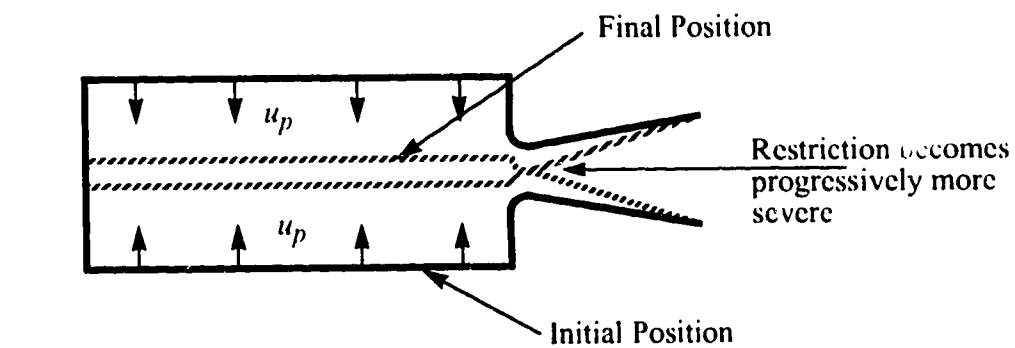
Initial Position
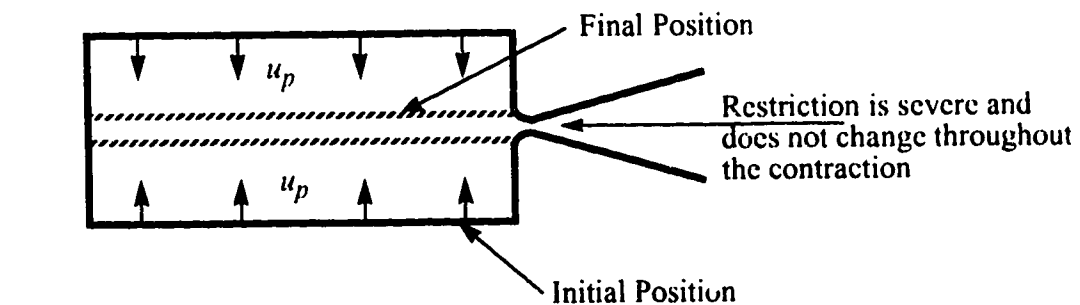
(c) severe fixed restriction

Figure 1.6: Laboratory Model Configurations

restriction capable of simulating a severe aortic valvular stenosis was tested for comparison purposes. Measurements of the mid-line pressure at discrete points along the flow were made, along with the corresponding wall positions. Flow visualization was performed using dyed fluid illuminated with laser light to provide a whole field picture of the flow for each configuration. The development and testing of this model is discussed in Chapter 5.

1.4.1.2 Steady Flow Laboratory Model (Two-dimensional)

To compare the computational fluid dynamics results directly with a laboratory model, a steady flow laboratory model was constructed. This model used flow through a pair of opposed porous plates to simulate the transient planar piston model with a steady flow. Two configurations were tested: mildly restricted and severely restricted. Flow visualization was performed in a similar fashion to the transient planar piston model. The pressure differences determined using the quasi-steady computational fluid dynamics model will be shown to be in agreement with this laboratory model, except where flow separation occurred. The development and testing of this model is discussed in Chapter 6.

1.4.2 Mathematical Modelling

1.4.2.1 Order of Magnitude Analysis (One-dimensional)

An order of magnitude analysis was performed to quantify the important forces acting on the fluid. This analysis used simple functions for the wall velocity to produce closed form solutions for flow parameters. By estimating the relative magnitude of the various forces contributing to the fluid pressures (inertial acceleration forces, viscous drag forces and spatial acceleration forces), it will be shown that viscous drag forces are negligible when compared to inertial and spatial acceleration forces. The force ratios determined using this analysis will also be used when comparing the laboratory and mathematical models to the *in vivo* situation to ensure proper modelling of the flow.

1.4.2.2 Inviscid Numerical Analysis (One dimensional)

When attempting mathematical analysis, one would like to use the simplest possible model while still incorporating the essential physics. The simplest model is a one-dimensional unsteady inviscid approximation. The advantage of this model was the ease with which variations of the geometry could be evaluated. A further variation of this model was the addition of a sudden expansion just downstream of the maximum constriction. By performing this analysis, a fully separated flow was simulated. This was useful for comparing to the laboratory models, where flow separations were found to exist.

1.4.2.3 Quasi-Steady Computational Fluid Dynamics Analysis (Two-dimensional)

As previously mentioned, there are no reported numerical simulations of HCM. In attempting to model HCM numerically, it became apparent that beginning with an exact replica of the left ventricle, complete with all its valves, and accounting for wall elasticity, would be impractical given current computational techniques and facilities. Instead, the approach taken was to begin with a simple model, utilizing a quasi-steady approach. A commercial computer code (FLOW3D) was utilized to solve a two-dimensional geometry similar to the shape used in the unsteady laboratory model. It will be shown that this model gives good predictions for highly obstructed flows where geometry-induced pressure loss is much larger than that caused by time-dependent flow acceleration, but does not predict the flow separation seen in the steady flow laboratory model. It will also be shown to give a good estimate of pressure loss in a severe HCM case.

1.4.3 Comparisons With *In Vivo* Results

A new way of analyzing HCM pressure-flow data will be developed by presenting the *in vivo* pressure-flow data as a non-dimensional pressure difference between the left ventricle and aorta *vs.* the fraction of volume ejected. The shape and magnitude of the resulting curve is a useful indicator for various types of left ventricle ejections. This technique separates HCM cases into either unobstructed or progressively obstructed

classifications. It shows that HCM patients with large non-dimensional pressure differences may indeed be experiencing a progressively restricted outflow, consistent with the obstructed flow theory (SAM).

CHAPTER 2 • ORDER OF MAGNITUDE FLOW ANALYSIS

2.1 INTRODUCTION

When undertaking numerical or laboratory modelling of fluid flows, it is often necessary to make simplifications to obtain solutions. These may take the form of:

- geometric simplifications, either in shape or size. In the present study, a simplified shape and enlarged size was used for numerical and laboratory modelling. The heart, which is approximately axisymmetric, was modelled in the laboratory using a two-dimensional planar flow model, with a scale factor of eight times the *in vivo* volume.

- the type of flow (steady *vs.* unsteady, laminar *vs.* turbulent, compliant walls *vs.* rigid walls, etc.). For example, the flow in this study was modelled both as unsteady to match the *in vivo* conditions and quasi-steady to allow a simplified computational analysis. Also, both laminar and turbulent computational flow modelling were used to analyze the two-dimensional planar flow model.

When making such simplifications, it is imperative that the important characteristics of the flow are retained. This can be achieved by ensuring that the ratios of various types of forces acting on the fluid are the same in the model and the *in vivo* situation. In this chapter, the important force ratios will be determined for an axisymmetric heart model. The axisymmetric shape was chosen because the cross-section of the left ventricle is approximately circular. The force ratios for the two-dimensional planar heart approximation used in the laboratory model are determined in Appendix A. A comparison between steady and unsteady flow forces will be developed. This will show that a steady flow simplification (quasi-steady analysis) of the *in vivo* flow may be valid where significant flow restrictions exist.

2.1.1 Flow Parameters

In order to decide what laboratory model to use, the parameters governing the models were first evaluated. The first concern was the fluid to use for the modelling. This should match the rheological properties of blood. Blood is a non-Newtonian fluid and consists of a collection of cells suspended in plasma, see Charm & Kurland (1974). The viscosity of blood increases with hematocrit (the volume percentage of cells) and increases to a lesser extent at low shear rates, see Cooney (1976). The hematocrit for adult males ranges from 40 to 50 percent, and from 35 to 45 percent for adult females, see Tortora, Evans & Anagnostakos (1982) and Liepsch (1986). This range in hematocrit causes the viscosity to vary from three to four times that of water. The common value used by most researchers is a viscosity of $0.038 \text{ cm}^2/\text{s}$, see for example Schultz, Tunstall-Pedoe, Lee, Gunning, and Bellhouse (1969). Research performed by Kunz and Coulter (1967) and Brech and Bellhouse (1973) determined that blood behaves as a Newtonian fluid when considered in larger vessels, such as arteries and capillaries, due to the presence of a plasma skimming layer near the vessel walls. The plasma skimming layer is a cell-free layer near the vessel wall that counteracts the increase in viscosity at low shear rates, see Cooney (1976, page 54). Recent work by Hogan and Henriksen (1989) has confirmed that velocities and streamlines are unaffected by non-Newtonian viscosity in larger vessels, even though there may be differences in shear stresses. In the present study, blood was modelled as a Newtonian fluid, and simulated using water in the experimental studies.

The second parameter to be considered was one that characterizes the flow during systole. Some researchers have used the Reynolds number (Re), which is the ratio of inertial to viscous forces acting on the fluid. There is about a factor of two variation in experimentally-determined Reynolds. This is to be expected, given the wide variance of body sizes and physical fitness in a normal population. For example, Jones (1969) used a peak Reynolds number of 5000 (based on the maximum flow rate and aortic diameter, for

a normal adult), Bellhouse and Bellhouse (1969) suggest a value of 3455 at rest and 8500 during exercise, and Cooney (1976) used a value of 3600 at rest and 5800 during exercise.

Other researchers, such as Bellhouse and Talbot (1969) have used the Strouhal number (St) to account for the pulsatile nature of the flow. The Strouhal number is the ratio of unsteady acceleration forces to dynamic pressure forces acting on the fluid in a constant geometry system (*i.e.* it does not account for moving walls). Another parameter is based on a combination of the Reynolds number and Strouhal number and is called the Womersley parameter α. This is defined as

$$\alpha = \left[\frac{\text{inertia force}}{\text{viscous force}} \frac{\text{unsteady acceleration force}}{\text{dynamic pressure force}} \right]^{0.5} = [ReSt]^{0.5}. \qquad (2.1)$$

This parameter is the ratio of stroke-averaged inertial to viscous forces for a fixed geometry. The Womersley parameter has been used by several researchers, such as Lutz, Hsu, Menawat, Zrubek and Edwards (1983) and Liepsch (1986) for flow in arteries. It is particularly well suited to arterial pulsatile flows.

2.2 ORDER OF MAGNITUDE ANALYSIS: AXISYMMETRIC HEART MODEL

Simple one and two-dimensional models were used to simulate the ejection period of the left ventricle. One way to determine dynamic similarity parameters is to compare ratios of the forces acting on the fluid. In the human heart, there are three forces to consider:

- **viscous** drag forces;
- **inertial** acceleration forces caused by the time dependant contraction;
- **spatial** acceleration forces caused by changes in geometry.

These forces will be referred to by the names in boldface, for convenience. Since there are three forces, two independent ratios are possible. The two ratios chosen here are the spatial to inertial forces, and the inertial to viscous forces (the third ratio, of spatial to viscous

forces, is just the product of the first two ratios). It was found that the spatial to inertial force ratio depends only on the geometry of the heart, while the inertial to viscous force ratio depends on fluid properties, flow rate parameters and geometry.

2.2.1 Simplified Heart Model

Consider the simplified axisymmetric heart model shown in Figure 2.1. The left
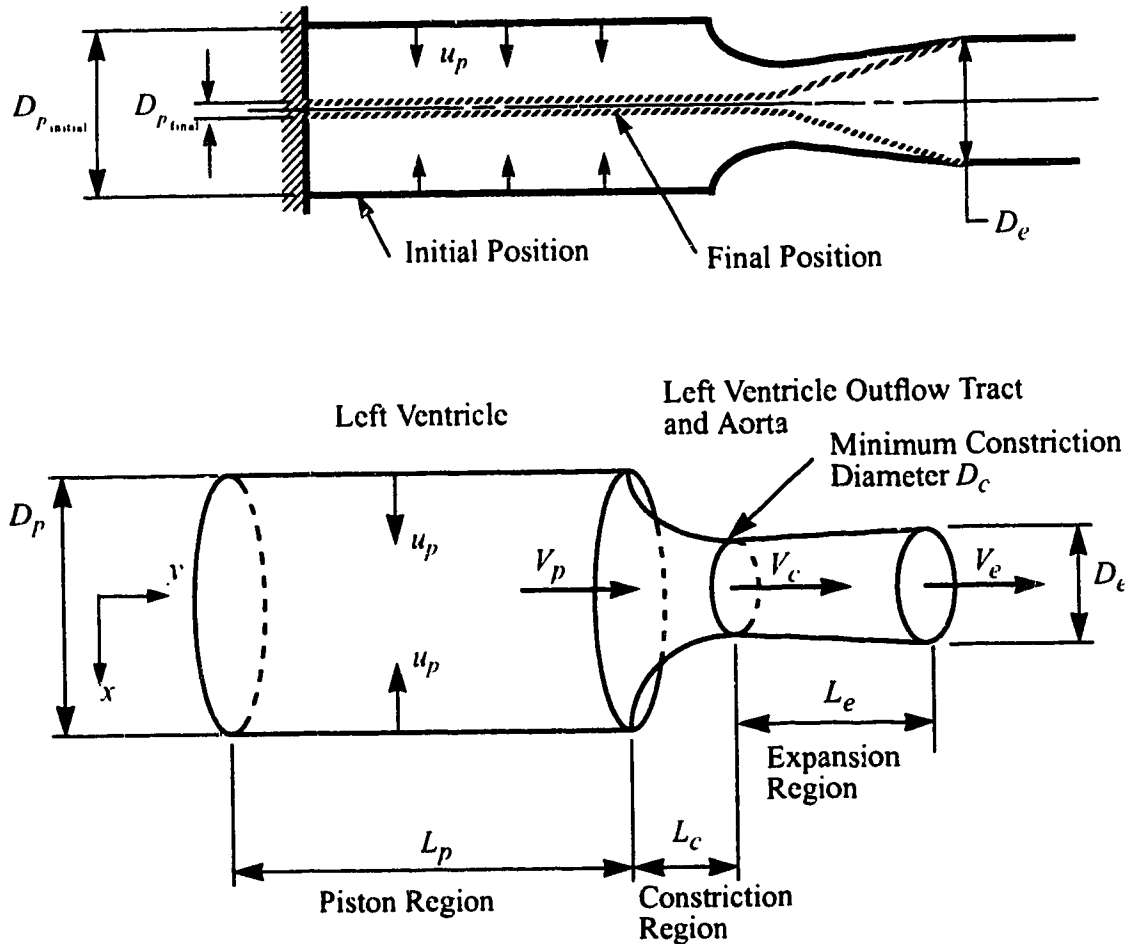
Figure 2.1: Contracting Cylinder Ventricle Model

ventricle is simulated as a radially contracting cylinder (piston), forcing the fluid through a smooth transition into the aorta. This transition may contain a restriction, with a minimum constriction diameter D_c. The aorta is modelled as a round tube of diameter D_e. The piston contracts with a radial wall velocity u_p.

To determine the forces involved, several assumptions were made:

> There is a period of constant flow acceleration, followed by a period of constant deceleration, as shown in Figure 2.2(a). This causes the variation in the exit velocity as shown in Figure 2.2(b) This triangular velocity-time curve approximates the *in vivo* HCM condition, shown in Figure 2.3.

(a) fluid acceleration at expansion exit   (b) fluid velocity at expansion exit (aorta)
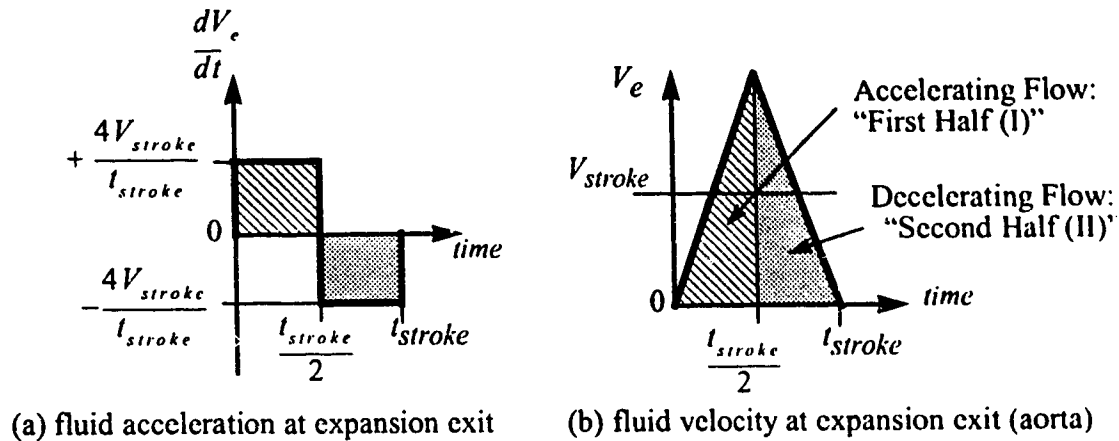
Figure 2.2: Idealized Fluid Velocity and Acceleration for Order of Magnitude Analysis
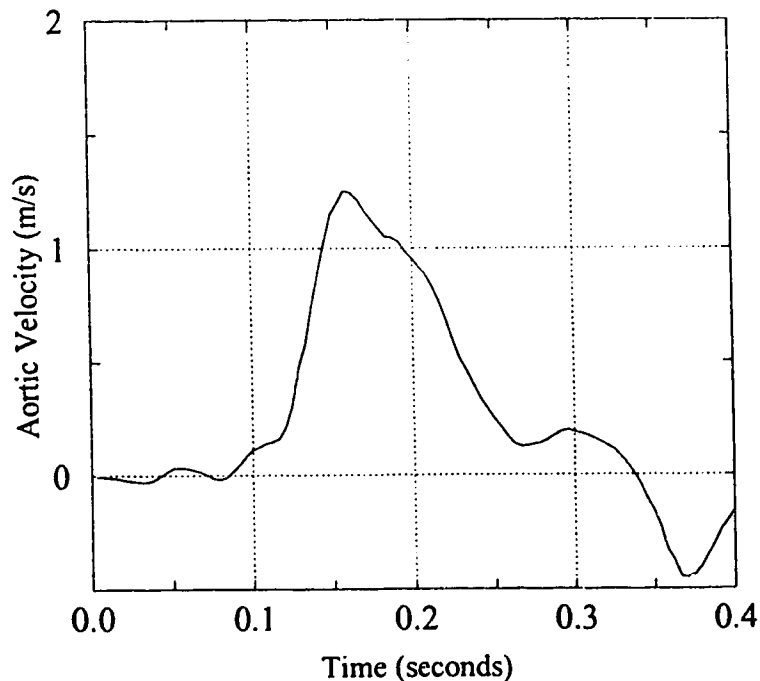
Figure 2.3: HCM Aortic Velocity From *In Vivo* Measurements by Murgo *et al* (1980).

- Flow separation may occur downstream from the restriction.

- The flow is uniform, with a flat cross-stream velocity profile.

Before determining the magnitudes of the fluid forces, some general flow parameters will be developed. These include the stroke volume and stroke velocity. The stroke volume is given by

$$\text{stroke volume} = \frac{\pi}{4}[D^2_{P_{initial}} - D^2_{P_{final}}]L_p,$$

where

$D_{P_{initial}}$ is the initial piston diameter;

$D_{P_{final}}$ is the final piston diameter;

L_p is the length of the piston region.

If the length L_p of the ventricle is approximated as $2D_{P_{initial}}$ (based on the left ventricular anatomy, see Teichholz, Kreulen, Herman, Gorlin (1976), used to simplify the analysis), the stroke volume becomes

$$\text{stroke volume} = \frac{\pi}{2}D_{P_{initial}}[D^2_{P_{initial}} - D^2_{P_{final}}].$$ (2.2)

The ejection time t_{stroke} is the time during which blood is flowing out of the left ventricle, and may be less than the systolic period. For this analysis, the ejection period is divided into two equal intervals, each $t_{stroke}/2$ in duration. These correspond to the acceleration (first half) and deceleration (second half) periods, as shown in Figure 2.2.

The velocity V_e at the exit of the flow expansion region, shown in Figure 2.2(a), is averaged over the ejection time to define an effective "stroke velocity" V_{stroke}

$$V_{stroke} = \frac{\text{stroke volume}}{(\text{expansion exit area})(\text{ejection time})}.$$ (2.3)

The stroke velocity is written in terms of the stroke volume (amount of blood ejected from

the left ventricle in each heartbeat), exit area and ejection time to allow direct comparison with *in vivo* data. For *in vivo* situations, the exit (aortic) velocity is rarely available. However, the stroke volume and stroke time are often measured, and the aortic diameter D_e for a normal adult is typically 25 mm, see Bellhouse & Bellhouse (1969). Because of difficulties in determining the exact start and end point of the flow period, the *in vivo* values are estimated as

$$V_{stroke} \approx \frac{(90\% \text{ of stroke volume})}{(\text{exit area})(\text{time for } 90\% \text{ of volume ejected})}.$$ (2.4)

In terms of the geometry of Figure 2.1,

$$V_{stroke} \approx \frac{2D_{P_{initial}}[D^2_{P_{initial}} - D^2_{P_{final}}]}{D^2_e t_{stroke}}.$$

In HCM, the stroke volume is large compared to the final volume (end systolic volume), so that $D_{P_{initial}}$ is much greater than $D_{P_{final}}$. In this case, $D_{P_{final}}$ in equation (2.4) is neglected, so that

$$V_{stroke} \approx \frac{2D^3_{P_{initial}}}{D^2_e t_{stroke}}$$ (2.5)

$$\text{stroke volume} \approx \frac{\pi}{2}D^3_{P_{initial}}.$$ (2.6)

The stroke volume can now be expressed in terms of the stroke velocity and the stroke time as

$$\text{stroke volume} \approx \frac{\pi}{4}D^2_e V_{stroke} t_{stroke}.$$ (2.7)

Having defined V_{stroke} and t_{stroke} and determined the stroke volume in terms of these parameters, the average inertial, viscous and spatial forces during the first half (acceleration) and second half (deceleration) of the stroke period will be determined. This will allow the calculation of the average inertial to viscous force ratio, and the average spatial to inertial force ratio.

2.2.2 Unsteady Inertial Acceleration Force, $F_{inertial}$

The unsteady inertial acceleration force $F_{inertial}$ required to accelerate the fluid volume is the mass of the fluid m multiplied by its acceleration a. The average value of $F_{inertial}$ will be found from

$$F_{inertial_{ave}} = \frac{1}{t}\int_0^t ma\, dt \tag{2.8}$$

Since the acceleration in the each half of the ejection period is constant, the average value of $F_{inertial}$ in each time interval is determined by the product of the acceleration and time averaged mass of fluid. Referring to Figure 2.2(a), the acceleration in the first half of the ejection period (acceleration) is given by

$$\frac{4V_{stroke}}{t_{stroke}} \tag{2.9}$$

and in the second half of the ejection period (deceleration) is

$$-\frac{4V_{stroke}}{t_{stroke}}. \tag{2.10}$$

The mass fluid in the control volume being accelerated is the mass within the piston region: the mass within the constriction and expansion regions is small in comparison and thus neglected. During the ejection period, the fluid mass decreases with time because the piston volume is decreasing. The flow rate through the expansion region exit increases and decreases linearly as shown in Figure 2.4(b).

The mass flow rate is

$$\dot{m} = \rho V_e \frac{\pi D_e^2}{4}, \tag{2.11}$$

where V_e varies with time as shown in Figure 2.2(b). During the first half of the ejection period (acceleration), this velocity is

$$V_{e_1} = 4V_{stroke}\frac{t}{t_{stroke}}, \tag{2.12}$$

while during the second half of the ejection period (deceleration) is

(a) Mass in control volume　　　　　(b) Flow rate through expansion exit
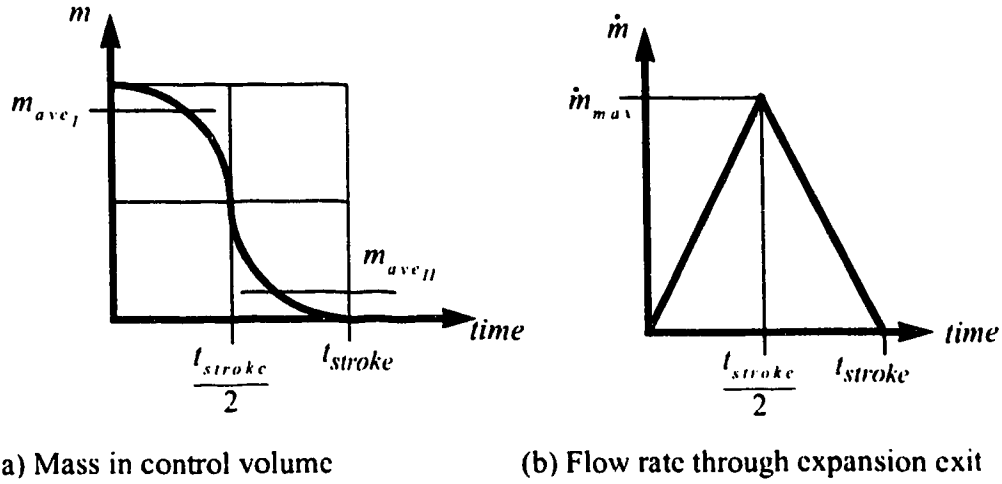
Figure 2.4: Fluid Mass Variation in the Axisymmetric (Cylindrical) Heart Model

$$V_{e_{II}} = 2V_{stroke}\left[1 - 2\left[\frac{t - \frac{t_{stroke}}{2}}{t_{stroke}}\right]\right]. \qquad (2.13)$$

The subscripts *I* and *II* will be used throughout to denote the first and second halves of the ejection period. At any time, the mass being accelerated can be determined from the flow rate $\dot{m}$

$$m(t) = m_{initial} - \int \dot{m}dt \qquad (2.14)$$

where $m_{initial}$ is the initial mass in the control volume, and the flow rate is given by equations 2.11-2.13. The average mass being accelerated in each time interval is

$$m_{ave} = \frac{1}{t_2 - t_1}\int_{t_1}^{t_2} m(t)\, dt. \qquad (2.15)$$

For the first half (acceleration) of the ejection, this becomes

$$m_{ave_I} = \frac{5}{24}\pi\rho D_e^2 V_{stroke} t_{stroke}, \qquad (2.16)$$

while for the second half (deceleration) the average mass is

$$m_{ave_{II}} = \frac{1}{24}\pi\rho D_e^2 V_{stroke} t_{stroke}. \qquad (2.17)$$

As shown in Figure 2.4(a), the average mass accelerated in the first half is much more than

the average mass decelerated in the second half of the ejection period. Multiplying the average mass with the constant acceleration (equations 2.9 and 2.10), the average inertial force is

$$F_{inertial_I} = \frac{5}{6}\pi D_e^2 \rho V_{stroke}^2 \tag{2.18}$$

during the first half (acceleration) and

$$F_{inertial_{II}} = -\frac{1}{6}\pi D_e^2 \rho V_{stroke}^2 \tag{2.19}$$

during the second half (deceleration) of the ejection period. Due to the mass variation with time, the inertial force is five times larger during the first half of the ejection period. The direction of the inertial force reverses for the second half of the ejection period, as fluid is decelerated. Forces due to geometric changes and viscosity are not included here because they will be accounted for in the spatial and viscous forces.

2.2.3 Viscous Drag Force, $F_{viscous}$

The viscous force acting on the fluid during the ejection period (systole) can be estimated from the wall shear stress τ_w as

$$F_{viscous} = \tau_w \, (\text{shear surface area}) . \tag{2.20}$$

In this section, the instantaneous wall shear stress will be determined for each half of the ejection period, followed by an estimation of the instantaneous shear surface area. Using these values, the instantaneous viscous force will be determined and averaged. For laminar flow, the wall shear stress may be estimated from

$$\tau_w = \mu \frac{\partial U}{\partial x}$$

$$\tau_w \approx \frac{\mu V_p}{\delta_{ave}}, \tag{2.21}$$

where V_p is the velocity in the piston region and δ_{ave} is the average boundary layer thickness. The boundary layer growth along the piston walls is approximated by a suddenly

accelerated plane wall of infinite length. Nerem and Seed (1972) suggested this accelerated infinite wall approximation for the boundary layer thickness is a reasonable estimate for the aortic wall boundary layer. For the case considered here, this approximation is less valid because the wall is not infinite in length and thus has a leading edge. As a result, using the accelerated infinite wall approximation may overestimate the boundary layer thickness for the finite length piston wall. The classic solution of Stokes problem, Schlichting (1979, page 91), gives the boundary layer thickness of a suddenly accelerated plane wall moving at a constant velocity as

$$\delta \approx 4\sqrt{vt} \tag{2.22}$$

where v is the kinematic viscosity and t is the time from the onset of motion. In equation 2.22 the boundary layer thickness is the point where the fluid velocity has decreased to 1% of the wall velocity.

The time-average boundary layer thickness for the first half (acceleration) of the ejection period is then

$$\delta_{ave_I} \approx 2\,[vt_{stroke}]^{1/2}. \tag{2.23}$$

During the second half (deceleration) of the ejection period

$$\delta_{ave_{II}} \approx 2\sqrt{3}\,[vt_{stroke}]^{1/2}. \tag{2.24}$$

Since the boundary layer thickness is increasing with time, the wall shear stress should decrease. However, the velocity V_p is simultaneously increasing, causing the wall shear stress to increase with time. This variation in piston velocity will now be determined. Instantaneous values will be used rather than determining the time averaged values to avoid problems caused by $V_p \rightarrow \infty$ as $t \rightarrow t_{stroke}$.
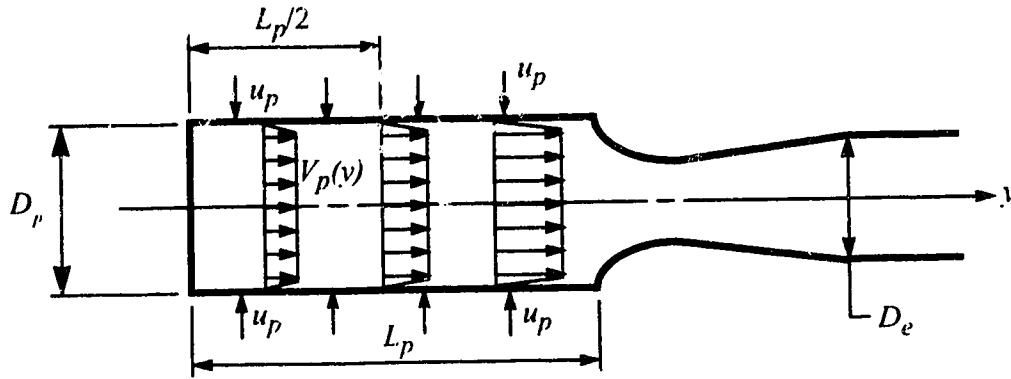
Figure 2.5: Variation in Piston Region Velocity

The velocity V_p in the piston region increases linearly along the piston length, as shown in Figure 2.5. This velocity will vary with time and position, so that

$$V_p(y,t) = \frac{\left[\dfrac{dA_p}{dt}\right]y}{A_p} \tag{2.25}$$

where A_p is the cross-sectional area of the piston region at any time t. The spatial average velocity along the piston region at time t will be the velocity at $y = L_p/2$, because the velocity varies linearly between $y=0$ and $y=L_p$. For the first half (acceleration) of the ejection period, the instantaneous fluid velocity is

$$V_{p_I}\left(y=\frac{L_p}{2},t\right) = \frac{4D_{p_{initial}}\,t}{\left[1-2\left[\dfrac{t}{t_{stroke}}\right]^2\right]t_{stroke}^2}, \tag{2.26}$$

and for the second half (deceleration) is

$$V_{p_{II}}\left(y=\frac{L_p}{2},t\right) = \frac{4D_{p_{initial}}}{\left[1-2\left[\dfrac{t-\dfrac{t_{stroke}}{2}}{t_{stroke}}\right]\right]t_{stroke}}. \tag{2.27}$$

Note that as previously mentioned, $V_{p_{II}} \rightarrow \infty$ as $t \rightarrow t_{stroke}$. The time averaged value dur-

ing the second half (deceleration) of the ejection period would then be infinite. This problem is avoided by noting that the shear surface area simultaneously approaches zero. If the instantaneous values of velocity and surface area are used to determine the viscous force, the two effects cancel and a finite value is obtained.

The instantaneous shear surface area is given by

$$A_{surf_I} = \pi D^2_{P_{initial}} \left[1 - 2\left[\frac{t}{t_{stroke}} \right]^2 \right]^{1/2}$$ (2.28)

during the first half (acceleration) and

$$A_{surf_{II}} = \sqrt{2}\pi D^2_{P_{initial}} \left[1 - 4\left[\frac{t - \frac{t_{stroke}}{2}}{t_{stroke}} \right] + 4\left[\frac{t - \frac{t_{stroke}}{2}}{t_{stroke}} \right]^2 \right]^{1/2}$$

during the second half (deceleration) of the ejection period. This reduces to

$$A_{surf_{II}} = \sqrt{2}\pi D^2_{P_{initial}} \left[1 - 2\left[\frac{t - \frac{t_{stroke}}{2}}{t_{stroke}} \right] \right].$$ (2.29)

Using the approximation for the boundary layer thicknesses (equations 2.23 and 2.24), velocities (equations 2.26 and 2.27) and surface areas (equations 2.28 and 2.29), the instantaneous viscous force (equation 2.20) during the first half (acceleration) becomes

$$F_{viscous_I} \approx 4\pi\rho \sqrt{\frac{\nu}{t_{stroke}}} \frac{D^3_{P_{initial}}}{t^2_{stroke}} \frac{t}{\left[1 - 2\left[\frac{t}{t_{stroke}} \right]^2 \right]^{0.5}}$$ (2.30)

and

$$F_{viscous_{II}} \approx 1.6\pi\rho \sqrt{\frac{\nu}{t_{stroke}}} \frac{D^3_{P_{initial}}}{t_{stroke}}$$ (2.31)

during the second half (deceleration) of the ejection period. As equation 2.31 shows, the

effect of the piston velocity $V_p \to \infty$ as $t \to t_{stroke}$ has been balanced by the surface area $A_{surf} \to 0$. Thus the two time dependant terms have cancelled, causing the viscous force to be constant in the second half of the ejection period. The average viscous force for each half of the ejection period is found from

$$F_{viscous_{ave}} \approx \frac{1}{t_2 - t_1} \int_{t_1}^{t_2} F_{viscous} \, dt.$$

The average viscous force during the acceleration period is

$$F_{viscous_{I_{ave}}} \approx 1.2 \pi \rho \sqrt{\frac{\nu}{t_{stroke}}} \; \frac{D^3_{P_{initial}}}{t_{stroke}}, \qquad (2.32)$$

and during the deceleration period is

$$F_{viscous_{II_{ave}}} \approx 1.6 \pi \rho \sqrt{\frac{\nu}{t_{stroke}}} \; \frac{D^3_{P_{initial}}}{t_{stroke}}. \qquad (2.33)$$

Thus the viscous force is on average 25% larger during the second half (deceleration) in comparison to the first half (acceleration) of the ejection period.

2.2.4 Spatial Acceleration Force, $F_{spatial}$

The spatial acceleration force required to push the fluid through the constriction is modelled two different ways. The first is to model the downstream side of the constriction as a sudden expansion, shown in Figure 2.6. This simulates a separated flow which gives
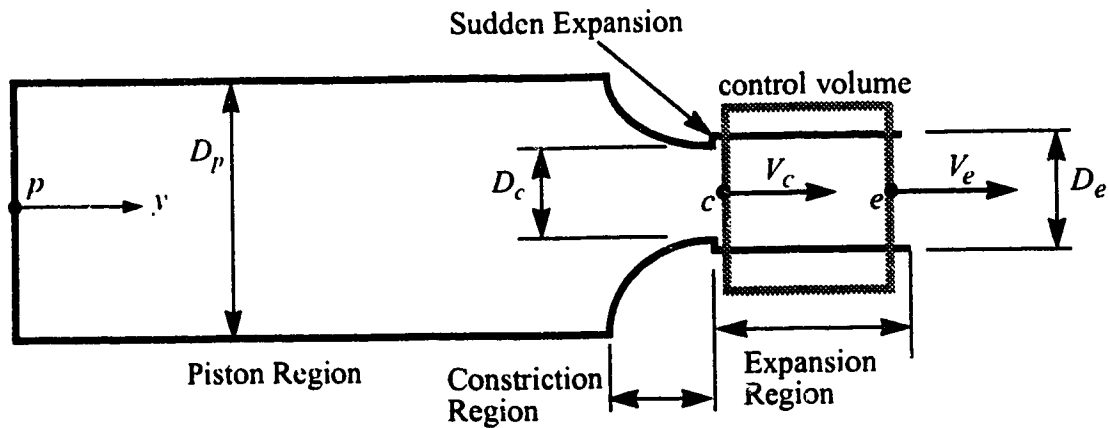
Figure 2.6: Constriction Geometry With Sudden Expansion
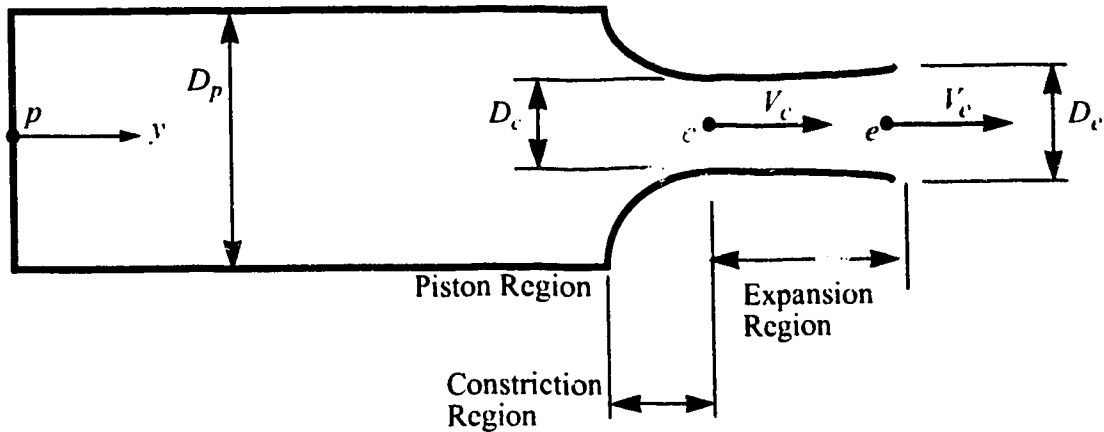
Figure 2.7: Constriction Geometry Without Sudden Expansion

the least amount of pressure recovery in the expansion (separated flow is flow with a high velocity core and reverse flow near the walls; this type of flow does not recover pressure well). The second method is to assume no separation and use the Bernoulli equation to estimate the pressure difference between c and e. The geometry for the second case is shown in Figure 2.7.

The reason for using two different models was to set the upper and lower bounds on pressure difference: separated flow where the kinetic energy loss is large, and fully attached flow where the kinetic energy loss is zero. Both methods first determine the pressure drop between p and e, then determine the spatial acceleration force $F_{spatial}$ by multiplying the pressure drop by the flow area.

2.2.4.1 First Case: Sudden Expansion to Induce Flow Separation

For a sudden expansion, pressure differences will be determined using the Bernoulli equation between p and c, and a linear momentum analysis for the sudden expansion between c and e. Rather than use the unsteady form of the Bernoulli equation,

which includes both spatial and inertial acceleration effects, the steady form of the Bernoulli equation is used. This avoids including the inertia terms, as these are accounted for in $F_{inertial}$.

Noting that the velocity at p is zero (p is located against a fixed wall), the instantaneous pressure drop between p and c will be

$$P_p - P_c \approx \frac{1}{2}\rho V_c^2.$$

Using continuity to relate the velocity V_c to V_e,

$$P_p - P_c \approx \frac{1}{2}\rho V_e^2 \left[\frac{D_e}{D_c}\right]^4. \tag{2.34}$$

Note that D_c may vary with time, depending on the situation being modelled. For the normal heart, fixed stenosis and unobstructed HCM case, D_c will be a constant value, while for the progressive restriction HCM cases, D_c will become smaller during the ejection period.

Consider the control volume shown in Figure 2.6. This control volume starts just downstream of the constriction. It is assumed that the pressure across the control volume at c is uniform and equal to P_c. Applying a linear momentum analysis along the control volume from c to e, the instantaneous pressure difference is

$$P_c \frac{\pi}{4}D_e^2 - P_e \frac{\pi}{4}D_e^2 = \rho V_c^2 \frac{\pi}{4}D_c^2 - \rho V_e^2 \frac{\pi}{4}D_c^2. \tag{2.35}$$

Recognizing that V_c is related to V_e through continuity, equation 2.35 becomes

$$P_e - P_c = \rho V_c^2 \left[1 - \left[\frac{D_e}{D_c}\right]^2\right]. \tag{2.36}$$

Equating the two pressure equations 2.34 and 2.36, the instantaneous pressure difference is

$$P_p - P_c \approx \frac{\rho V_c^2}{2}\left[2 - 2\left[\frac{D_e}{D_c}\right]^2 + \left[\frac{D_e}{D_c}\right]^4\right]. \tag{2.37}$$

The instantaneous spatial force required to overcome this pressure loss is

$$F_{spatial} \approx \frac{\pi D_p^2 \rho V_e^2}{4} \left[1 - \left[\frac{D_c}{D_e} \right]^2 + \frac{1}{2} \left[\frac{D_c}{D_e} \right]^4 \right].$$ (2.38)

The minimum constriction diameter D_c may vary with time and its average value for the ejection period is denoted as $D_{c_{ave}}$. The average spatial acceleration force is determined from

$$F_{spatial_{ave}} = \frac{1}{t} \int_0^t F_{spatial} dt$$ (2.39)

During the first half (acceleration) of the ejection period,

$$F_{spatial_{I_{ave}}} \approx 0.233 \pi D_{p_{initial}}^2 \rho V_{stroke}^2 \left[1 - \left[\frac{D_c}{D_{c_{ave}}} \right]^2 + \frac{1}{2} \left[\frac{D_c}{D_{c_{ave}}} \right]^4 \right]$$ (2.40)

and during the second half (deceleration) of the ejection period

$$F_{spatial_{II_{ave}}} \approx 0.100 \pi D_{p_{initial}}^2 \rho V_{stroke}^2 \left[1 - \left[\frac{D_c}{D_{c_{ave}}} \right]^2 + \frac{1}{2} \left[\frac{D_c}{D_{c_{ave}}} \right]^4 \right].$$ (2.41)

2.2.4.2 Second Case: No Separation

The second method of determining the spatial force is to have no flow separation through the expansion region. In this case, kinetic energy as well as momentum is conserved. Using the steady form of the Bernoulli equation to find the instantaneous pressure difference between p and e (Figure 2.7),

$$P_p - P_e = \frac{1}{2} \rho [V_e^2 - V_p^2]$$ (2.42)

Again, $V_p = 0$, and the instantaneous spatial force required to overcome this pressure loss is

$$F_{spatial} \approx \frac{\pi D_p^2 \rho V_e^2}{8}.$$ (2.43)

The average spatial acceleration force is determined as before (equation 2.39) for the first half (acceleration) of the ejection period to give

$$F_{spatial_{I_{ave}}} \approx 0.117\pi D_{P_{initial}}^2 \rho V_{stroke}^2 \qquad (2.44)$$

while during the second half (deceleration) of the ejection period

$$F_{spatial_{II_{ave}}} \approx 0.050\pi D_{P_{initial}}^2 \rho V_{stroke}^2. \qquad (2.45)$$

2.2.5 Dimensionless Parameters

A dimensionless parameter that may be used to describe the flow f om the left ventricle into the aorta is obtained from the ratio of the average acceleration force $F_{inertial}$ (equations 2.18 and 2.19) to the average viscous force $F_{viscous}$ (equations 2.32 and 2.33) during each half of the ejection period. This yields, during acceleration

$$\left. \frac{F_{inertial}}{F_{viscous}} \right|_{I} \approx 2.8 \left[\frac{D_{P_{initial}}}{D_c} \right]^3 Re_D^{0.5} St_D^{0.5} \qquad (2.46)$$

and during deceleration

$$\left. \frac{F_{inertial}}{F_{viscous}} \right|_{II} \approx 0.4 \left[\frac{D_{P_{initial}}}{D_e} \right]^3 Re_D^{0.5} St_D^{0.5} \qquad (2.47)$$

where

$$St_D = \text{Strouhal Number} = \frac{D_c}{V_{stroke} t_{stroke}} = \frac{\text{unsteady acceleration force}}{\text{dynamic pressure force}},$$

$$Re_D = \text{Reynolds Number} = \frac{V_{stroke} D_c}{\nu} = \frac{\text{inertia force}}{\text{viscous force}},$$

The subscript D is used to denote that the parameter is based on aortic diameter. The Womersley parameter α is defined as

$$\alpha = Re_D^{0.5} St_D^{0.5}$$

and is often used to characterize the motion of blood in an artery, see Womersley (1955). Variations of this parameter have been used by researchers to characterize the flow in arteries. Liepsch (1986), for example, used the definition given here, while Lutz et al (1983) used $[0.5\pi Re_D St_D]^{0.5}$ rather than $[Re_D St_D]^{0.5}$ for α, so care must be taken

when comparing values of α given in the literature. Averaging the force ratio equations 2.46 and 2.47, and denoting $[Re_D St_D]^{0.5}$ as α_D, the overall average during the ejection period is

$$\frac{F_{inertial}}{F_{viscous}} \approx 1.6\beta_D^3\alpha_D,$$ (2.48)

where

$$\beta_D = \text{geometry factor} = \frac{D_{P_{initial}}}{D_e}.$$

Defining α_D in terms of the square root of $Re_D St_D$ is logical, as it gives a linear relationship between α_D and the inertial to viscous force ratio. Equation 2.48 shows that flow from the left ventricle into the aorta may be characterized with the Womersley parameter and a geometry factor. Thus, a laboratory model will match the *in vivo* situation if it has the same Womersley parameter and is geometrically similar. Some typical values of the Womersley parameter α for left ventricular ejection are shown in Table 2.1, based on data from Murgo *et al* (1980) and Clark (1976a) and a 25 mm diameter aorta (D_e).

Table 2.1: Comparison of Dimensionless Parameters for the Human Heart

Heart Configuration	Re_D	St_D	α_D	β_D	$\dfrac{F_{inertial}}{F_{viscous}}$
normal heart	6311	0.138	29.5	1.5	159
HCM: resting	7443	0.132	31.3	1.5	169
HCM: provoked	13580	0.090	35.0	1.8	327
severe aortic valvular stenosis	1876	0.175	18.1	1.4	79

As Table 2.1 shows, the inertial to viscous force ratio is almost the same for a normal heart and the resting HCM heart. However, the provoked HCM heart (the resting HCM heart caused to eject at a higher rate) has a ratio twice the normal heart, while the severe aortic stenosis ratio is a factor of two smaller than the normal heart. This difference is due primarily to the high rate of ejection in the provoked HCM heart, and the low rate of ejection of the stenosed heart with its obstructed outlet. In general, this ratio seems to be a sensitive indicator of the degree of impediment to ejection. The severe aortic valvular

stenosis gives a low value (79). The provoked HCM case, which ejected the blood in the left ventricle more completely (higher ejection fraction) and more quickly, gives a high value (327) for inertial to viscous forces.

The inertial to viscous force ratio is shown graphically in Figure 2.8. Clearly, the higher the Womersley parameter (faster rates of ejection) and the larger the geometry factor, the more the inertial forces dominate over the viscous forces. This would suggest that an inviscid analysis may be adequate, especially for HCM cases.
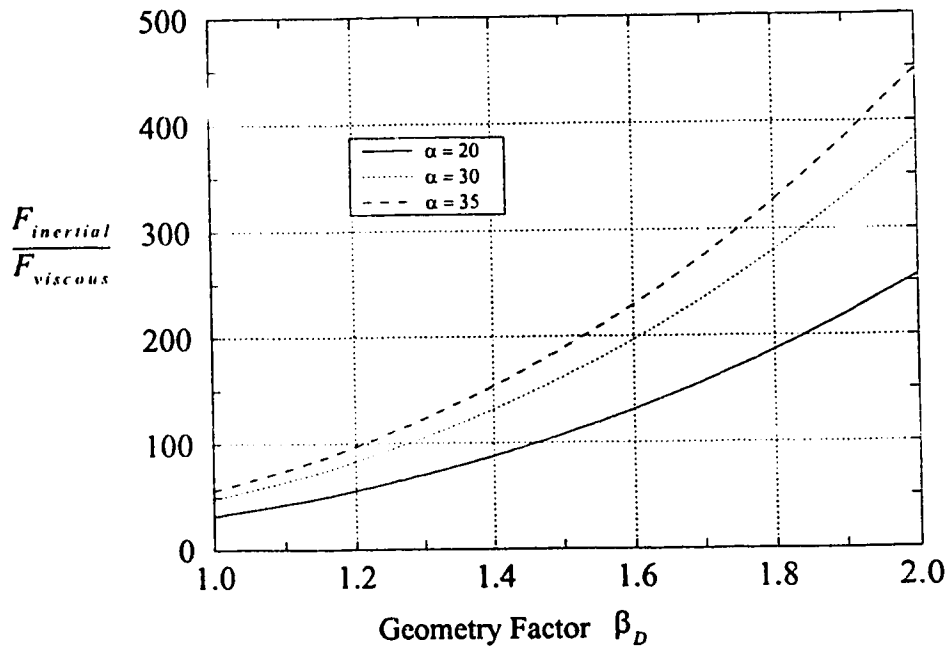
Figure 2.8: **Fffect of Womersley Parameter** $\alpha = Re^{0.5}St^{0.5}$ **and Geometry Factor on Inertial/Viscous Force Ratio**

A second dimensionless parameter may be obtained from the ratio of the spatial force with the sudden expansion (equations 2.40 and 2.41) and inertial force (equations 2.18 and 2.19):

$$\left.\frac{F_{spatial}}{F_{inertial}}\right|_I \approx 0.25 \left[\frac{D_{P_{initial}}}{D_e}\right]^2 \left[1 - \left[\frac{D_e}{D_c}\right]^2 + \frac{1}{2}\left[\frac{D_e}{D_c}\right]^4\right]$$

$$\left.\frac{F_{spatial}}{F_{inertial}}\right|_{II} \approx 0.60 \left[\frac{D_{P_{initial}}}{D_e}\right]^2 \left[1 - \left[\frac{D_e}{D_c}\right]^2 + \frac{1}{2}\left[\frac{D_e}{D_c}\right]^4\right].$$

The overall average of the acceleration and deceleration ratios is

$$\frac{F_{spatial}}{F_{inertial}} \approx 0.44 \left[\frac{D_{P_{initial}}}{D_e}\right]^{0.5} \left[1 - \left[\frac{D_e}{D_c}\right]^2 + \frac{1}{2}\left[\frac{D_e}{D_c}\right]^4\right] \qquad (2.49)$$

This can be expressed using the geometry factor β_D and a restriction factor η_D:

$$\frac{F_{spatial}}{F_{inertial}} \approx 0.44\beta_D^2 \left[1 - \eta_D^2 + \frac{1}{2}\eta_D^4\right] \qquad (2.50)$$

where

$$\eta_D = \text{restriction factor} = \frac{D_e}{D_c}$$

If the spatial force for the unseparated expansion is used in the ratio,

$$\left.\frac{F_{spatial}}{F_{inertial}}\right|_{\text{unseparated expansion}} \approx 0.22\beta_D^2. \qquad (2.51)$$

It is interesting to note that the spatial to inertial force ratio depends only on geometry. Table 2.2 shows typical values for the ratios based on *in vivo* data. The restricted cases of HCM use an average restriction factor of 1.5 and 2 to simulate systolic anterior motion of the mitral valve. The unrestricted case of HCM uses the same restriction factor as a normal heart. The normal and severe restriction factors are from Clark (1976a). The initial piston region diameters are based on the data of Murgo *et al* (1980).

When full pressure recovery is assumed, the inertial force is dominant, especially in the first half of systole. If sudden expansion is assumed, the spatial/inertial force ratio depends on the restriction factor, because the geometry factor does not vary significantly. When the restriction becomes severe, the spatial force dominates, see Figure 2.9. For the case of severe aortic valvular stenosis, the inertial forces are negligible compared with the spatial forces provided flow separation occurs. The ratio $F_{spatial}/F_{inertial}$ is a sensitive
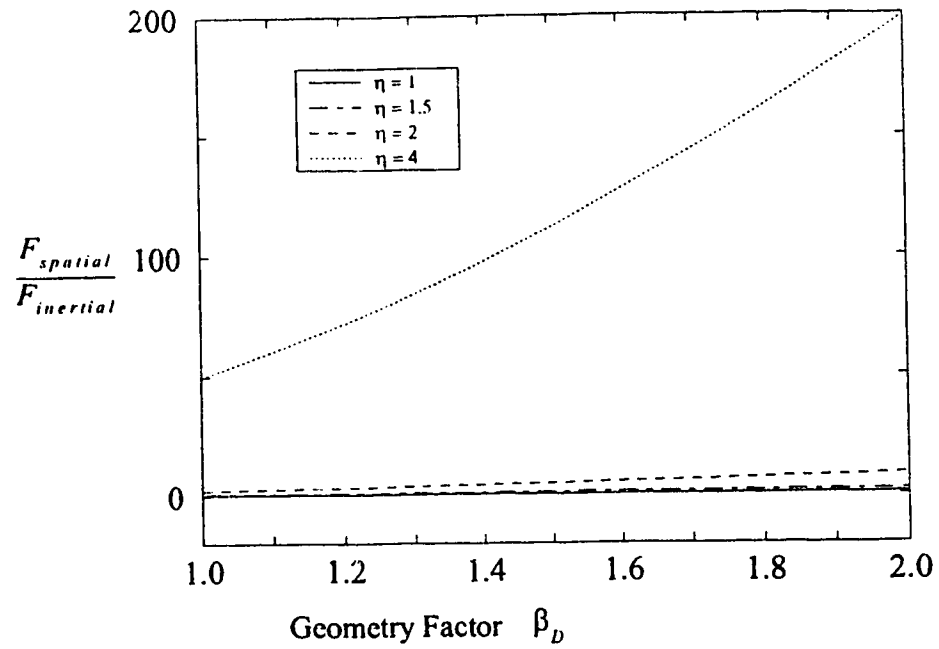
Figure 2.9: Effect of Restriction and Geometry Factor $\beta_D = \dfrac{D_{p_{initial}}}{D_e}$ and Restriction Factor $\eta_D = \dfrac{D_c}{D_c}$ on Spatial to Inertial Force Ratio.
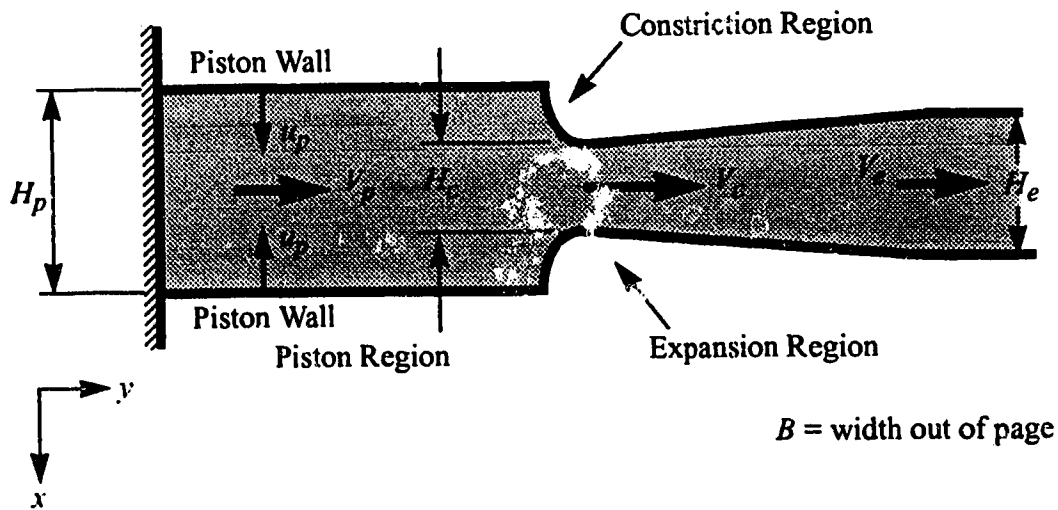
Figure 2.10: Planar Heart Model Geometry

Table 2.2: Comparison of Spatial/Inertial Force Ratio for *In Vivo* Hearts

Heart Configuration	η_D	β_D	$\dfrac{F_{spatial}}{F_{inertial}}$	
			Sudden Expansion	Unseparated Expansion
normal heart	1.05	1.5	0.99	0.50
HCM: unrestricted, resting	1.05	1.5	0.99	0.50
HCM: unrestricted, provoked	1.05	1.8	1.4	0.71
HCM: mildly restricted, resting	1.5	1.5	1.3	0.50
HCM: mildly restricted, provoked	1.5	1.8	1.8	0.71
HCM: very restricted, resting	2.0	1.5	5.0	0.50
HCM: very restricted, provoked	2.0	1.8	7.1	0.71
severe aortic valvular stenosis	4.0	1.4	97	0.43

indicator of flow separation effects, especially in obstructed outlet conditions.

2.2.6 Comparison With Planar Configuration

The laboratory models were planar with opposed flat, rectangular pistons rather than an axisymmetric circular configuration. This planar geometry was also analyzed to determine dimensionless parameters. The details may be found in Appendix A.1. The configuration that was used is shown in Figure 2.10. Two flat piston walls move towards each other, driving the fluid past a constriction into an exit channel. The average ratio of inertial to viscous forces is (equation A.43):

$$\left. \frac{F_{inertial}}{F_{viscous}} \right|_{planar} \approx 1.9\beta_H^2 \alpha_H. \tag{2.52}$$

The average ratio of spatial to inertial forces for the sudden expansion became (equation A.47)

$$\left. \frac{F_{spatial}}{F_{inertial}} \right|_{\substack{planar \\ sudden \\ expansion}} = 0.44\beta_H \left[1 - \eta_H + \frac{1}{2}\eta_H^2 \right] \tag{2.53}$$

while for the unseparated expansion (equation A.48)

$$\left.\frac{F_{spatial}}{F_{inertial}}\right|_{\substack{planar \\ unseparated \\ expansion}} = 0.22\beta_{II}$$

(2.54)

where

$$\alpha_{II} = \text{Planar Womersley Parameter} = [Re_H St_H]^{1/2}$$

$$St_{II} = \text{Planar Strouhal Number} = \frac{H_e}{V_{stroke} t_{stroke}},$$

$$Re_{II} = \text{Planar Reynolds Number} = \frac{V_{stroke} H_e}{v}$$

$$\eta_{II} = \text{Planar restriction factor} = \frac{H_e}{H_c}$$

$$\beta_{II} = \text{Planar geometry factor} = \frac{H_{P_{initial}}}{H_e}.$$

The spatial to inertial force ratio is identical to the axisymmetric ratio, if the restriction and geometry factors are redefined in terms of area:

$$\eta_{area} = \frac{A_e}{A_c} = \frac{H_e B}{H_c B} = \frac{D_e^2}{D_c^2}$$

so

$$\eta_{II} = \eta_D^2$$

and

$$\beta_{area} = \frac{A_{P_{initial}}}{A_e} = \frac{H_{P_{initial}} B}{H_e B} = \frac{D_{P_{initial}}^2}{D_e^2},$$

so

$$\beta_{II} = \beta_D^2.$$

2.3 QUASI-STEADY APPROXIMATION IN ONE-DIMENSIONAL UNSTEADY FLOW

When using the quasi-steady approach to determine pressures in an unsteady flow, the unsteady inertial effects are neglected. If the unsteady inertial acceleration forces are small compared to the steady dynamic forces from spatial acceleration (e.g. changes in area) or the viscous drag forces, this may be a good approximation. It would be useful to know if this approximation may be used for left ventricular ejection, for either normal or diseased hearts. This allows the use of steady flow models (numerical and laboratory) to analyze the unsteady situation, making the entire analysis much simpler. The quasi-steady results for pressure would then be multiplied by a correction factor (the force ratio). The following order of magnitude analysis will define the relevant dimensionless parameter for evaluating the conditions in which the quasi-steady approximation is accurate. This parameter will be determined from the ratio of forces including the inertial force to forces neglecting the inertial force,

$$\frac{F_{total}}{F_{quasi-steady}} = \frac{F_{inertial} + F_{viscous} + F_{spatial}}{F_{viscous} + F_{spatial}}.$$

The model used is the same axisymmetric configuration considered in Section 2.2, shown in Figure 2.1. The forces derived in that section will be used here as well.

2.3.1 Total Force

The average total force F_{total} is given by the sum of $F_{inertial} + F_{viscous} + F_{spatial}$:

$$F_{total}\bigg|_{\substack{sudden \\ expansion}} = \frac{\pi}{2}\rho D_e^2 V_{stroke}^2 + 1.4\pi\rho\left[\frac{\nu}{l_{stroke}}\right]^{\frac{1}{2}}\left(\frac{D_{P_{initial}}^3}{l_{stroke}}\right)$$

$$+ 0.17\pi\rho D_{P_{initial}}^2 V_{stroke}^2\left[1 - \left[\frac{D_e}{D_c}\right]^2 + \frac{1}{2}\left[\frac{D_e}{D_c}\right]^4\right] \qquad (2.55)$$

using $F_{spatial}$ for the sudden expansion. For the unseparated expansion

$$F_{total}\bigg|_{\substack{unseparated \\ expansion}} = \frac{\pi}{2}\rho D_e^2 V_{stroke}^2 + 1.4\pi\rho\left[\frac{\nu}{t_{stroke}}\right]^{\frac{1}{2}}\left(\frac{D_{P_{initial}}^3}{t_{stroke}}\right)$$

$$+ 0.084\pi\rho D_{P_{initial}}^2 V_{stroke}^2 \qquad . \qquad (2.56)$$

2.3.2 Quasi-Steady Limit

Using a quasi-steady approach, the force required to move the fluid will not include the inertial force. Thus for the sudden expansion

$$F_{quasi-steady}\bigg|_{\substack{sudden \\ expansion}} = 1.4\pi\rho\left[\frac{\nu}{t_{stroke}}\right]^{\frac{1}{2}}\left(\frac{D_{P_{initial}}^3}{t_{stroke}}\right)$$

$$+ 0.17\pi\rho D_{P_{initial}}^2 V_{stroke}^2\left[1 - \left[\frac{D_e}{D_c}\right]^2 + \frac{1}{2}\left[\frac{D_e}{D_c}\right]^4\right] \qquad (2.57)$$

nile for the unseparated expansion

$$F_{quasi-steady}\bigg|_{\substack{unseparated \\ exp\text{a}\,\cdot\,on}} = 1.4\pi\rho\left[\frac{\nu}{t_{stroke}}\right]^{\frac{1}{2}}\left(\frac{D_{P_{initial}}^3}{t_{stroke}}\right)$$

$$+ 0.084\pi\rho D_{P_{initial}}^2 V_{stroke}^2 \qquad (2.58)$$

The ratio of the total force to quasi-steady force for the sudden expansion is

$$\frac{F_{total}}{F_{quasi-steady}} = 1 + \frac{0.5 D_e^2 V_{stroke}^2}{1.4\frac{D_{P_{initial}}^3}{t_{stroke}}\left[\frac{\nu}{t_{stroke}}\right]^{\frac{1}{2}} + 0.17 D_{P_{initial}}^2 V_{stroke}^2\left[1 - \left(\frac{D_e}{D_c}\right)^2 + \frac{1}{2}\left(\frac{D_e}{D_c}\right)^4\right]}$$

$$(2.59)$$

and for the unseparated expansion

$$\frac{F_{total}}{F_{quasi-steady}}\bigg|_{\substack{unseparated \\ expansion}} = 1 + \frac{0.5 D_e^2 V_{stroke}^2}{1.4\frac{D_{P_{initial}}^3}{t_{stroke}}\left[\frac{\nu}{t_{stroke}}\right]^{\frac{1}{2}} + 0.084 D_{P_{initial}}^2 V_{stroke}^2} . \qquad (2.60)$$

These ratios may be expressed in terms of dimensionless variables:

$$\left.\frac{F_{total}}{F_{quasi\text{-}steady}}\right|_{\substack{sudden\\expansion}} = 1 + \frac{1}{\dfrac{0.63}{\beta_D^3\,[St_D Re_D]^{0.5}} + 0.44\beta_D^2\left[1 - \eta_D^2 + \dfrac{1}{2}\eta_D^4\right]}, \qquad (2.61)$$

and

$$\left.\frac{F_{total}}{F_{quasi\text{-}steady}}\right|_{\substack{unseparated\\expansion}} = 1 + \frac{1}{\dfrac{0.63}{\beta_D^3\,[St_D Re_D]^{0.5}} + 0.22\beta_D^2}, \qquad (2.62)$$

where

$$St_D = \text{Strouhal Number} = \frac{D_e}{V_{stroke} t_{stroke}} = \frac{\text{unsteady acceleration force}}{\text{dynamic pressure force}}$$

$$Re_D = \text{Reynolds Number} = \frac{V_{stroke} D_e}{\nu} = \frac{\text{inertia force}}{\text{viscous force}}$$

$$\eta_D = \text{restriction factor} = \frac{D_e}{D_c}$$

$$\beta_D = \text{geometry factor} = \frac{D_e}{D_{p_{initial}}}.$$

The product $Re_D^{0.5} St_D^{0.5}$ is the Womersley parameter α. Using this parameter, the force ratio equation 2.61 for the sudden expansion may be written as

$$\left.\frac{F_{total}}{F_{quasi\text{-}steady}}\right|_{\substack{sudden\\expansion}} = 1 + \frac{1}{\dfrac{0.63}{\beta_D^3 \alpha_D} + 0.44\beta_D^2\left[1 - \eta_D^2 + \dfrac{1}{2}\eta_D^4\right]}. \qquad (2.63)$$

This reveals the parameters for deciding if a quasi-steady approach may be used to determine the pressure. It shows that the quasi-steady approach should be valid for small Womersley parameters and large restriction factors, for example

- slow closure rates;
- severe aortic valvular stenosis;
- severe sub-aortic valvular stenosis.

The most important factor is the restriction factor. As the restriction factor gets larger (more obstructed flow), the quasi-steady approximation gets better.

The force ratio determined using the fully recovered spatial force (equation 2.62) may also be written in terms of the Womersley parameter α:

$$\left.\frac{F_{total}}{F_{quasi-steady}}\right|_{\substack{unseparated \\ expansion}} = 1 + \frac{1}{\dfrac{0.63}{\beta_D^3 \alpha_D} + 0.22\beta_D^2} \cdot \qquad (2.64)$$

This shows that if the flow does not separate, the difference between the quasi-steady and unsteady approaches should not be influenced by the degree of restriction.

Using *in vivo* aortic flow rates and geometric data from normal and HCM hearts determined by Murgo, Alter, Dorethy, Altobelli & McGranaaan (1980), and from a severe aortic stenosis obtained by Clark (1976a), the force ratios were obtained for the first half of systole, as shown in Table 2.3.

Table 2.3: Comparison of Unsteady and Quasi-Steady Forces

Flow Configuration	η_D	β_D	α_D	$\dfrac{F_{total}}{F_{quasi-steady}}$	
				Sudden Expansion	Unseparated Expansion
normal heart	1.05	1.5	29.5	3.0	3.0
HCM: unrestricted, resting	1.05	1.5	31.3	3.0	3.0
HCM: unrestricted, provoked	1.05	1.8	35.0	2.4	2.4
HCM: mildly restricted, resting	1.5	1.5	31.3	1.8	3.0
HCM: mildly restricted, provoked	1.5	1.8	35.0	1.5	2.4
HCM: very restricted, resting	2.0	1.5	31.3	1.2	3.0
HCM: very restricted, provoked	2.0	1.8	35.0	1.1	2.4
severe aortic stenosis	4.0	1.4	18.1	1.01	3.3

These force ratio values indicate that the quasi-steady approach will be good for a severe stenosis and very restricted HCM hearts if separation occurs, but quite poor for all other

cases (*i.e.* the quasi-steady approach is reasonable when $F_{total}/F_{quasi-steady}$ lies between 1.0 and 1.2). The HCM ratios vary, depending on the degree of restriction one assumes.

Clark (1976b) used the Strouhal number alone as a deciding factor in determining if a quasi-steady approach was valid. This was utilized in his study of flow from the left ventricle into the aorta through an aortic stenosis. He suggested that the Strouhal number could be thought of as a ratio of acceleration effects due to the flow changing with time to that due to spatial acceleration caused by the reduction of area. Thus if the Strouhal number was very small, the unsteadiness in the flow would be relatively unimportant, allowing the problem to be treated as quasi-steady. It should be noted that his definition for the Strouhal number was based on the minimum diameter of the outflow tract and thus included the effect of the restriction. As he was examining two extreme cases only (normal hearts where the quasi-steady approach clearly could not be used, and severe aortic valvular stenosis where the quasi-steady approach was well suited), this approach was sufficient. His conclusions were similar: the quasi-steady analysis is adequate for a severe restriction, but becomes poor for a mild restriction.

The planar configuration was also examined to determine the unsteady/quasi-steady ratio. This is given in detail in Appendix A.2. The ratio gave similar results for the sudden expansion and unseparated expansion (equations A.53 and A.54):

$$\left.\frac{F_{total}}{F_{quasi-steady}}\right|_{\substack{\text{planar}\\\text{sudden}\\\text{expansion}}} = 1 + \cfrac{1}{\dfrac{0.53}{\beta_H \alpha_H} + 0.44\beta_H\left[1 - \eta_H + \dfrac{1}{2}\eta_H^2\right]} \qquad (2.65)$$

and

$$\left.\frac{F_{total}}{F_{quasi-steady}}\right|_{\substack{\text{planar}\\\text{unseparated}\\\text{expansion}}} = 1 + \cfrac{1}{\dfrac{0.53}{\beta_H \alpha_H} + 0.22\beta_H} \qquad (2.66)$$
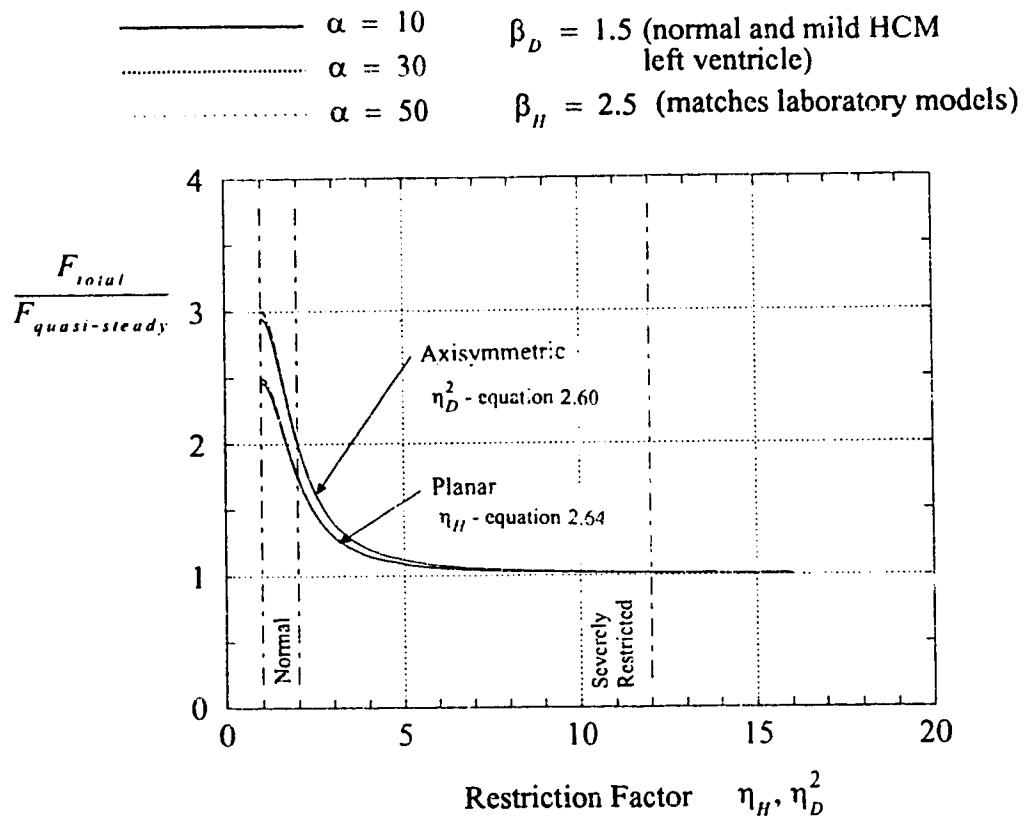
Figure 2.11 Variation of Force Ratio With Restriction Factor η
(sudden expansion case shown)

where the restriction, geometry and Womersley parameters have the definitions given in Section 2.2.6. Again, it should be noted that if the restriction and geometry factors were redefined in terms of area, the ratio would have the same form as the axisymmetric case.

Figure 2.11 shows the variation in the total to quasi-steady force ratio with restriction for Womersley parameters of 10, 30, and 50 for both the axisymmetric case (equation 2.63 and 2.64) and the planar case (equations 2.65 and 2.66). It is immediately evident that the Womersley parameter has little effect; the variation is due almost entirely to the restriction factor η. This means that the viscous forces are negligible compared to spatial acceleration forces for the laminar flow model used here.

2.4 SUMMARY

The order of magnitude analysis and the quasi-steady approximation described in this chapter have shown the following:

- the order of magnitude analysis revealed the appropriate dimensionless parameters used for modelling left ventricular ejection. These are η, the restriction factor; β, the geometry factor; and α, the Womersley parameter;

- the inertial force to viscous force ratio may be used to indicate the degree of impediment to ejection: high values (150 to 350) indicate little impedance, while low values (less than 150) indicate significant impedance. The very large values of this ratio indicate that viscous forces are negligible in both normal and HCM hearts;

- the spatial to inertial force ratio gives a good indication of flow separation effects, as shown by the differences between the sudden and unseparated expansions;

- the quasi-steady approximation shows that viscous forces are negligible compared to spatial acceleration forces, at least for the laminar flow model considered here;

- the quasi-steady approximation becomes better as the restriction factor increases.

CHAPTER 3 • UNSTEADY ONE-DIMENSIONAL NUMERICAL ANALYSIS

3.1 INTRODUCTION

An unsteady one-dimensional inviscid momentum analysis of the flow in an idealized left ventricle-aorta shape would quantif⸱ the relative importance of the various components contributing to the pressure difference between the ventricle region and the outflow tract. This chapter describes this analysis, in which the unsteady Bernoulli equation for a flow bounded by moving walls is utilized. It will be shown that this equation is the same as the unsteady Bernoulli equation for stationary walls. This one-dimensional analysis gives an inviscid estimate of the pressure along the mid-line of the left ventricle model, at the expense of being unable to determine flow separation effects.

To evaluate the significance of time-dependant flow acceleration effects, a quasi-steady analysis was also undertaken. This analysis used the steady Bernoulli equation, which differed from the unsteady analysis only by the absence of time-dependant flow acceleration terms. Three general classes of heart flows were modelled: unobstructed (normal), progressively restricted (systolic anterior motion or SAM) and fixed restriction (stenosis). By comparing results of the unsteady and quasi-steady Bernoulli analysis methods, it will be shown that the pressure caused by the time-dependant flow acceleration is not significant compared to the pressure caused by a significant flow restriction. However, the pressure due to time-dependant flow acceleration is dominant in less restricted flows. These results agree with the order of magnitude analysis in Chapter 2.

3.2 MATHEMATICAL DEVELOPMENT: UNSTEADY ANALYSIS

3.2.1 Model Configuration

The geometry used for the momentum analysis was the simplified version of the

Geometry is symmetrical
about the mid-line.
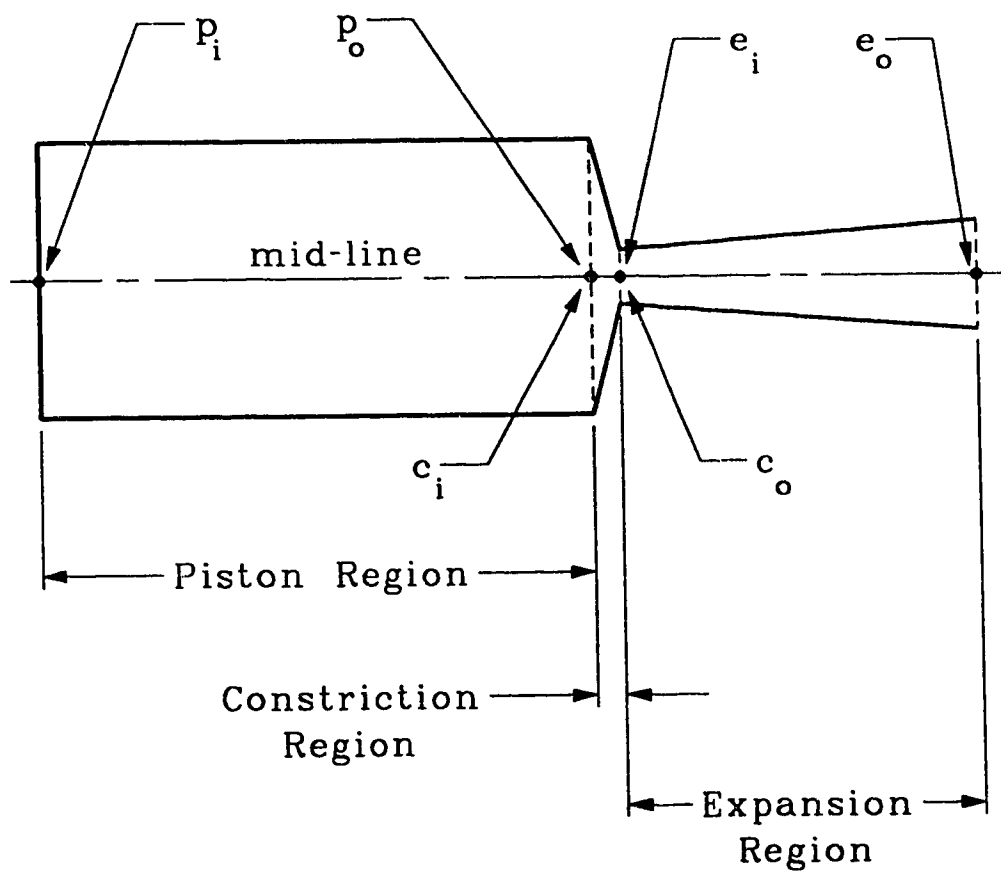
Figure 3.1: Model Regions
        Inlet locations denoted with subscript "i";
        Outlet locations denoted with subscript "o".

left ventricle model shown in Figure 3.1. The flow was divided into three regions: piston (left ventricle), constriction and expansion. The piston, constriction and expansion walls moved together to simulate three different model conditions: unobstructed, progressive restriction and fixed restriction. All walls started simultaneously from the maximum opening position (Figure 3.2) and stopped at the minimum opening position. The piston wall position, velocity and acceleration were obtained from experimental data taken from the unsteady laboratory model.

(a) unobstructed

(b) progressive restriction

(c) fixed restriction
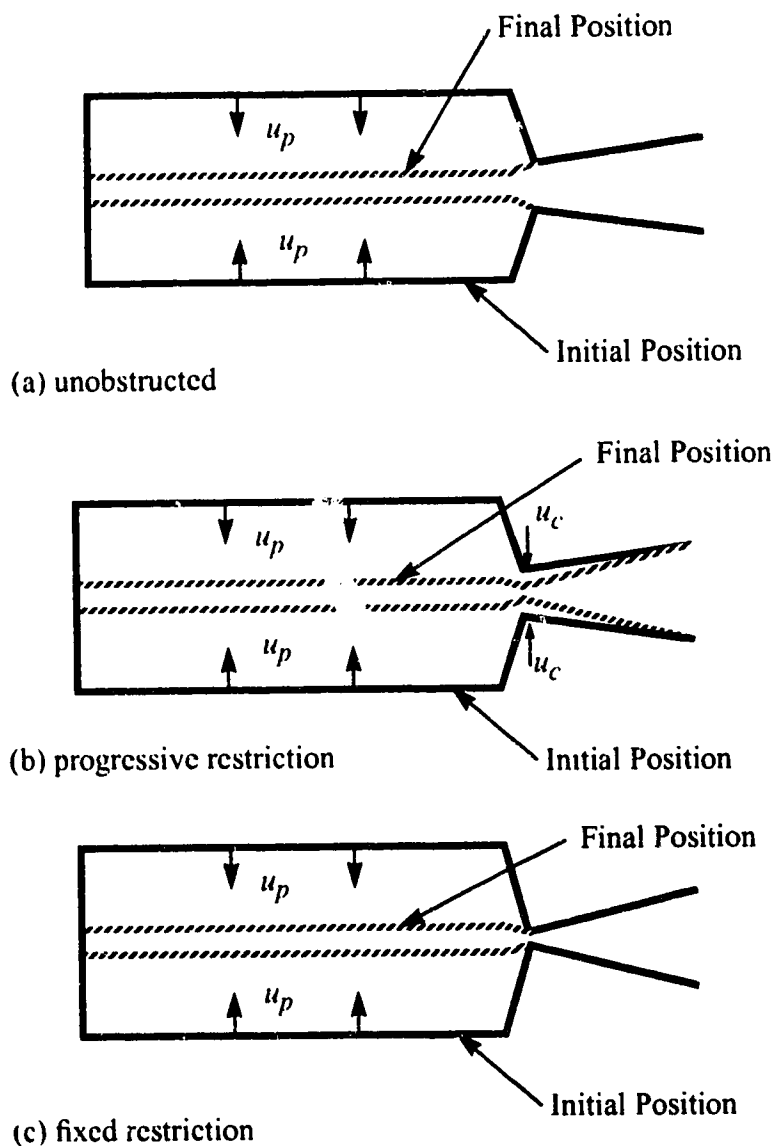
Figure 3.2: Geometry for One-Dimensional Analysis

3.2.2 Assumptions and Simplifications

Consider the general case of a symmetric planar constriction, shown in Figure 3.3. The flow is one-dimensional with a uniform velocity across the cross section. The flow was assumed to be inviscid, so that wall friction could be ignored. The flow profile was uniform at every cross-section (plug flow). No flow separation was allowed and the shape was assumed to be symmetric about the mid-line.
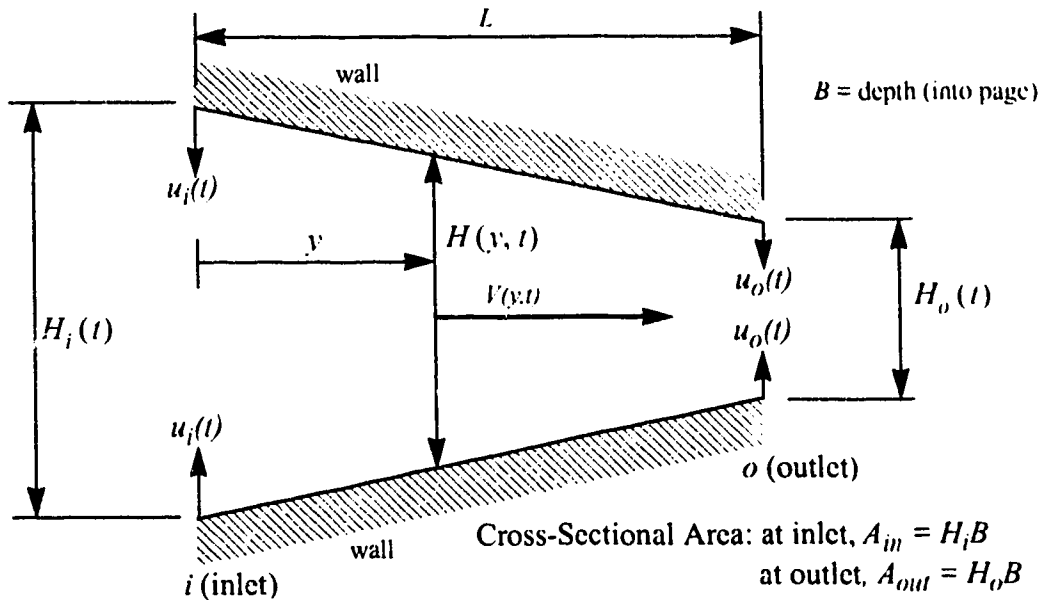
Figure 3.3: General Planar Symmetric Moving Wall Geometry

The unsteady Bernoulli equation, including the effect of the moving walls, will be used. The derivation of this equation is given in Appendix B.1 (equation B.8) and is repeated here for convenience:

$$\frac{\partial V}{\partial t} dy + \frac{dp}{\rho} + V dV = 0.$$

(3.1)

The development of this equation differs from the usual development, see for example White (1986, page 147), in that here $\frac{\partial A}{\partial t} \neq 0$. The final form of the equation is identical because the $\frac{\partial A}{\partial t}$ terms are cancelled as they appear in both mass conservation and momentum conservation equations. The unsteady Bernoulli equation 3.1 may be integrated along the streamwise direction (v) to give

$$p(y) - p_{inlet} = \rho \left\{ - \int_{inlet}^{y} \frac{\partial V}{\partial t} dy - \frac{1}{2} [V(y)^2 - V_{inlet}^2] \right\}. \tag{3.2}$$

If the velocity V is constant with time, equation 3.2 reduces to the familiar steady form of the Bernoulli equation (with no change in elevation):

$$p(y) - p_{inlet} = -\frac{\rho}{2} [V(y)^2 - V_{inlet}^2] \tag{3.3}$$

For the general case of a linear constriction, shown in Figure 3.3, the velocity of the fluid at any cross-section may be determined by dividing the volume flow rate by the cross-sectional area. The velocity may then be differentiated with time to determine the acceleration. These relationships account for the fluid displaced by the moving walls through the conservation of mass. The derivation of these equations is given in Appendix B.2, and the results (equations B.20 and B.21) are repeated here:

$$V(y,t) = \frac{V_i H_i(y,t) + 2u_i(t)y - (u_i(t) - u_o(t))\frac{y^2}{L}}{H_i(t) - (H_i(t) - H_o(t))\frac{y}{L}} \tag{3.4}$$

$$\frac{\partial V}{\partial t} = \frac{\frac{\partial V_i}{\partial t} H_i - 2V_i u_i + 2y\frac{\partial u_i}{\partial t} - \frac{y^2}{L}\left[\frac{\partial u_i}{\partial t} - \frac{\partial u_o}{\partial t}\right]}{H_i - (H_i - H_o)\frac{y}{L}}$$

$$- \frac{\left[V_i H_i + 2u_i y - (u_i - u_o)\frac{y^2}{L}\right]\left[-2u_i + \frac{2y}{L}(u_i - u_o)\right]}{\left[H_i - (H_i - H_o)\frac{y}{L}\right]^2} . \tag{3.5}$$

With these general equations for the velocity and acceleration of the fluid at axial position y, it is possible to determine the pressure in each of the three flow regions (piston region, constriction region and expansion region).

3.2.3 Piston Region Pressure Equation

The geometry for the piston region is shown in the following figure:
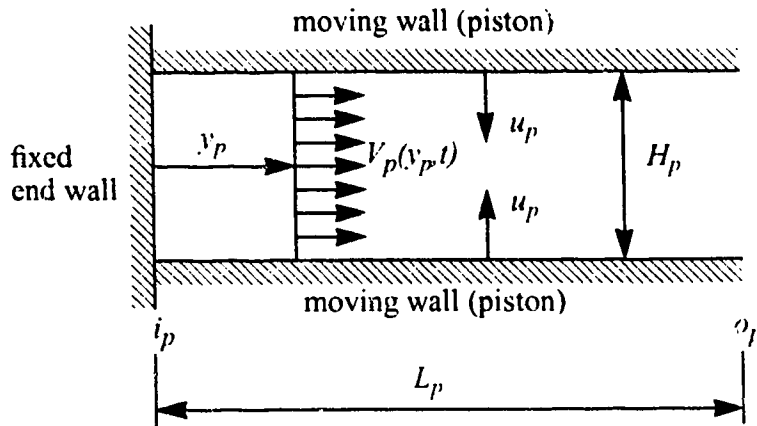
Figure 3.4: Piston Region Geometry

For this case, $V_i = 0$,

$$u_i = u_o = u_p,$$

and $H_i = H_o = H_p(t)$.

Substituting these into the mass conservation equations 3.4 and 3.5,

$$V_p(y_p, t) = \frac{2u_p y_p}{H_p},$$

(3.6)

$$\frac{\partial V_p}{\partial t} = \frac{2y_p}{H_p}\frac{\partial u_p}{\partial t} + \frac{4u_p^2}{H_p^2}y_p.$$

(3.7)

These equations may then be substituted into the unsteady Bernoulli equation 3.2 to give the pressure difference between the piston end wall (i_p) and any point (y_p) along the piston region mid-line

$$p(y_p) - p_{i_p} = \rho\left\{-\int_{i_p}^{y_p}\frac{\partial V_p}{\partial t}dy_p - \frac{V_p(y_p, t)^2}{2}\right\}.$$

(3.8)

3.2.4 Constriction Region Pressure Equation

The geometry for the constriction region is shown in the following figure:
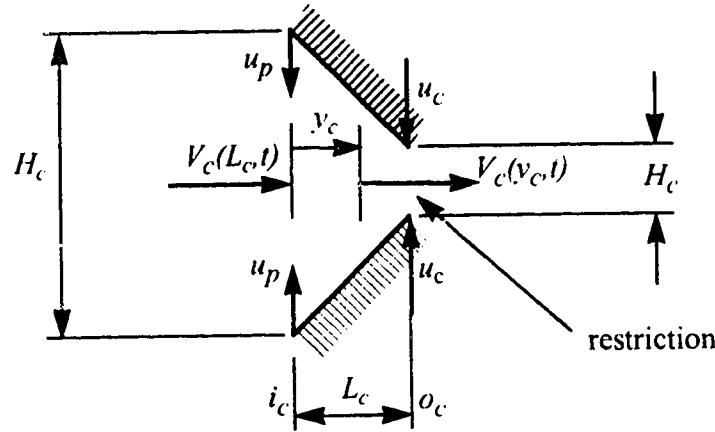
Figure 3.._ Constriction Region Geometry

For this case, $V_i = V_p(L_p,t)$ (the outlet velocity of the piston region), which may be determined from equation 3.6 using $y_p = L_p$

$$V_i = V_p(L_p, t) = \frac{2u_p L_p}{H_p}.$$ (3.9)

The wall velocity at the inlet, u_p, is the same as the piston wall velocity used previously. Unlike the piston region, the inlet wall velocity (u_p) does not equal the outlet wall velocity (u_c). Substituting these values into the mass conservation equation 3.- gives

$$V_c(y_c,t) = \frac{V_p(L_p, t)H_p + 2u_p y_c - (u_p - u_c)\frac{y_c^2}{L_c}}{H_p - (H_p - H_c)\frac{y_c}{L_c}},$$ (3.10)

and in equation 3.5 yields

$$\frac{\partial V_c}{\partial t} = \frac{2L_p\frac{\partial u_p}{\partial t} + 2y_c - \frac{y_c^2}{L_c}\left[\frac{\partial u_p}{\partial i} - \frac{\partial u_c}{\partial t}\right]}{H_p - (H_p - H_c)\frac{y_c}{L_c}}$$

$$-\frac{\left[2u_p L_p + 2u_p y_c - (u_p - u_c)\frac{y_c^2}{L_c}\right]\left[-2u_p + \frac{2y_c}{L_c}(u_p - u_c)\right]}{\left[H_p - (H_p - H_c)\frac{y_c}{L_c}\right]^2}.$$ (3.11)

These equations may then be substituted into the unsteady Bernoulli equation 3.2 to give the pressure difference between any point along the constriction region mid-line $(p(y_c))$ and the constriction region inlet $(p(y_c=0) = p_{i_c})$

$$p(y_c) - p_{i_c} = \rho \left\{ -\int_{i_c}^{y_c} \frac{\partial V_c}{\partial t} dy_c - \frac{1}{2} [V_c(y_c, t)^2 - V_p(L_p, t)^2] \right\}.$$ (3.12)

3.2.5 Expansion Region Pressure Equation

The geometry for the expansion region is shown in the following figure:
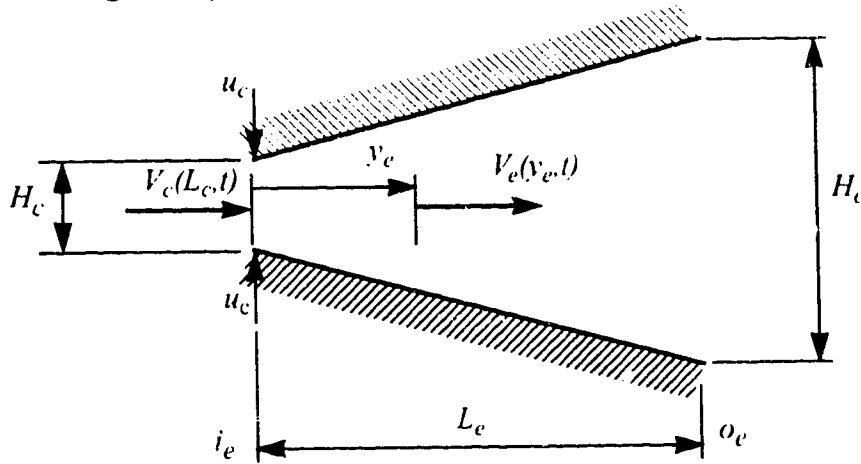
Figure 3.6: Expansion Region Geometry

For this case, $V_i = V_c(L_c, t)$ (the outlet velocity of the constriction region), which may be determined from equation 3.10 using $y_c = L_c$,

$$V_c = \frac{2u_p L_p + u_p L_c + u_c L_c}{H_c}.$$ (3.13)

Also, the wall velocity at the inlet (u_i) is the same as the outlet wall velocity of the constriction region (u_c). Further, the wall at the outlet is stationary $(u_o = 0)$. Substituting these values into the mass conservation equations 3.4 and 3.5,

$$V_e(y_e, t) = \frac{2u_p L_p + u_p L_c + u_c L_c + 2u_c y_e - \frac{u_c y_e^2}{L_e}}{H_c - (H_c - H_e)\frac{y_e}{L_e}},$$ (3.14)

$$\frac{\partial V_e}{\partial t} = \frac{\left[2L_p \frac{\partial u_p}{\partial t} P + L_c \frac{\partial u_p}{\partial t} P + L_c \frac{\partial u_c}{\partial t} + 2v_e \frac{\partial u_c}{\partial t} - \frac{v_e^2}{L_d} \frac{\partial u_c}{\partial t} \right]}{H_c - (H_c - H_e) \frac{v_e}{L_e}}$$

$$- \frac{\left[2u_p L_p + u_p L_p + u_c L_c + 2u_c v_e - \frac{u_c v_e^2}{L_e} \right] \left[-2u_c + 2\frac{v_e}{L_c} u_c \right]}{\left[H_c - (H_c - H_e) \frac{v_e}{L_c} \right]^2}$$

(3.15)

These equations may then be used in the unsteady Bernoulli equation 3.2 to give the pressure difference at any point in the expansion region

$$p(v_e) - p_{i_e} = \rho \left\{ -\int_{i_e}^{v_e} \frac{\partial V}{\partial t} dv_e - \frac{1}{2} [V_e(v_e, t)^2 - V_e(L_c, t)^2] \right\}.$$

(3.16)

3.3 QUASI-STEADY LIMIT OF THE UNSTEADY BERNOULLI EQUATION

If the quasi-steady approximation is made, the steady Bernoulli equation 3.3 is used to determine the pressure at any point in the flow, using the same assumptions and simplifications as the unsteady analysis. The same nomenclature and configuration applies here. This approach neglects only the time-dependant flow acceleration terms.

3.3.1 Piston Region Pressure Equation

At any point in time, the pressure along the piston region mid-line (v) may be estimated from the steady Bernoulli equation 3.3, noting that the velocity at the fixed piston end wall $V_i = V_p(v_p=0,t) = 0$

$$p(v_p) - p_{i_p} = -\rho \frac{V_p(v_p, t)^2}{2}.$$

(3.17)

where $V_p(v_p, t)$ is given by equation 3.6. The pressure at the piston end wall, p_{i_p}, is unknown and must be specified.

3.3.2 Constriction Region Pressure Equation

At any point in time, the pressure for any y value in the constriction region may be estimated from the steady Bernoulli equation 3.3

$$p(y_c) - p_{i_c} = -\frac{\rho}{2} [V_c(y_c, t)^2 - V_p(L_p, t)^2],$$ \hfill (3.18)

where $V_p(L_p, t)$ is given by equation 3.9, and $V_c(y_c, t)$ is given by equation 3.10. The inlet pressure for this region p_{i_c} was identical to the outlet pressure of the piston region.

3.3.3 Expansion Region Pressure Equation

At any point in time, the pressure for any y value in the expansion region may be estimated from the steady Bernoulli equation 3.3

$$p(y_e) - p_{i_e} = -\frac{\rho}{2} [V_e(y_e, t)^2 - V_c(L_c, t)^2],$$ \hfill (3.19)

where $V_c(L_c, t)$ is given by equation 3.13, and $V_c(y, t)$ is given by equation 3.14. The inlet pressure p_{i_e} for this region was identical to the outlet pressure of the constriction region.

3.4 SOLUTION OF UNSTEADY AND QUASI-STEADY PRESSURE EQUATIONS

3.4.1 General Approach

A computer program was written to calculate the pressures along the mid-line for both the unsteady and quasi-steady pressure equations. The pressures were determined for every one per cent of piston closure, beginning from 0% (fully open: $H_p = 64$ mm) to 100% (fully closed: $H_p = 12$ mm). The dimensions used (H, L and B values) were chosen to match the unsteady laboratory model, as the wall speeds and accelerations were obtainable from this model. Such information from the *in vivo* situation is not available.

At each position, the piston wall speed u_p and acceleration $\frac{\partial u_p}{\partial t}$ values from the unsteady laboratory model were calculated. For the examples in this chapter, the piston position was measured in the planar heart model laboratory simulation. The piston

velocity and acceleration were calculated from these measured values using second order forward-finite-difference approximations (second order terms in the Taylor-series expansion are included). Forward-difference methods were used to allow calculations to begin from time $t=0$. Because the piston position data contained some noise, smoothing was required before the derivatives were calculated. The methods used for this data analysis are discussed in section 5.4.2.

Pressures were calculated along the mid-line by dividing each of the region lengths (L_p, L_c, L_e) into equally spaced intervals or steps. The step sizes were determined by trial and error. If the step sizes were too large, excessive errors would occur in the integral term, especially in the constriction region. A reasonable step size was $\Delta y = 0.1$ mm, with a reduced step size of $\dfrac{\Delta y}{10} = 0.01$ mm for the numerical integration of $\dfrac{\partial V}{\partial t}$. In other words, the integral was the sum over ten smaller steps of 0.01 mm. This gave pressure values at 2096 equally spaced intervals of 0.1 mm along the model. The integrations were performed using the Simpson's one-third rule, James, Smith & Wolford (1977), page 330, dividing each step into four areas. This made the effective step size for integration 0.0025 mm. Thus the integral was evaluated as

$$\int_{y(i)}^{y(i+1)} \frac{\partial V}{\partial t}\,dy = \frac{\Delta y}{12}\left[\left.\frac{\partial V}{\partial t}\right|_{y(i)} + 4\left.\frac{\partial V}{\partial t}\right|_{y(i)+\frac{\Delta y}{4}} \right. $$

$$\left. 2\left.\frac{\partial V}{\partial t}\right|_{y(i)+\frac{2\Delta y}{4}} + 4\left.\frac{\partial V}{\partial t}\right|_{y(i)+\frac{3\Delta y}{4}} + \left.\frac{\partial V}{\partial t}\right|_{y(i)+\Delta y}\right] \tag{3.20}$$

The pressure was normalized by dividing by a pressure based on the time averaged velocity of the fluid at the expansion exit (i.e. the stroke velocity)

$$\Phi = \frac{P(y,t) - P(y_e=L_e,t)}{\Delta P_{stroke}} \tag{3.21}$$

where

$$\Delta P_{stroke} = \frac{\rho\,(V_{stroke})^2}{2}.$$ (3.22)

The stroke velocity V_{stroke} was calculated using equation 2.3, repeated here for convenience:

$$V_{stroke} = \frac{(\text{90\% of stroke volume})}{(\text{expansion exit area})\,(\text{90\% of stroke time})}.$$ (3.23)

The stroke volume is defined as the amount of fluid displaced from the start of wall motion to the end of wall motion. This parameter was chosen to allow comparisons with the physiological situation, where stroke volume data is often available, but stroke velocity is not. The stroke time is the time for the piston to move from its initial position to its final position. As it was difficult to find the exact start and end points in time, the stroke time and stroke velocity were evaluated between the 5% closed and 95% closed positions.

Pressure differences were evaluated between the piston region and the point of maximum restriction. The piston region pressure was determined towards the center of the piston region at $y_p = 65$ mm. This is similar to the location used for left ventricular pressure measurements. It also matches the location used for pressure measurements in the unsteady laboratory model. The point of maximum restriction was taken as the exit from the constriction region. The normalized pressure difference was then

$$\Upsilon = \frac{P\,(y_p=65\ \text{mm},\,t)\ -\ P\,(y_c=L_c,\,t)}{\Delta P_{stroke}}$$ (3.24)

The distance along the mid-line y was normalized by dividing by the distance to the maximum restriction, y_r.

$$\xi = \frac{y}{y_r}.$$ (3.25)

The constriction exit was the point of maximum constriction, so that at this location

$\xi = 1.$

3.4.2 Unobstructed Configuration

The unobstructed case had no restriction; the constriction width was kept at the same value as the expansion width during closure of the pistons. This value was

$$H_c = \text{constant} = 25.4 \text{ mm}.$$

This corresponds to a restriction value of $\eta_H = 1.0$. The pistons were initially 63.5 mm apart, giving the model a geometry factor of $\beta_H = 2.5$. The piston velocities were obtained from the laboratory model in its mildly restricted configuration. The other values, chosen to match the unsteady laboratory model, were $L_p = 127$ mm, $L_c = 6.35$ mm, $L_e = 76.2$ mm, and $\rho = 998 \text{kg/m}^3$. The pressure at $v_p = 0$ was set to 0 Pa to carry out the calculations. Once the calculations were completed, the pressures were adjusted to have the same pressure at the outlet of the expansion, which was the desired reference point for pressure. The outlet pressure was chosen to avoid negative pressures upon normalization. The pressures were then normalized as described in 3.4.1.

The normalized pressures are plotted in Figure 3.7. These plots show the variation in pressure along the mid-line for different values of piston closure. This case shows the importance of including the time dependent flow acceleration terms. Because there is no significant restriction, the relative importance of the inertial acceleration is much greater. During periods of maximum acceleration and deceleration, (piston closure from 0% to 15%, and 85% to 100%), the error caused by ignoring these terms exceeds 10%, peaking at 50% error at a piston closure of 98%. For the periods of less acceleration (piston closure from 15% to 85%), the error is less than 10%. These results show that the quasi-steady approach is very poor for cases where inertial acceleration forces are dominant.

The quasi-steady and unsteady results differ significantly when determining the maximum pressure difference between the piston region and the constriction exit, as shown by Figure 3.8(a). The pressure difference was determined between pressures at $v_p =$
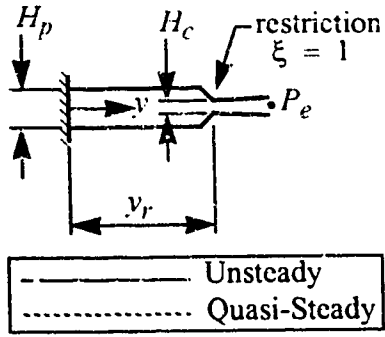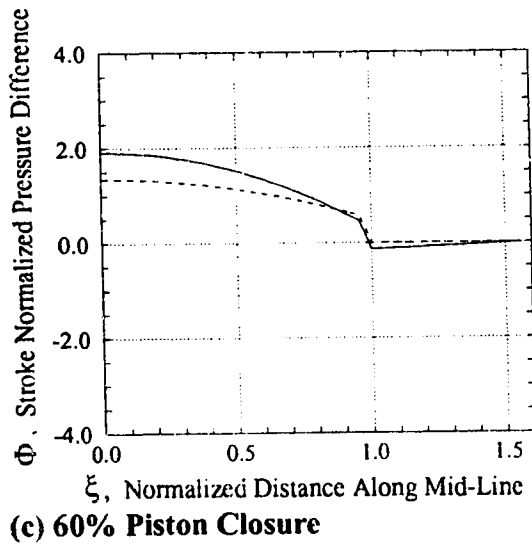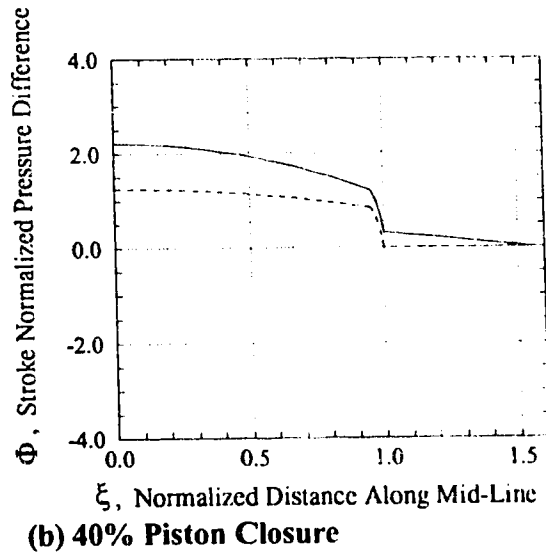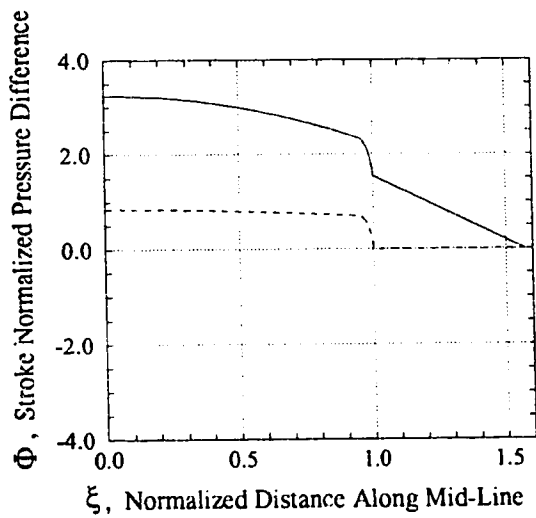
Figure 3.7: Normalized Mid-Line Pressure Differences at Various Restrictions: Unobstructed Configuration

65 mm and $y_c = L_c = 6.35$ mm $(P_p - P_c)$. The normalized pressure difference was determined as previously described. The unsteady and quasi-steady pressure differences do not match well during periods of high acceleration and deceleration because the time-dependant flow acceleration terms are a major contributor in the pressure difference. The largest deviation between the two methods in determining the maximum normalized pressure difference was $\Upsilon = 1.6$, occurring at 98% of piston closure. It interesting to note that at this point, the unsteady Bernoulli approach has predicted a negative pressure difference while the quasi-steady approach has not. In Chapter 7 it will be shown that this negative pressure difference is also found *in vivo* for a normal systolic flow. Again, this illustrates the importance of including the inertial acceleration terms in the analysis for an unobstructed situation.

For *in vivo* measurements in the heart, pressures are usually measured in the left ventricle (piston region) and aorta (expansion exit). Thus, to compare to physiological data, the correct pressure difference is between the piston region and expansion exit. This is plotted in Figure 3.8(b), which shows the pressure difference between $y_p = 65$ mm and $y_e = L_e = 76.2$ mm $(P_p - P_e)$. The inertial acceleration terms have an even greater effect, reaching a deviation between the two methods in determining the maximum normalized pressure difference of $\Phi_{mid} = 3.7$, occurring at 98% of piston closure.

3.4.3 Fixed Restriction Configuration

This case contained a fixed restriction; the constriction exit was kept at a small constant opening throughout the piston movement,

$$H_c = 1.7 \text{ mm}.$$

This corresponds to a restriction factor of $\eta_H = 14.9$, a severe stenosis. The piston velocities were obtained from the laboratory model in its fixed restriction configuration. The other values, chosen to match the unsteady laboratory model, were the same as the unob-

$$\% \text{ Piston Closure} = \frac{H_{P_{initial}} - H_p}{H_{P_{initial}} - H_{P_{final}}} \times 100$$

$$\Upsilon = \frac{P_p - P_c}{\Delta P_{stroke}}$$

$$\Phi_{mid} = \frac{P_p - P_e}{\Delta P_{stroke}}$$

$$\Delta P_{stroke} = 529 \text{ Pa}$$

$y_p = 65$ mm

——— Unsteady
·············· Quasi-Steady
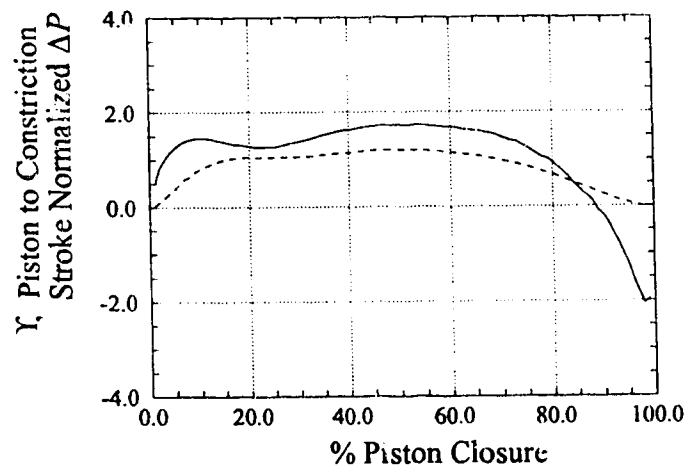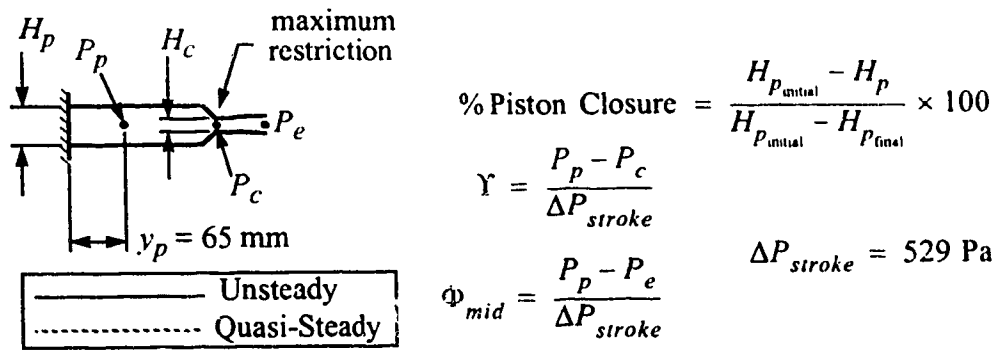
(a) Constriction Exit Pressure Difference
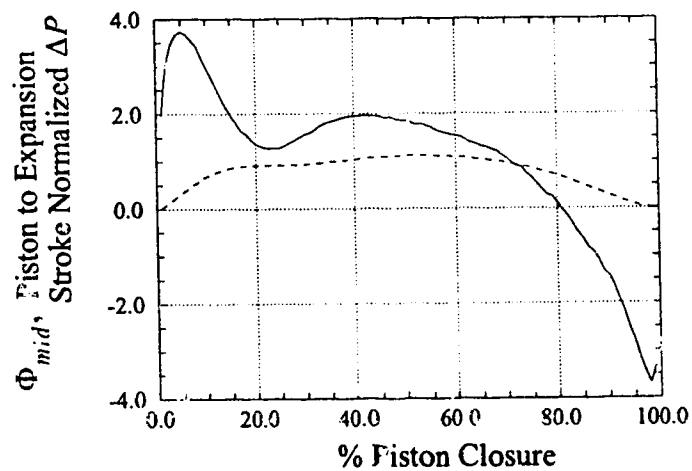
(b) Expansion Exit Pressure Difference

Figure 3.8: Pressure Differences Between Piston Region and Points Downstream: Unobstructed Configuration.

structed case: $L_p = 127$ mm, $L_c = 6.35$ mm, $L_e = 76.2$ mm, $\beta_H = 2.5$, and

$\rho = 998 \text{kg/m}^3$. The pressure at $y_p=0$ was set to 0 Pa to carry out the calculations. Once the calculations were completed, the pressures were adjusted and normalized in the same way as the unobstructed configuration.

The normalized pressures are plotted in Figure 3.9. These plots show the variation in pressure along the mid-line for different values of piston closure. This case shows the pressure difference caused by the time-dependent flow acceleration terms to be insignificant. Since there is a severe restriction, the relative importance of the acceleration terms are greatly reduced. The per cent error caused by ignoring these terms is determined from the difference between the unsteady Bernoulli pressures and the quasi-steady pressures, compared to the peak pressure at that piston position. The error is a maximum of 8% at 99% piston closure, and had less than 1% error for piston closures between 17% to 94%. Thus for the majority of the piston motion, the difference between the unsteady Bernoulli and quasi-steady pressures is minimal.

The quasi-steady and unsteady results give nearly identical results for the maximum pressure difference between the piston region and the constriction exit, see Figure 3.10(a). The unsteady and quasi-steady pressure differences match much better than the unobstructed case because the time-dependant flow acceleration terms are not a significant factor in the pressure difference. The largest deviation between the two methods in determining the maximum normalized pressure difference was $\Upsilon = 8.4$, occurring at 99% of piston closure. This was only 2% of the maximum pressure difference.

The pressure difference between the piston region and expansion exit is shown in Figure 3.10(b). The quasi-steady approach gives fairly good results for most of the piston closure, but fails at the initial and final positions. This is caused by high initial acceleration
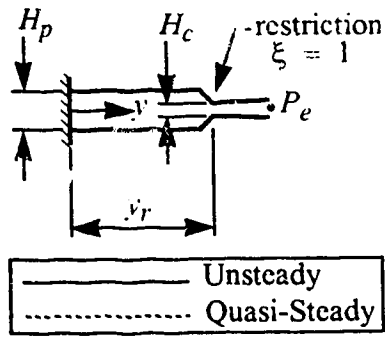
H_p H_c -restriction
        $\xi = 1$

$\bullet P_e$

v_r

$$\xi = \frac{v}{v_r}$$

$$\% \text{Piston Closure} = \frac{H_{p_{initial}} - H_p}{H_{p_{initial}} - H_{p_{final}}} \times 100$$

———— Unsteady
·················· Quasi-Steady

$$\Phi = \frac{P(v,t) - P_e}{\Delta P_{stroke}} \; ; \;\; \Delta P_{stroke} = 159 \, \text{Pa}$$

(a) 10% Piston Closure

(b) 40% Piston Closure

(c) 60% Piston Closure

(d) 90% Piston Closure
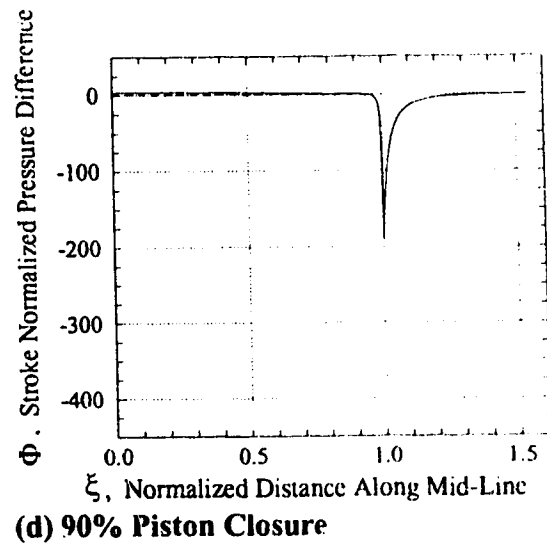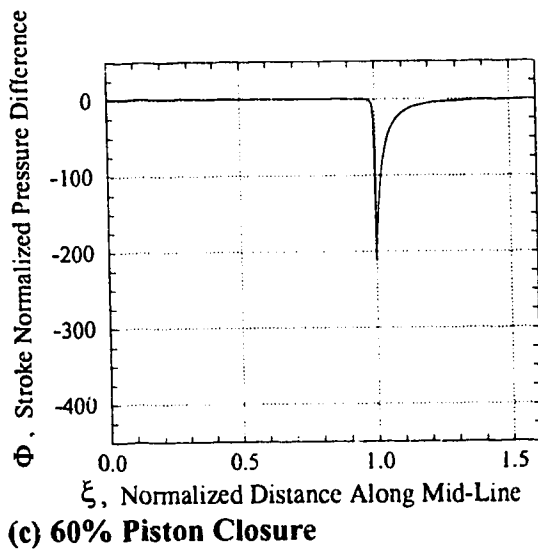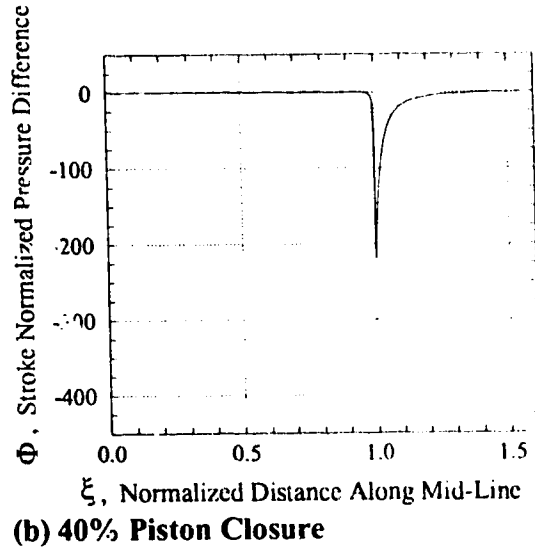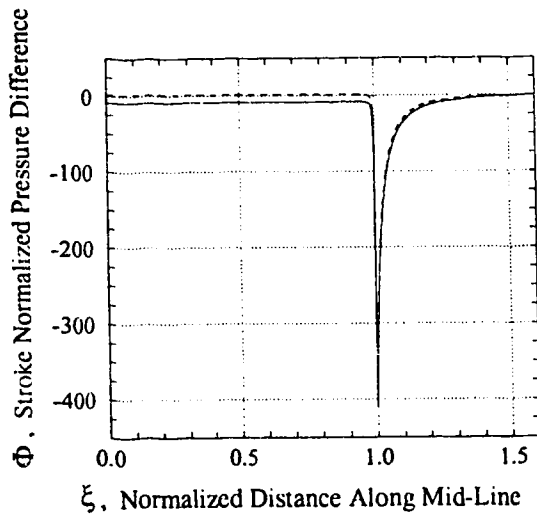
Figure 3.9: Normalized Mid-Line Pressure Differences at Various Restrictions: Severe Restriction Configuration

H_p P_p H_c maximum restriction

P_e

P_c

$y_p = 65$ mm

——— Unsteady
·············· Quasi-Steady

$$\% \text{ Piston Closure} = \frac{H_{P_{initial}} - H_p}{H_{P_{initial}} - H_{P_{final}}} \times 100$$

$$\Upsilon = \frac{P_p - P_c}{\Delta P_{stroke}}$$

$$\Phi_{mid} = \frac{P_p - P_e}{\Delta P_{stroke}}$$

$$\Delta P_{stroke} = 159 \text{ Pa}$$
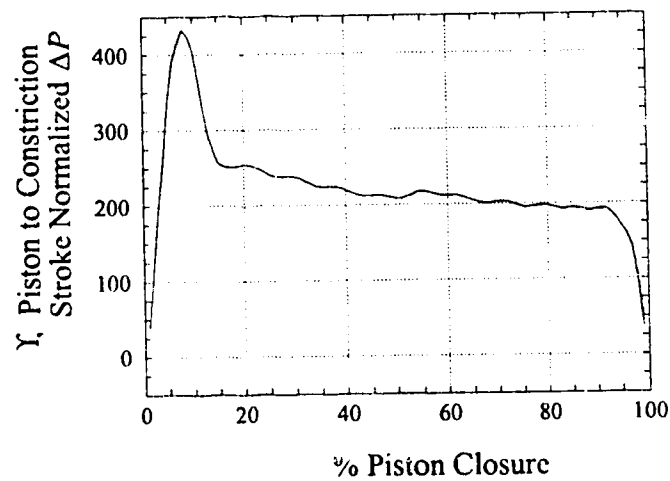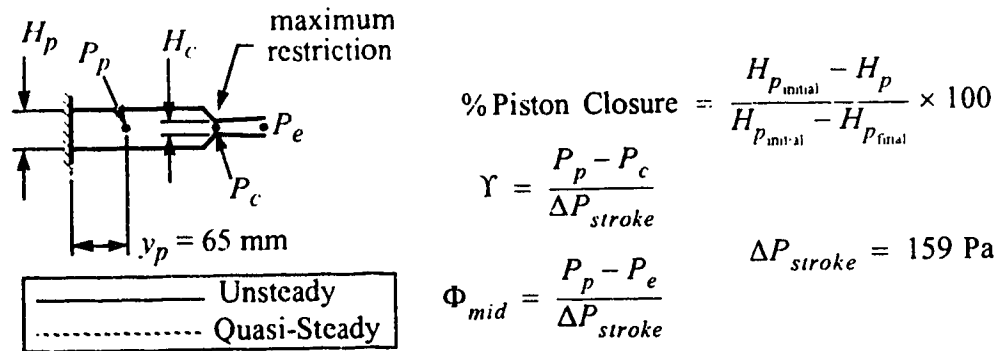
(a) Constriction Exit Pressure Difference
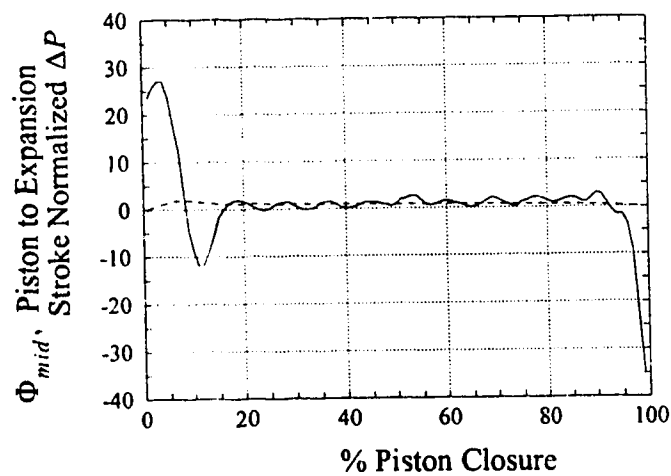
(b) Expansion Exit Pressure Difference

Figure 3.10: Pressure Differences Between Piston Region and Point of Maximum Constriction - Severe Restriction Configuration.

and final deceleration of the piston walls, with a period of near zero acceleration in between.

3.4.4 Progressive Restriction Configuration

The progressive restriction configuration, which simulates the systolic anterior motion concept (S/ M) incorporates a restriction that has an opening of H_c = 10 mm at the initiation of flow, and a final opening of H_c = 0.25 mm. This degree of restriction is linearly related to the piston position, such that when the piston is fully open, the restriction is fully open, and *visa versa*. The constriction wall speed and acceleration were calculated from the unsteady laboratory model's piston velocity, acceleration and geometry as

$$u_c = \frac{u_p}{5.250} \tag{3.37}$$

$$\frac{\partial u_c}{\partial t} = \frac{1}{5.250} \frac{\partial u_p}{\partial t}. \tag{3.38}$$

The average restric   r is $\eta_{l'}$ = 3.4, which corresponds to the very restricted HCM

case. The oth   = 127 mm, L_c = 6.35 mm, L_c = 76.2 mm, H_c = 25.4 mm,

and ρ   he other configurations). The pressure at v_p=0 was

arbit   t the calculations. Once the calculations were complete,

the pi   rmalized as before.

.tion region proved to be the critical area of the flow, as the velocity in this region became very high as the opening narrowed. The pressure drop was dominated by the degree of restriction, as can be seen in Figure 3.11. Each curve shows the pressure drop along the mid-line at different piston positions for both the unsteady and quasi-steady pressure equations. The peak pressure drop always occurred at ξ = 1, which is the point of maximum velocity and restriction.

The unsteady approach gives higher pressures at the piston fixed end wall (v_p = 0)
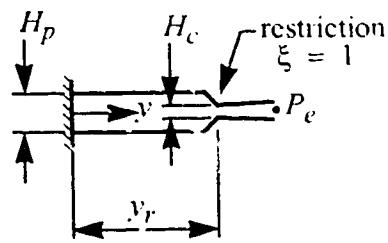
H_p H_c restriction $\xi = 1$

P_e

y

y_r

$\xi = \dfrac{y}{y_r}$

%Piston Closure $= \dfrac{H_{p_{initial}} - H_p}{H_{p_{initial}} - H_{p_{final}}} \times 100$

Unsteady
Quasi-Steady

$\Phi = \dfrac{P(y,t) - P_e}{\Delta P_{stroke}}$; $\Delta P_{stroke} = 739\,\text{Pa}$

(a) 10% Piston Closure

(b) 40% Piston Closure

(c) 60% Piston Closure

(d) 90% Piston Closure

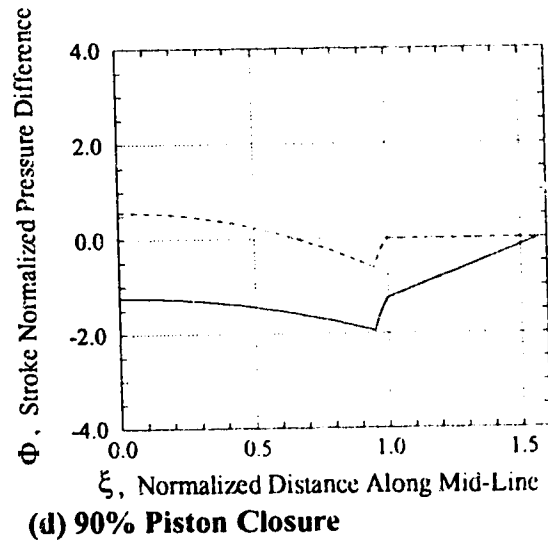ξ, Normalized Distance Along Mid-Line
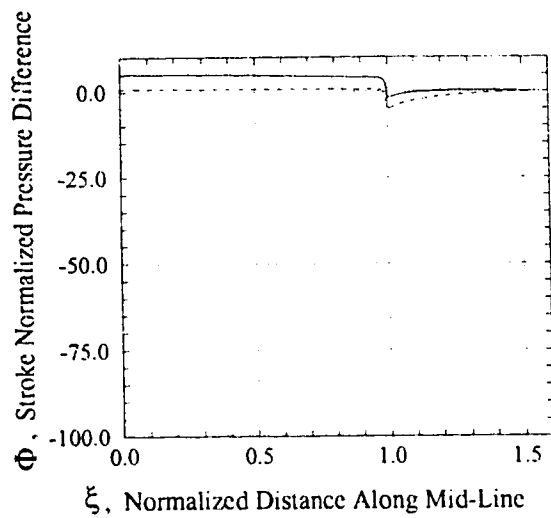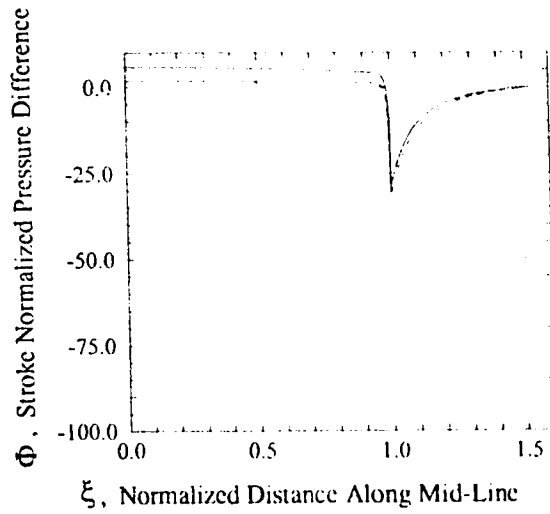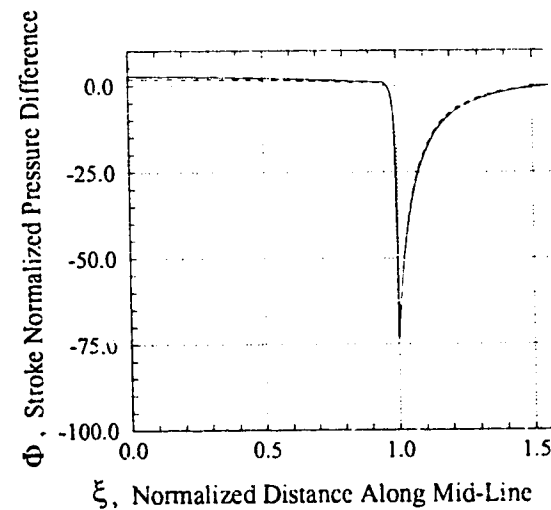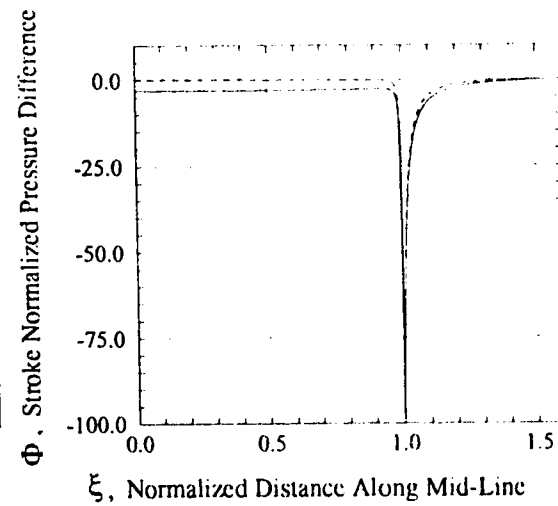
Φ, Stroke Normalized Pressure Difference

Figure 3.11: Normalized Mid-Line Pressure Differences at Various Restrictions: Progressive Restriction Configuration

than the quasi-steady approach when the piston wall is accelerating (Figure 3.11: 10% to 60% piston closure). The opposite happens as the piston decelerates, with the unsteady approach pressure being somewhat lower (Figure 3.11: 90% piston closure). The error in the quasi-steady pressure is less than 5% throughout the piston closure. This suggests that for significant restriction, the quasi-steady approach gives a reasonable estimate of the pressure, but may be in error for lesser restrictions.

An interesting observation is that the quasi-steady and unsteady results do not differ significantly when determining the maximum pressure difference between the piston region and the constriction exit, see Figure 3.12(a). These pressure differences match well because the time-dependant flow acceleration terms are not a major contributing factor in the pressure drop due to the restriction. The largest deviation between the two methods in determining the maximum normalized pressure difference was $\Upsilon = 1.5$, occurring at a 95% restriction. The minor oscillations in the pressures at the peak values are due to noise in the unsteady laboratory model data.

The pressure difference between the piston region and expansion exit are plotted in Figure 3.12(b). The quasi-steady approach gives very poor results for this pressure difference, as was the case with the fixed restriction and unobstructed configurations. The reason is simple: the time dependant flow acceleration terms make up the majority of the pressure loss in the absence of a restriction. If the expansion exit were severely restricted or if the piston wall velocity remained fairly constant, the quasi-steady approach would give very good results.

3.5 MODELLING FLOW SEPARATION IN THE PRESSURE EQUATIONS

The previously derived pressure equations did not allow for any separation in the flow. However, as will be shown in Chapters 5 and 6, flow separation did occur in the

$$\% \text{Piston Closure} = \frac{H_{P_{initial}} - H_P}{H_{P_{initial}} - H_{P_{final}}} \times 100$$

$$\Upsilon = \frac{P_P - P_c}{\Delta P_{stroke}}$$

$$\Delta P_{stroke} = 739 \text{ Pa}$$

$$\Phi_{mid} = \frac{P_P - P_e}{\Delta P_{stroke}}$$
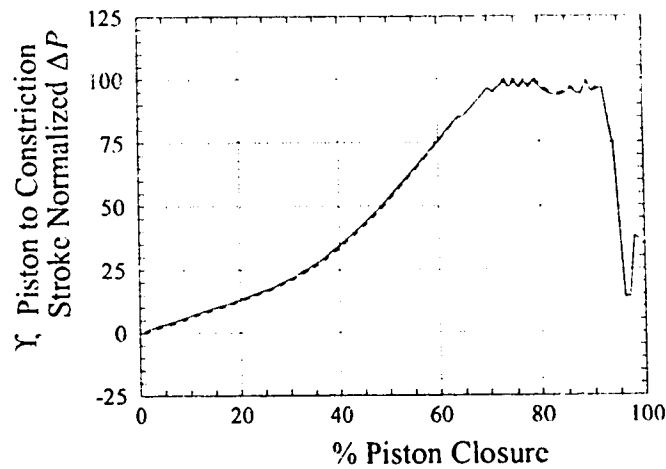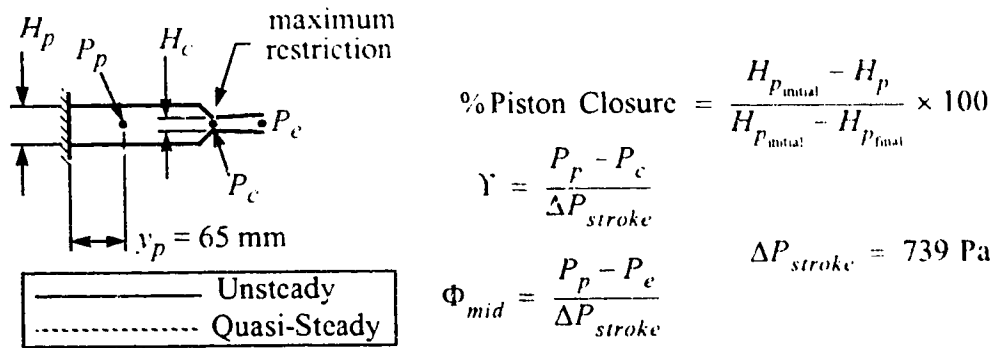
(a) Constriction Exit Pressure Difference
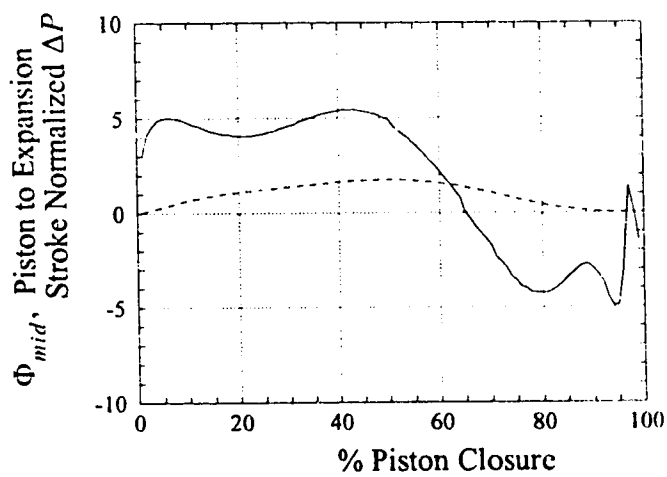
(b) Expansion Exit Pressure Difference

Figure 3.12: Pressure Differences Between Piston Region and Point of Maximum Constriction - Progressive Restriction Configuration

unsteady and steady flow laboratory models. One way to account for this would be to change the expansion region from a smooth expansion to a sudden expansion, as shown in figure 3.13. By using a linear momentum analysis for the control volume shown, the expansion exit pressure may be estimated.
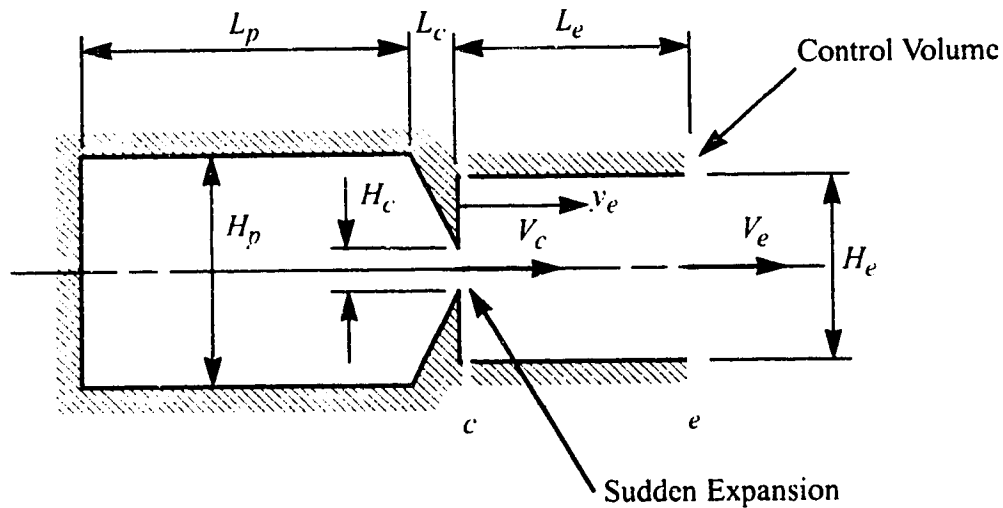
Figure 3.13: Sudden Expansion Geometry

3.5.1 Quasi-Steady One-dimensional Inviscid Approach With Sudden Expansion

The control volume is situated just downstream of the minimum constriction. It is assumed that the pressure across the control volume at this point is uniform and equal to $P(v_e=0,t)$. For the quasi-steady case, the linear momentum balance in the y-direction is

$$P_c(H_e B) - P_e(H_e B) = V_e(\rho V_e)(H_e B) - V_c(\rho V_c)(H_c B). \qquad (3.26)$$

The expansion exit velocity V_e may be expressed in term of the constriction exit velocity V_c using continuity:

$$V_e = V_c \frac{H_c}{H_e}. \qquad (3.27)$$

Substituting this into the momentum balance, the pressure difference between c and e becomes

$$P_v - P_e = \rho V_c^2 \frac{H_c}{H_e}\left[\frac{H_c}{H_e} - 1\right]. \tag{3.28}$$

3.5.2 Unsteady Approach With a Sudden Expansion

For the unsteady case, the linear momentum balance for the control volume is given by

$$-H_e B dP = \rho A \frac{\partial V}{\partial t} dy + \dot{m} dV. \tag{3.29}$$

The mass flow rate is

$$\dot{m} = \rho V_c H_c B = \rho V_e H_e B \tag{3.30}$$

If a linear variation in velocity from c to e is assumed, the velocity becomes

$$V(y_e, t) = V_c\left[\frac{y_e}{L_e}\left(\frac{H_c}{H_e} - 1\right) + 1\right].$$

If this is differentiated with time,

$$\frac{\partial V}{\partial t} = \frac{\partial V_c}{\partial t}\left[\frac{y_e}{L_e}\left(\frac{H_c}{H_e} - 1\right) + 1\right] \tag{3.31}$$

Substituting this expression along with the mass flow rate (equation 3.30) into the momentum equation (equation 3.29), and integrating from c to e,

$$-\int_c^e H_e B dp = \int_c^e \left[\frac{\partial V_c}{\partial t}\left[\frac{y_e}{L_e}\left(\frac{H_c}{H_e} - 1\right) + 1\right]\right] dy + \int_c^e \rho V_c H_c B dV.$$

This gives the desired pressure difference

$$P_v - P_e = \rho \frac{\partial V_c}{\partial t}\left[\frac{L_e}{2}\left(\frac{H_c}{H_e} - 1\right) + L_e\right] + \rho V_c^2 \frac{H_c}{H_e}\left(\frac{H_c}{H_e} - 1\right). \tag{3.32}$$

3.5.3 Results for Sudden Expansion

The previously examined severe fixed restriction and progressive restriction configurations were analyzed using the sudden expansion approximation. The pressure differences obtained are plotted in Figures 3.14 and 3.15, along with the unsteady Bernoulli results obtained previously. For all cases, there is very little pressure recovery downstream of the constriction for the sudden expansion, so that the pressure difference

$$\text{\% Piston closure} = \frac{[H_{p_{\text{initial}}} - H_{p_{\text{final}}}] - [H_p - H_{p_{\text{final}}}]}{H_{p_{\text{initial}}} - H_{p_{\text{final}}}} \times 100$$

maximum restriction

H_p P_p H_c $\bullet P_e$

$y_p = 65$ mm

$$\Phi_{mid} = \frac{P_p - P_e}{\Delta P_{stroke}} \qquad \Delta P_{stroke} = 159 \text{ Pa}$$

——— Unsteady
············· Quasi-Steady
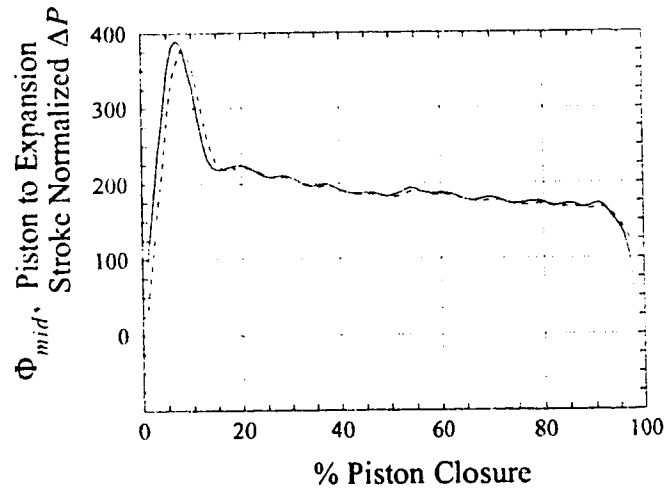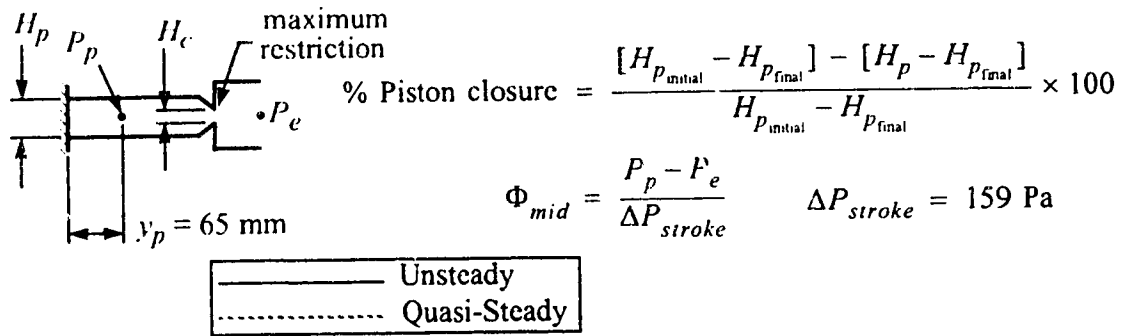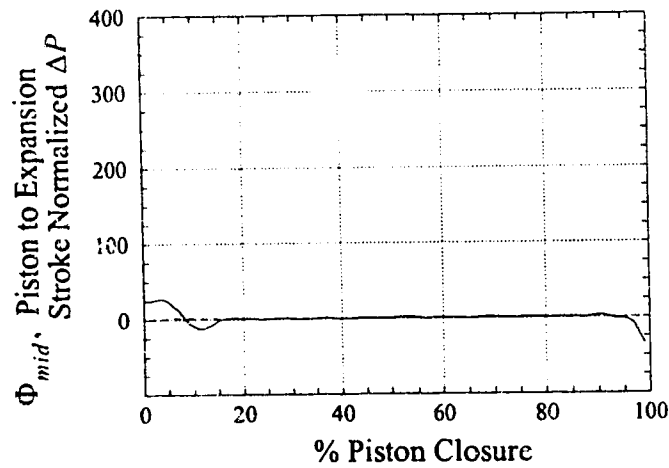
(a) Sudden Expansion

(b) No Separation

Figure 3.14: Normalized Pressure Differences $P_p - P_e$ With Sudden Expansion: Severe Restriction Configuration

$$\% \text{ Piston closure} = \frac{[H_{P_{initial}} - H_{P_{final}}] - [H_p - H_{P_{final}}]}{H_{P_{initial}} - H_{P_{final}}} \times 100$$

$$\Phi_{mid} = \frac{P_p - P_e}{\Delta P_{stroke}} \qquad \Delta P_{stroke} = 739 \text{ Pa}$$

Unsteady
Quasi-Steady
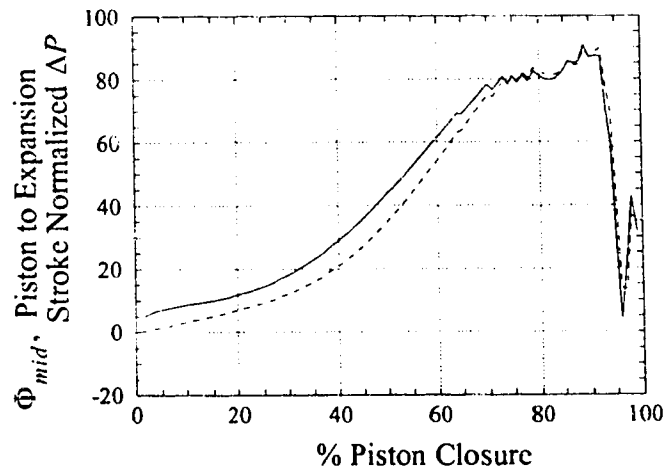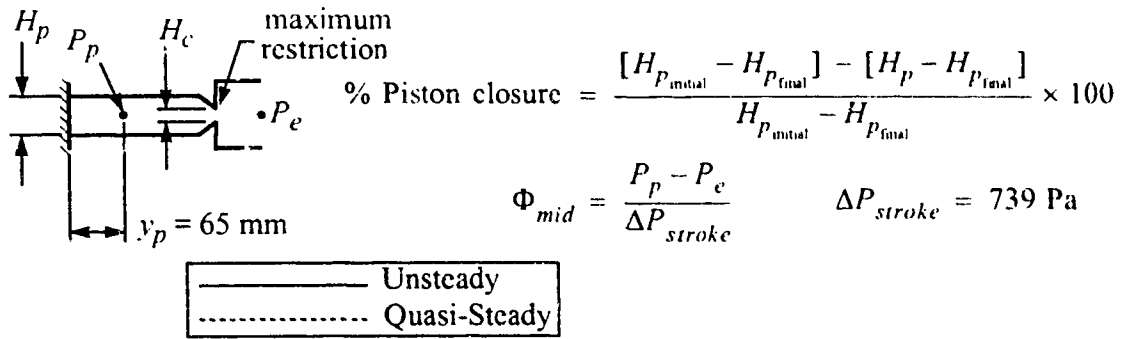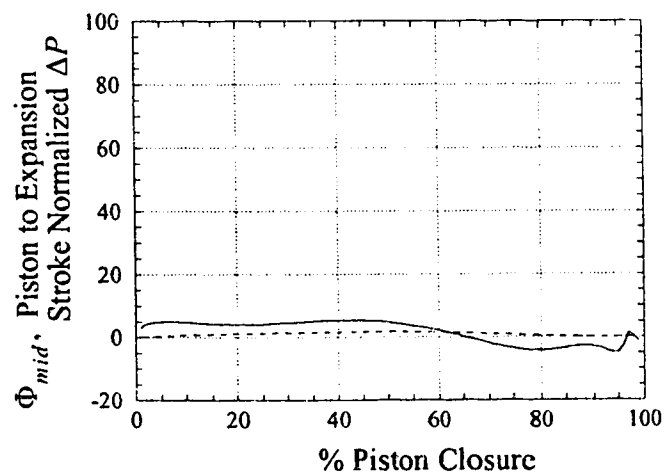
(a) Sudden Expansion

(b) No Separation

Figure 3.15: Normalized Pressure Differences P_p - P_e With Sudden Expansion: Progressive Restriction Configuration

becomes very large. This represents a limiting case, that will be used when comparing results with the unsteady laboratory model in Chapter 7.

3.6 SUMMARY

The following observations may be made based on the analysis described in this chapter:

- The unsteady Bernoulli equation for the case of moving walls is identical to the usual unsteady Bernoulli equation;

- The one-dimensional quasi-steady analysis gives a similar estimate of the constriction exit pressure difference as that predicted by the one-dimensional unsteady analysis for the progressive restriction and severe restriction configurations, but not for the unobstructed configuration;

- The quasi-steady approach gives inaccurate results for the pressure difference between the piston region and expansion exit. This is caused by the time dependant flow acceleration terms that make up the majority of the pressure loss in the absence of a restriction. If the expansion exit were severely restricted or if the piston wall velocity remained fairly constant, the quasi-steady approach gives a good estimate of the pressure difference;

- The pressure differences between the piston region and expansion exit are much larger for the sudden expansion than for the case of no separation.

CHAPTER 4 • QUASI-STEADY TWO-DIMENSIONAL COMPUTATIONAL ANALYSIS

4.1 INTRODUCTION

Two major limitations of the one-dimensional models described in Chapter 3 are their inability to predict flow separation regions and viscous effects. As the flow may separate downstream of the restriction, the pressure calculated by a one-dimensional analysis may be inaccurate in this zone. Further, if viscous drag is significant, the pressure losses in the flow will be under predicted. To account for these effects, a two-dimensional analysis that includes viscosity should be used; however, this requires the solution of the incompressible Navier-Stokes equations. As very few analytical solutions exist for these equations, one must turn to computational fluid dynamics techniques.

One advantage of the computational technique is that more complex physical geometries may be modelled. As noted by Kiris *et al* (1993), computational studies of blood flow in hearts with moving boundaries has been quite limited. The method of Peskin and McQueen (1989) is perhaps the most notable, but requires significant computational facilities. The simulation of the moving boundaries is a very challenging problem for computational fluid dynamics. Further, the discretization of the physical domain often present significant difficulties for a complex geometry. The techniques utilized by Kiris *et al* (1993) utilized a less complex, well defined geometry with prescribed wall motion and was quite successful for predicting unsteady flow in a left ventricle assist device. The left ventricle assist device was designed at Pennsylvania State University and is comprised of a flat disc-shaped chamber that incorporates a piston that moves up and down within the chamber, see Tarbell, Gunshinan, Geselowitz, Rosenburg, Shung and Pierce (1986).

There are also generalized codes available that can be used to model flows with moving walls. For example, KIVA is a three-dimensional code that was originally

developed by the Los Alamos National Laboratory to simulate internal combustion engines. The grid is an array of arbitrary hexahedra that can move in an arbitrary way relative to the fluid, so Eulerian and Lagrangian calculations are special cases of having the grid fixed and moving with the fluid speed, respectively. In a typical engine simulation, the grid motion is determined by the piston motion so a reasonable mesh is maintained that models the engine geometry as a function of time. The fluid is allowed to flow through this grid however it wants, so the typical calculation is neither Eulerian nor Lagrangian. Each hydrodynamic time step   rformed as a Lagrangian time step followed by a rezoning onto the new-tim   The code also contains models for real gas equations of state, turbulence, chemistry in . gas-phase combustion, and fuel sprays (personal communications with Larry Cloutman, Lawrence Livermore National Laboratory). While this code was written with simple piston cylinder geometries in mind, it may be possible to make modifications to allow the simulation of more complex geometries.

For the present study a quasi-steady approximation was used to simplify the analysis. The quasi-steady approach approximates the unsteady case by solving the flow equations at an instant in time, assuming the walls are not moving and treating the flow as steady. A moving piston, for example, would be treated as stationary, but with the face of the piston replaced with a fluid flow inlet having a prescribed fluid velocity equal to the velocity of the moving piston. By solving the flow at several points along the piston travel, a simulation of a moving piston may be constructed, at the expense of not including the unsteady acceleration effects or including the flow history. This simplification should yield reasonable results for the pressures and pressure differences for the case considered here, as time-dependent fluid acceleration effects on the pressure are often small compared to effects of obstructions. For example, the one-dimensional analysis (refer o Section 3.4.4, and Figures 3.13 and 3.16) showed this effect to be less than 5% for the progressive restriction case.

Since the intent of this research was not to develop new computational fluid dynamics (CFD) solution techniques, a commercial code was utilized. The code chosen was FLOW3D Release 3.2. This is a state of the art flow modelling package, capable of laminar and turbulent flow predictions including heat transfer.

This chapter will present the two-dimensional, viscous computational fluid dynamics analysis. The computational technique used by the commercial code requires two distinct steps: (1) develop a computational grid to describe the physical geometry and (2) solve the flow equations using this grid. It is essential to generate a good grid to avoid computational instability and errors in solving the highly non-linear flow equations. A critical review of grid development methods will be discussed below, followed by a description of the flow solutions.

Given that the Reynolds numbers for the flows under consideration reached values in excess of 42,000 (based on the width of the expansion exit), a turbulent analysis was used. This analysis did not predict any flow separation, which is different than both the quasi-steady and unsteady laboratory models which both showed some flow separation. Since the flow will initially be laminar, there must be a transition point to turbulent flow. As this point is difficult to predict in an accelerating flow, a laminar analysis was also used for comparison. It will be shown that the laminar solutions predicted pressure differences closer to the unsteady laboratory model results, but that solutions were limited by numerical convergence problems.

4.2 COMPUTATIONAL GRID DEVELOPMENT

4.2.1 General Configuration

The shape used for computational analysis is shown in Figure 4.1. This shape was selected to closely approximate the progressive restriction configuration of the laboratory unsteady flow model in a two-dimensional sense. The only significant deviation in shape
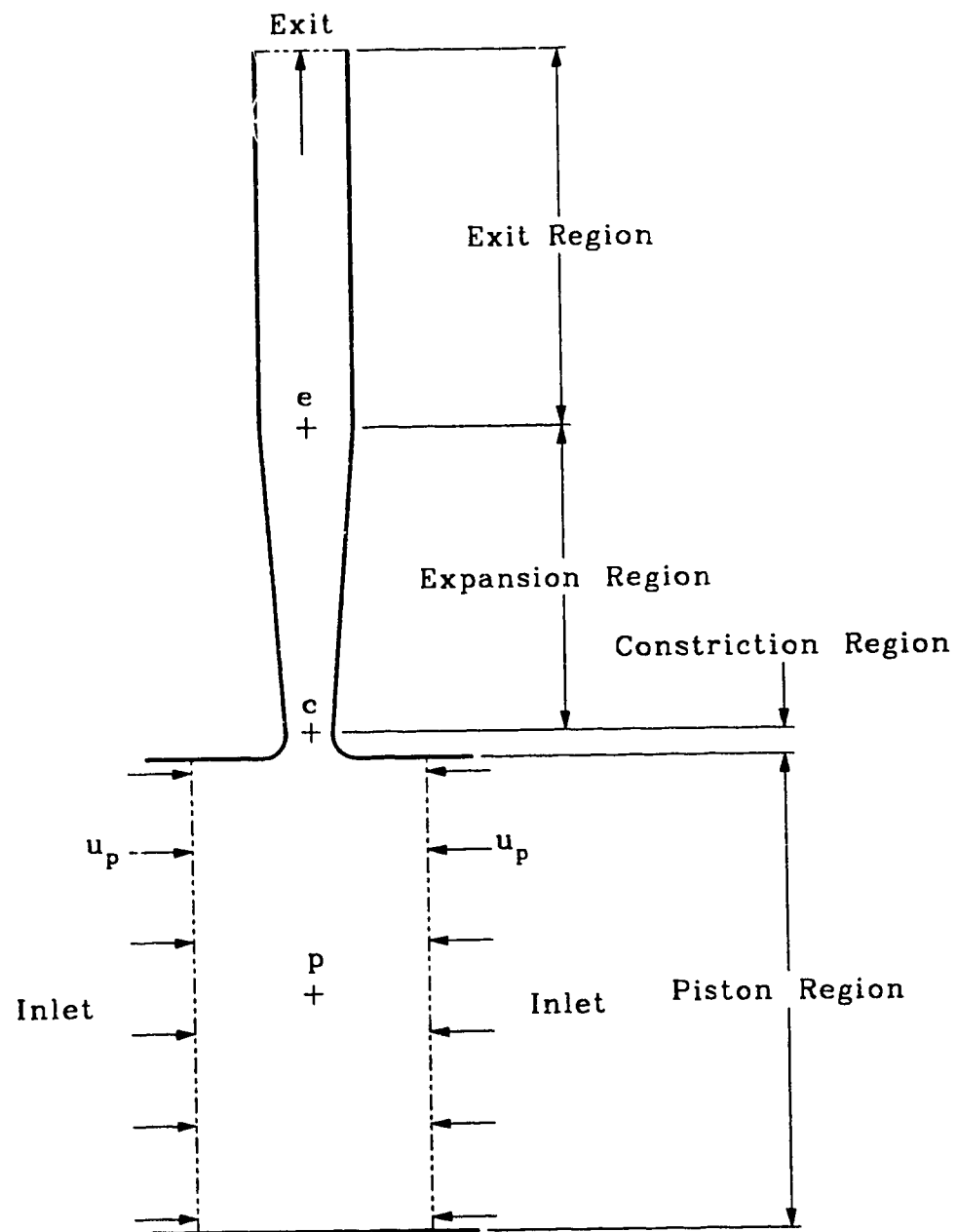
Figure 4.1: Geometry for Computational Fluid Dynamics Analysis

was the downstream exit region. The laboratory model had circular flow exit holes on the upper and lower surfaces (Figure 4.2). These could not be simulated in the two dimensional plane flow computations. There are three choices for the computational model to simulate these three-dimensional (circular) exits in a two-dimensional (plane channel) calculation:

- ignore this effect, and continue the outflow region without any change in cross-section (Figure 4.3(a));

- add a flow restriction of equal magnitude, continuing the flow in the same direction as the upstream section (Figure 4.3(b));

- add a flow restriction of equal magnitude, and have the flow undergo a 90° change in direction (Figure 4.3(c)).

Given that the flow in the laboratory model is subject to a flow restriction and a 90° change in direction, the third option was chosen.

The width of the exit channel was chosen to have the same cross-sectional area as the circular exit holes in the laboratory model. Since the laboratory model has a combined exit cross-sectional area of 1013 mm^2 for a section depth of $B = 102$ mm, a combined exit cross-sectional area of 9.94 mm^2/mm on a unit depth basis was required. Thus the width of each exit channel was set to 4.97 mm. An arbitrary corner radius of 12.8 mm was used to give a smooth transition through the corner. The length of the exit channel was set to 1 m (200 times the width) to allow the flow to return to fully developed flow.

Different grids were generated for each restriction analyzed. The restrictions analyzed were

- $\eta_{H} = 2.6$ (5% piston closure) to $\eta_{H} = 10$ (75% piston closure) in steps of 10% piston closure increments;

- $\eta_{H} = 10$ (75% piston closure) to $\eta_{H} = 50$ (95% piston closure) in steps of 5% piston closure increments.

Uppei Exit

Lower Exit

Not to scale
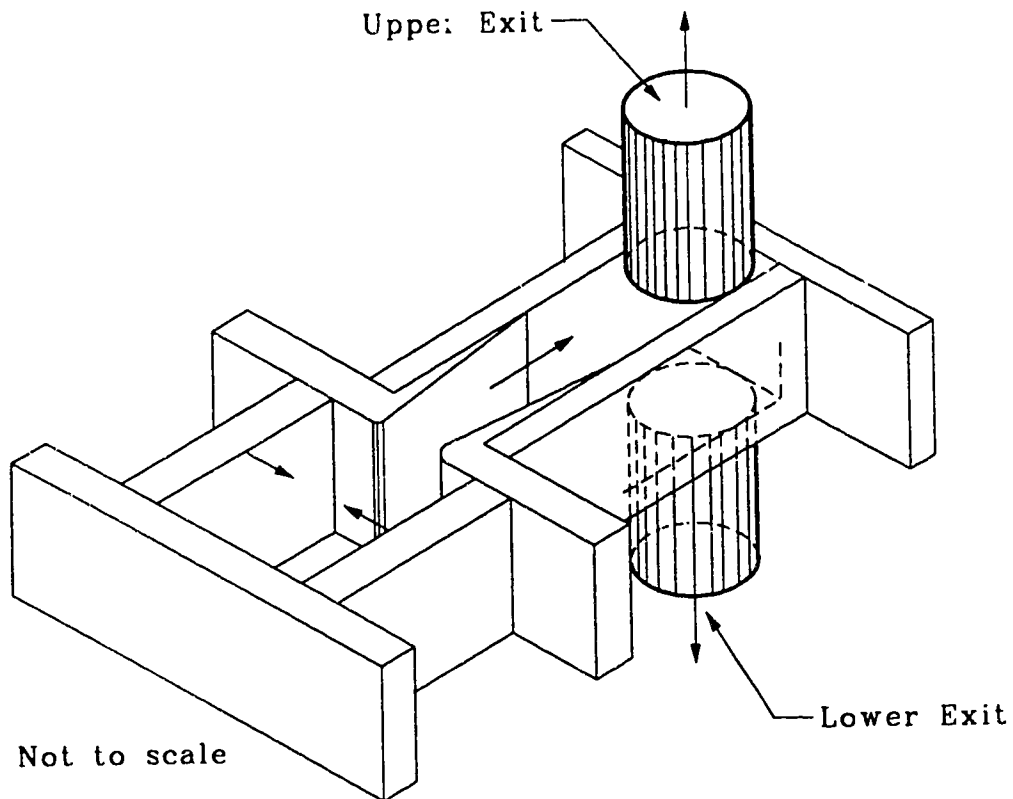
Figure 4.2: Unsteady Physical Model Exit Configuration
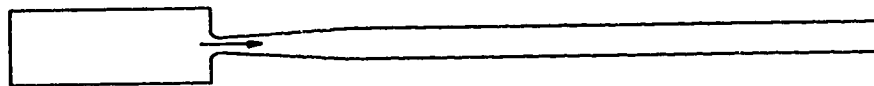
(a) Ignore exit effect
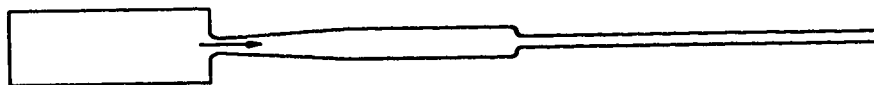
(b) Add an equivalent restriction
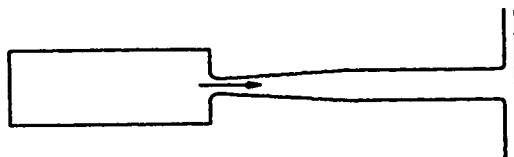
(c) Add an equivalent restriction and a flow direction change

Figure 4.3: Possible Exit Configurations

The reason for changing to a 5% piston closure increment when analyzing the more severe restrictions was to increase the time resolution at the point where the pressure differences reached their peak. While grids and flow solutions could be generated for smaller increments (to match the step size used in the unsteady Bernoulli and quasi-steady analysis described in Chapter 3), computer memory space required for such an undertaking would have been excessive, as each grid and its associated flow solution required 10 megabytes of disk storage. As will be seen from the results, the increments used gave adequate results.

The position of the piston walls at each restriction were chosen to match those of the unsteady laboratory model. Thus the pistons began 61 mm apart at the 5% piston closure position, and ended 17 mm apart at the 95% piston closure position. The variation of piston spacing with restriction was linear. The restriction began 9.7 mm apart at 5% piston closure and ended 0.76 mm apart at 95% piston closure.

As shown in Figure 4.4, grids were developed for only one side of the symmetrical shape. There were two reasons for doing this. The first was to prevent asymmetry in the solution. This allowed a direct comparison with the one-dimensional analysis of Chapter 3 (but deviated from the asymmetry observed in the laboratory models at higher restrictions described in section 5.5). The second reason for utilizing symmetry was to reduce the computer memory space required for the grids and flow solutions, and reduce the computational time required to generate the grids and solve the flow equations. The full geometry was also modelled to allow for asymmetry and will be discussed separately in section 4.5.

4.2.2 Grid Details

This section gives a general review of grid generation that expands on the limited description in the FLOW3D Release 3.2 User Manual, (1992). One of the features of

OUTLET

OUTLET

x

y

SYMMETRY LINE

This side only
used to create
grid

+

+

+

+

SYMMETRY LINE

INLET

INLET
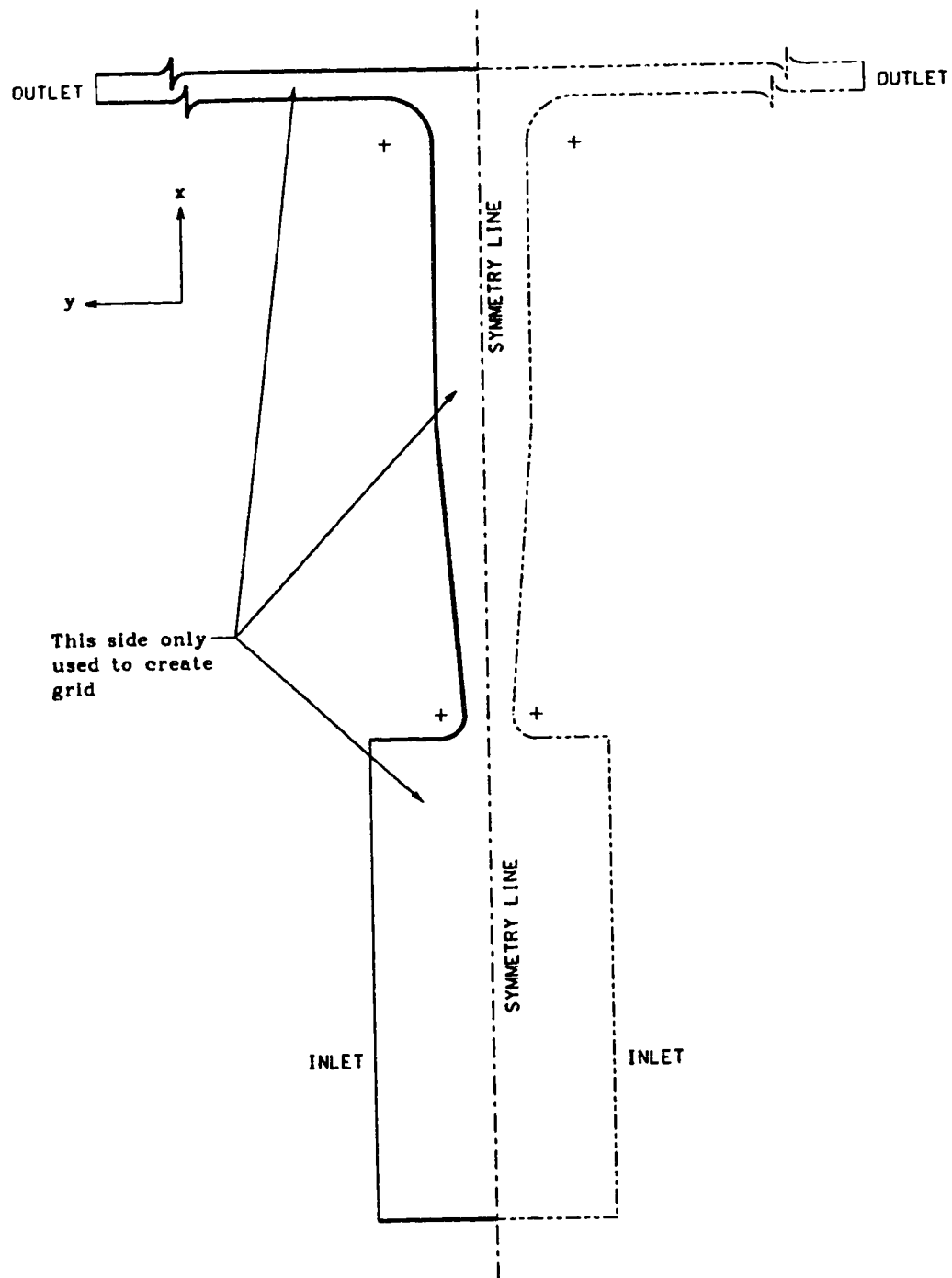
Figure 4.4: Use of Symmetry for Grid Generation

commercial finite difference flow codes is automatic grid generation. A common method, used by FLOW3D, is the boundary fitted coordinate system. First introduced by Wir.. low in 1966, the boundary fitted coordinate method has since been modified, expanded and improved by many subsequent researchers, the most notable of whom has been J.F. Thompson (1984). This coordinate system has several advantages that make it appropriate for creating a grid on which to solve the Navier-Stokes equations. First, the method can map irregular boundaries onto a fixed, rectangular computational grid, allowing for the use of a standardized flow equation solver. In other words, the curved shape shown in Figure 4.5(a) becomes the rectangular, equally spaced grid in the computational plane shown in Figure 4.5(b). Second, the method does not require interpolation at the boundaries, as each flow boundary is formed by a line of coordinates. Other important features are that the method automatically generates internal coordinates with a high degree of control on spacing and concentration, and the computer code used to generate the coordinates may be independent of the physical boundaries involved.

FLOW3D uses a multiple block grid, in which the grid is pieced together from a series of four sided blocks. For example, developing a grid for a tee-shape using a single block approach requires grid cells in useless areas, as shown in Figure 4.6(a). This causes a large amount of computer memory to be wasted. To reduce this waste, the multi-block method is employed, in which the tee is made from two separate blocks (Figure 4.6(b)). These blocks are joined at the connecting boundary. The blocks overlap each other so that a boundary surface on one block is in the interior of the other block. At each flow solution iteration, the boundary values of one block can be updated using interior values of the adjacent block.

The FLOW3D code requires grid lines in each block to line up with those in the next block, as illustrated in Figure 4.7. However, this was found to cause some limitations, as shown in Figure 4.8. If smaller control volumes are desired in block B, smaller control

(a) Physical plane grid

(b) Computational plane grid
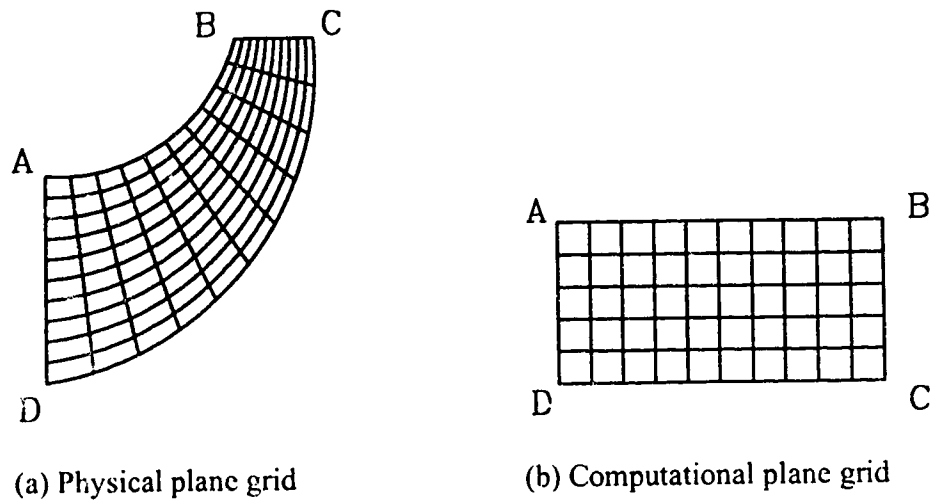
Figure 4.5: Physical and Computational Grids for Boundary Fitted Coordinates

Tee Shape

wasted cells

Block 2

Block 1

(a) Single block

(b) Multi-block
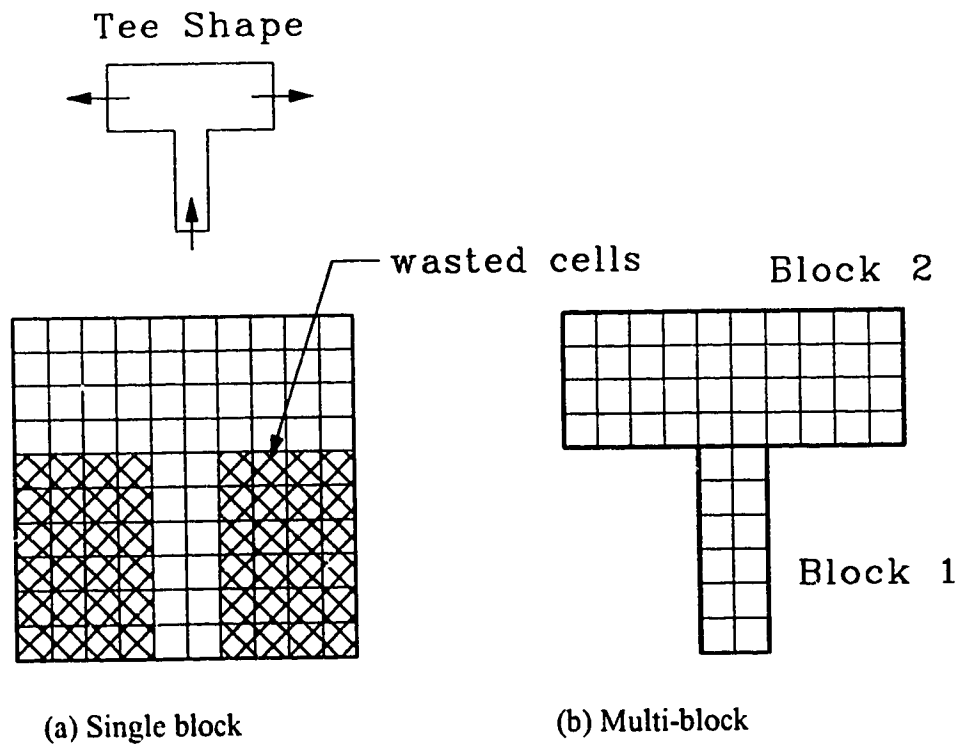
Figure 4.6: Use of Multiple Blocks to Avoid Wasted Cells in Grid Generation for a Tee-shaped Channel

volumes will also result in blocks A and C, resulting in wasted memory (Figure 4.8(a)). Alternatively, if a reasonable spacing of control volumes is used in blocks A and C, there spacing in block B may coarser than desired (Figure 4.8(b)). In some cases, this problem can be overcome by careful selection of blocks.

Another feature of boundary fitted coordinates is the control of coordinate spacing along the boundaries. While the computational grid will always be regularly spaced, no such requirement exists for the physical grid. Indeed, it is often desirable to concentrate grid lines in areas of sharp gradients, such as sudden changes in geometry. The commercial code allows the user to specify control parameters to facilitate this.

It should be noted that the FLOW3D code is fully three-dimensional; two-dimensional grids are generated by considering a unit thickness. Thus a two-dimensional grid is made up of control volumes with a unit thickness throughout. The upper and lower faces of these control volumes are considered to be symmetry planes, effectively restricting the problem to two-dimensions.

When breaking a complex shape into a series of blocks, there are three ways to increase computational accuracy: (1) concentrate grid points in areas of large gradients; (2) avoid making control volumes with large angles; and (3) make the grid vary smoothly without large jumps in grid spacing. Figure 4.9 shows one possibility for dividing the geometry into blocks. This grid caused problems for the flow solver, with unrealistic velocities occurring at location A. The problem is one of a control volume with excessive skewness, that causes significant numerical error and failure to converge to a steady solution.

The block configuration shown in Figure 4.10 overcomes this problem by reducing sharp control volume angles. This orientation was used throughout the analysis. Figure
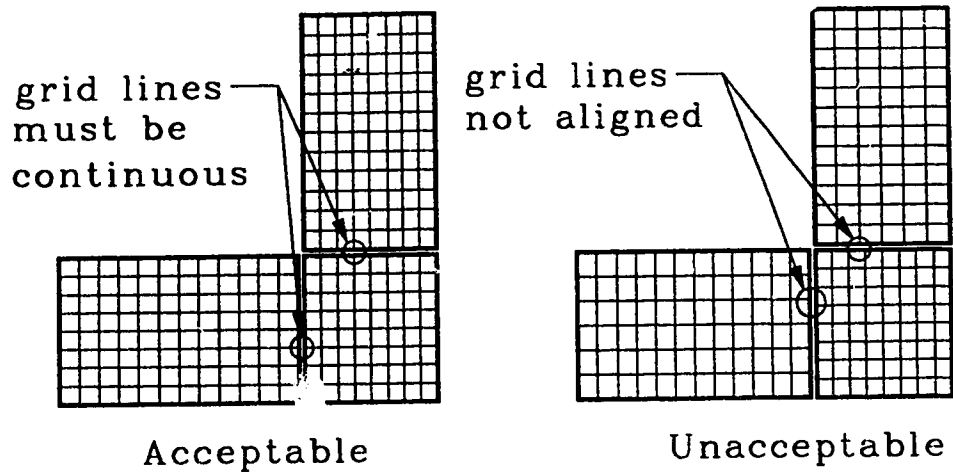
Figure 4.7: Grid Alignment Requirements in FLOW3D

(a) Not enough cells in Block 2

(b) Excessive cells in blocks 1 and 3.
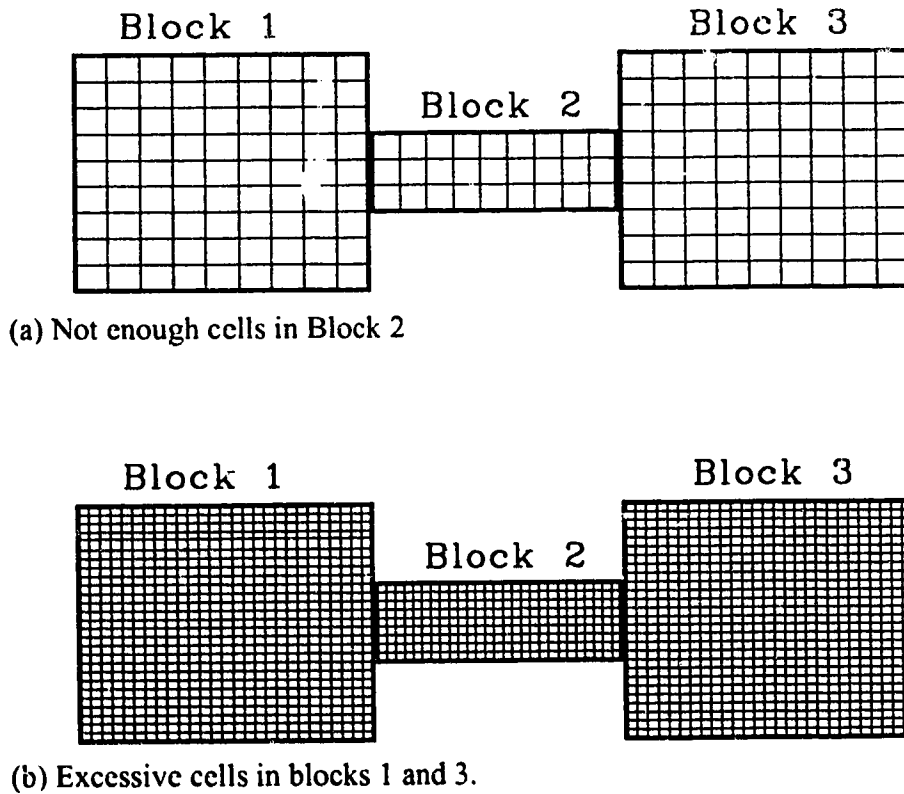
Figure 4.8: Grid Line Limitations Imposed by Alignment Requirements
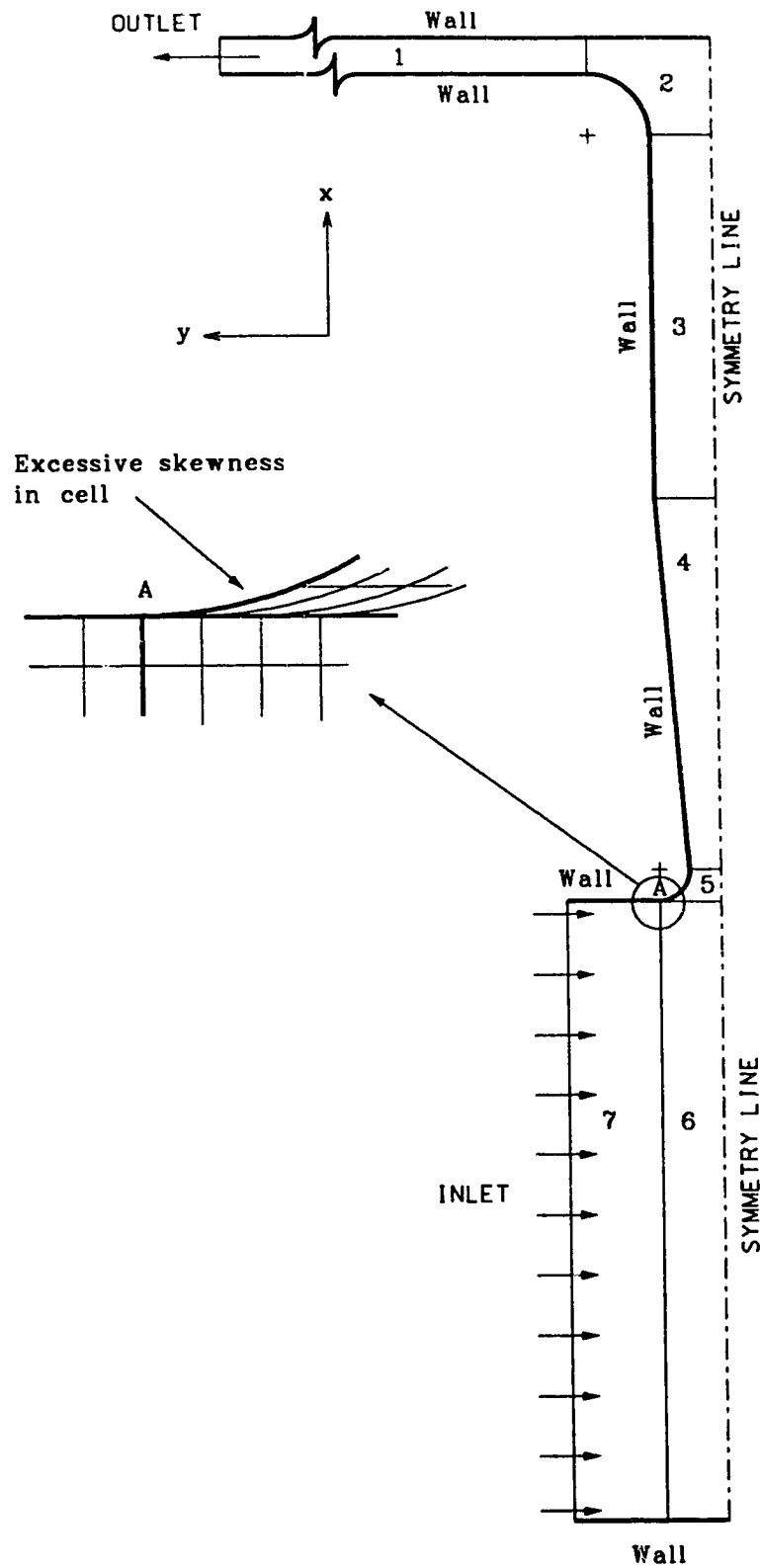
Figure 4.9: Block Configuration: First Trial

4.11 shows an enlargement of the 50% piston closure grid near the constriction region.

The commercial code allowed for either algebraic or elliptic solution of the grid. The advantage of an elliptic solution is that boundary discontinuities are not transmitted into the interior of the grid, and the resulting smoothness of the interior is likely to give better results, see Fletcher (1988). An algebraic solution allows more interior control of the grid points, avoiding overly dense or sparse areas. Because there were regions of strong curvature in the geometry considered here, an elliptic solution was used. All grids generated converged to a tolerance of less than 5×10^{-11} m (less than 5×10^{-9}% of the constriction width).

4.3 TURBULENT FLOW QUASI-STEADY ANALYSIS

4.3.1 Boundary Conditions

The first step in solving for the flow is to specify appropriate boundary conditions. The commercial code uses a logarithmic velocity profile near the wall. This assumes that near-wall regions have constant shear stress with distance normal to the wall. This is a common assumption, supported by some experimental evidence, see Coles and Hirst (1969). A further assumption used is that the length scale of a typical turbulent eddy in this region is proportional to distance from the wall. This is also supported by experimental evidence, see Wilcox (1993, page 47). By using this profile in the near-wall region, the rapid variance of variables near the wall is accounted for without the need for an extremely fine grid. Along the mid-line (Figure 4.4), an axis of symmetry was specified. FLOW3D requires all variables to be mathematically symmetric along this axis, resulting in no diffusion across the symmetry line.

There were two flow boundaries specified: an inlet boundary and a mass flow boundary at the exit. The inlet boundary (Figure 4.4) was used to specify the inlet velocity. In all cases, this velocity was laminar and normal to the boundary (no x-component) and
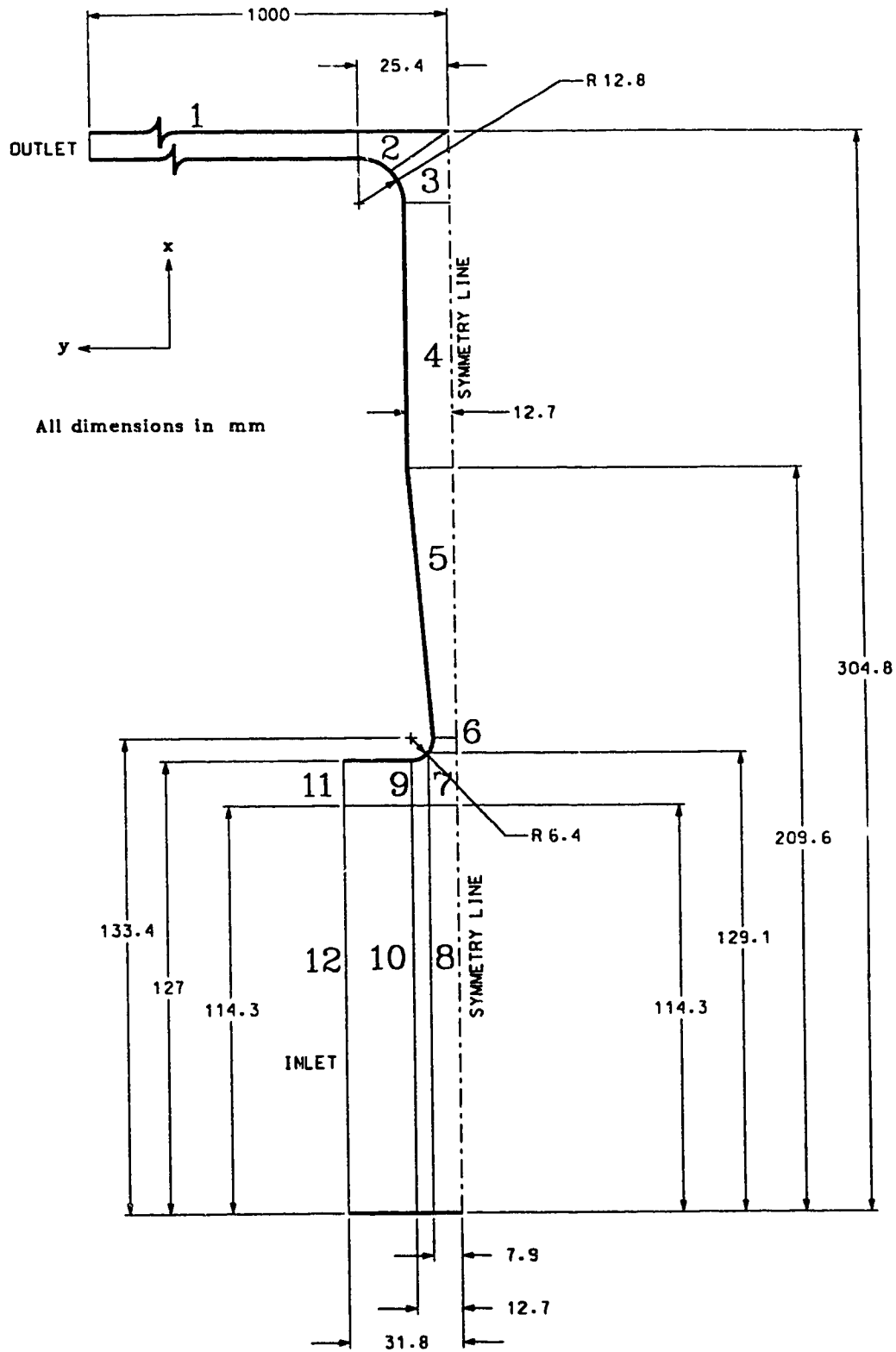
Figure 4.10: Final Block Orientation for Half-Grid Configuration

1.6 grid points per mm
(in y-direction)

7.0 grid points per mm
(in y-direction)
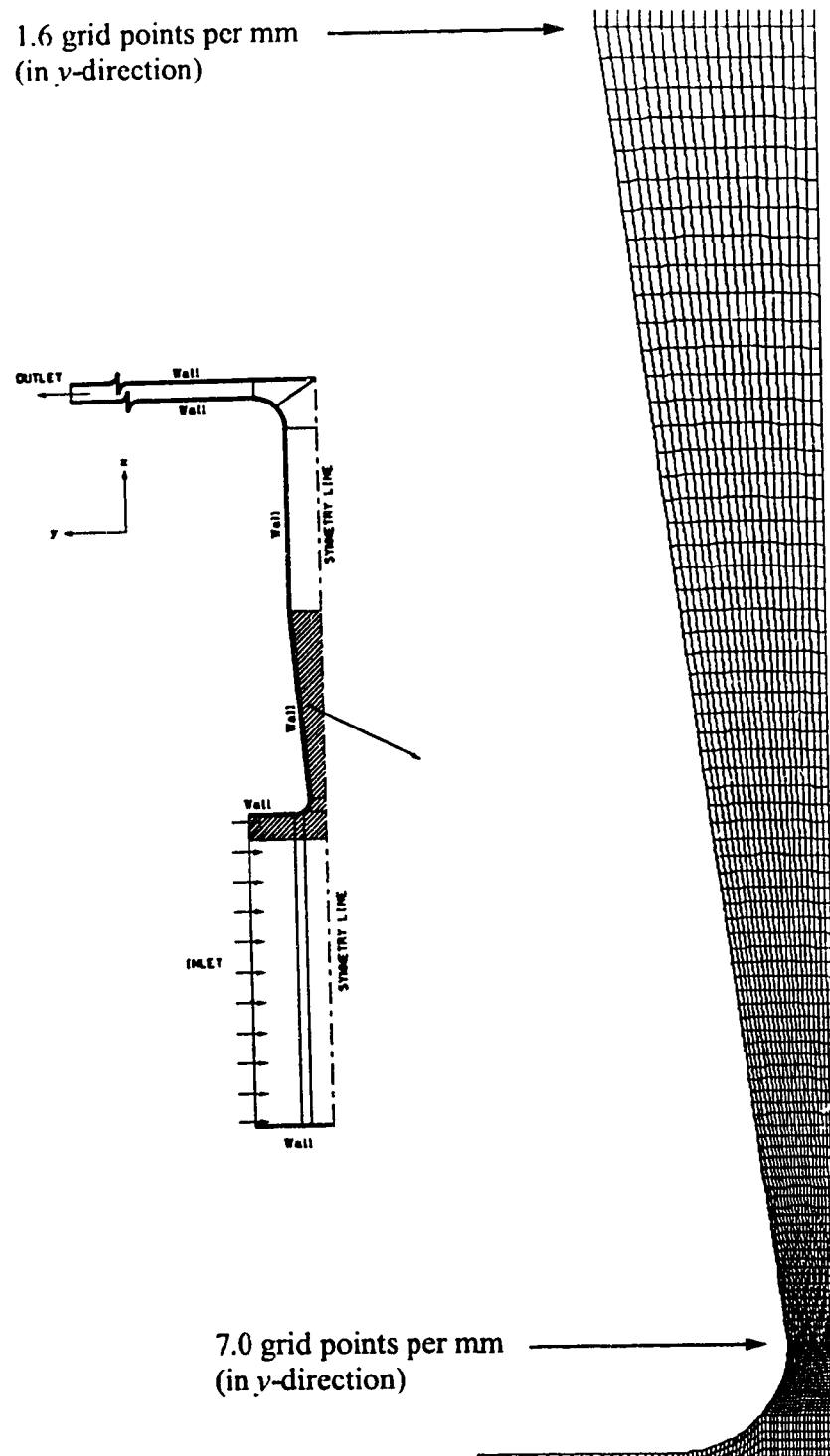
Figure 4.11: Grid for 45% Piston Closure

uniform across the entire boundary (plug flow). This was done to match the instantaneous velocity of the moving piston used in the unsteady laboratory model. The velocity chosen was the piston velocity derived from measurements on the unsteady laboratory model at the corresponding piston closure. Values of the inlet velocity for each solution are shown in Figure 4.12, along with the corresponding Reynolds numbers. The Reynolds numbers are based on the average velocity at the expansion exit and the channel width at this location. Inlet values of k of 0.0001 m^2/s^2 (about 5% of the maximum inlet velocity) and ε of 0.0001 m^2/s^2 were used throughout the analysis.

The mass flow boundary was specified at the exit location shown in Figure 4.4. FLOW3D carried out the following calculations:

- Applying a Neumann boundary condition at the boundary

$$\frac{\partial U^i}{\partial n} = 0;$$
(4.1)

where n = direction normal to the boundary,

U^i = velocity at the boundary.

- Determining the difference between the actual mass flow rate out of the domain, M^i, and the desired mass flow rate, M, where

$$M^i = \rho U^i A,$$
(4.2)

$$M = \rho U A;$$
(4.3)

A = cross sectional flow area at the boundary

- Scale the boundary velocity U^i to give the desired mass flow rate M at the boundary.

This specification is equivalent to fully developed flow at the outlet. As is the case for the problem considered, it gives good accuracy only if the outlet is placed far downstream and the width of the channel is unchanging at the outlet.
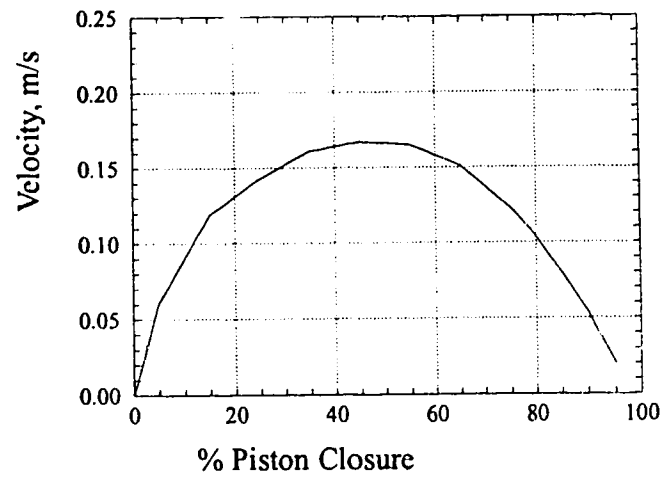
(a) Velocities at inlet (u_p)
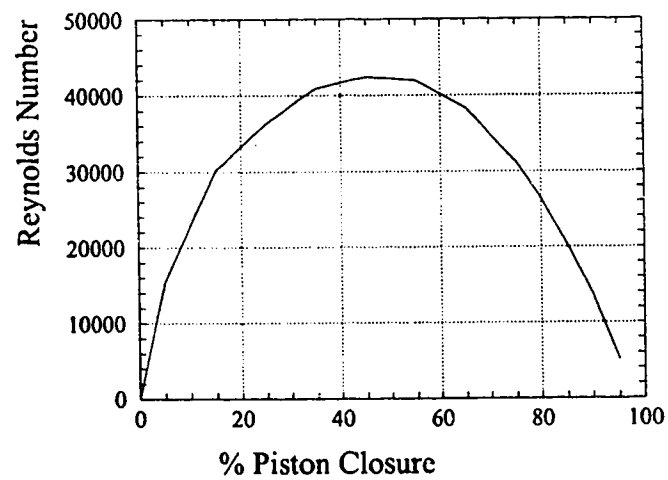
(b) Reynolds Numbers

Figure 4.12: CFD Input Velocities and Reynolds Numbers
(discontinuities in the curves due to distinct points being plotted)

4.3.2 k-ε Turbulence Equations

The commercial code utilizes the k-ε model to solve for the turbulent velocities and the associated pressures. This approach uses the continuity and momentum equations defined in terms of the turbulence kinetic energy k and the turbulence dissipation rate ε

$$\frac{\partial \rho}{\partial t} + \nabla \cdot (\rho \vec{U}) = 0 \tag{4.4}$$

$$\frac{\partial}{\partial t}(\rho \vec{U}) + \nabla \cdot (\rho \vec{U} \times \vec{U}) - \nabla \cdot (\mu_{eff} \nabla \vec{U}) = -\nabla p' + \nabla \cdot (\mu_{eff}(\nabla \vec{U})^T) + \vec{B} \tag{4.5}$$

where ρ is the mean fluid density, U is the mean fluid velocity, B is the body force, and μ_{eff} is the effective viscosity. The effective viscosity is defined in terms of the turbulence kinetic energy k and the turbulence dissipation rate ε by the eddy (turbulent) viscosity μ_T:

$$\mu_{eff} = \mu + \mu_T \tag{4.6}$$

where

$$\mu_T = C_\mu \rho \frac{k^2}{\varepsilon}, \tag{4.7}$$

and C_μ is a constant. The default value recommended by FLOW3D of $C_\mu = 0.09$ was used throughout the analysis. The transport equations for the turbulence kinetic energy k and the turbulence dissipation rate ε are

$$\frac{\partial}{\partial t}\rho k + \nabla \cdot (\rho \vec{U} k) - \nabla \cdot \left(\left(\mu + \frac{\mu_T}{\sigma_k}\right)\nabla k\right) = P - \rho \varepsilon \tag{4.8}$$

and

$$\frac{\partial}{\partial t}\rho \varepsilon + \nabla \cdot (\rho \vec{U} \varepsilon) - \nabla \cdot \left(\left(\mu + \frac{\mu_T}{\sigma_\varepsilon}\right)\nabla \varepsilon\right) = C_1 \frac{\varepsilon}{k} P - C_2 \rho \frac{\varepsilon^2}{k}. \tag{4.9}$$

The recommended default values of the empirical constants $C_1 = 1.44$ and $C_2 = 1.92$ were used throughout (Launder and Spalding, 1974). P is the shear production defined by

$$P = \mu_{eff} \nabla \vec{U}(\nabla \vec{U} + (\nabla \vec{U})^T) - \frac{2}{3}\nabla \cdot \vec{U}(\mu_{eff}\nabla \cdot \vec{U} + \rho k). \tag{4.10}$$

FLOW3D determines convergence by testing the error in continuity, which is called the mass source residual. The mass source residual is the sum of the absolute values of the net

mass fluxes into or out of every cell in the flow. A value of 0.05 kg/s, which corresponded to a reduction of the initial mass source residual by four orders of magnitude, was found to give acceptable results for all solutions. Further iterations did not significantly reduce the residual beyond this point.

4.4 LAMINAR FLOW QUASI-STEADY ANALYSIS

4.4.1 Boundary Conditions

As with the turbulent model, the first step in solving for the flow is to specify the appropriate boundary conditions. FLOW3D used a quadratic velocity profile (*i.e.* fully developed) near the wall, combined with a no slip velocity boundary condition at the wall.

The other boundary conditions specified were identical to the turbulent model. Along the mid-line (Figure 4.4), an axis of symmetry was specified. The inlet boundary (Figure 4.4) was used to specify a uniform velocity normal to the boundary. The velocity chosen was the piston velocity obtained from the unsteady physical model for the corresponding piston closure, and is the same as those used for the turbulent computations. The mass flow boundary was specified at the exit location (Figure 4.4).

4.4.2 Laminar Flow Equations

The commercial code solves the continuity and momentum equations

$$\frac{\partial \rho}{\partial t} + \nabla \cdot (\rho \vec{U}) = 0 \tag{4.11}$$

$$\frac{\partial}{\partial t}(\rho \vec{U}) + \nabla \cdot (\rho \vec{U} \times \vec{U}) = \vec{B} + \nabla \sigma \tag{4.12}$$

where σ is the stress tensor defined by

$$\sigma = -p\delta + \mu (\nabla \vec{U} + (\nabla \vec{U})^T). \tag{4.13}$$

The same convergence criteria used in the turbulent solutions were used for laminar flow solutions. However, as the restriction became more severe, FLOW3D was unable to con-

verge. This seemed to be due to a numerically unstable flow separation in the expansion region. The solutions affected were for piston closures between 35% and 85%. A variety of techniques were used to try to attain proper convergence. These included denser grids in the expansion region (Blocks 4 and 5 in Figure 4.10), running the code in double precision mode, and using a previously converged solution for a slower flow rate as an initial guess. None of the methods proved satisfactory, giving only slight improvements. It is possible the interface between Blocks 4 and 5, which lies in the flow separation region, could have caused some of the convergence problems. The numerical interpolations necessary at this interface could be adding considerable numerical error due to the strong velocity gradients in this region.

4.5 FLOW SOLUTIONS

4.5.1 Turbulent and Laminar Flow Solutions

Velocity plots of the flow in the area downstream of the restriction are shown in Figure 4.13 for piston closures of 45% (a restriction factor of $\eta_{ff} = 4.5$) and 85% ($\eta_{ff} = 16.7$) for both the turbulent and laminar flow cases. These plots show cross-stream profiles of the y-component of velocity (v is positive in the downstream direction) at three locations: the piston region, at the maximum constriction and at the exit of the expansion region. The cross-stream distance (x-direction) was normalized using the width in the x-direction; the velocity was normalized with the maximum velocity at each location. The step increase in velocity for all solutions occurring near x/H_{local} of zero is due to the grid spacing at the wall. An interesting feature is the lack of flow separation in the turbulent flow solutions. This was true of all the turbulent flow solutions, regardless of the restriction factor. This suggests that if the flow through the restriction were a turbulent steady flow, there would be no separation. However, it will be shown that separation occurs in the steady flow physical model for a restriction factor of $\eta_{ff} = 16.7$, and that the flow was turbulent. The laminar solutions show a very strong flow separation,

Restriction Factor at 45% Piston Closure: $\eta_H = 4.5$
Restriction Factor at 85% Piston Closure: $\eta_H = 16.7$

H_{local} is the channel
width at any location

Piston: $y = 65$ mm

Constriction:
$y = 133$ mm

Expansion:
$y = 209$ mm

Inlet

———— Piston
— — — Constriction
— · — Expansion
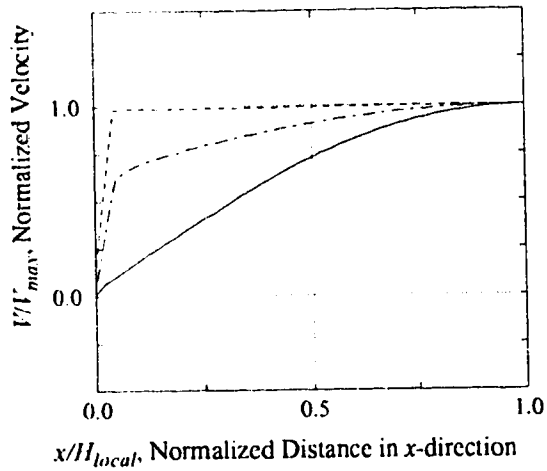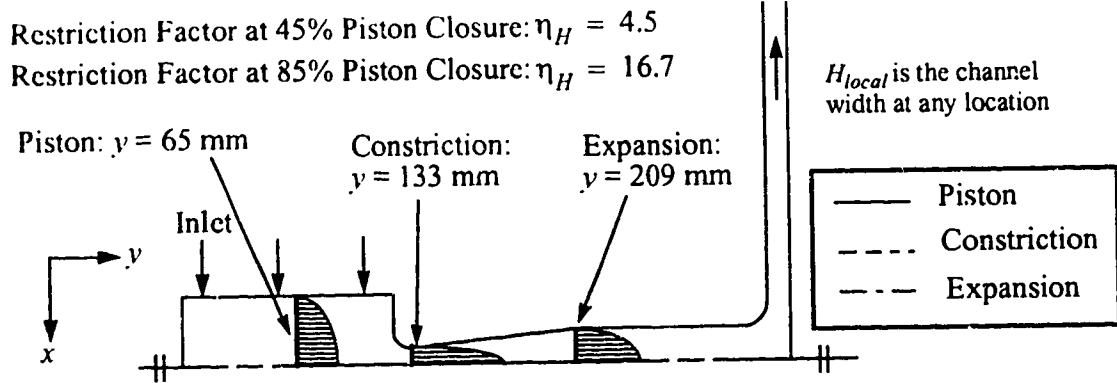
(a) Turbulent Flow, 45% Piston Closure
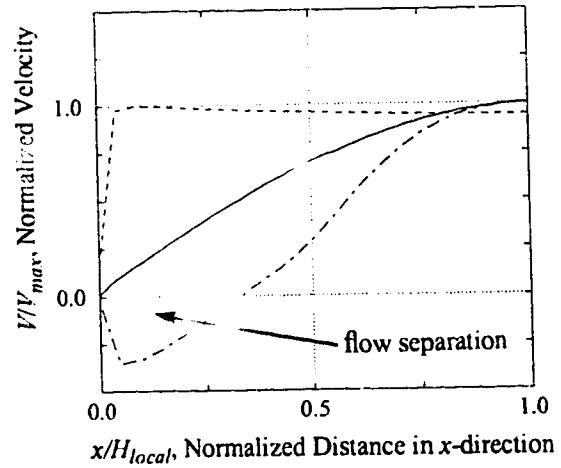
(b) Laminar Flow, 45% Piston Closure
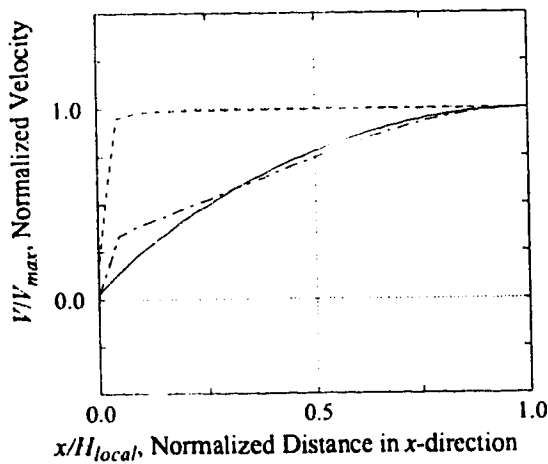
(c) Turbulent Flow, 85% Piston Closure
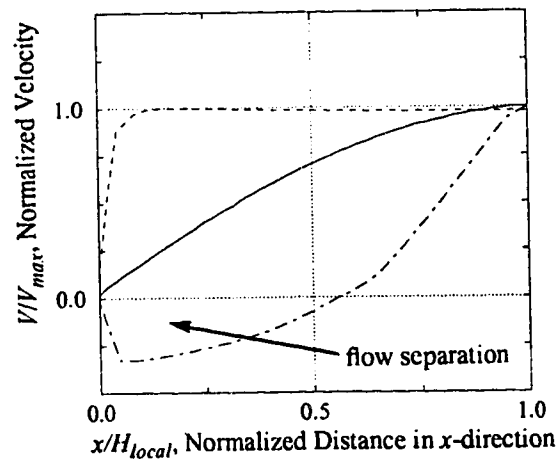
(d) Laminar Flow, 85% Piston Closure

Figure 4.13: y-**Component Normalized Velocities at Various Flow Cross Sections for Turbulent and Laminar Solutions**

indicated by the negative normalized velocities. This separation began at a piston closure of 25% (η_H = 3.3). The laminar separated flow for η_H = 16.7 was numerically unstable and FLOW3D failed to converge.

The one-dimensional inviscid analysis described in Chapter 3 used a uniform flow profile at every cross-section. The velocity profiles determined using FLOW3D, shown in Figure 4.13, show a parabolic profile in the piston region, a uniform profile across the constriction and a somewhat parabolic profile across the expansion exit. Since the velocity in the piston region is quite small when compared to the velocity at the constriction (on average, about 10 times smaller), this will not introduce an appreciable error when using the one-dimensional analysis to determine the pressure difference between the piston and constriction regions. However, some error will occur when using the one-dimensional analysis to determine the pressure difference between the piston and expansion regions.

Pressures were adjusted and normalized in the same manner as the one-dimensional solutions in Section 3.4.1. However, rather than set all solutions to have the same pressure at the expansion region exit, the reference point was the intersection of the mid-line and the downstream wall, shown in Figure 4.14. This formed a more consistent reference point, as it was a stagnation point and thus unaffected by flow separations.

Figure 4.14 shows the normalized mid-line pressures from the turbulent and laminar solutions for different piston closure positions. In all cases, minimum pressure occurs at the maximum constriction, which is the location of the maximum velocity in the flow. Due to the flow separation in the laminar solutions, pressure recovery is reduced. The spatial oscillations of pressure in the expansion region of the laminar solutions for piston closures of 55% to 85% are due to the numerically unstable laminar separation.

The pressure difference between the piston region and the point of maximum

H_p H_c ⟶restriction
$\xi = 1$

$\xi = \dfrac{y}{y_r}$

P_e

$\rightarrow v$

y_r

——— Turbulent
·············· Laminar

% Piston Closure $= \dfrac{H_{p_{initial}} - H_p}{H_{p_{initial}} - H_{p_{final}}} \times 100$

$\Phi = \dfrac{P(y) - P_e}{\Delta P_{stroke}}$; $\Delta P_{stroke} = 739\,\text{Pa}$

(a) 15% Piston Closure

(b) 45% Piston Closure

(c) 65% Piston Closure

(d) 85% Piston Closure

ξ, Normalized Distance Along Mid-Line

Φ, Stroke Normalized Pressure Difference
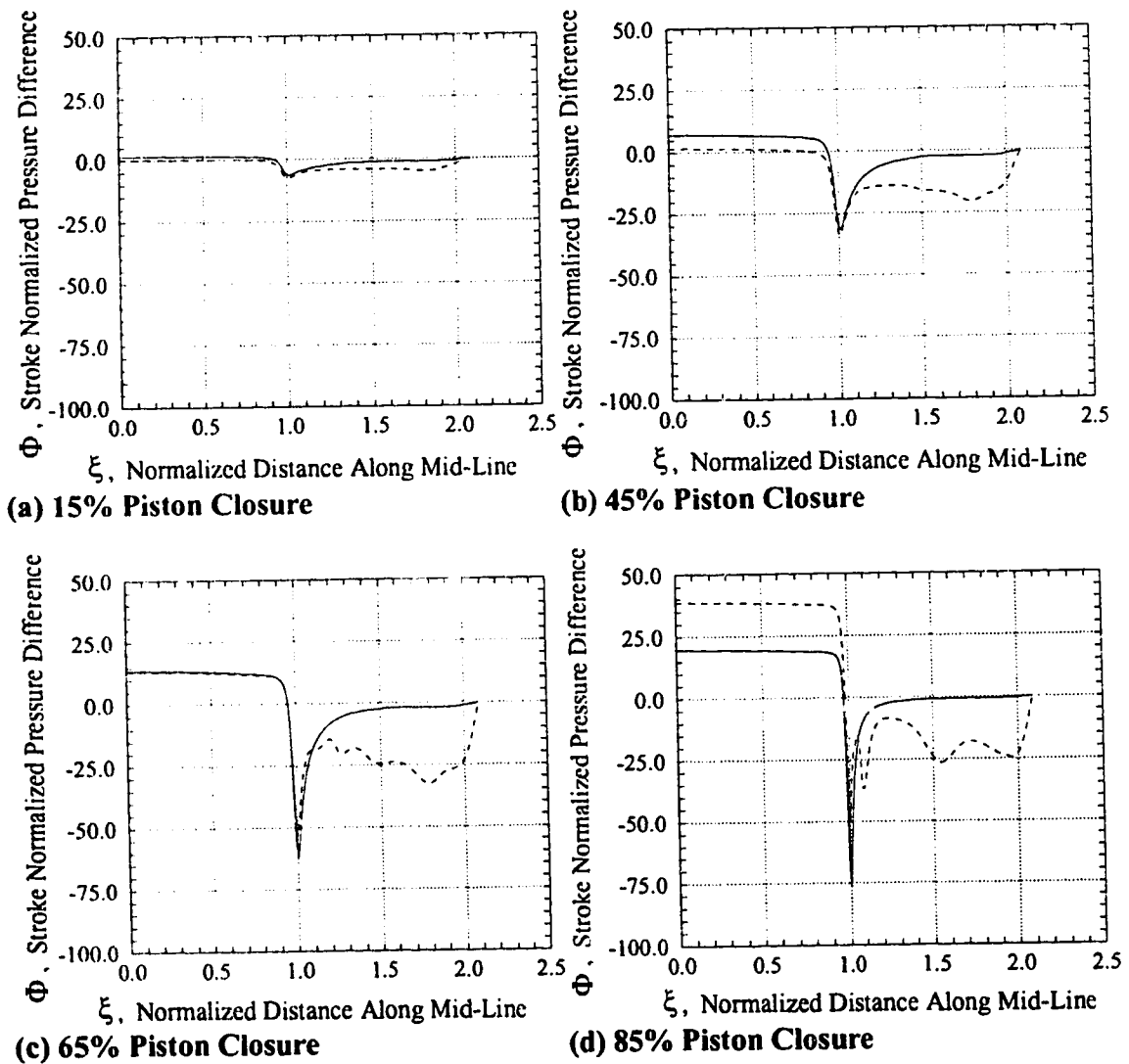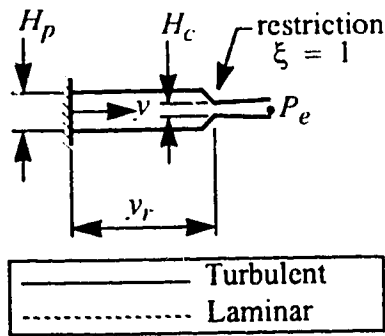
Figure 4.14: Normalized Mid-Line Pressure Difference at Various Restrictions

restriction is plotted in Figure 4.15(a). The pressure differences for the two solutions are similar, with the greater loss occurring for turbulent flow. This is due in part to the turbulent solution having a slightly higher velocity at the constriction mid-line (point c, Figure 4.15). For example, for a piston closure of 80% (a severe restriction or stenosis), the pressure differences based on velocities alone is $\Upsilon_{turbulent} = 91.4$ and $\Upsilon_{laminar} = 83.6$, compared with the actual values of $\Upsilon_{turbulent} = 102.3$ and $\Upsilon_{laminar} = 85.5$. Thus at this point 89% of the turbulent flow pressure drop and 98% of the laminar flow pressure drop is due to the change in velocity. Only 11% of the turbulent flow pressure drop and 2% of the laminar flow pressure drop is due to viscous losses.

The pressure difference between the piston region and the exit from the expansion region is plotted in Figure 4.15(b) for both the turbulent and laminar flows, again normalized by the stroke pressure. At this point, the pressure drop for the laminar flow exceeds that for the turbulent flow by a factor of two. This is due to the flow separation that occurred only for the laminar flow.

4.5.2 Turbulent Solutions Allowing for Asymmetry

It will be shown in Chapter 6 that the steady flow physical model exhibited an unsteady asymmetric separation (*i.e.* a strongly fluctuating point of separation in the expansion with a jet down one side and reverse flow up the other side) in the expansion region for a restriction factor of $\eta_H = 16.7$ (piston closure of 85%). As the previous computational solutions made use of symmetry, asymmetry in the flow about the mid-line of the configuration was prevented. In order to ascertain if the computational solution would become asymmetric, a complete grid, illustrated in Figure 4.16, was solved for the 85% piston closure case. The boundary conditions and inlet velocities were specified as before for the turbulent model (Section 4.3.1).

Solutions were obtained for the same inlet velocity used previously (0.080 m/s), as
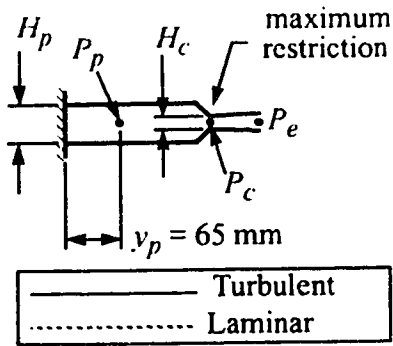
$$\text{\% Stroke closure} = \frac{H_{P_{initial}} - H_p}{H_{P_{initial}} - H_{P_{final}}} \times 100$$

$$\Upsilon = \frac{P_p - P_c}{P_{stroke}}; \quad \Delta P_{stroke} = 739 \text{ Pa}$$

$$\Phi_{mid} = \frac{P_p - P_e}{\Delta P_{stroke}}$$

$y_p = 65$ mm

——— Turbulent

·············· Laminar
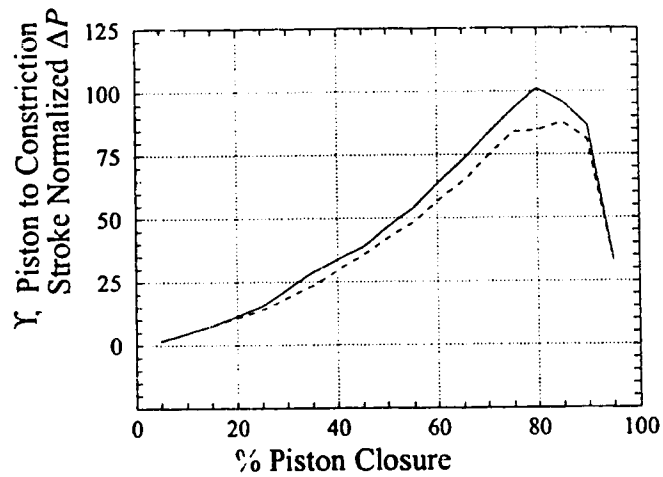
(a) Constriction Exit Pressure Difference
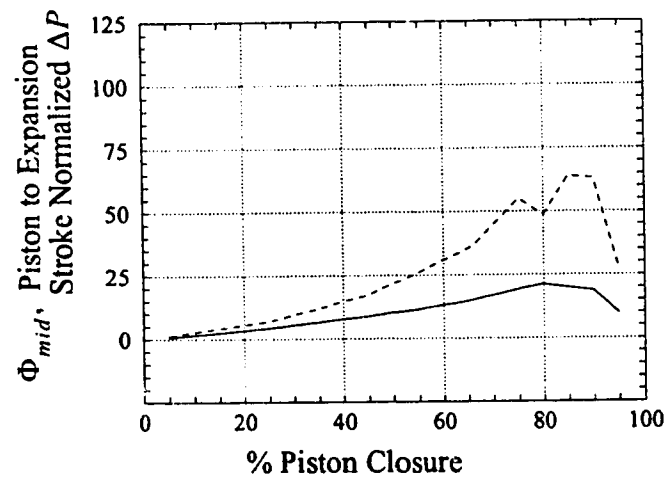
(b) Expansion Exit Pressure Difference

Figure 4.15: Normalized Pressure Differences Between Piston Region and Points Downstream
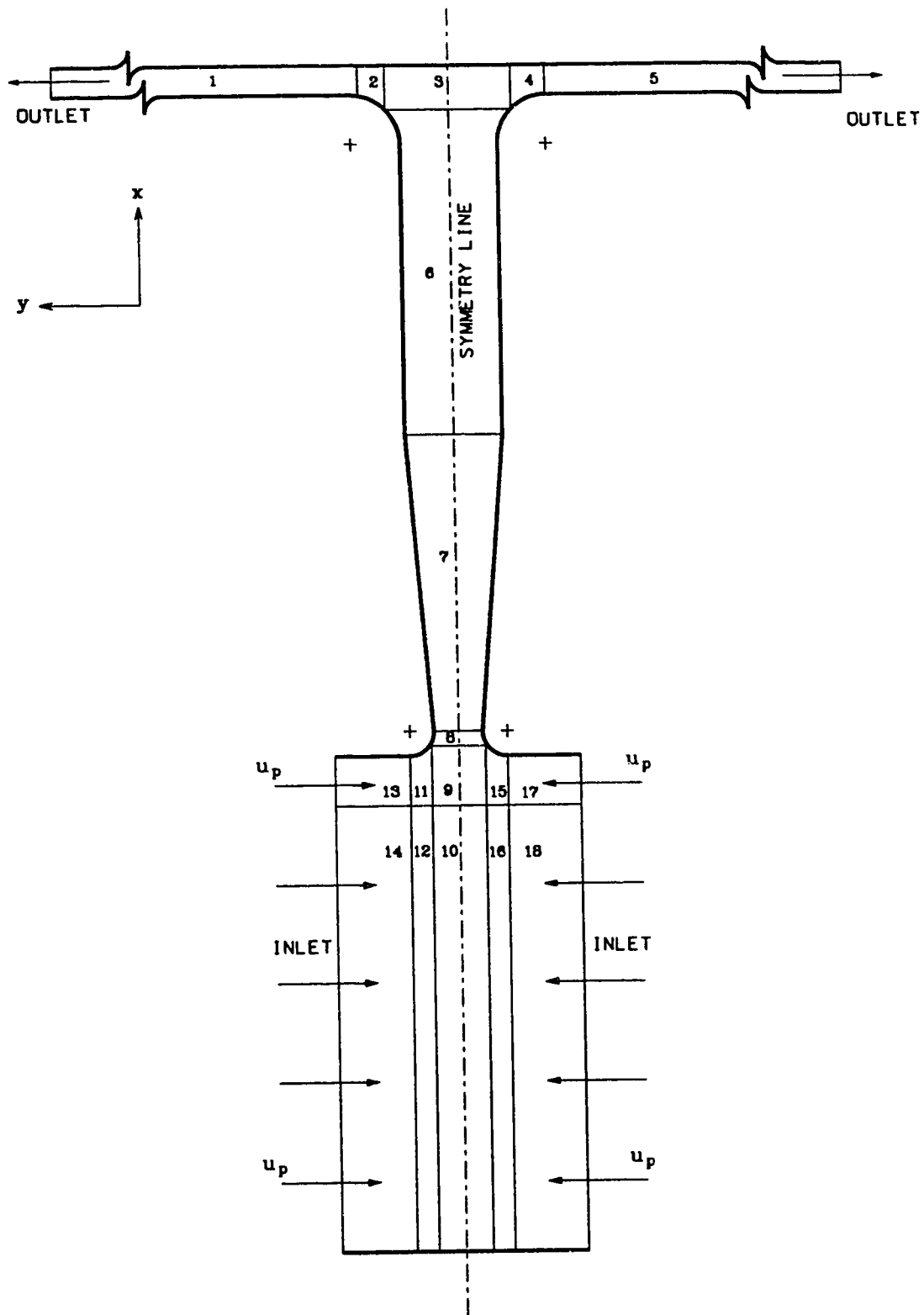
Figure 4.16: Block Configuration for Full Grid Geometry

well as a factor of two larger and smaller (0.16 m/s and 0.040 m/s) to test for sensitivity to Reynolds number in the expected physiological range of heart flows. The normalized y-component of velocity is plotted in Figure 4.17 for all three solutions at several locations in the model. The velocities were normalized by the maximum velocity at each section, and the x-distance was normalized by the cross-stream width. The solutions were quite symmetric about the configuration mid-line at all flow rates solved. The slight asymmetry in the expansion and downstream regions is likely due to minor numerical round off error in the FLOW3D grid generation or flow solution programs.

In an attempt to cause the flow in the expansion region to become asymmetric, the constriction was made slightly asymmetric by moving the lower curved profile towards the mid-line by 0.090 mm (4.4% of the constriction width), as illustrated in Figure 4.18. This corresponded to a five per cent increase in the restriction factor and moved the constriction slightly off center. The solution was obtained for the same inlet velocity used previously (0.080 m/s) and was solved using both single and double precision. There was no significant difference between the single and double precision solutions. The y-component of velocity is plotted in Figure 4.19 for the double precision solution and shows that the flow becomes slightly asymmetric but does not separate downstream of the constriction. The flow in the piston region remains symmetric, being unaffected by the asymmetry downstream.

The lack of flow separation could be due in part to the k-ε model used. This model will typically cause transition to turbulence to occur too soon (Schmidt and Patankar, 1991), thus causing the region where flow separation occurs to be turbulent when the actual flow in the laboratory model is laminar. Because laminar flows are more prone to flow separation, the unsteady flow laboratory model separates while the turbulent flow CFD model does not. Setting the inlet values of k to near-zero ($k \approx 5x10^{-8}\%$ of the inlet flow velocity) to try to delay the transition to turbulence had no significant effect.
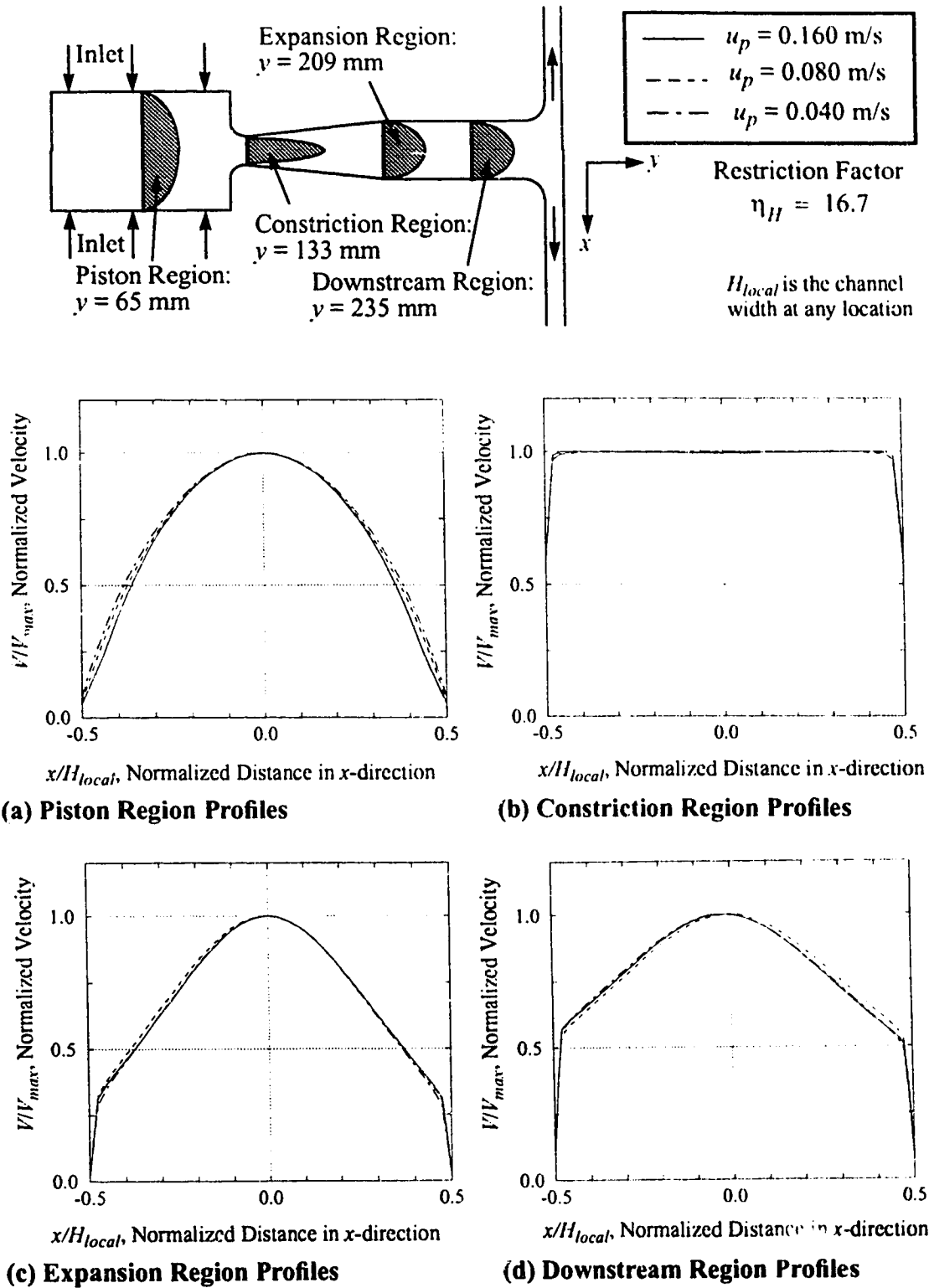
Figure 4.17: *y*-Component Normalized Velocity Profiles for the Full Grid Turbulent Flow Solutions at a Piston Closure of 85% for Various Flow Rates
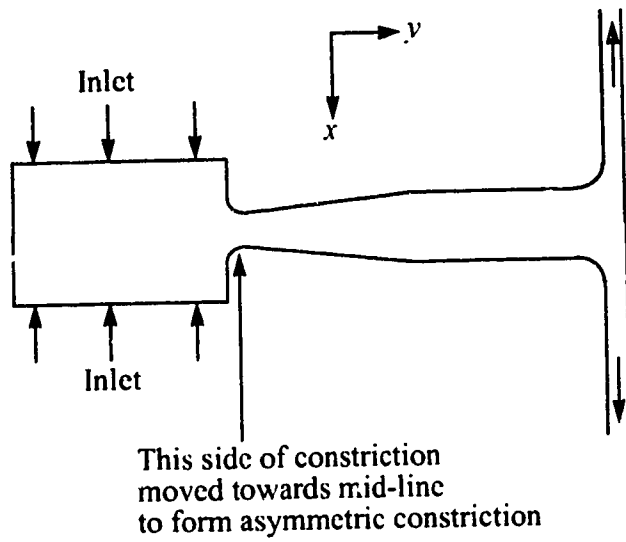
Figure 4.18: Location of Asymmetric Constriction for Piston Closure of 85%

Expansion Region B:
$y = 209$ mm

Expansion Region C:
$y = 235$ mm

Inlet

Piston Region A:
$y = 35$ mm

Inlet

Expansion Region A:
$y = 175$ mm

Piston Region B:
$y = 65$ mm

Piston Region C:
$y = 95$ mm

H_{local} is the channel
width at any location

Piston Region

——— Location A

– – – Location B

— ·— Location C

V/V_{max}, Normalized Velocity

1.0

0.5

0.0

-0.5   0.0   0.5

x/H_{local}, Normalized Distance in x-direction
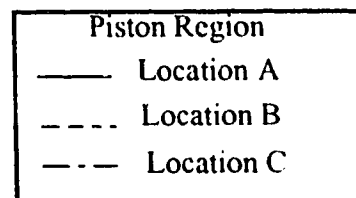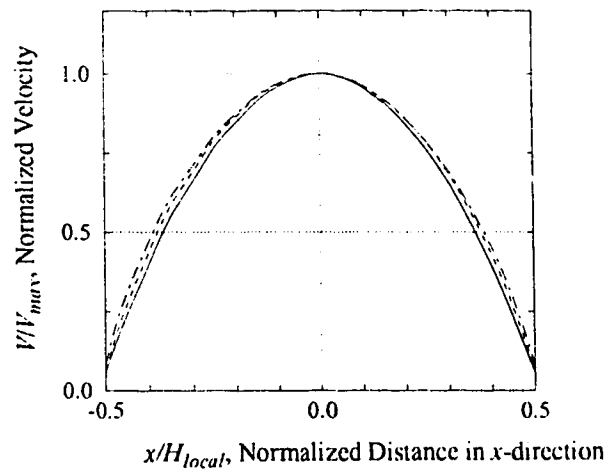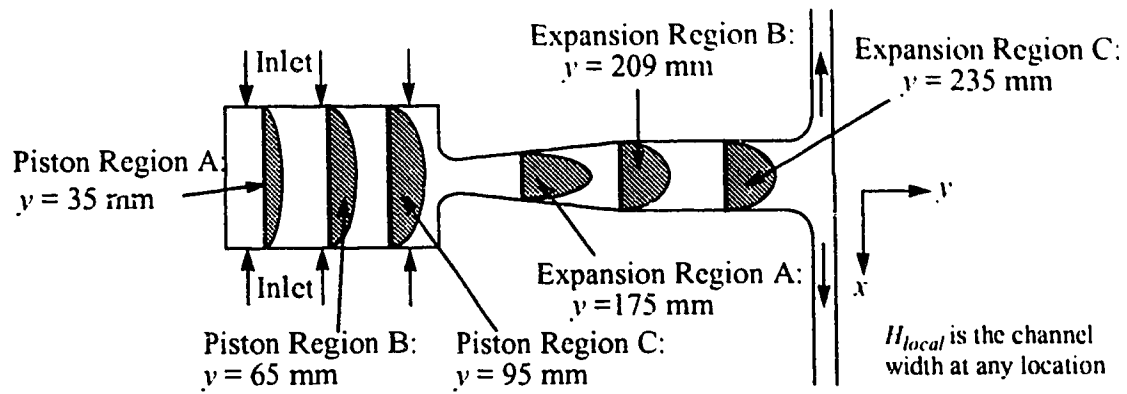
(a) Velocity Profiles in Piston Region

Expansion Region

——— Location A

– – – Location B

— ·— Location C

V/V_{max}, Normalized Velocity

1.0

0.5

0.0

-0.5   0.0   0.5

x/H_{local}, Normalized Distance in x-direction
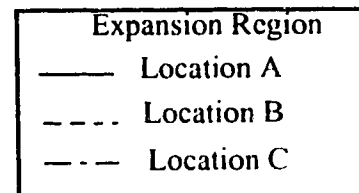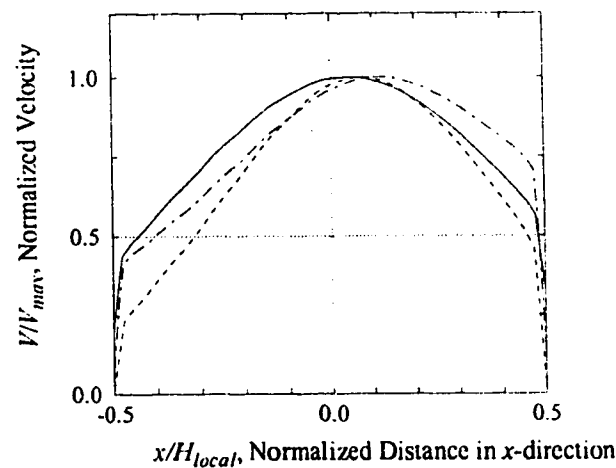
(c) Velocity Profiles in Expansion Region

**Figure 4.19: y-Component Normalized Velocity Profiles for the Full Grid Turbulent
Flow Solutions at a Piston Closure of 85% With Asymmetric Constriction**

4.7 SUMMARY

The FLOW3D program was used to solve both turbulent and laminar flows using a quasi-steady approach. The flow solutions showed the following:

- the turbulent solutions showed no signs of flow separation;

- the laminar solutions showed flow separation in the expansion region, but also had difficulties with numerical convergence;

- when the constriction was made slightly asymmetric, the turbulent flow solutions showed no signs of flow separation.

- the flow profiles downstream of the constriction were significantly parabolic, which suggests that the one-dimensional assumption of plug flow is poor.

CHAPTER 5 • UNSTEADY LABORATORY MODELLING

5.1 INTRODUCTION

As noted in the first chapter, only a few laboratory models of the left ventricle have been tested. The complexity of the anatomy is such that a geometrically correct model would be exceedingly difficult. Although the model of White *et al* (1967) attempted to simulate the *in vivo* situation, it was designed to model only an unobstructed configuration, making comparison to the progressive obstruction (SAM) difficult. The model fabricated by Criley and Siegel (1986) greatly simplified the *in vivo* geometry, but was incapable of modelling a progressive obstruction. Neither model could measure the wall positions during the contraction, making quantitative measurements difficult.

To avoid these shortcomings, it was decided to use a simple, well controlled model. The configuration for this model was the two-dimensional tee-shape, similar to that used for the computational fluid dynamics analysis. This chapter will present the details of the development and testing of this model. It will be shown that the model had controlled, repeatable wall movement for all three constriction configurations. The means of incorporating compliance into the piston and constriction regions will be described. In addition, a dyed fluid flow visualization technique will be evaluated for use in this model. The flow will be shown to be essentially symmetric for the all geometries, unless flow separation occurred. When flow separation occurred, it was only on one side of the expansion region, usually becoming noticeable during the deceleration period of the ejection.

5.2 MODEL CONFIGURATION

5.2.1 Development

The goal for developing the unsteady laboratory model was to design a simplified

geometry capable of accurately simulating the contraction phase (systole) of the left ventricle. The two-dimensional planar tee (see Figure 1.5) was a simple shape that could be used to model the left ventricle. Three-dimensional shapes were considered, but measurement and control of wall positions for such models would be very difficult. As the two-dimensional shape was capable of modelling the important features of the contraction, it was selected for the laboratory model.

Several important features were essential for the laboratory model. A variable contraction rate was needed, along with the capability for different constriction conditions. This would allow simulation of flows that were mildly restricted, progressively restricted and severely restricted. In addition, a method for altering the compliance (elasticity) of the piston and constriction walls was needed. Means of measuring flow parameters such as the pressure were to be incorporated. Further, it was desired to obtain a whole-field picture of the fluid motion using flow visualization techniques.

5.2.2 Model Geometry

The initial goal of the research was to simulate the systolic (contraction) phase of the human heart, so a model based on a single contraction was designed. A size with a much greater stroke volume than the human heart was used; the larger-than-life size gave the spatial resolution necessary for accurate measurements of pressure and increased the contraction time. The model was comprised of two rectangular movable walls (pistons), 102 mm high by 127 mm wide, with a stroke of 23 mm. This gave the model a stroke volume of 600 ml, about eight times the volume processed by an average human heart per beat, see Bellhouse and Talbot (1969).

A cutaway schematic view of the mechanical section of the model is shown in Figure 5.1. The two rectangular pistons were driven toward each other at the same speed, ejecting the fluid between them through the constriction and into the expansion. To
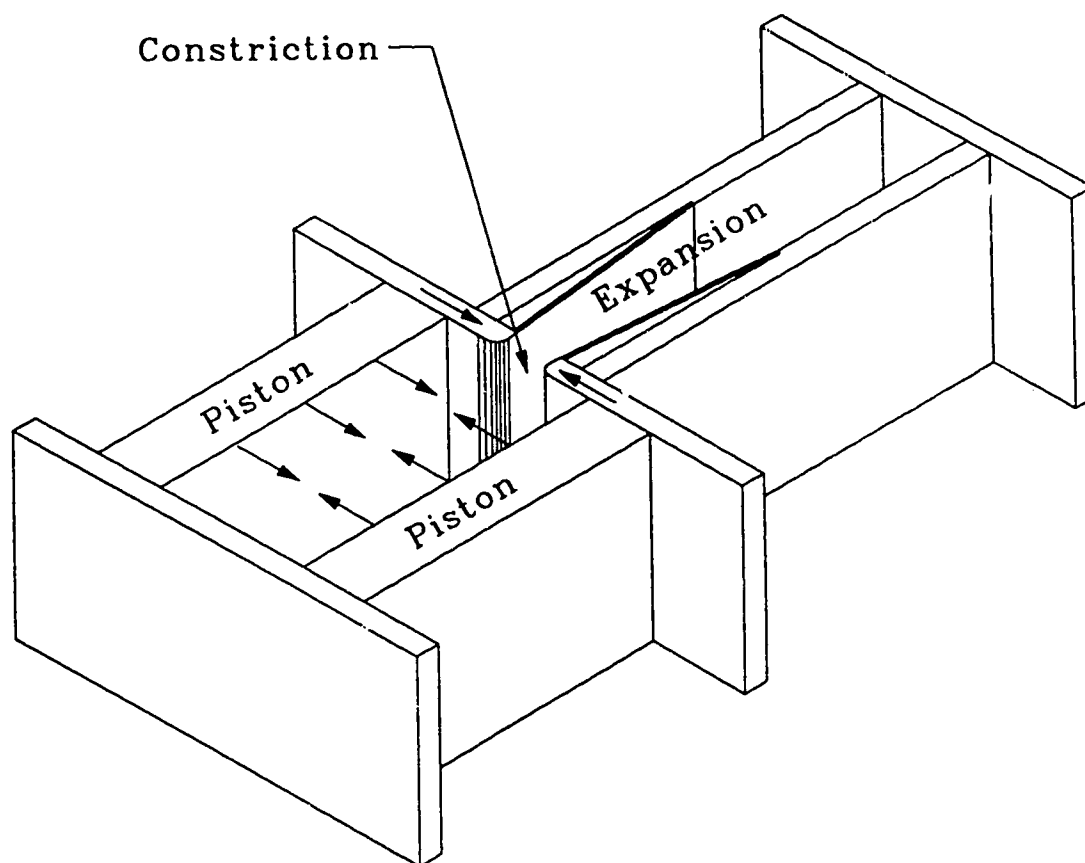
Figure 5.1: Cutaway View of Physical Unsteady Flow Model

provide three different constriction conditions, the motion of the constriction walls was controlled independently of the piston walls. Figure 5.2 shows the three different constriction conditions tested: mild restriction, progressive restriction, and severe restriction. The mildly restricted case allowed the piston walls to move toward each other with the constriction region walls held fixed at the minimum restriction (maximum opening). With the progressive restriction case, the piston and constriction region walls started moving simultaneously, but at different speeds (the constriction walls moved at a slower speed). In this case, the piston and constriction walls all began moving from the maximum opening and ceased moving when the minimum opening was reached. For the case of the severe restriction, the constriction walls were positioned with a narrow gap between them and held fixed while the piston walls moved.

The model dimensions are as shown in Figure 5.3. The pistons were initially 63.5 mm apart, and stopped 5 mm from each other. The constriction walls could be positioned with a maximum opening of 10 mm and a minimum opening of 0 mm (full contact). The final design is shown in Figures 5.4, 5.5 and 5.6.

Fluid left the test section at the end of the outflow channel through two 25 mm diameter tubes (one above and one below), and was simultaneously returned to the area behind the pistons through four other tubes. In this way the height of the fluid in the reservoir (Figure 5.4) remained constant throughout each closure event, maintaining a constant back pressure.

5.2.3 Wall Compliance

Two different types of pistons were utilized: non-compliant and compliant. These are shown in Figures 5.7. The non-compliant pistons had aluminum faces, while the compliant pistons had faces made from 9 mm thick closed cell plastic foam glued to the piston. The overall dimensions of the two types of pistons were kept the same to allow for

Constriction at maximum opening

Expansion Walls

Constriction Walls

Piston Walls

Only the piston walls move

Fully Open   Fully Closed

(a) mild restriction

Expansion Walls

Constriction Walls

Piston Walls

Piston walls and constriction walls move simultaneously

Fully Open   Fully Closed

(b) progressive restriction (SAM)

Constriction set for severe restriction

Expansion Walls

Constriction Walls

Piston Walls

Only the piston walls move

Fully Open   Fully Closed
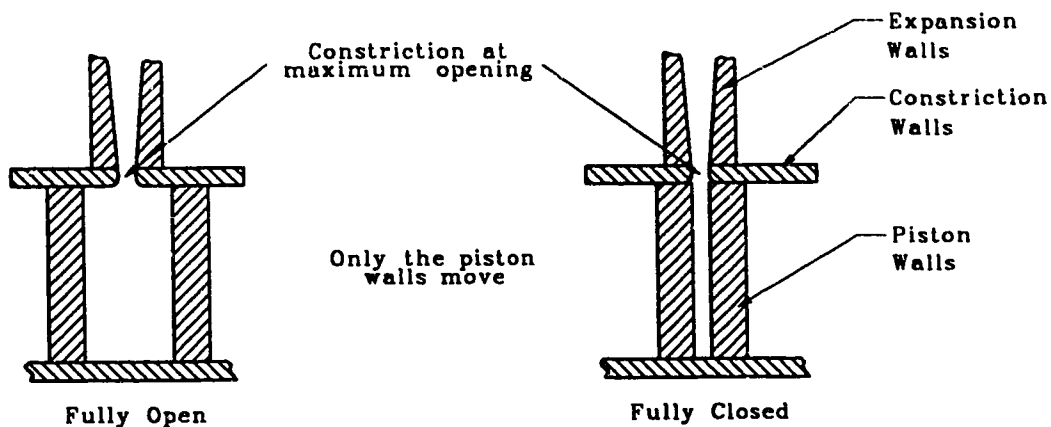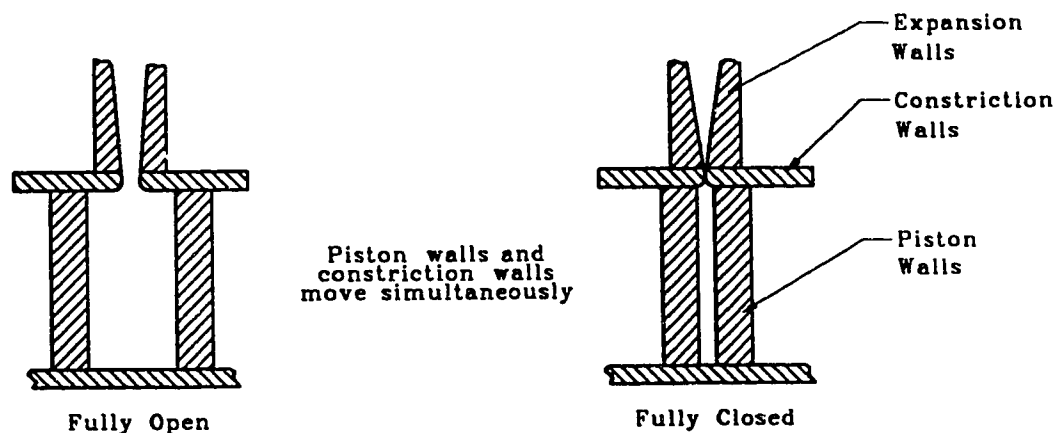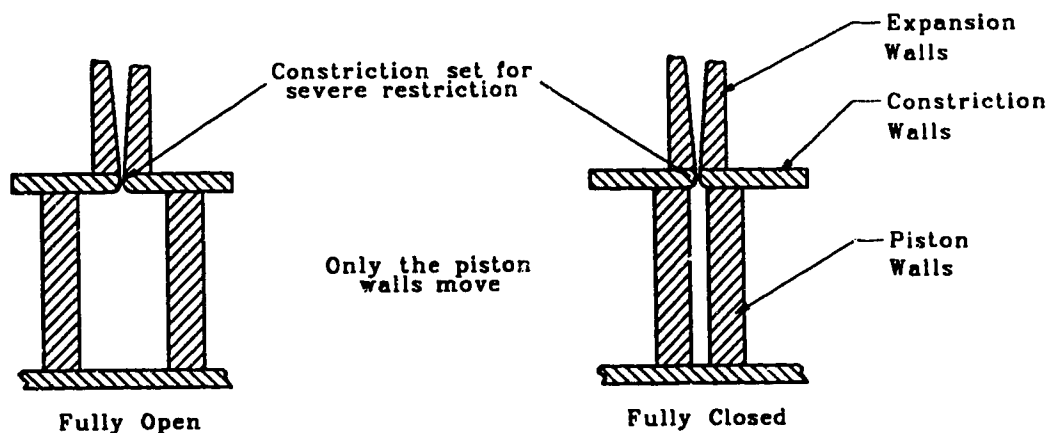
(c) severe restriction (severe stenosis)

Figure 5.2: Constriction Configurations
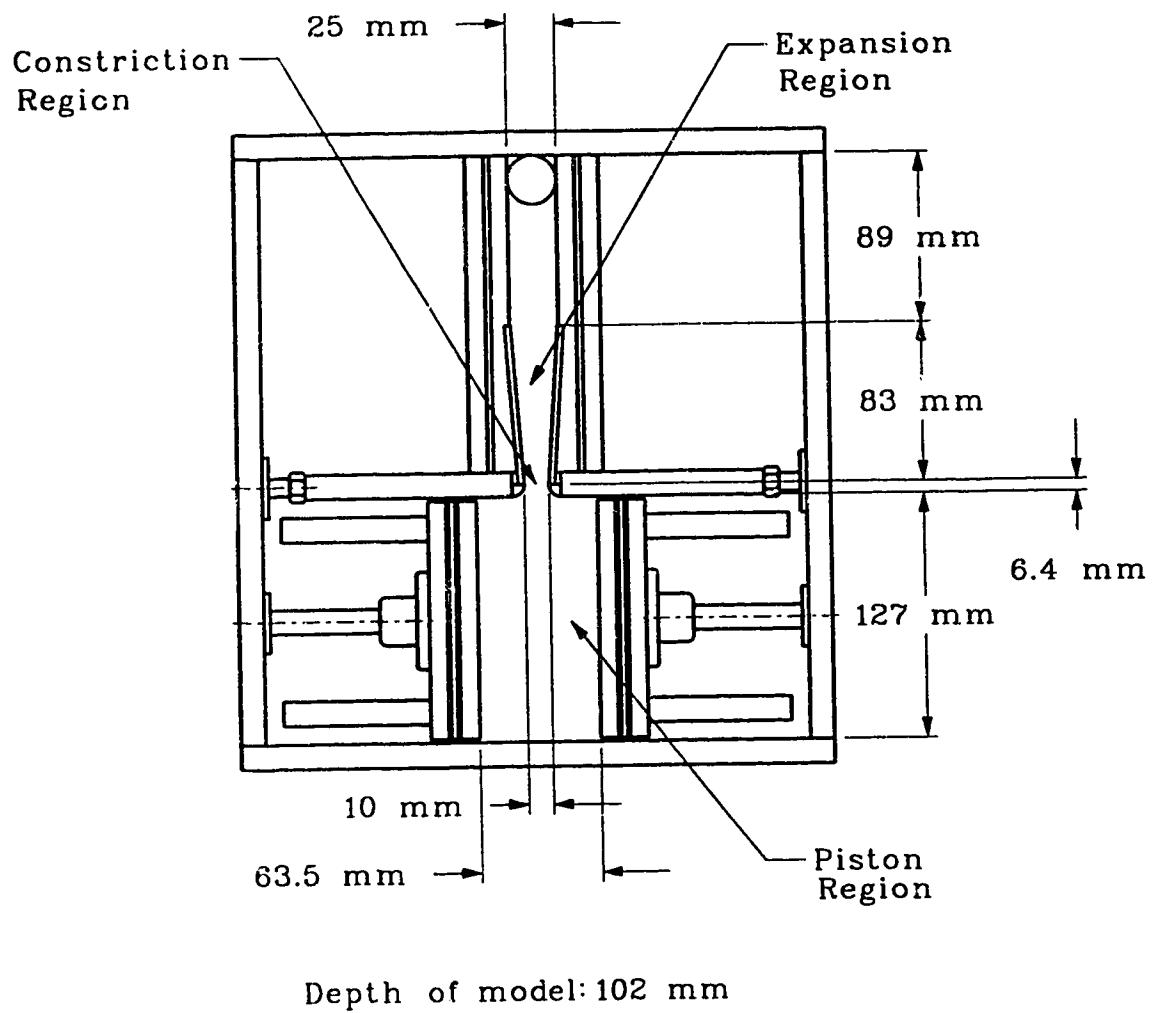
Figure 5.3: Top View of Model, Showing Important Dimensions
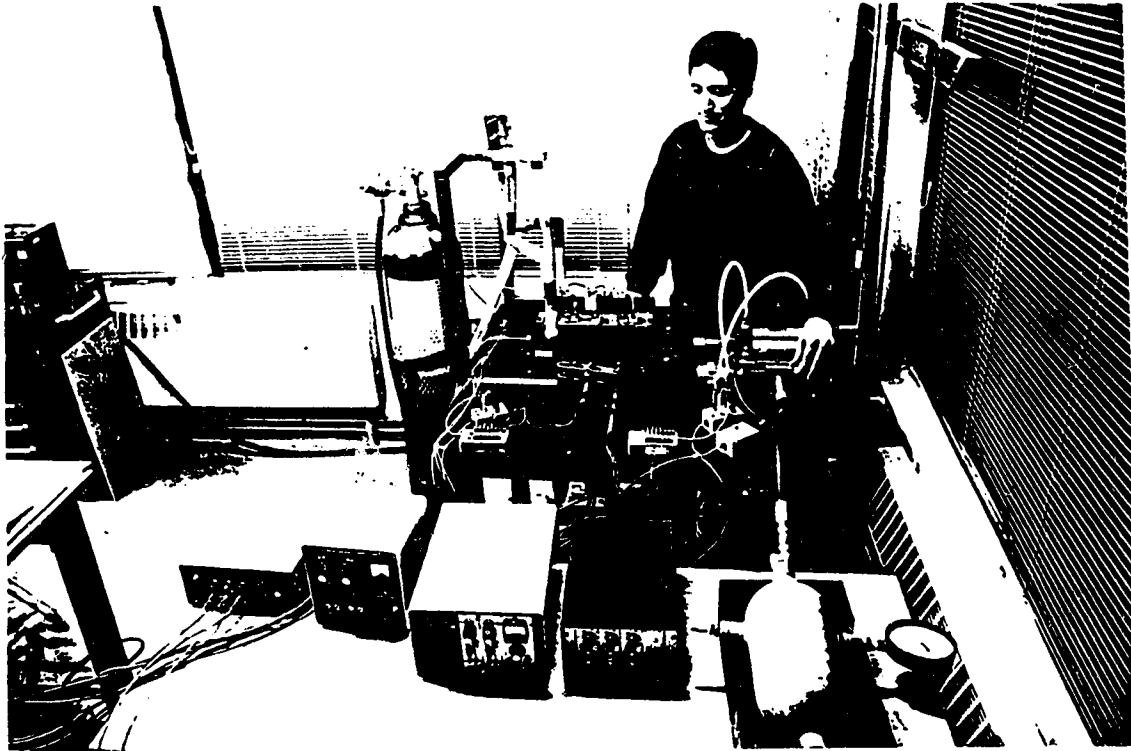
Figure 5.4: Overall View of the Unsteady Laboratory Model
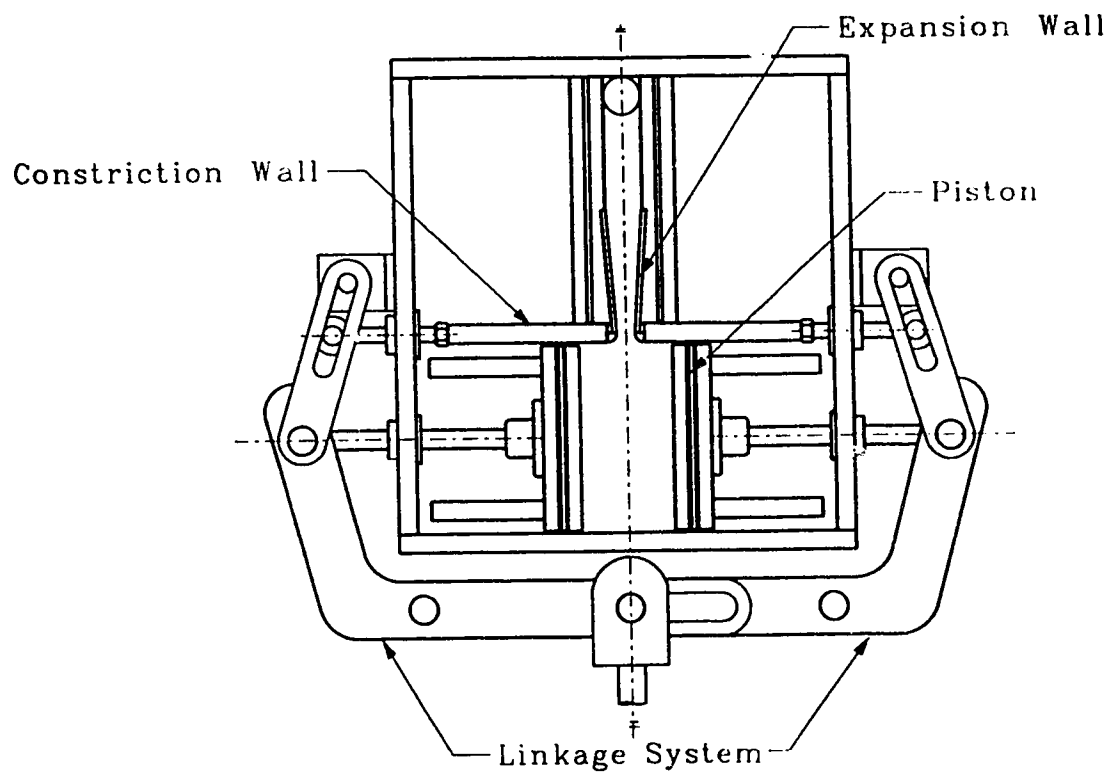
Figure 5.5: Top View of Experimental Apparatus: Fully Open Position
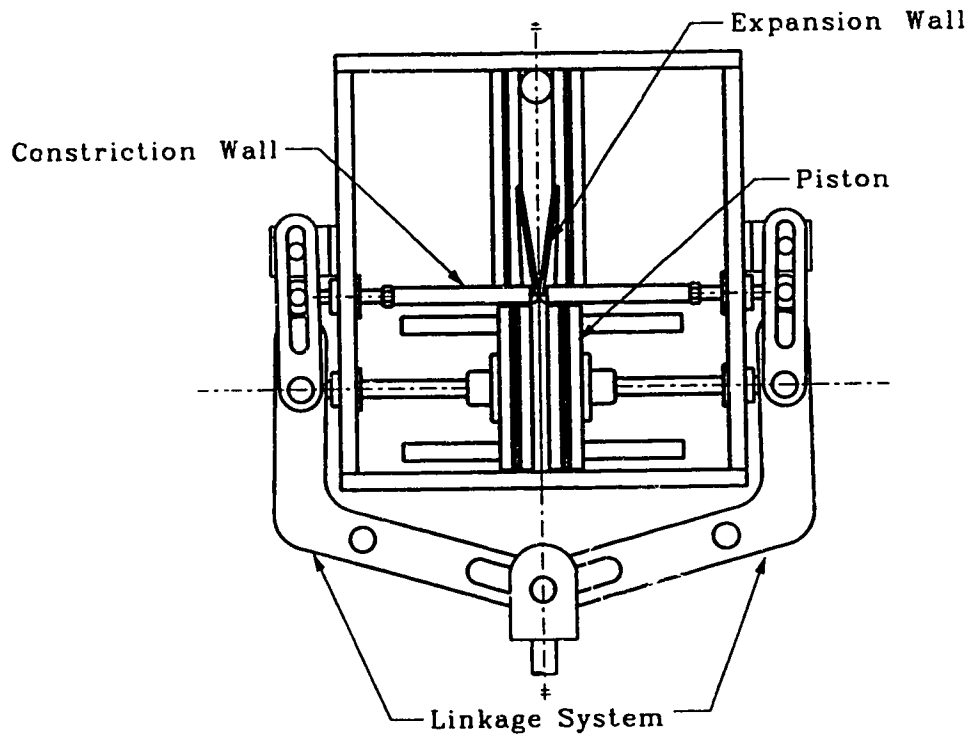
Figure 5.6: Top View of Unsteady Laboratory Model: Fully Closed Position

(a) Compliant Piston   (b) Non-compliant Piston
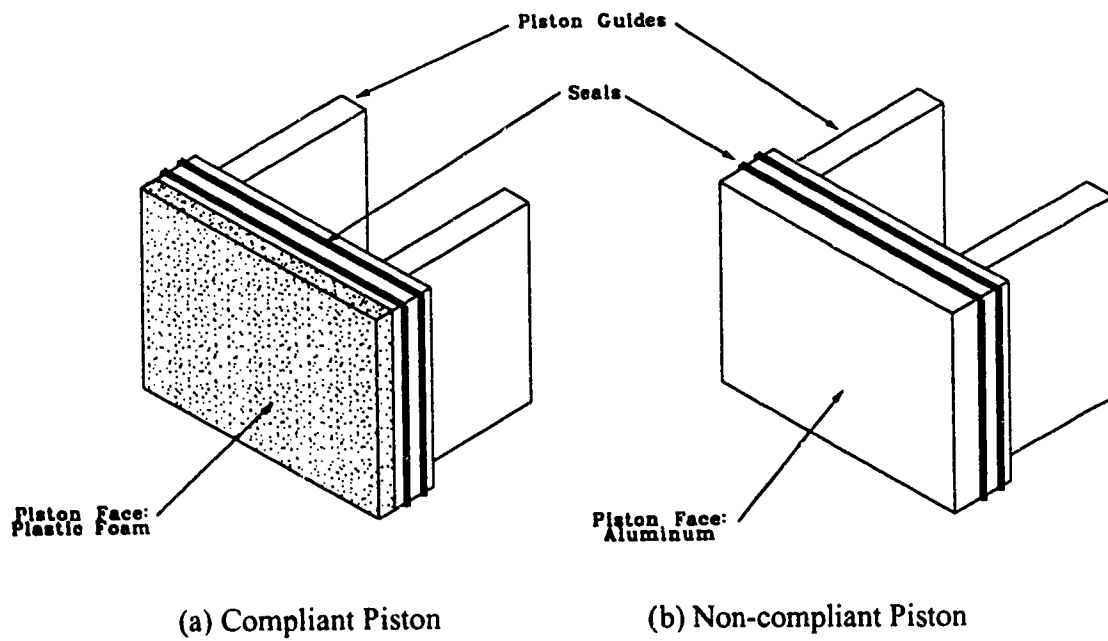
Figure 5.7: Compliant and Non-compliant Pistons

identical starting and stopping positions.

Two different types of constriction walls were used: non-compliant and compliant. Initially, the model used a simple sharp edged shape (Figure 5.8a), as described by Hay, Mioduchowski & Faulkner (1993). Since this was physically unrealistic and caused problems from a computational fluid dynamic modelling view point, a more refined curved shape was incorporated (Figure 5.8b). The design and fabrication of these constriction walls was rather complex, due to the requirements of scaling and maintaining downstream flexibility with minimal compliance.

The non-compliant constriction walls were made as follows (refer to Figure 5.9). A brass quarter round (6.5 mm radius) was fixed to the sliding wall with three recessed screws. The countersinks were then filled with epoxy and sanded smooth to give a continuous contour. To make the smooth transition from the quarter round to the downstream outflow tract, 3.2 mm thick stiff nitrile rubber was attached using clamping plates. These plates held the stiff nitrile rubber to the sliding wall at one end and the outflow tract wall at the other. The sliding wall clamping plate was then covered with flexible rubber to give a smooth, continuous contour from the quarter round. The downstream end that attached to the outflow tract wall was kept flush with the outflow tract by the recess in the outflow tract wall. In order to give a smoother transition in this region and to add stiffness to the stiff nitrile rubber, a 0.76 mm stainless steel sheet was attached further downstream, such that it covered the white nitrile wall from 8 mm downstream of the quarter round to the end of the outflow tract.

The compliant constriction walls (refer to Figure 5.10) were made in the following manner. Two thin stainless steel shims of 0.76 mm thickness with the desired curved profile were fixed to the top and bottom of the sliding wall. Closed cell plastic foam was glued to the face of the sliding wall between the shims and then carefully sanded to the

Constriction Wall —————→ ————Sharp corners

Flow

————Piston
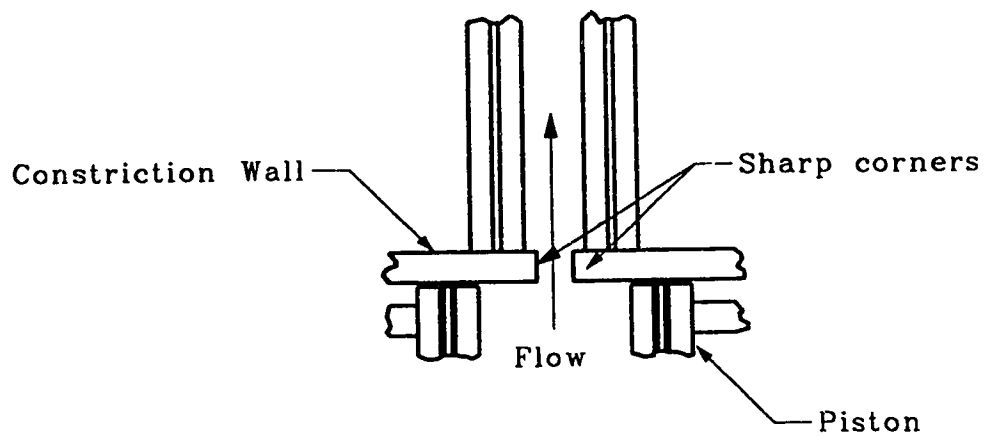
(a) Sharp Corner Configuration

————Smooth transition

Expansion ————

————Rounded corners

Flow
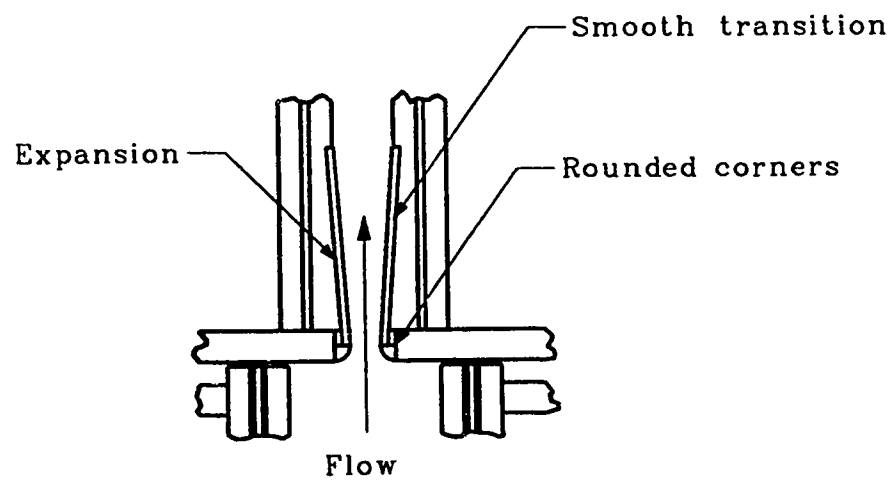
(b) Rounded Corner Configuration

Figure 5.8: Constriction - Expansion Region Profiles

Expansion Wall

Shim

Constriction Wall

Brass Corner

Shim

Sheet Rubber

Stainless Steel
Cover Plate
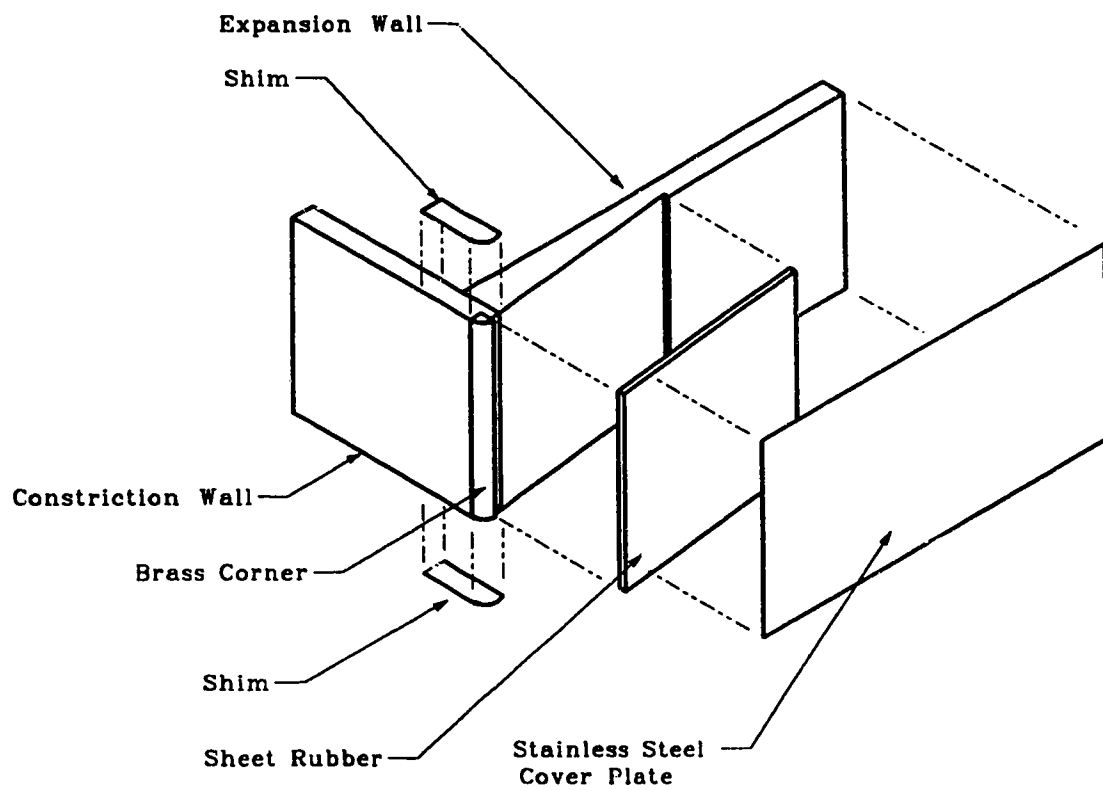
Figure 5.9: Smooth Profile Exit Details - Non-compliant Constriction

Expansion Wall

Shim

Constriction Wall

Shim

Plastic Foam

Stainless Steel
Cover Plate
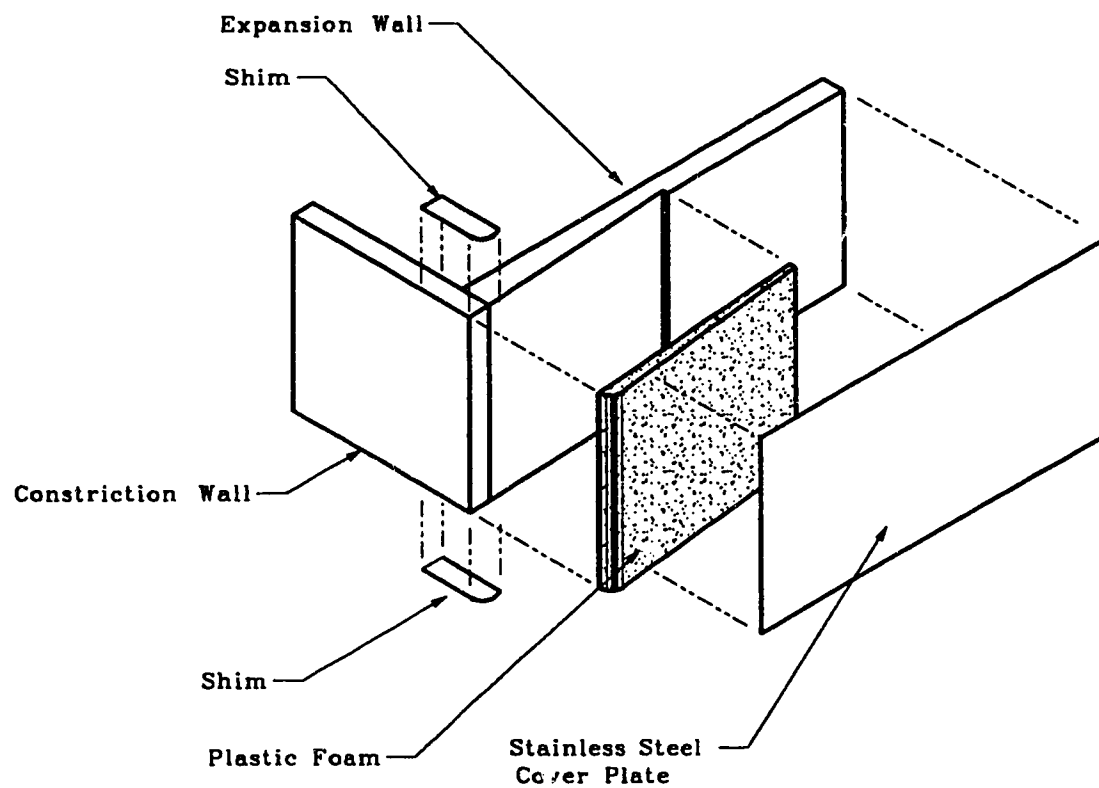
Figure 5.10: Smooth Profile Exit Details: Compliant Constriction

profile of the shims. The same downstream clamping arrangement used for the non-compliant constriction walls was used to attach the foam to the outflow tract. As with the non-compliant constriction walls, the stainless steel plates were used to reduce the compliance of the downstream portion of the closed cell plastic foam while providing a smooth transition into the downstream outflow tract.

5.2.4 Motion Control

The piston walls were driven by a single pneumatic cylinder through the linkages shown in Figure 5.11. This ensured that both pistons moved at the same velocity. The rate of piston movement was controlled by the regulated pressure supplied to the pneumatic cylinder. The gas used for the pneumatic system was high pressure bottled nitrogen with the pressure controlled through a regulator. An accumulator was used to help maintain constant pressure to the cylinder throughout each test.

In order to maintain consistency between tests, a pressure relief valve was used. By increasing the pressure in the accumulator until the relief valve opened, then waiting until the pressure in the accumulator decreased to the relief valve set point, a consistent pressure for each test run was ensured. The relief valve was adjustable, so different working pressures, and hence different piston movement speeds, could be obtained. Operation of the pneumatic cylinder was controlled by a spool valve. Initial tests showed that a manually controlled spool valve caused inconsistency. This was overcome by using an electric solenoid two-way spool valve, controlled by the computer data acquisition system.

The position of the constriction walls was controlled to produce the required types of constriction, both fixed and time-varying. For both the severe and mild restriction cases, the constriction walls were positioned and locked in place. The linkage system shown in Figures 5.5 and 5.6 was used to provide the movement required for the progressive
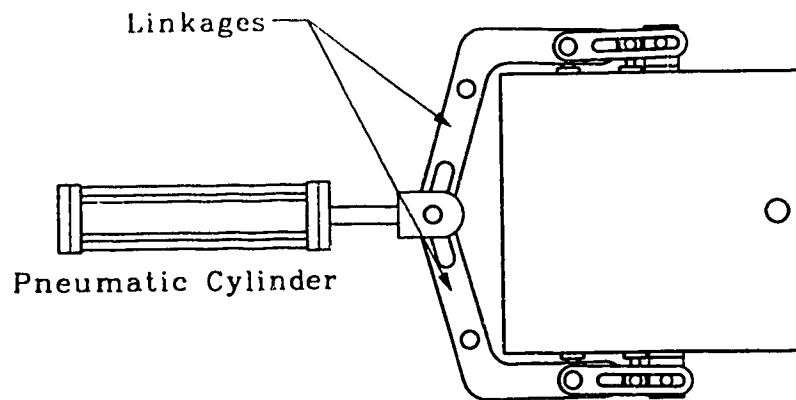
(a) Cylinder and linkage arrangement
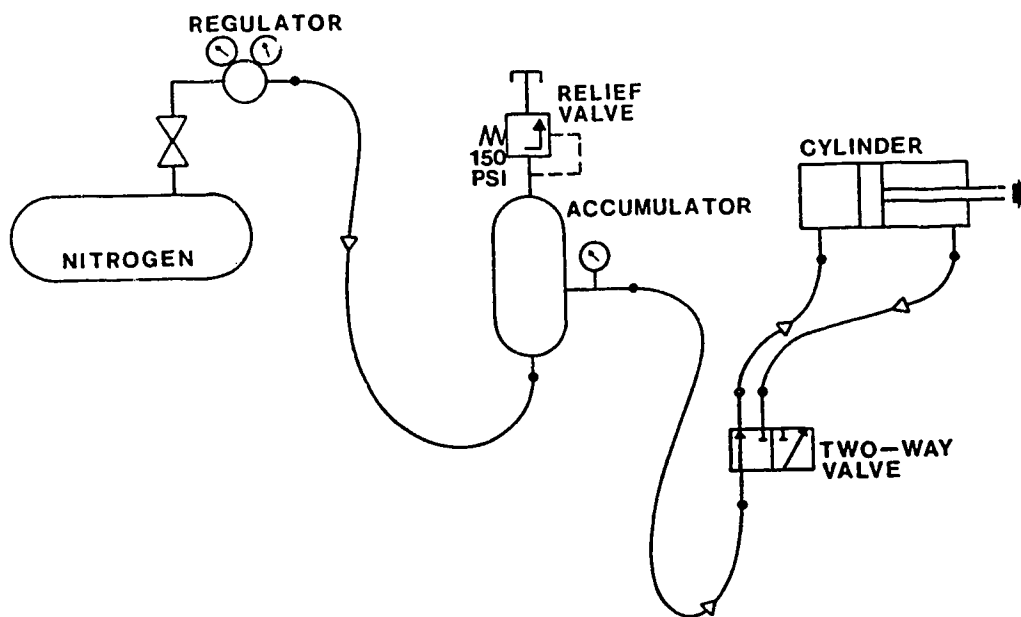
(b) Pneumatic Circuit

Figure 5.11: Piston Drive System

restriction case.

5.2.5 Miscellaneous Features

The model was fabricated mostly from anodized aluminum, with stainless steel for more highly stressed components. This minimized corrosion effects from the working fluid (water). One of the most difficult problems was providing good seals for the moving piston and constriction walls. The best design found for the pistons was to use two sheets of nitrile rubber sandwiched between the plates of aluminum that made up the piston. The nitrile was cut nearly flush with the edges of the piston, so that when the piston plates were tightened together, the nitrile sheets were extruded slightly around the edges. This, combined with a carefully adjusted fit within the model, provided a very effective seal around the piston. With extensive use, seal breakdown became apparent. This was overcome by replacing the seals at regular intervals

Providing an adequate seal for the constriction wall was important, but it was not possible to provide a mechanical seal used by the pistons. Instead, the exit wall was proportioned such that the gap between the exit wall and adjoining upper and lower covers was in the order of a tenth of a millimeter. While this allowed some fluid leakage, it was minor in comparison to the main flow.

The apparatus was designed to work with different fluids including several blood analogs, such as Separan and Xanthan gum solutions (Mann, Deutsch, Tarbell, Beselowitz, Rosenberg, and Pierce (1987): J. M. Tarbell, personal communications). Since blood behaves as a Newtonian fluid in large vessels, as was noted in Chapter 2, water was used as the working fluid. Water also has the advantage of not requiring any special disposal methods after use. Further, water was a good choice for flow visualization work, as it is transparent or may be dyed with rhodamine or fluorescein.

5.3 INSTRUMENTATION

The parameters measured in the experimental model included fluid pressure and wall position with time. The pressure measurements were made using probes and pressure transducers while the wall positions, and hence the wall velocities, were measured using displacement transducers.

5.3.1 Pressure Measurements

The most important parameter was the pressure, because it is the most commonly used variable measured *in vivo* for HCM diagnosis. The method selected to measure the pressures used wall static pressure taps with diaphragm pressure transducers. Three Validyne variable inductance metal diaphragm pressure transducers were placed at key positions in the flow: the piston region, the constriction region exit and the expansion region exit (refer to Figure 5.12). The variable inductance pressure transducers were attached to the 1/8" diameter stainless steel tubes as shown in Figure 5.13a. The length of the tube was kept to a minimum length of 41 mm to increase the frequency response. All fast response pressure data presented in this thesis was taken with the Entran EPX-10 stainless steel semiconductor diaphragm transducer (Figure 5.13b). Specifications for these transducers are listed in Appendix C, and their calibration is described in Appendix D. The primary purpose of the semiconductor diaphragm transducer was to compare pressures to an adjacent variable inductance transducer, to ensure the variable inductance transducer's frequency response was sufficient to capture the transient signal. As the semiconductor transducer had a minimum rated frequency response of 5000 Hz and the transients measured were all less than 30 Hz, it provided an adequate standard.

The variable inductance pressure transducers were conditioned and amplified using a Validyne CD19 Carrier Demodulator. The output signals were passed through a tunable low pass filter, set to a cutoff frequency of 60 Hz, before being sent to the data acquisition system. This filter was necessary to eliminate a high frequency oscillation
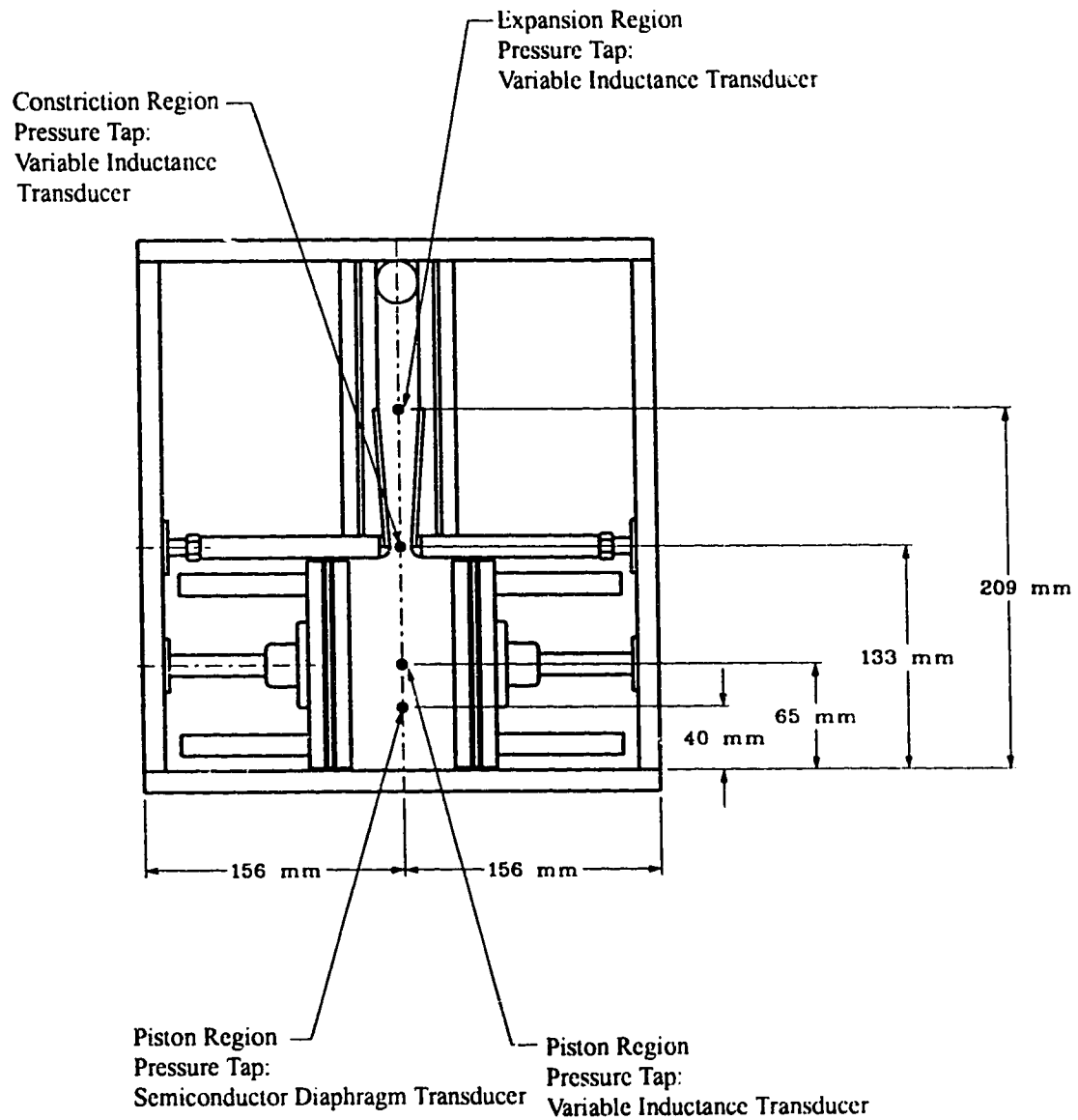
Figure 5.12: Pressure Measurement Locations
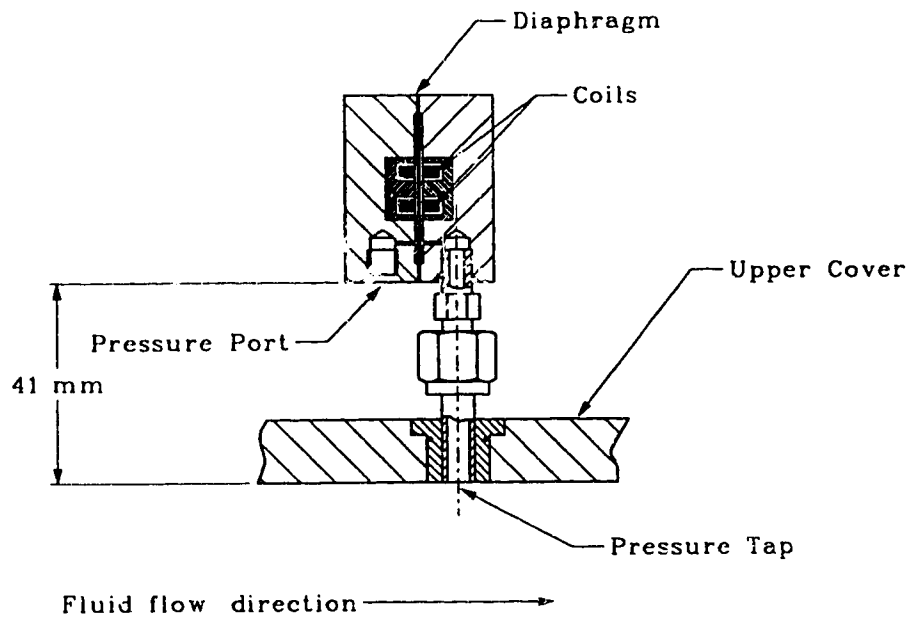
(a) Validyne Variable Inductance Pressure Transducer Mounting Arrangement
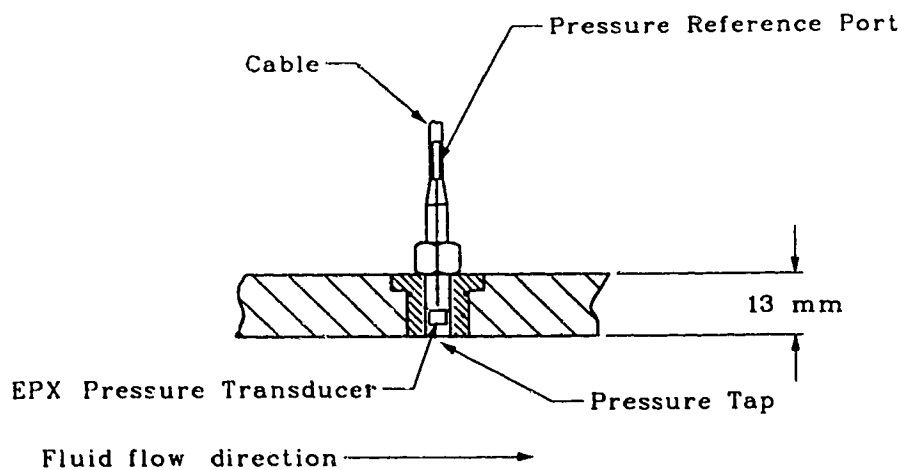
(b) Entran EPX Stainless Steel Diaphragm Semiconductor Mounting Arrangement

Figure 5.13: Pressure Transducer Mounting Arrangements

from the signals, which will be explained in section 5.4. Details of this filter are given in Appendix C. The electrical analog output of the semiconductor pressure transducer was amplified using a Vishay 2120 Strain Gage Conditioner.

5.3.2 Displacement Measurements

Another parameter required was the rate of movement of the pistons and constriction walls. This closure need was obtained by measuring the wall position using Schaevitz linear variable c ‴ al transformers (L.V.D.T.). A 50 mm range L.V.D.T. was connected to the piston rod, while a 25 mm range L.V.D.T. was connected to the constriction wall rod. The calibration of these transducers is given in Appendix D.

The output of each Schaevitz L.V.D.T. was amplified using a Vishay 2120 Strain Gage Conditioner, which required the use of a Vishay L.V.D.T. Adapter 1601. Due to electrical noise in these signals, a low pass filter was used. It was also found that if the two L.V.D.T.'s were placed beside each other, as shown in Figure 5.14(a), the magnetic fields of one transducer would interfere with the adjacent transducer. This was eliminated by offsetting the L.V.D.T.'s as shown in Figure 5.14(b).

5.3.3 Data Collection System

All six of the amplified analog signals were converted into digital signals using a Metrabyte DASH-8, an eight channel 12 bit high speed analogue/digital converter (Figure 5.15). The data were then transferred to an IBM RISC workstation for analysis. Specifications of the data acquisition board are given in Appendix C.

5.4 DATA ANALYSIS

For each test condition (progressive restriction without compliance, progressive restriction with compliant piston, progressive restriction with compliant constriction, mild and severe restriction), six wall closure speeds were tested to obtain the pressure response

Constriction Wall

Piston

25 mm L.V.D.T.

50 mm L.V.D.T.
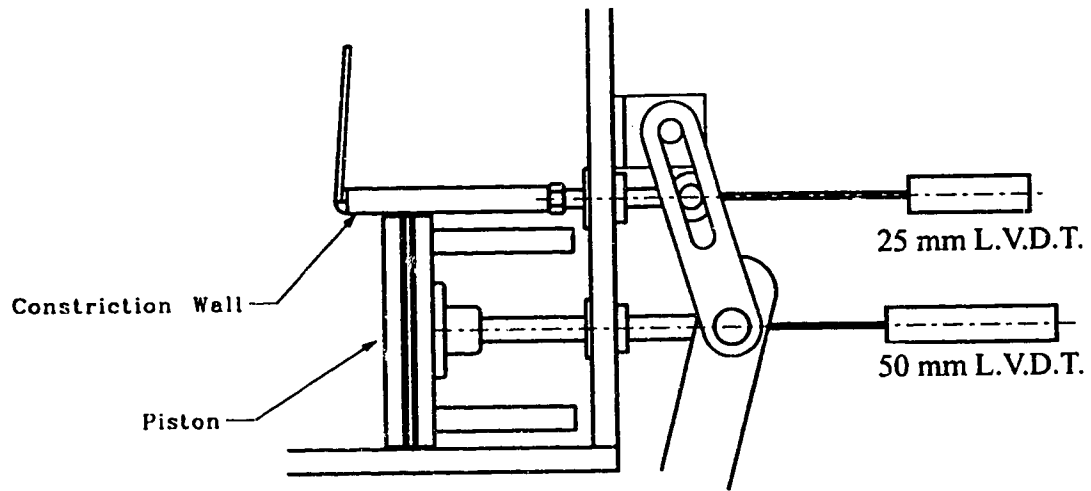
(a) Side-by-side Arrangement

Constriction Wall

Piston

25 mm L.V.D.T.

50 mm L.V.D.T.
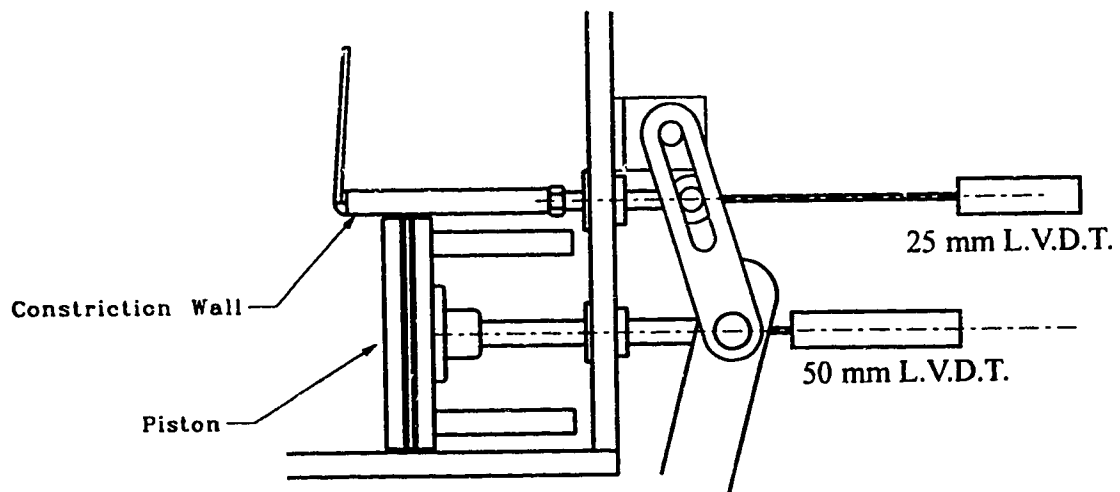
(b) Offset Arrangement

Figure 5.14: LVDT Mounting Arrangements
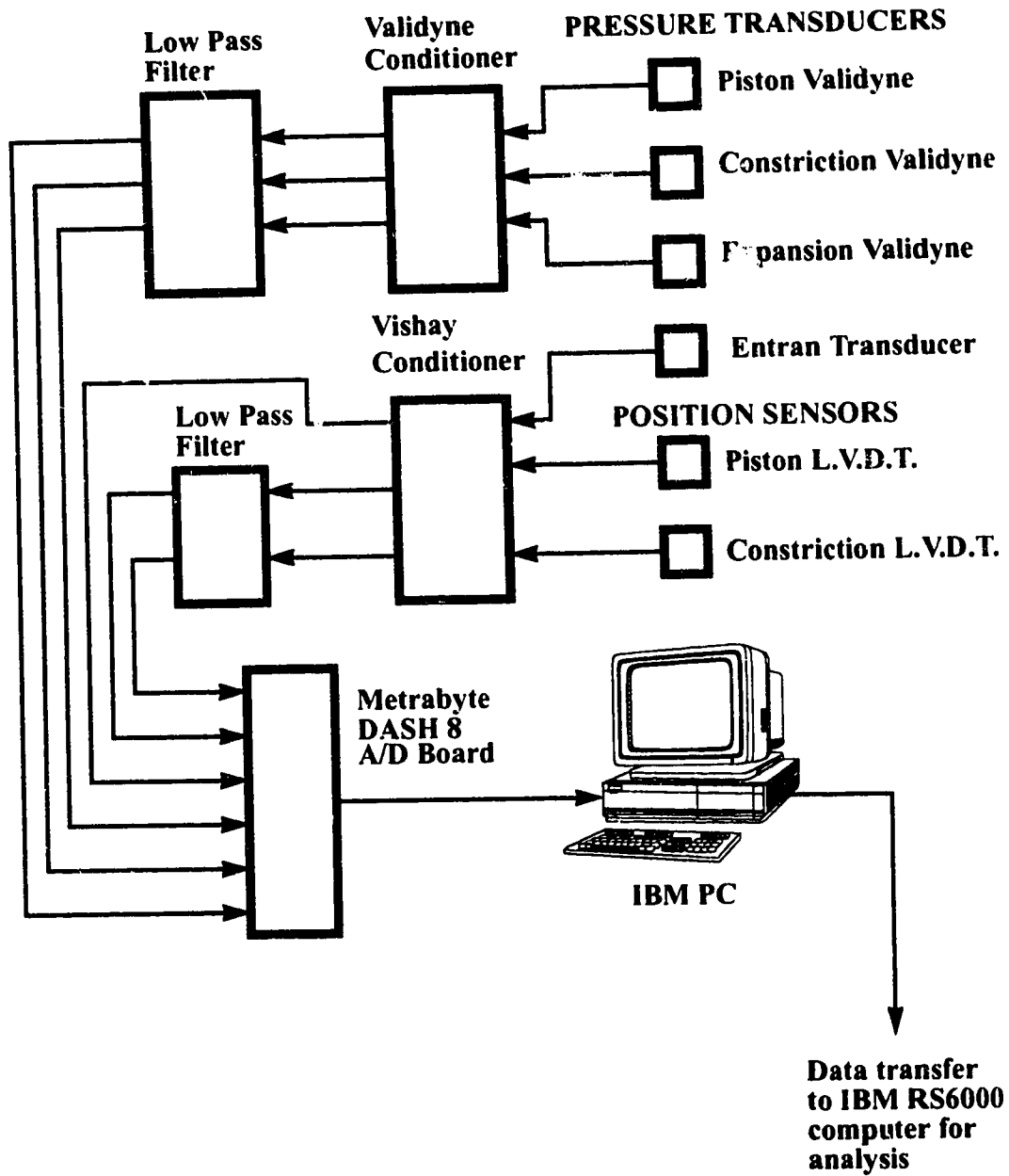
Figure 5.15: Data Acquisition System

of the model. For each well closure speed, a set of ten tests were performed. The results for every set of ten tests were combined together to obtain a mean value at each point in time for every measurement.

5.4.1 Data Acquisition Rate

The rate of data acquisition for the data acquisition board was set through the data acquisition program. Due to the short time period involved in the test (event time of less than 0.5 second), the highest possible data acquisition rate was desired. The maximum rate possible with this board was 4320 Hz, which must be divided between the six signals being sampled. This allowed each of the six signals to be collected at a maximum rate of 720 readings per second, so a piston closure of 0.3 second was represented by 216 points 0.00139 second apart. The rate at which the signals were being sampled was verified using a square wave signal. The square wave was provided by a Wavetek Model 182A Function Generator and set to 10.00 Hz, measured with a Hewlett Packard Model 5314A Universal Counter.

5.4.2 Wall Position, Velocity and Acceleration

The piston wall position data was analyzed to determine the standard deviation for each set of ten tests. The values for all tests are shown in Figure 5.16, with values of standard deviation ranging from 0.30% to 1.65% of piston travel. This shows that the consistency within each set of ten tests is adequate.

The mean piston wall velocity was based on the time and distance of piston wall movement from 5% closure to 95% closure. These results are plotted in Figure 5.17. The reason for choosing a 5% closure starting position was to avoid the difficulties in differentiating the beginning of piston movement from signal noise. Using a 95% closure as the stopping position overcame problems in determining the exact point in time where the piston ceased moving. This difficulty was caused by a small amount of piston
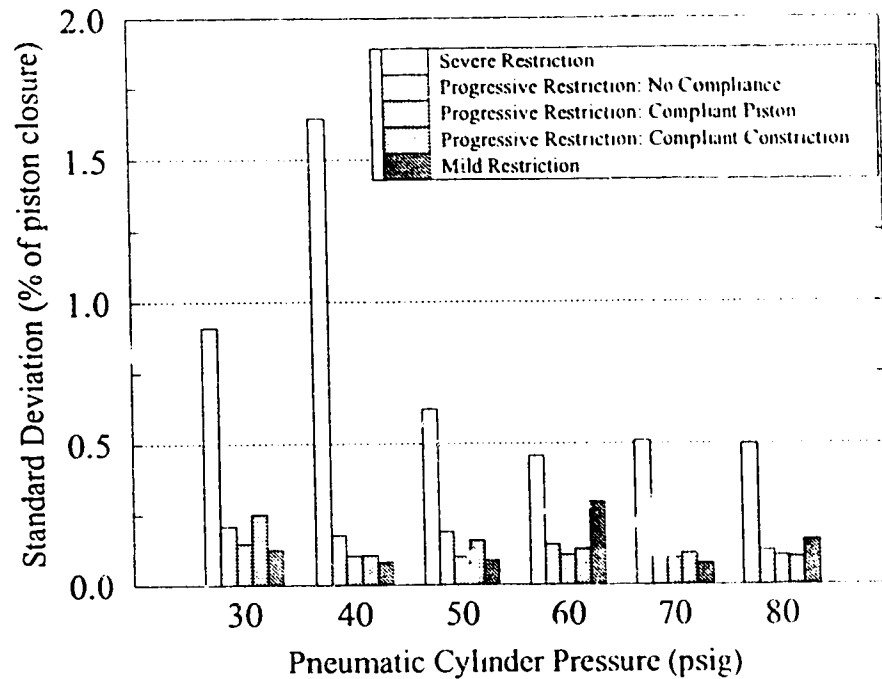
Figure 5.16: Standard Deviation for Piston Wall Position Measurements
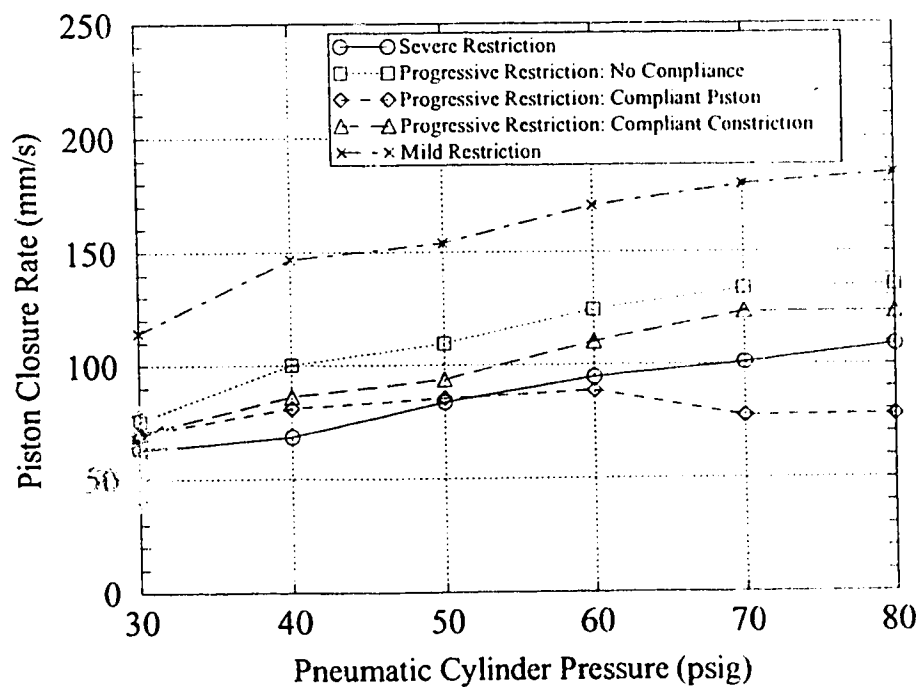
Figure 5.17: Piston Closure Rates for Different Constriction Configurations

movement that occurred as the pressure in the accumulator recovered near the end of the test.

Figure 5.17 shows the piston closure rate increased with increasing drive pressure, as expected. For any given drive pressure, the mean rate of closure varied for the different model configurations, mainly due to the variations in pressures w' .ıı the piston region. For example, the severe restriction had the slowest rate of closure, caus̄d by the high pressure generated within the piston region. The mildly restricted ca·e ·ad the fastest rate of closure, nearly twice as fast as the severe restriction, as there was very little resistance to the fluid flow from the piston region. This will be discussed further in Section 7.3. Another cause in the variation of closure rate for different configurations was the differing friction within the model. The compliant piston, for example, caused more friction due to the closed cell plastic foam contacting the model walls during closure. This effect became more significant as the pressure on the foam increased, causing it to press against the walls with more force.

The velocity and acceleration of the piston wall were also calculated, as these were needed as input for the CFD analysis. Second-order forward differencing was used to calculate these values (forward differencing allowed calculations to be performed at the initial data points). Due to noise in the L.V.D.T. signal, numerical smoothing was employed to eliminate the noise in the signal before differentiating. This was the method used by Press, Flannery, Teukolsky & Vetterling (1988, page 514). It incorporated a moving window of points to remove any linear trend, followed by a low-pass filter by a Fast Fourier Transform, and then reinsertion of the linear trend. The effective filter frequency for this method is

$$f_{\text{effective}} = \frac{1}{N\Delta t} \tag{5.1}$$

where N is the number of points filtered and Δt is the time between points. Figure 5.18

Displacement: mm
Velocity: mm/s
Acceleration: $(mm/s^2)/100$
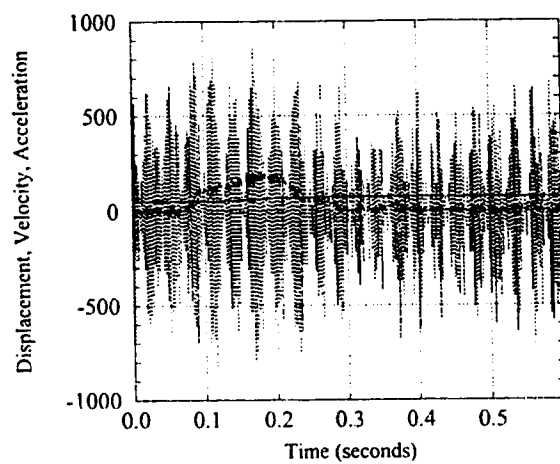
(a) Unfiltered
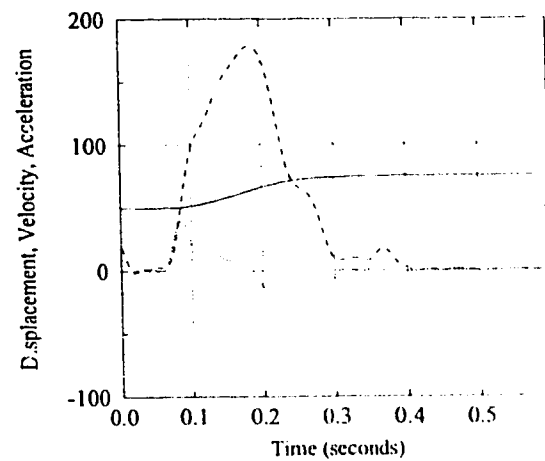
(b) 20 point filter
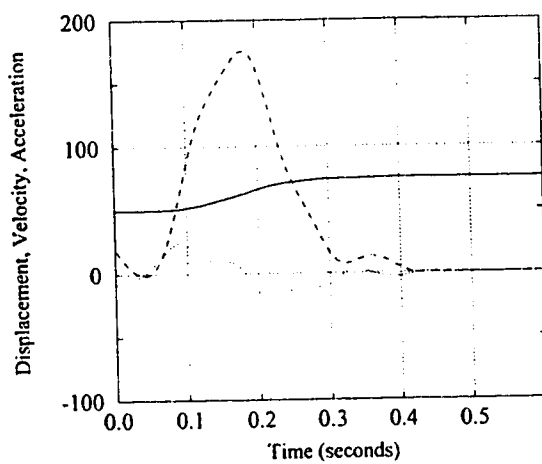
(c) 40 point filter
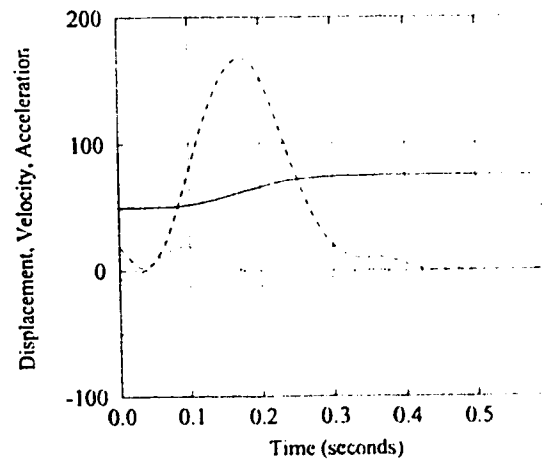
(d) 60 point filter

Figure 5.18: Effect of Window Size on Filtering

shows the effects of different window sizes. The 40 point window gave the best compromise for removing noise without excessive smoothing of the transients. This corresponded to an effective filter frequency of 18 Hz.

5.4.3 Pressure Readings

The pressure signals from the variable inductance transducers were compared to those obtained by the semiconductor transducer. Figure 5.19(a) shows the unfiltered signals for a typical test (high pressures are due to fast closure rate and large stroke volume of eight times the normal human heart). As is evident, the variable inductance transducer signals had an oscillatory response of about 80 Hz when subjected to a very sharp rise or fall in pressure. This behavior was not noticeable in the semiconductor transducer signal and may have been due to a resonant response of the variable inductance transducer itself. It would not appear to be resonant frequency of the tube and transducer volume alone, which Doebelin (1990) approximates as

$$f_{res} = \frac{c}{2\pi L_{eff}} \left[\frac{2Vol_{tube}}{Vol_{tube} + 2Vol} \right]^{\frac{1}{2}} \approx 8 \text{ kHz}, \tag{5.2}$$

where f_{res} = resonant frequency; L_{eff} = effective length of tube used;
Vol_{tube} = volume inside tube; Vol = volume inside pressure transducer.

This calculated resonant frequency was 100 times larger than the observed 80 Hz resonance. Thus, although the exact cause of this resonance was ʳ ᵗt determined, it was unlikely to be a flow resonance relevant to the real heart.

It was decided to filter the variable inductance transducer signals to eliminate this problem. This was a feasible only because the undesired oscillations had a much higher frequency than the dominant 0.5 Hz closure frequency. All three variable inductance transducer signals were filtered by a 60 Hz low-pass filter. Figure 5.19(b) shows the result of filtering. Since the signals were passed through the filter, there was a time delay of 1/60 second, which was taken into account in all data analysis.

(a) Unfiltered Signals
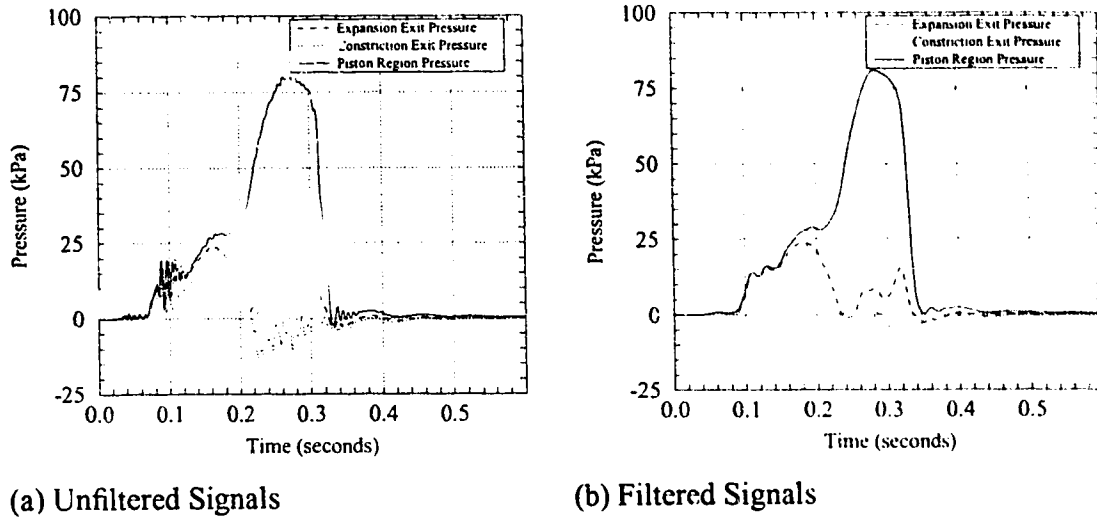
(b) Filtered Signals

Figure 5.19: Unfiltered and Filtered Pressure Response
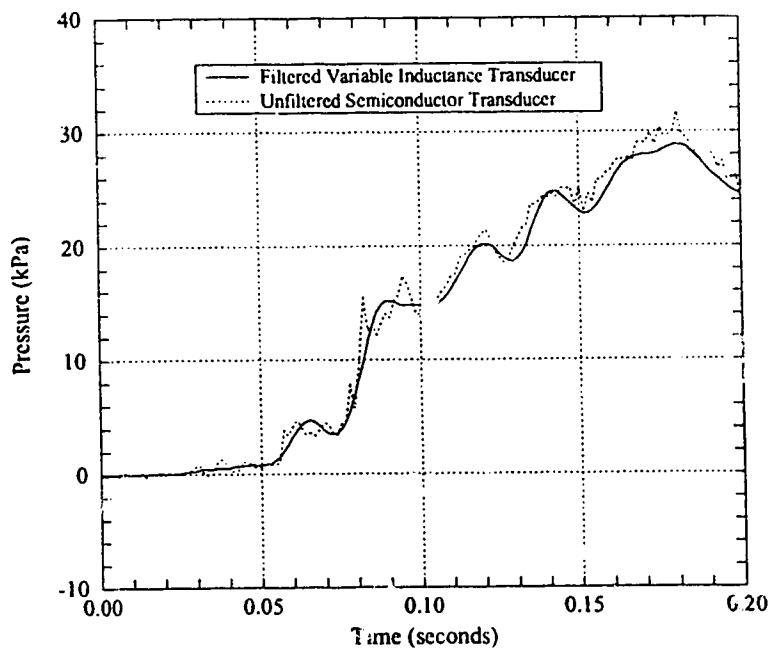
Figure 5.20: Comparison Between Filtered Variable Inductance and Semiconductor Pressure Transducer Response

Figure 5.20 compares a filtered variable inductance transducer signal with an unfiltered semiconductor transducer signal from a typical test sequence. The two transducers were located in the model in the piston region along the mid-line 25 mm apart (previously shown in Figure 5.12). The pressures at these locations should be nearly identical, differing by no more than 200 Pa based on the unsteady Bernoulli analysis of Chapter 3. The variable inductance transducer signal follows the semiconductor signal very well, damping out the minor transients. This damping of these minor transients was desirable, as they were not of interest for the analysis being considered here.

Each set of ten repeat closures were combined to determine the mean pressure at each point in time for the variable inductance transducer signals. The sample standard deviation at each time was also calculated to determine the average for each test sequence. The per cent standard deviation in the stroke normalized pressure differences was then determined, assuming that errors were uncorrelated. For example, to determine the standard deviation in Υ, recall that this normalized pressure difference is determined from

$$\Upsilon = \frac{P_p - P_c}{\Delta P_{stroke}}.$$ (5.3)

If the errors are uncorrelated, the standard deviation may be determined from

$$\sigma_\Upsilon^2 \propto \sigma_p^2 + \sigma_c^2,$$ (5.4)

so that

$$\frac{\sigma_\Upsilon}{\Upsilon} = \frac{\sqrt{\sigma_p^2 + \sigma_c^2}}{\Delta P_{stroke}\Upsilon_{max}}.$$ (5.5)

These values for all test configurations and wall speeds are shown in Figures 5.21 and 5.22. The largest deviations occurred for the mild restriction, which had standard deviations ranging from 6% to 10.5% of the normalized pressure difference. The compliant constriction case also showed standard deviations ranging up to 10.2%. All other test configurations had standard deviations of less than 5% of the normalized pressure difference. These values are conservative, due to the assumption that the errors
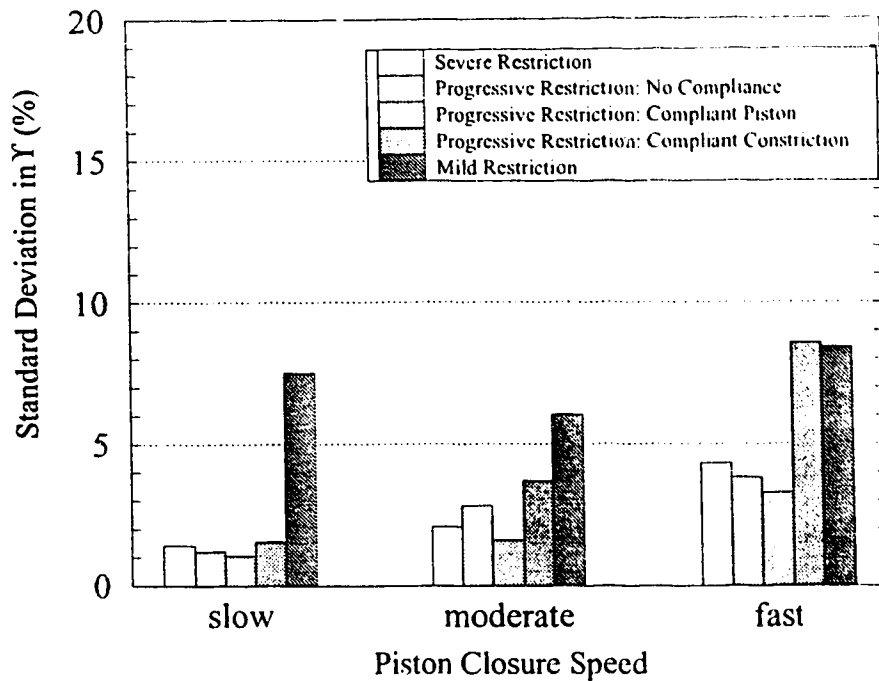
Figure 5.21: Standard Deviation for Normalized Piston-Constriction Pressure Differences Recorded by Variable Inductance Pressure Transducer
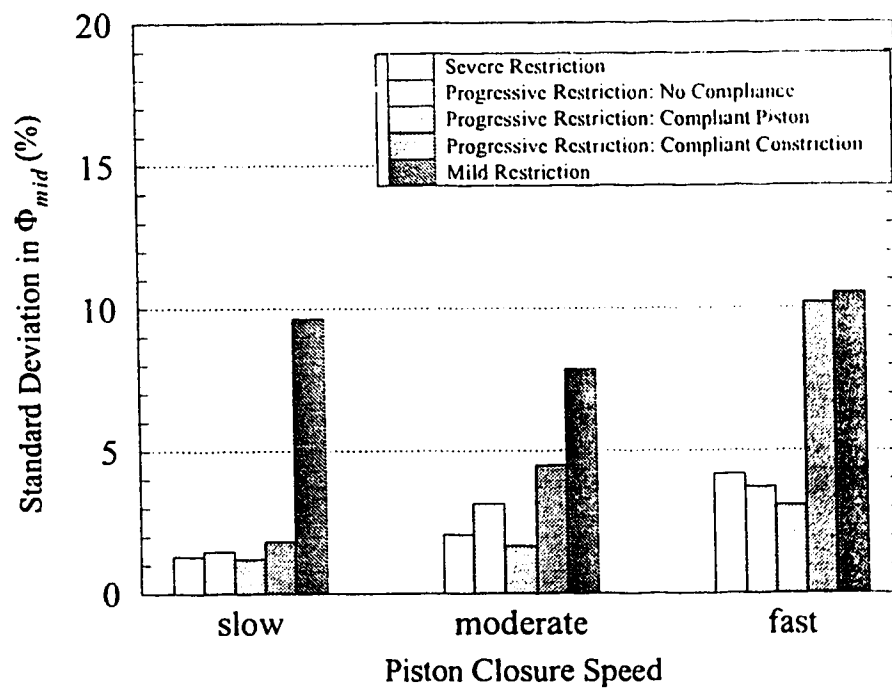
Figure 5.22: Standard Deviation for Normalized Piston-Exit Pressure Differences Recorded by Variable Inductance Pressure Transducer

arc uncorrelated. If the errors are correlated, the standard deviation between tests would be reduced. These results indicate that the repeatability between the pressure signals is adequate, with less than 5% standard deviation in most cases.

5.5 LABORATORY *VS. IN VIVO* FORCE RATIOS

It is important to ensure that *in vivo* ejection and the laboratory model match in terms of the force ratios determined in Section 2.2.5 ($F_{viscous}/F_{inertial}$ and $F_{inertial}/F_{spatial}$). The force ratios for the planar piston model were determined in Appendix A and are as follows: the viscous to inertial force ratio (equation A.43)

$$\frac{F_{inertial}}{F_{viscous}} \approx 1.9\beta_H^2\alpha_H;$$

(5.6)

the spatial to inertial force ratio for the sudden expansion (equation A.47)

$$\frac{F_{spatial}}{F_{inertial}} \approx 0.44\beta_H[1 - \eta_H + \eta_H^2]$$

(5.7)

and the spatial to inertial force ratio for the unseparated expansion (equation A.48)

$$\frac{F_{spatial}}{F_{inertial}} \approx 0.22\beta_H$$

(5.8)

where

$$\beta_H = \frac{H_{P_{initial}}}{H_e} \text{ (geometry factor),}$$

$$\eta_H = \frac{H_e}{H_c} \text{ (restriction factor),}$$

$$\alpha_H = Re^{0.5}St^{0.5} \text{ (Womersley parameter).}$$

The inertial to viscous force ratios determined for the different configurations are given in Table 5.1, along with the *in vivo* results determined in Section 2.2.5. All the tests for the mild and progressive restrictions, which simulate HCM, fall above the range calculated for the resting and provoked *in vivo* HCM cases. The *in vivo* values were based on a geometry factor using an aortic diameter of 2.5 cm. Some researchers have also used an

aortic diameter of 2.0 cm for evaluating left ventricular ejection, see Jones (1969), in which case the *in vivo* values of the inertial to viscous force ratio will exceed the laboratory values. To make comparisons more meaningful, the mild restriction with the slowest closure rate and the progressive restriction with the fastest closure rate were chosen for comparison, as both had similar inertial to viscous force ratios ($F_{inertial}$/

Table 5:1 Inertial to Viscous Force Ratios for Unsteady Laboratory Model

Heart Configuration			Force Ratio $\dfrac{F_{inertial}}{F_{viscous}}$	
	β_{II}	α_{II}	**laboratory**	*in vivo*
Mild Restriction Fastest closure rate	2.5	66.5	790	327 provoked, HCM to 169 resting, HCM
Mild Restriction: Slowest closure rate	2.5	59.1	702	
Progressive Restriction: Fastest closure rate	2.5	58.7	697	
Progressive Restriction: Slowest closure rate	2.5	47.3	561	
Severe Fixed Restriction Fastest closure rate	2.5	49.4	587	79 severe valvular aortic stenosis
Severe Fixed Restriction Slowest closure rate	2.5	37.7	448	

$F_{viscous}$ of about 700). The inertial to viscous force ratio for the severe fixed restriction also did not match the severe valvular aortic stenosis case, even when an aortic diameter of 2.0 cm was used. Slower closure rates were attempted, but inconsistent wall closure speeds from test to test resulted, due to a frictional stick-slip problem. Thus the comparisons with the *in vivo* were done at the lowest fixed restriction closure rate attainable, recognizing that the force ratio did not match. Fortunately, viscous drag forces are negligible in both the model and the *in vivo* situations, ranging from about 0.3% to

1.3% of the inertial acceleration force. Viscous forces can have a significant effect on pressure ̄ough their influence on flow separation. The Reynolds number for the *in vivo* left ventricles (based on aortic diameter) ranges from about 3000 to 15,000, while the Reynolds number for the laboratory model (based on exit channel width) ranges from 13,000 to 41,500. This indicates that the laboratory model will be more likely to have flow separation than the corresponding *in vivo* situation.

The spatial to inertial force ratio values for the different configurations are shown graphically in Figure 5.23, along with the corresponding *in vivo* values determined in Section 2.2.5. As is evident, the laboratory model and the *in vivo* situation have similar ranges of the spatial to inertial force ratio between the unseparated expansion and the sudden expansion cases.

Unseparated Expansion | Sudden Separated Expansion

```
        0.5    0.99
        |------|  in vivo mild HCM
    |--------------|  laboratory model
    0.15         1.33
```
Mild Fixed Restriction

Unseparated Expansion | Sudden Separated Expansion

```
    0.71              7.1
    |-----------------|  in vivo severe HCM
    |--------------------|  laboratory model
    0.15              10.2
```
Progressive Restriction

Unseparated Expansion | Sudden Separated Expansion

```
    0.43                        97
    |---------------------------|  in vivo severe aortic valvular stenosis
    |-------------------------------|  laboratory model
    0.15                          149
```
Severe Fixed Restriction

Figure 5.23: Comparison of Spatial to Inertial Force Ratios for Unsteady Laboratory Model

5.6 FLOW VISUALIZATION

An important use for the experimental model was to obtain a whole field picture of the flow. The fluid in the piston region was dyed with fluorescein. In order to dye only the fluid in this region, a sliding separation wall was placed between the piston region and the exit/outflow regions, as shown in Figure 5.24. Once the fluid in the piston region was thoroughly mixed with dye, the separation wall was pulled away sharply, simultaneously activating the piston drive system.

A single laser light sheet was placed through the model from the downstream end of the expansion region. A four watt Argon Ion Coherent Innova 70 laser was used to provide laser light at a suitable intensity. The laser beam was routed through a fiber optic cable and passed through a cylindrical lens to create a sheet of laser light. This arrangement had about 50% light power transmission efficiency with a light sheet approximately three to four millimetres in thickness. A Sony video camera was used to record the images produced. This camera was capable of 30 frames a second and was used with a shutter speed of 1/250 second. The Kodak Wratten gelatin filter was used to filter out the background laser light, allowing only the dye fluoresced light to pass through the camera lens. The flow sequence was recorded on video tape using a Mitsubishi VCR. Once the testing was complete, single frame images were digitized from the video tape and stored on a computer for analysis, using the technique developed by Campbell (1991).

The images obtained were then digitally false-coloured using an existing computer algorithm to give a clear picture of the flow. Generally, seven to fifteen images were required to capture a complete flow sequence, depending on the rate of closure.

A typical flow sequence is shown for the progressive restriction in Figure 5.25. In the first four frames, the undyed fluid being ejected from the piston region pushes the dyed fluid downstream. The undyed/dyed fluid interface has a fairly blunt profile during this

Handle allows
partition to be
р .shed in or out

Sliding Partition Wall

Expansion Region
filled with dyed fluid

Piston region separated
from dyed fluid
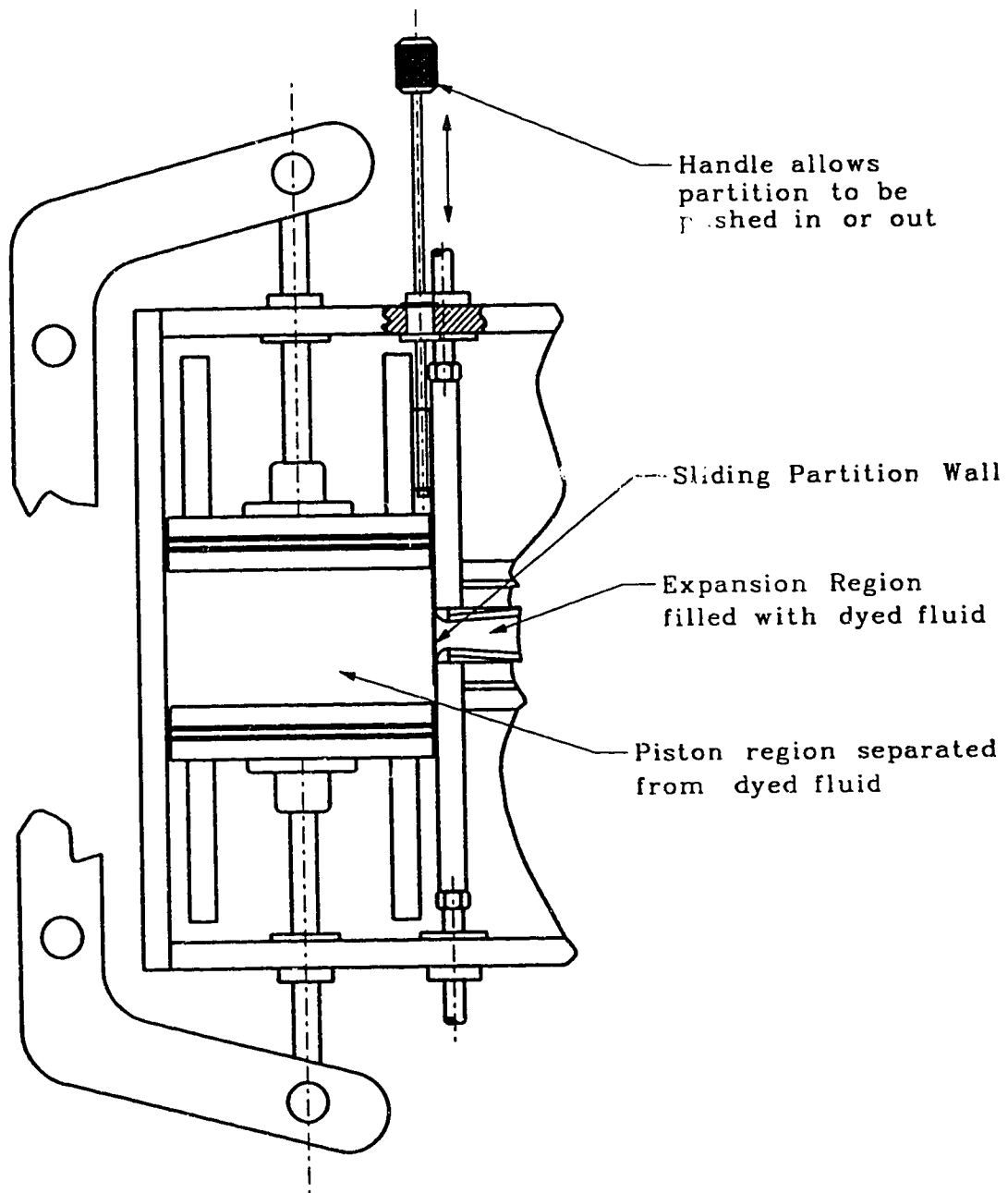
Figure 5.24: Sliding Wall Partition for Flow Visualization

Flow

Exit

Flow

Area shown below
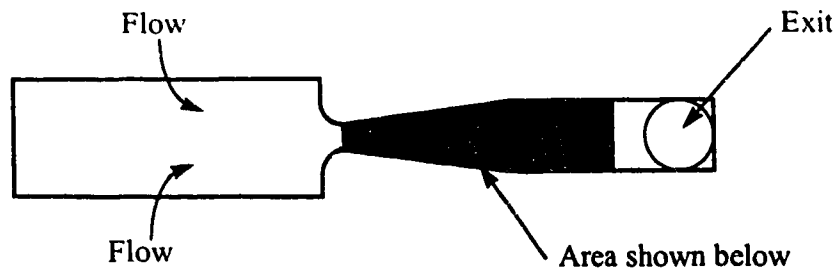
Expansion region filled with dyed fluid
time: 0 second (0% piston closure)
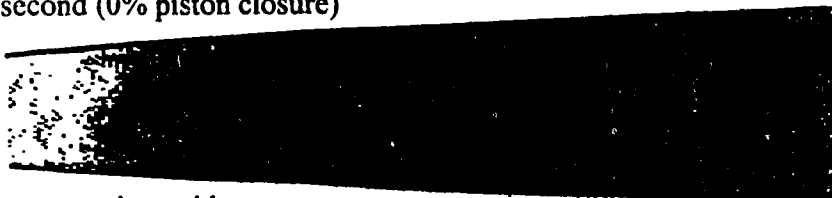
Flow begins, no separation evident
time: 1/30 second (7% piston closure)
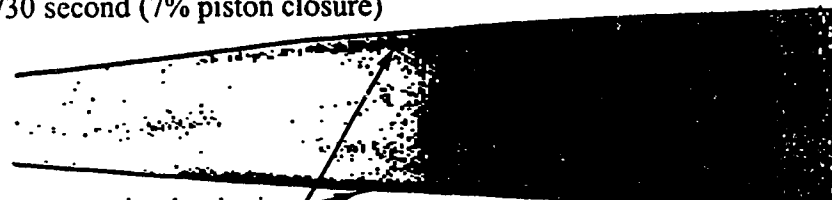
Flow continues, separation beginning
time: 2/30 second (25% piston closure)
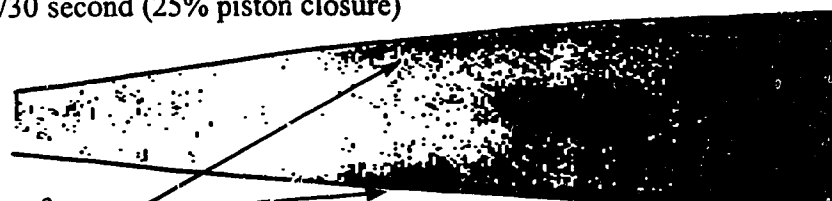
Separation zone forms
time: 3/30 second (48% piston closure)
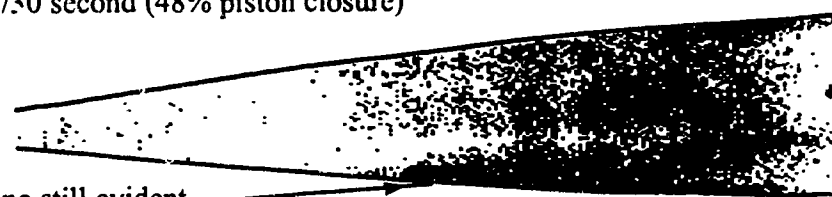
Separation zone still evident
time: 4/30 second (68% piston closure)

Figure 5.25: Flow Visualization for Progressive Restriction (fast closure rate)

period, which represents the first half of the ejection. There is no evidence of flow separation at this point. In the last four frames, it is clear that flow separation is occurring. The flow is asymmetric, separating in an unsteady fashion. This sequence of separation occurring in the second half of ejection was noted for the progressive restriction, regardless of the rate of closure.

The severe fixed restriction showed signs of flow separations from the onset of ejection, and the separation persisted throughout the ejection period. The flow was very asymmetric, separating on one side only. The degree of separation increased throughout the ejection period and seemed somewhat unsteady. As with the progressive restriction, the separation formed regardless of the rate of ejection.

The mild restriction configuration showed no signs of separation throughout the majority of the ejection. The last frame appeared to show separation, but it is difficult to determine if this was just after the ejection period had finished. Overall, regardless of the rate of ejection, there was no indication of separation throughout the majority of the ejection period. The undyed/dyed fluid interface showed a fairly blunt profile during the first half of ejection. Little else may be said about the flow profile, as this interface was swept downstream out of range of the picture by the end of the first half of the ejection period.

The three configurations may thus be described as follows:

- mild fixed restriction: no evidence of flow separation; blunt flow profile evident at undyed/dyed fluid interface during first half of ejection period;

- progressive restriction: no evidence of flow separation during first half of ejection, asymmetric flow separation during second half of flow separation, blunt flow profile evident at undyed/dyed fluid interface during first half of ejection period;

- severe fixed restriction: flow separation evident throughout ejection period, asymmetric flow profile evident at undyed/dyed fluid interface during first half of ejection period.

5.7 SUMMARY

The unsteady laboratory model that was designed and tested had the following capabilities:

- three different configurations were tested: mild fixed restriction, progressive restriction and severe fixed restriction;

- both compliant and non-compliant configurations were tested;

- the piston closure rate for each configuration could be adjusted as desired;

- the model gave consistent, repeatable results in terms of wall position and pressure measurements;

- the dyed fluid flow visualization method gave useful results, showing no flow separation for the mild fixed restriction, flow separation during the deceleration phase for the progressive restriction, and flow separation throughout the ejection for the severe fixed restriction.

CHAPTER 6 • LABORATORY MODELLING OF QUASI-STEADY FLOW

6.1 INTRODUCTION

The computational fluid dynamics solutions presented in Chapter 4 were based on a quasi-steady approach and did not show any flow separation (reverse flow near the walls of expansion region) for the turbulent flow c.ses. The laminar case did separate, but the solutions had convergence problems at the Reynolds numbers of 35,000 to 43,000 (convergence was achieved on identical grids for Reynolds numbers of 500 to 1000). Since the unsteady laboratory model showed significant flow separation, a question arose: was the quasi-steady approach poor because flow separation did not occur for the steady flow, or was the computational fluid dynamic model in error by not predicting separation? To answer this question a steady flow laboratory model was built with the same geometry as the unsteady laboratory model. By comparing results from the steady flow laboratory model at various constrictions, it was be possible to verify if the pressures predicted by the computational method were correct. In addition, through the use of flow visualization, flow separation could be detected.

This chapter will describe the construction of the quasi-steady laboratory model. The flow and pressure measurements will be discussed and results from the flow visualization presented. It will be shown that flow separation occurs when the flow is highly restricted and that the flow is turbulent in nature.

6.2 MODEL CONFIGURATION

6.2.1 Fluid Flow Through the Quasi-Steady Flow Laboratory Model

The geometry of the quasi-steady laboratory model was chosen to match the unsteady laboratory model with a progressive restriction configuration at piston closure
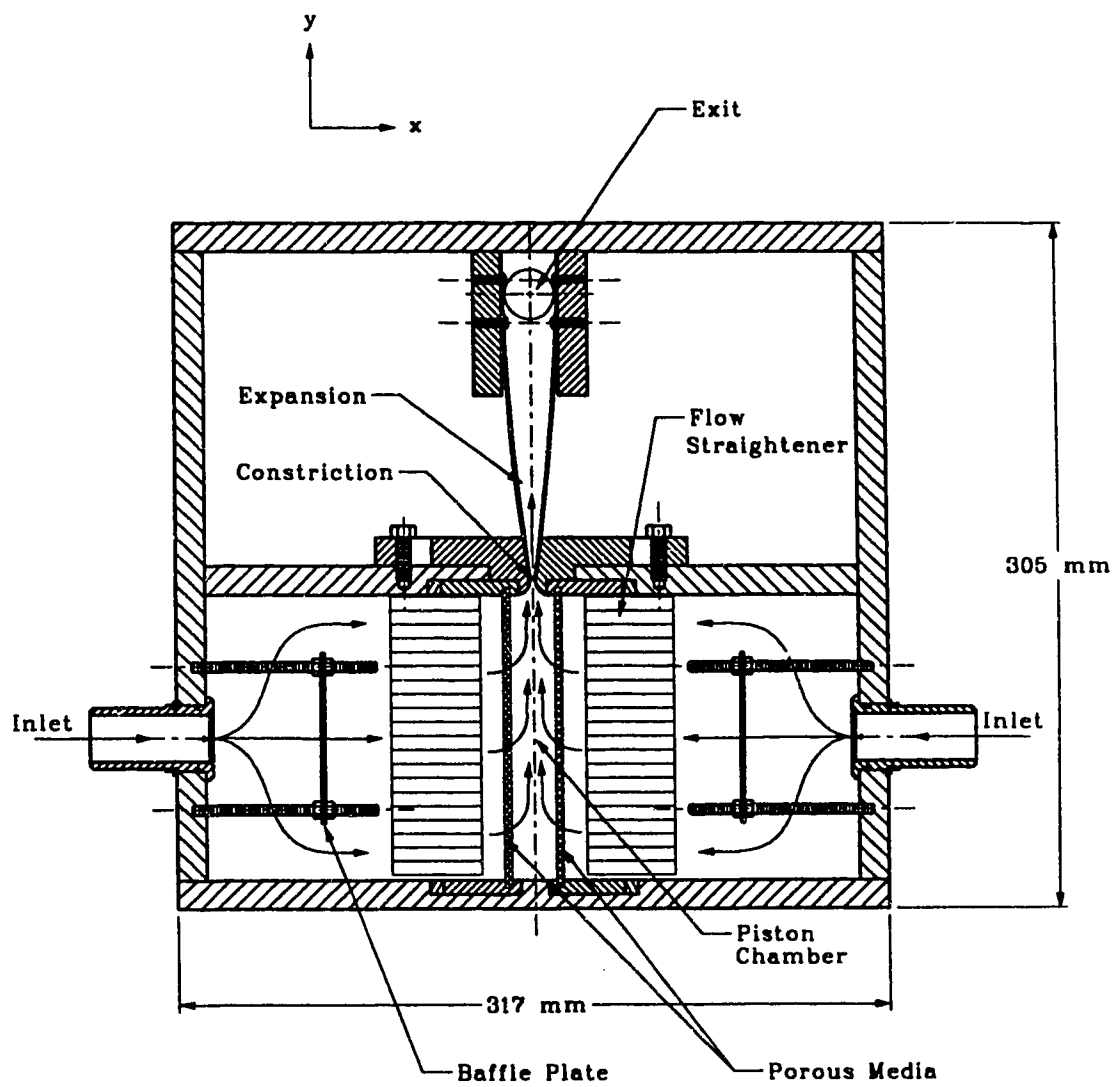
Figure 6.1: Quasi-Steady Laboratory Model (Top View)

locations of either 50% or 85%. The configuration is shown in Figure 6.1. Most of the

model was fabricated from Lexan sheets, a strong transparent polycarbonate plastic. Fluid

entered the model at the left and right sides and passed through porous plates to enter the

piston region. The fluid turned 90° (from x to y direction, see Figure 6.1) in the "piston"

chamber and then passed through the constriction and expansion regions before leaving

the model through the outlet tubes. The exit locations and sizes were identical to the

unsteady laboratory model (see section 5.2.2).

The fluid used in the model was filtered tap water from the building supply. As

shown in Figure 6.2, the water was first pumped by a centrifugal pump into a header that

provided equal flow to both sides of the model. With the pump running, the maximum

flow rate was achieved. This flow rate could be adjusted using the gate valve downstream

of the pump. The pump was not needed to obtain the lower flow rates, as the building

supply pressure was adequate. Paper cartridge type filters were placed downstream of the

tee to remove rust and scr'- from the water. These filters were necessary, as small particles

would clog the porous pl ' 2s used in the model (the first set of porous plates were used

without a filter; they quici . ' clogged and then plastically deformed due to the resulting

pressure drop).

6.2.2 Inlet Flow Uniformity

The entrance regions shown in Figure 6.3 were included to provide as uniform a

velocity profile as possible at the simulated position of the piston faces. Fluid entering the

settling chamber was first obstructed by a baffle plate, to eliminate the fluid jet entering the

settling chamber. The fluid then passed through a flow straightener made from plastic

straws with a 6 mm diameter and length of 36 mm to eliminate large scale turbulence

upstream of the porous plate. There was also a small gap of 10 mm just upstream of the

porous plate to even out pressure differences across the flow. Finally, the fluid was forced
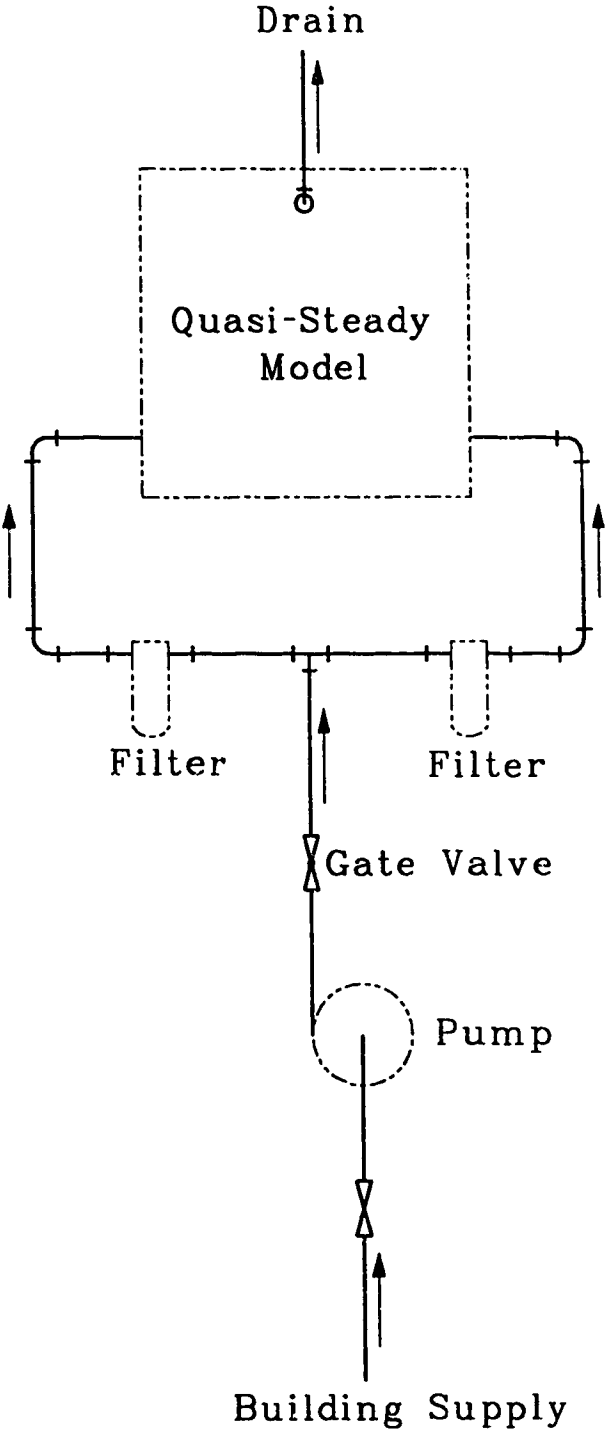
Figure 6.2: Flow Diagram for Quasi-Steady Laboratory Model
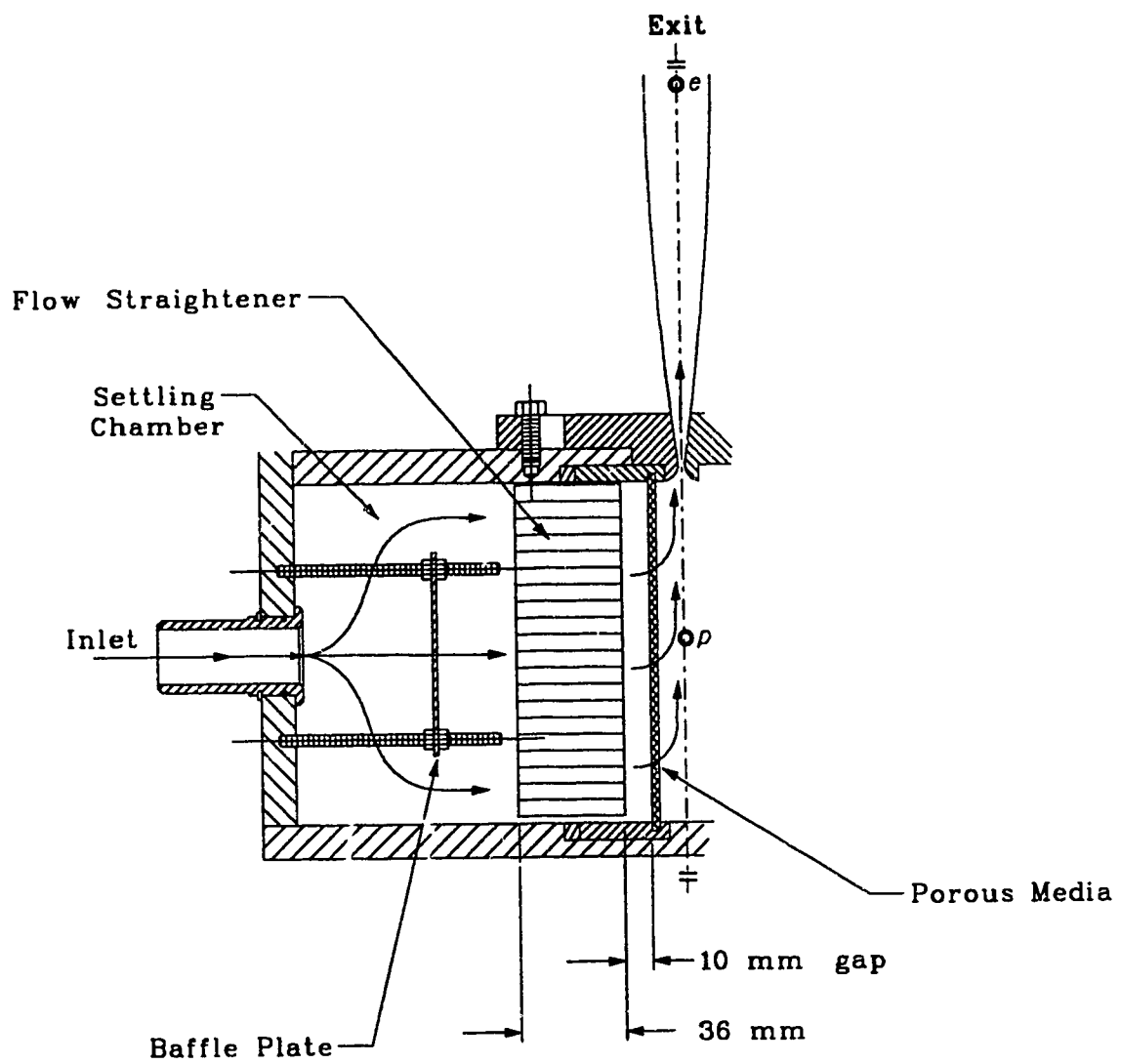
Figure 6.3: Details of Entrance Region of Quasi-Steady Laboratory Model (Top View)

through the porous plate and entered the piston region. The porous plates were fabricated from sintered stainless steel, and supplied by Mott Metallurgical Corporation.

By using porous plates with a porosity of 10 microns, two experimentally important effects were incorporated. First, these high-resistance ensured a large pressure drop across the plate compared to the pressure drop along the test section. For example, at a flow rate of 1 liter/second, the pressure drop across the porous plates was 140 kPa, but only 1.7 kPa from p to e (see Figure 6.1) in the test section. Since the pressure drop across the porous plate was two orders of magnitude greater than in the test section, pressure changes within the test section had a negligible effect on the uniformity of the inlet velocity. The second effect was that small scale turbulence was essentially eliminated, as fluid was forced through the small passages of the porous plates.

6.2.3 Construction Details

The p ... a: s were located to match the position of the unsteady laboratory model pistons : ... s of either 45% (restriction factor $\eta_{II} = \dfrac{H_c}{H_c} = 4.5$) or 85% ($\eta_{II} = 16.$; ... plates were held in frames, which in turn were recessed into the model (Figure 6.4). By reversing the position of the frames within the model, the plate positions could be moved from the 45% position to the 85% position.

The walls of the constriction were made from aluminum, due to that material's combination of excellent machinability and acceptable corrosion resistance. The curved wall profile was machined to match the unsteady laboratory model. The constriction opening could be adjusted to match either the 45% or 85% piston closure position. The walls of the expansion section were made from 0.76 mm thick stainless steel sheet. These were curved to give a wall profile very similar to the unsteady laboratory model. They were fastened to the walls of the constriction to ensure a smooth continuation of the constriction wall profile (Figure 6.5).

Maximum Restriction
85% Piston Closure Position

Poro media frames
may be reversed

Constriction walls
are adjustable

Minimum Restriction
45% Piston Closure Position
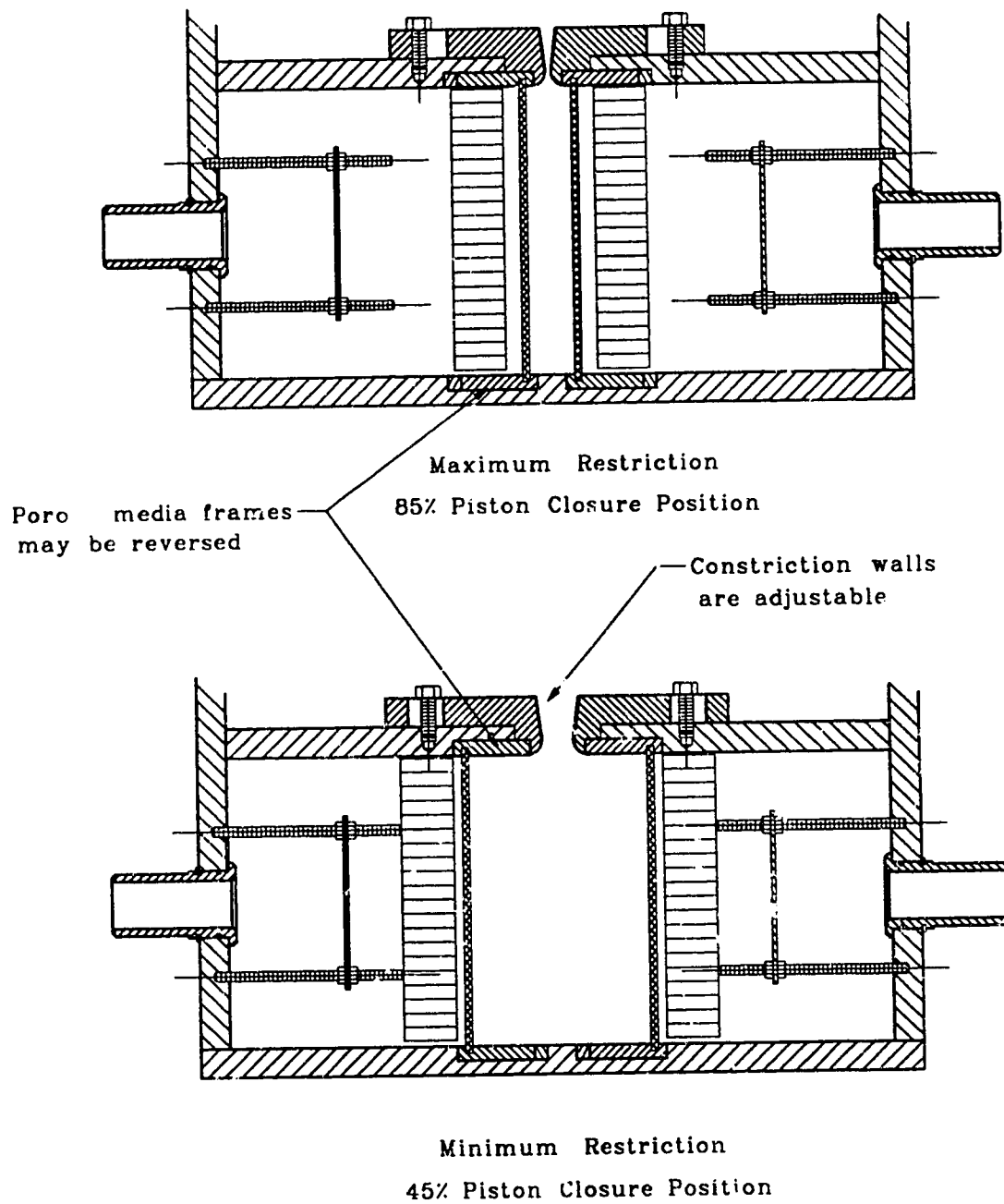
Figure 6.4: Porous Plate Mounting Arrangement (Top View)
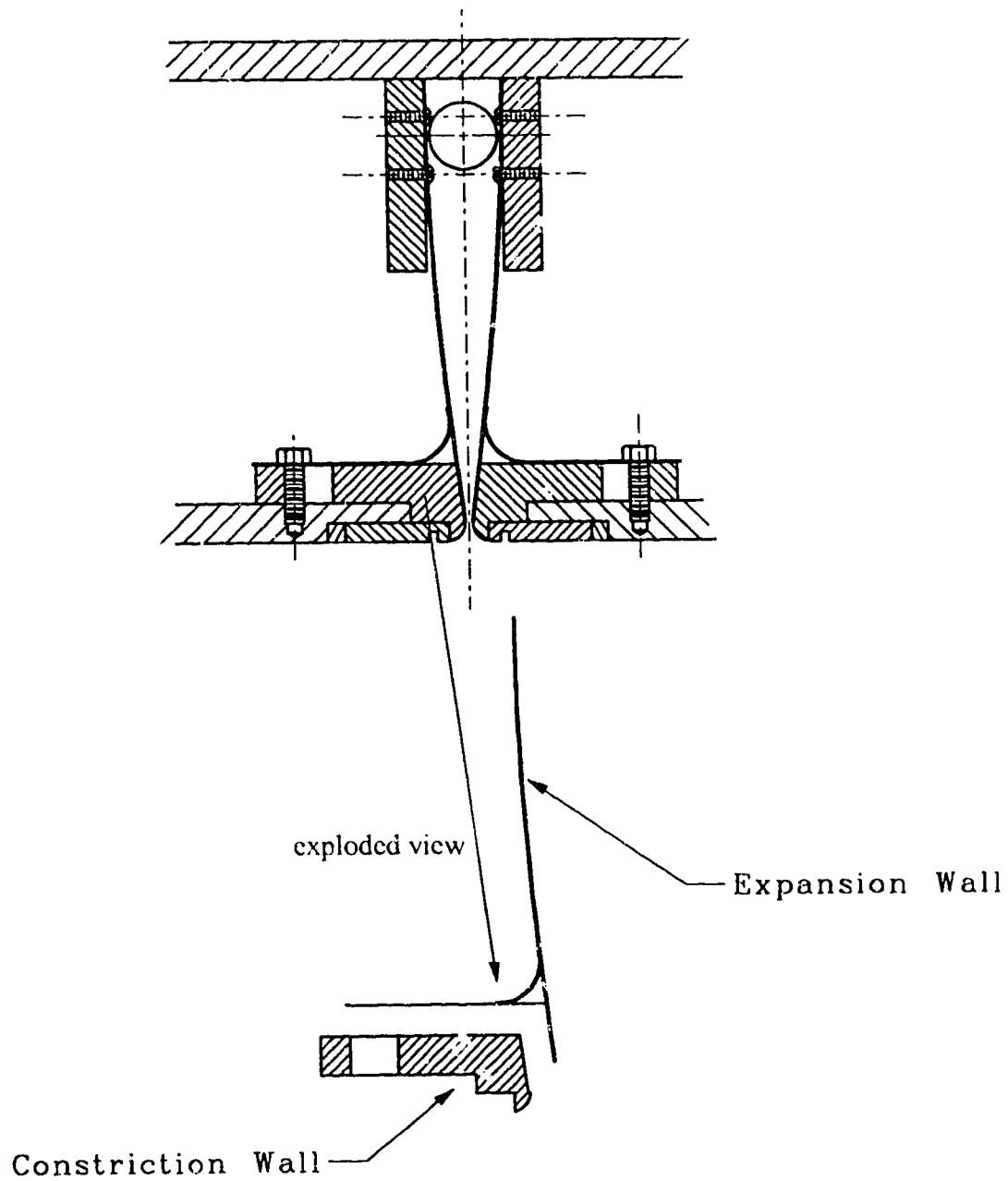
Figure 6.5: Constriction Wall Details

See also Figure 5.9 for unsteady model.
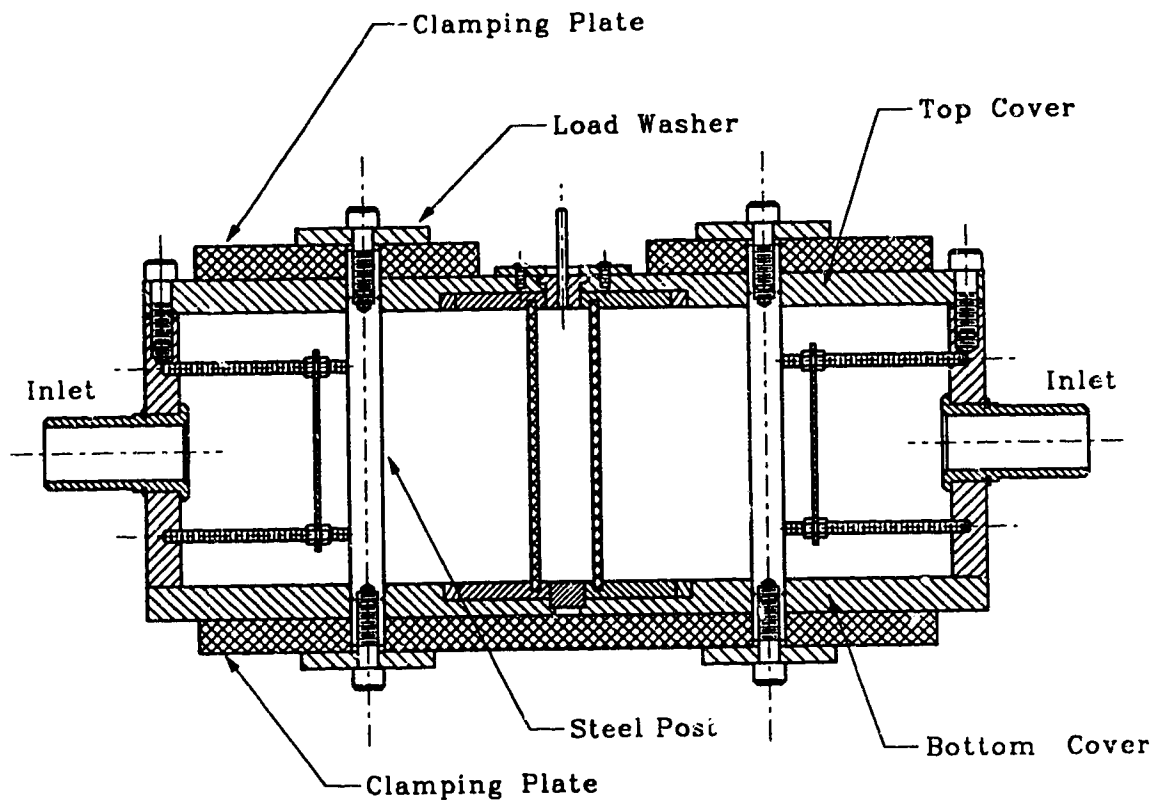
Cross-Section Through Model

Figure 6.6: Clamping Plate Arrangement to Add Stiffness

The polycarbonate plastic construction of the exterior of the model was appropriate for flow visualization purposes, but its flexibility caused an unanticipated problem. Due to the high pressure upstream of the porous plates, a significant amount of flexure of the upper and lower polycarbonate surfaces occurred. This gave the fluid within the model an alternate route: around, instead of through, the porous plates. The solution was simple and involved adding stiffness to the upper and lower polycarbonate surfaces. This was done by placing 12.7 mm thick aluminum plates over the surfaces and clamping them together through the model with stainless steel posts (Figure 6.6). The clamping plates did not cover the section over the piston, constriction or expansion regions, so that flow visualization was still possible.

6.3 MEASUREMENTS AND DATA ANALYSIS

The parameters measured in this model were the pressure at various points along the mid-line of the model as well as the flow rate. Two flow rates were used for each configuration: one with the pump running and one without. The flow rate was measured by diverting the exit flow and determining the time taken to fill a volume of 12 liters. Five readings were taken to find the mean flow rate for each test. The flow rates along with the associated standard deviations and Reynolds numbers (based on the expansion region exit width) are summarized in Table 6.1. The range of Reynolds numbers compares well to *in*

Table 6.1: Flow Rates for the Quasi-Steady Flow Laboratory Model

Configuration	Flow Rate	Standard Deviation	Reynolds Number Re_H
	liters/ second	liters/ second	
η_H = 4.5: High Flow Rate	1.00	0.017	9843
η_H = 4.5: Low Flow Rate	0.84	0.013	8268
η_H = 16.7: High Flow Rate	1.03	0.016	10140
η_H = 16.7: Low Flow Rate	0.83	0.016	8169
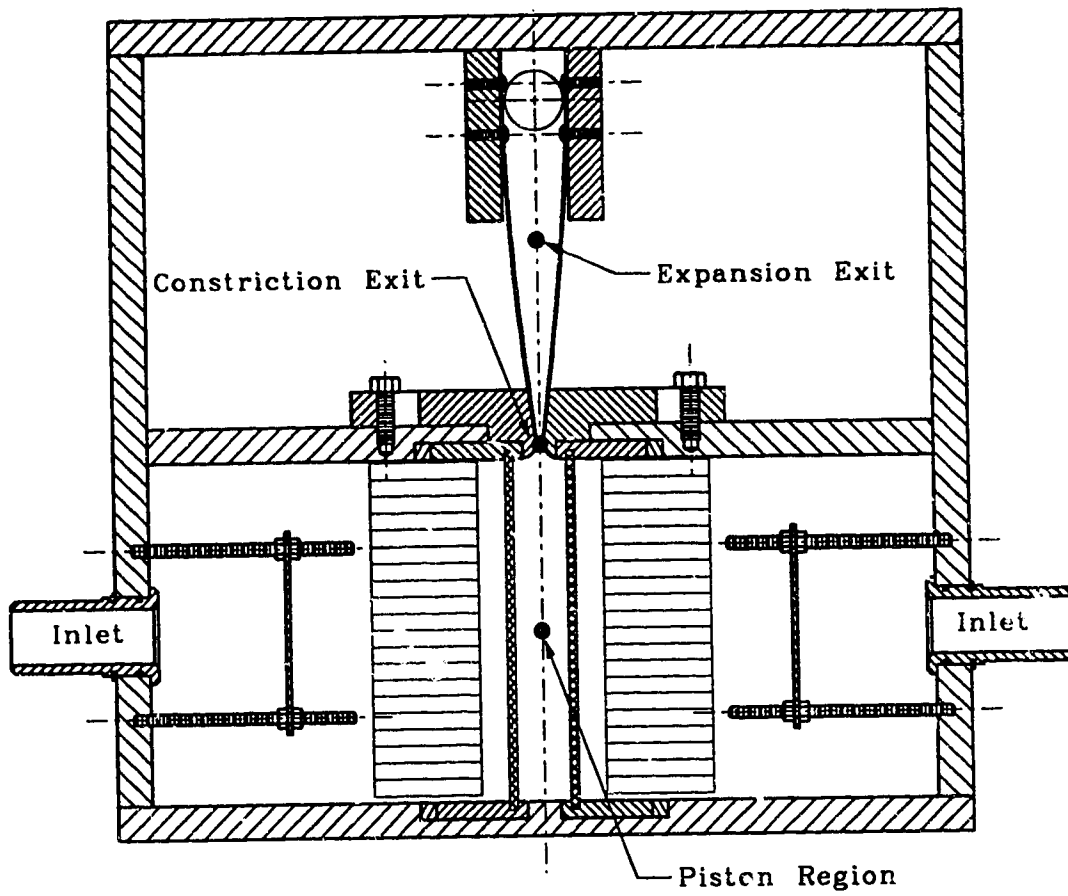
Figure 6.7: Pressure Measurement Locations

vivo situations, where peak Reynolds numbers for HCM hearts can reach values of 15,000.

The pressure measurements were made using the same variable inductance transducers described in Chapter 5. These transducers were calibrated before and after testing each configuration. The wall static pressure was measured in the piston region, constriction exit and expansion exit, as shown in Figure 6.7. These locations were essentially the same as those used in the unsteady laboratory model. The data acquisition system was also the same as that described in Chapter 5.

A total of ten pressure readings were taken for each test configuration. Each reading was the average value of 600 readings collected over a one second period. These average pressures were then used to determine the average stroke normalized pressure differences, summarized in Table 6.2. The percent error is also shown in Table 6.2. The pressure errors are correlate , u the error in Φ_{mid} and Υ is small (usually less than 5%).

Table 6.2: Pressure Measurements in Quasi-Steady Flow Laboratory Model

Configuration	Φ_{mid} Normalized Pressure Difference	Φ_{mid} %error	Υ Normalized Pressure Difference	Υ %error
$\eta_H = 4.5$ High Flow Rate	22.6	0.7%	8.0	7.8%
$\eta_H = 4.5$ Low Flow Rate	12.0	0.7%	8.0	1.6%
$\eta_H = 16.7$ High Flow Rate	128	3.9%	50.6	5.2%
$\eta_H = 16.7$ Low Flow Rate	90.6	1.8%	46.6	2.6%
All pressures normalized by $1/2\rho V_e^2 = 75.1$ Pa, with V_e based on 1 l/s flow rate.				

6.4 FLOW VISUALIZATION

The flow was visualized using the same equipment described in section 5.5. A laser light sheet was directed into the model from the expansion end, as shown in Figure 6.8. Fluorescein dye was injected where desired using the injector shown in Figure 6.8. This injector was constructed from 1.5 mm diameter stainless steel tubing and was placed into the model from the downstream end of the model. The main body of the injector was below the light sheet, with the curved tip allowing dyed fluid to be injected upwards into the light sheet. While the probe disturbed the flow, this effect was minimal. Most likely, if there was no flow separation with the probe in the flow, there also would be no flow separation without the probe there. The video camera was mounted above the expansion section. The images were recorded in Super VHS on a VCR at a rate of 30 images per second, then played back to the frame grabber for analysis in a similar fashion to that previously described in Section 5.5.

The flow for the restriction factor $\eta_H = \dfrac{H_e}{H_c} = 4.5$ appeared quite unsteady both in the piston region and downstream of the constriction. No flow separation was observed at any point downstream of the constriction. An interesting result was observed during initial testing. Due to a minor construction flaw, one side of the connection between the constriction and expansion wall had a rough edge, protruding into the flow approximately 0.5 mm. This was sufficient to produce an asymmetric flow with a large separation zone just downstream of the expansion region exit. When the model was reconstructed for final testing, this rough edge was removed and the flow no longer separated for this restriction factor.

The flow for the restriction factor $\eta_H = 16.7$ (severely restricted) was also fluctuating throughout the model. Downstream of the constriction, the flow separated intermittently on one side of the expansion region. This can be seen in the flow

Laser Beam

Lens

Light
Sheet

Top View
of Model

Sony CCD/RGB
Color Video Camera
Shutter speed: 1/250 second
Gain: 12 dB

Nikon 50 mm focus lens
fstop: 2.8

Top Cover

Flow Direction

Laser Light
Sheet

Piston
Region

Expansion
Region

Dye

Bottom Cover

Dye Injector

Side View
of Model
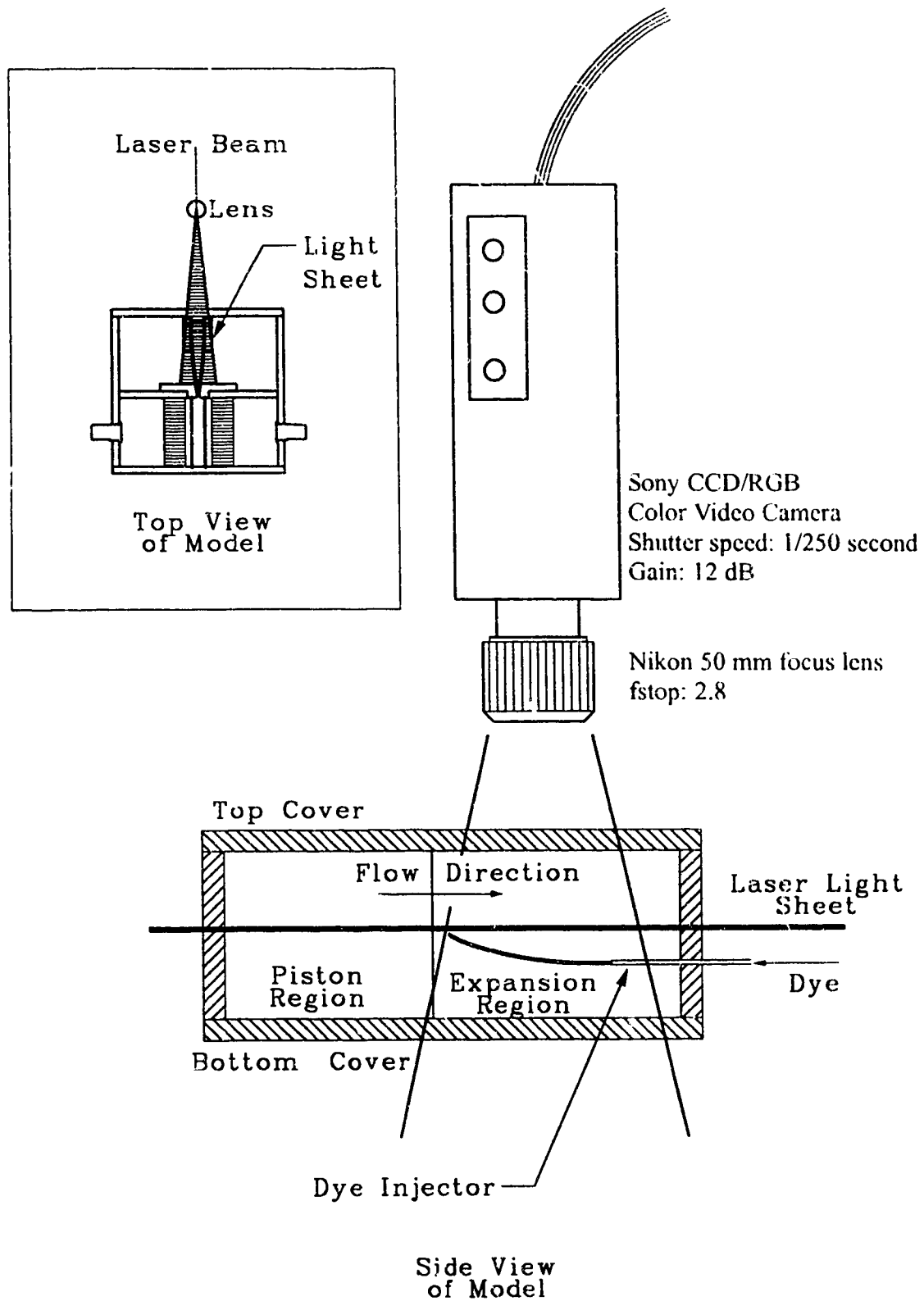
Figure 6.8: Laser Light Sheet and Video Arrangement

Flow

Dye Injection Location

Exit

restriction factor $\eta_H = 16.7$

Flow

Area shown below

No separation zone evident
time: 0 second

Dyed fluid begins to move upstream
time: 1/30 second

Dyed fluid moves further upstream
time: 2/30 second

Separation zone begins to break up
time: 3/30 second

Separation zone continues to move downstream
time: 4/30 second
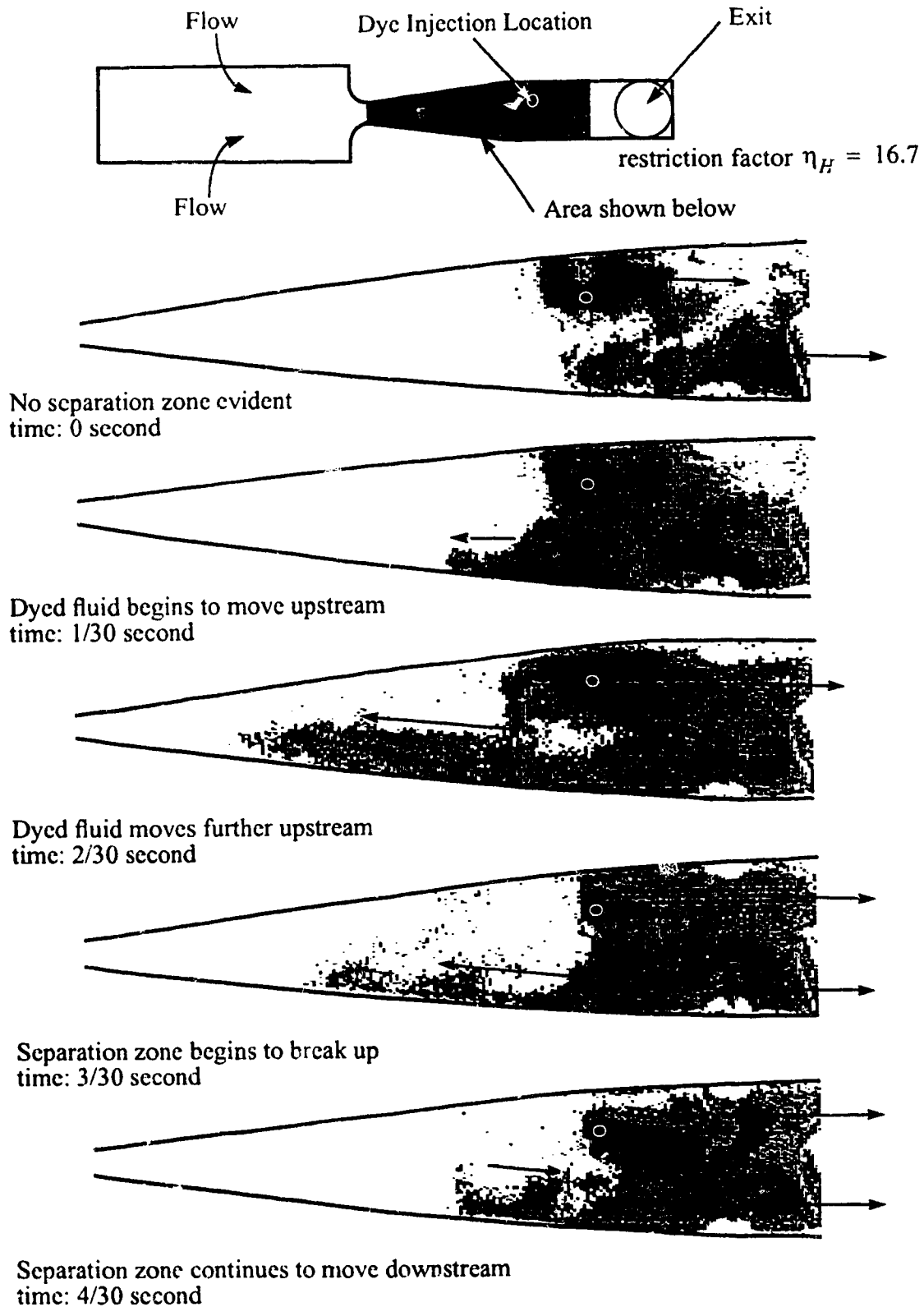
Figure 6.9: Flow Visualization Showing Unsteady Separation (Low Flow Rate)

visualization sequence shown in Figure 6.9. Each frame is 1/30th of a second apart. The dyed fluid is initially being swept downstream, shown by the first frame (time 0/30 second). The flow suddenly separates, sweeping the dyed fluid upstream (time 1/30 and 2/30 second). The separation then collapses and is swept downstream (time 3/30 anu 4/30 second). This intermittent separation was observed at both the low and high flow rates. The flow always separated on the same side of the expansion, regard' ; of the dye injection location.

Pressure measurements were made using the fast response semi-conductor transducer in the expansion region. Data was collected at the rate of 720 readings per second. These measurements showed a rap¡dly fluctuating pressure, with fluctuations occurring 10 to 15 times per second. This is quite consistent with the intermittent flow separation observed by the flow visualization. This clearly shows the difficulty of CFD analysis for steady flows that have embedded in them a fluctuating flow separation.

6.5 SUMMARY

The quasi-steady laboratory model showed the following:

- the flow in the expansion region of the mild restriction contained fluctuations, but showed no signs of flow separation for both flow rates tested;

- the flow in the expansion region of the severe restriction contained fluctuations and there was an intermittent, asymmetric flow separation for both flow rates tested;

- a rough edge in the constriction caused flow separation to occur in the mild restriction, indicating a sensitivity to constriction geometry;

- the pressure differences were repeatable, with a maximum percent error of less than 8%;

- the CFD code could not predict a fluctuating separation as was found in the quasi-steady laboratory model, which shows that using a quasi-steady CFD approach may be significantly inaccurate even for a simple geometry.

CHAPTER 7 • MODEL AND *IN VIVO* COMPARISONS

7.1 INTRODUCTION

In the previous chapters, several simplified left ventricle-to-aorta flow models were described. These models attempted to simulate the important characteristics of HCM (hypertrophic cardiomyopathy) for the unobstructed (mild fixed restriction) and SAM (progressively restricted systolic anterior motion of the mitral valve) theories. As well, a severe fixed restriction was modelled, for comparison with the severe aortic valvular stenosis case. The models utilized both quasi-steady and unsteady flow techniques to obtain pressure differences between the left ventricle (piston) and points downstream: the constriction and the outflow (expansion) regions.

It will be shown that the rate of ejection (wall closure rate) determines the magnitude of the pressure differences for any given geometry and that this effect is captured using the concept of a stroke-averaged pressure difference, ΔP_{stroke}. Each geometrical configuration produces a different dimensionless pressure difference curve that can be used to characterize HCM as either unobstructed or obstructed. This finding is significant, because it indicates that the pressure-flow characteristics of severe HCM are best explained by the progressive mitral valve obstruction (SAM) theory, while mild HCM is consistent with mildly restricted or unobstructed flow.

Before making comparisons between the models and *in vivo* data, results from theoretical and laboratory models will be discussed. A comparison of the unsteady models will be made first, followed by a comparison of the quasi-steady models. The quasi-steady computational model will then be compared to the unsteady models. It will be shown that the models compare reasonably well when predicting pressure loss at the constriction. However, significant differences exist downstream of the constriction, as the laboratory

models often have separation in the flow expansion region. Flow separation also exists in certain *in vivo* left ventricular flows, such as severe valvular aortic stenosis, Clark (1976a).

Finally, the effect of compliance is evaluated experimentally and shown to be insignificant in terms of the pressure difference developed during the ejection period for a progressively restricted configuration.

7.2 COMPARISON OF UNSTEADY FLOW MODELS

Three unsteady models were developed: a one-dimensional unsteady Bernoulli theoretical model with and without separation, and the unsteady flow laboratory model. The unsteady Bernoulli model was inviscid an could not predict flow separation. Instead, a sudden expansion was used to simulate a sep ration at the restriction. Results from all models were obtained for three configurations: a mild fixed restriction, a progressive restriction and a severe fixed restriction. The input positions, velocities and accelerations for the unsteady Bernoulli models were obtained from data from the unsteady flow laboratory model.

In general, the unseparated and separated (sudden expansion) unsteady Bernoulli model brackets piston to expansion pressure differences Φ_{mid} measured in the unsteady laboratory model. Φ_{mid} may be considered as a discharge coefficient; the larger the value of Φ_{mid}, the greater the pressure loss in the system. The unsteady Bernoulli model overpredicts the pressure difference between the piston and constriction region Y obtained from the unsteady laboratory model. This can be explained in part by the spatial averaging of the pressure transducers in the laboratory model (Figure 7.1). The inside diameter of the tubes used for the pressure taps was 4.5 mm. Thus the unsteady laboratory model's pressures were averaged over this distance, while the Bernoulli model gave the pressure precisely at the point of maximum constriction.
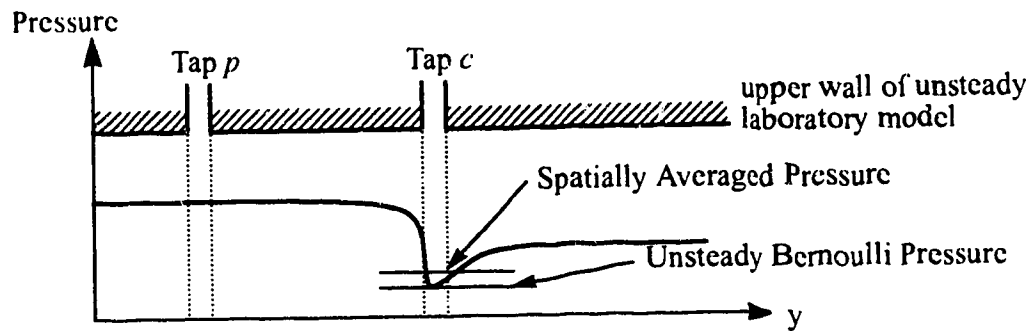
Figure 7.1: Effect of Spatial Averaging on Pressure Measurements

7.2.1 Mild Fixed Restriction Comparison

In Figure 7.2(a), the stroke normalized pressure difference Υ between the piston

region (location p) and the constriction exit (point c) is plotted as a function of per cent of

piston closure, for both the unsteady laboratory model and the unsteady Bernoulli model.

The quasi-steady Bernoulli model is also plotted for comparison. Both Bernoulli model

equations overpredict the pressure difference during the first 75% of piston closure, then

underpredict the pressure difference for the remaining 25% of piston closure. Since the

Bernoulli models were inviscid, one would expect that the pressure difference would be

underpredicted to some degree at all times.

The source of the deviation between the Bernoulli models and the unsteady

laboratory model cannot be caused by the unsteady inertial acceleration terms, because the

quasi-steady Bernoulli model did not include these and yet showed the same

overprediction. The restriction factor also cannot be responsible, because incorrect

matching would consistently over or underpredict the pressure difference throughout the

entire ejection. This leaves several possibilities:

- the piston wall velocities derived from piston position data were in error;
- the unsteady laboratory model had a significant amount of blow-by in the piston
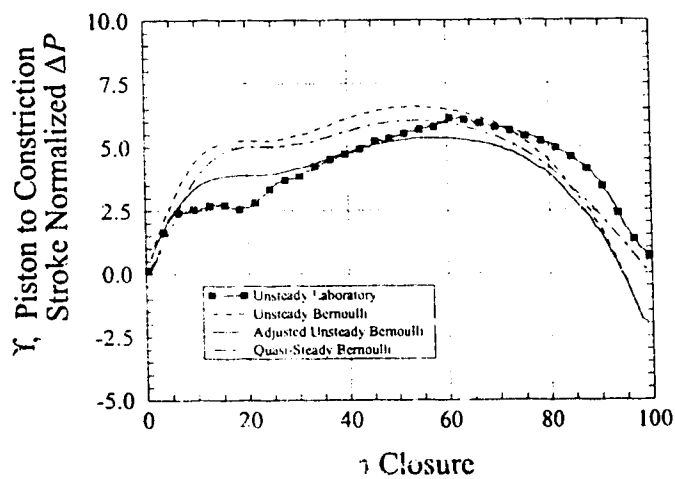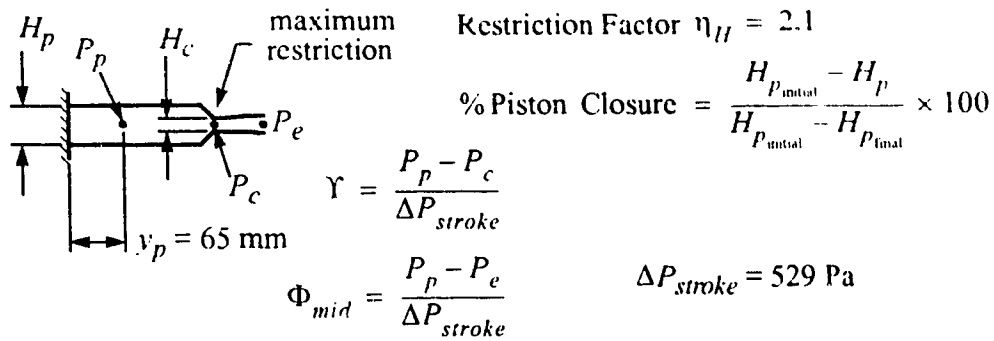
Restriction Factor $\eta_{ff} = 2.1$

$$\% \text{ Piston Closure} = \frac{H_{p_{initial}} - H_p}{H_{p_{initial}} - H_{p_{final}}} \times 100$$

$$\Upsilon = \frac{P_p - P_c}{\Delta P_{stroke}}$$

$$\Phi_{mid} = \frac{P_p - P_e}{\Delta P_{stroke}}$$

$$y_p = 65 \text{ mm}$$

$$\Delta P_{stroke} = 529 \text{ Pa}$$

Note: only every fifth symbol plotted for the unsteady laboratory model for clarity

(a) Normali‍   ‍triction Exit Pressure Difference
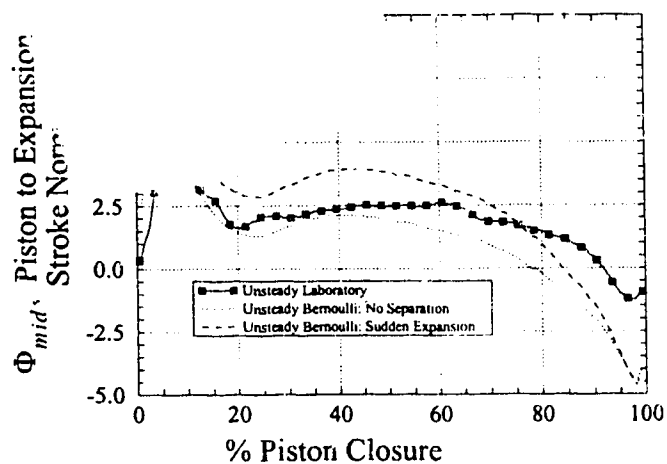
Note: only every fifth symbol plotted for the unsteady laboratory model for clarity

(b) Normalized Piston to Expansion Exit Pressure Difference

Figure 7.2: Comparison of Normalized Pressure for Mild Fixed Restriction Model

region:

- the pressure taps used in the unsteady laboratory model spatially averaged the
  pressures in the region of interest.

Each of these will be discussed in turn. The piston wall velocities were determined by differentiating measured displacements. This data contained a significant amount of noise and required smoothing, as discussed in Section 3.4.1. To examine the effect of the smoothing on the resulting pressures, three test cases were run: 20 point smoothing, 40 point smoothing (the normal amount used) and 60 point smoothing. For example, 40 points gives smoothing over a time period of 0.056 second, about 10% of the piston stroke for the fast closure rates). The resulting normalized pressure differences did not vary significantly. Thus errors introduced in smoothing the wall velocity are not the source of the problem.

While smoothing the data seemed acceptable, differentiating the experimental data could be introducing considerable inaccuracies. In Figure 7.2(b), the stroke normalized pressure difference between the piston (location p) and the expansion exit (location e) is shown for the mild fixed restriction. Both the unsteady laboratory model and the unsteady Bernouiii model with and without the sudden expansion are shown. The unsteady laboratory model pressure difference falls between the two extremes of the unsteady Bernoulli model. The unsteady Bernoulli model with and without separation overpredicts the effect of the deceleration, giving negative pressure differences from 86% and 78% of piston closure onwards, compared to 91% for the unsteady laboratory model. This could be due to errors incorporated by taking the second derivative of the smoothed piston position data (differentiating the piston position twice gives the acceleration).

The possibility of fluid leakage across the piston seals in the piston region is difficult to estimate. Due to the difficulty of making linear seals for rectangular pistons, there was some minor clearance possible between the seals and the model walls. If there

were a gap all around the piston of 0.5 mm, this would account for about 2% of the piston face area. The loss resulting loss of fluid and pressure is difficult to estimate, but could easily account for the deviation between the unsteady and quasi-steady Bernoulli models and the unsteady flow laboratory model.

The inside diameter of the tubes used for the pressure taps was 4.5 mm. Thus the unsteady laboratory model's pressures were measured over this distance, while the Bernoulli model gave the pressure precisely at the point of maximum constriction, as illustrated in Figure 7.1. To account for the spatial averaging in the unsteady laboratory model, a square equivalent in area to the pressure tap inside diameter was used. This weights the spatial averaging more towards the centre of the pressure tap. A spatial average is taken over a distance of 4 mm. This spatially averaged Bernoulli model pressure is plotted in Figure 7.2(a) and is labeled "Adjusted Unsteady Bernoulli" (all subsequent plots of the Bernoulli model pressure differences are adjusted for this effect). While spatial averaging has improved things, the spatially averaged pressure still overpredicts the pressure difference during the first 40% of piston closure, but then underpredicts the pressure difference during the final 50% of piston closure. This cross-over from overprediction to underprediction of the pressure difference is not consistent with spatial averaging but could be explained by the fluid leakage theory. Thus the total deviation may be explained by a combination of spatial averaging and fluid leakage.

7.2.2 Pressure Differences for the Severe Fixed Restriction

The stroke normalized pressure difference between the piston region (location p) and the point of maximum constriction (point c) is shown in Figure 7.3(a) for the severe fixed restriction configuration. It is immediately obvious that the unsteady Bernoulli model overpredicts the pressure difference occurring in the unsteady laboratory model. The pressure averaging mentioned in 7.2.1 works well for the mild restriction, but does
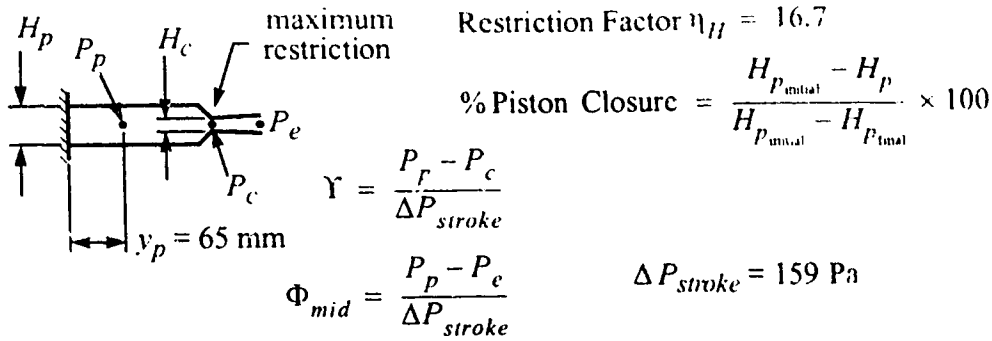
H_p P_p H_c maximum restriction

Restriction Factor $\eta_{H} = 16.7$

% Piston Closure $= \dfrac{H_{P_{initial}} - H_P}{H_{P_{initial}} - H_{P_{final}}} \times 100$

P_e

P_c

$\Upsilon = \dfrac{P_r - P_c}{\Delta P_{stroke}}$

$y_p = 65$ mm

$\Phi_{mid} = \dfrac{P_p - P_e}{\Delta P_{stroke}}$

$\Delta P_{stroke} = 159$ Pa

Note: only every fifth symbol plotted for the unsteady laboratory model for clarity
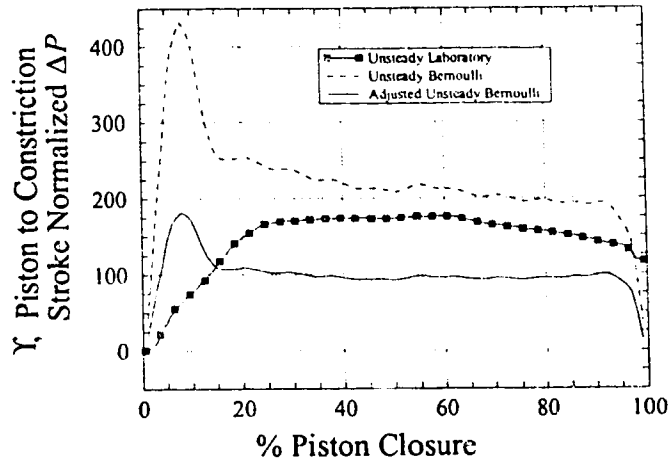
(a) Normalized Piston to Constriction Exit Pressure Difference

Note: only every fifth symbol plotted for the unsteady laboratory model for clarity
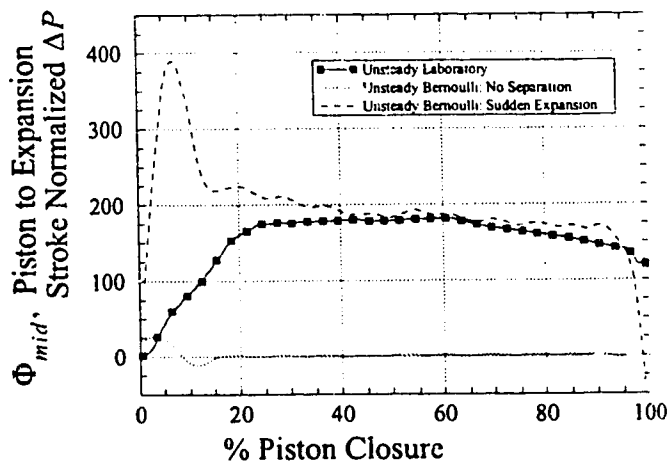
(b) Normalized Piston to Expansion Exit Pressure Difference

Figure 7.3: Comparison of Normalized Pressures for Severe Fixed Restriction Model

not help in the case of the severe fixed restriction. The spatial average of the pressure reduce; the pressure difference more than is desired for the deviation for piston closures from 0% onwards. While a lesser degree of pressure spatial averaging may give better results, there is something very different happening during the initial 20% of piston closure. Once again, unsteady inertial acceleration cannot be the cause, as the quasi-steady Bernoulli analysis gave the same result as the unsteady Bernoulli analysis.

The source of the calculated high initial pressure most likely due to errors in the velocity determined from the experimental data. The velocity was determined by differentiating the measured piston position with time. Only one of the pistons had its position measured; it was assumed that the other (off-side) piston would move simultaneously at the same rate, as the two pistons were physically linked together. However, through repeated use of the model, a small amount of play developed in the linkage. As the severe fixed restriction tests were conducted last, the results for these tests were the most affected. This linkage play allowed the off-side piston to remain stationary while the measured piston began to move. While this slack allowed the off-side piston to remain motionless for less than 2 or 3 mm of travel of the measured piston, this was quite significant in terms of the piston velocities calculated. The piston velocity will be overpredicted by a factor of two, which in turn causes the fluid velocity at the point of maximum constriction to be overpredicted by a factor of two. As pressure varies with the square of the velocity, the pressure will then be overpredicted by a factor of four. Comparisons between the two models should not be made during the first 15% of piston closure. It should be noted that this effect was not a significant problem with the other configurations (mild and progressive restrictions) as the restriction at this point of the ejection was still small, thus minimizing the error in the pressure, and the linkage system was also tighter during these tests.

In Figure 7.3(b), the stroke normalized pressure difference between the piston region (location p) and the expansion exit (location e) is shown for the unsteady laboratory model, as well as the unsteady Bernoulli model with and without the sudden expansion. Once again, comparisons should not be made for the first 20% of piston closure due to inaccuracies in determining the piston velocity. As with the mild fixed restriction, the unsteady laboratory model pressure difference falls between the two extremes of the unsteady Bernoulli model. In this case, the unsteady laboratory model has a pressure difference much closer to the unsteady Bernoulli model with the sudden expansion. This is consistent with the separation evident for the severe fixed restriction configuration of the unsteady laboratory model.

7.2.3 Progressive Restriction Comparison

The stroke normalized pressure difference between the piston region (location p) and the point of maximum constriction (point c) is shown in 7.4(a) for the progressive restriction configuration. The Bernoulli model pressure difference peaks sooner than the laboratory model. This may be caused by slight inaccuracies in calculating the constriction area with time. The unsteady Bernoulli model related the constriction motion directly to the piston motion. The unsteady laboratory model had the piston and constriction linked together directly, but the tolerances in the linkages may have resulted in minor differences from the theoretical degree of constriction.

In Figure 7.4(b), the stroke normalized pressure difference between the piston region (location p) and the expansion exit (location e) is shown for the progressive restriction. Results are plotted for the unsteady laboratory model, as well as the unsteady Bernoulli model with and without the sudden expansion. This case is quite interesting. The unsteady laboratory model and unsteady Bernoulli model without separation match reasonably well for the first 60% of piston closure. At this point, the pressure difference in
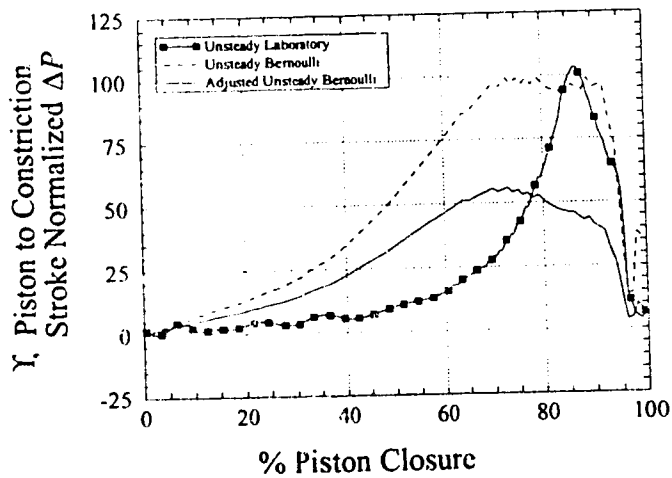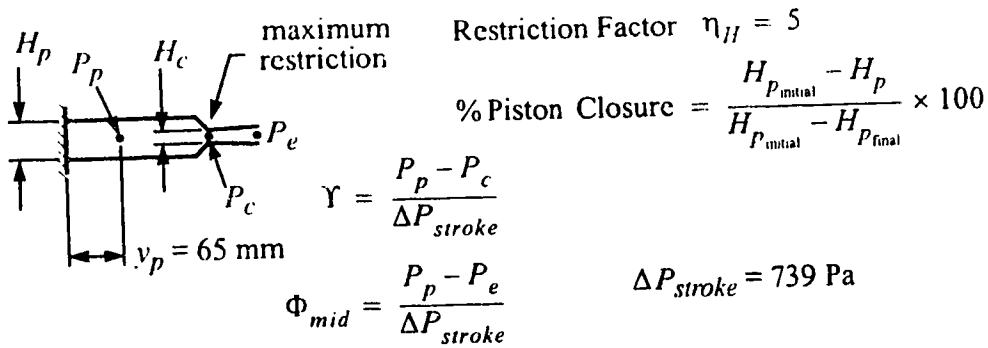
H_p P_p H_c maximum restriction   Restriction Factor $\eta_{II} = 5$

$\%\text{ Piston Closure} = \dfrac{H_{P_{initial}} - H_p}{H_{P_{initial}} - H_{P_{final}}} \times 100$

P_e

P_c $\Upsilon = \dfrac{P_p - P_c}{\Delta P_{stroke}}$

$y_p = 65\text{ mm}$

$\Phi_{mid} = \dfrac{P_p - P_e}{\Delta P_{stroke}}$ $\Delta P_{stroke} = 739\text{ Pa}$

Note: only every fifth symbol plotted for the unsteady laboratory model for clarity

(a) Normalized Piston to Constriction Exit Pressure Difference
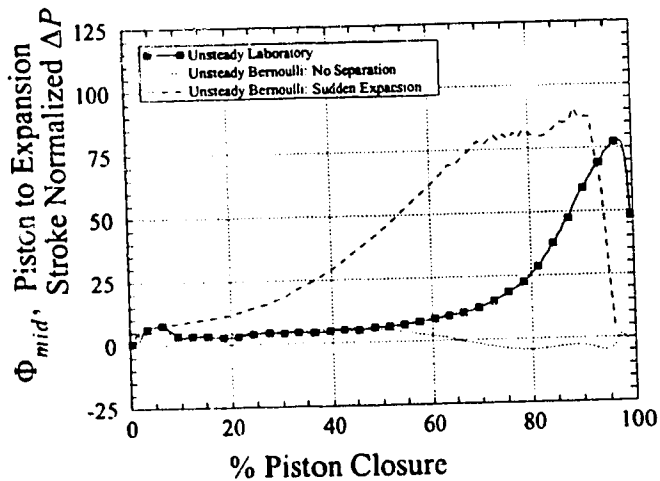
Note: only every fifth symbol plotted for the unsteady laboratory model for clarity

(b) Normalized Piston to Expansion Exit Pressure Difference

Figure 7.4: Comparison of Normalized Pressures for Progressive Restriction Model

the unsteady laboratory model rises sharply, becoming much closer to the prediction of the unsteady Bernoulli model with separation. This suggests that the flow in the expansion region of the unsteady laboratory model separates at this point.

7.3 COMPARISON OF QUASI-STEADY FLOW MODELS

The commercial computational code was used to analyze the progressive restriction configuration, both for turbulent and laminar flows. The stroke normalized pressure differences between the piston region (location p) and the point of maximum constriction (point c) is shown in Figure 7.5(a) for both computational models, along with results from the quasi-steady Bernoulli model. All three models predict similar pressure differences, with the turbulent flow model predicting somewhat higher pressure losses than the laminar flow model.

In Figure 7.5(b), the stroke normalized pressure difference between the piston region (location p) and the expansion exit (location e) is shown for both the turbulent and laminar flow computational models, as well as the unsteady Bernoulli model with and without the sudden expansion. One must be careful making comparisons for the laminar flow computational model, as convergence could not be achieved for piston closures between 35% and 85%. It is clear that the turbulent flow computational solution predicts a significantly greater pressure difference than the unsteady Bernoulli model without separation, but much less than the unsteady Bernoulli model with separation. As no flow separation occurred in this computational solution, the pressure loss must be due to the significantly different velocity profiles (see Figure 4.17). The turbulent flow computational solution has a downstream velocity profile which is quite parabolic, unlike the one-dimensional Bernoulli model's assumption of constant cross-stream velocity. This pressure difference becomes more significant as the degree of restriction increases, but falls off as the piston velocity decreases in the latter part of the flow cycle.

Restriction Factor $\eta_{H} = 5$

$$\% \text{Piston Closure} = \frac{H_{P_{initial}} - H_p}{H_{P_{initial}} - H_{P_{final}}} \times 100$$

maximum restriction

$$\Upsilon = \frac{P_p - P_c}{\Delta P_{stroke}}$$

$$\Phi_{mid} = \frac{P_p - P_e}{\Delta P_{stroke}}$$

$$\Delta P_{stroke} = 739 \text{ Pa}$$

$v_p = 65$ mm

——— Computational: Turbulent
············ Computational: Laminar
- - - - - Quasi-Steady Bernoulli

Υ, Piston to Constriction Stroke Normalized ΔP

% Piston Closure

(a) Normalized Piston to Constriction Exit Pressure Difference

——— Computational: Turbulent
············ Computational: Laminar
- - - - - Quasi-Steady Bernoulli (no separation)
— - — - — Quasi-Steady Bernoulli (sudden expansion)

Φ_{mid}, Piston to Expansion Stroke Normalized ΔP

% Piston Closure

(b) Normalized Piston to Expansion Exit Pressure Difference

Figure 7.5: Quasi-Steady Model Comparison Progressive Restriction Configuration

The commercial computational fluid dynamics code FLOW3D was also used to

compare with the quasi-steady laboratory model at restriction factors of $\eta_h = 4.5$ and

$\eta_h = 16.7$. The turbulent computational model was used for this comparison, and the

results are summarized in Table 7.1. As is evident, FLOW3D does reasonably well at

predicting the experimental pressure differences. The quasi-steady Bernoulli model was

also compared, and as Table 7.1 shows, it gave a poor estimate for the normalized pressure

loss. The piston to constriction pressure loss Φ_{mid} is reasonably close to the laboratory

model for the severe restriction $\eta_h = 16.7$, but very poor for the mild restriction

$\eta_h = 4.5$. This may indicate that the pressure loss for the severe constriction between the

piston and constriction region is primarily spatial in nature. The quasi-steady Bernoulli

Table 7.1 Quasi-Steady Laboratory and Computational Model Comparison

Flow Rate = 1 l/s	$\eta_h = 4.5$		$\eta_h = 16.7$	
	Φ_{mid}	Υ	Φ_{mid}	Υ
Laboratory Model	22.6	8.0	128	50.6
FLOW3D Turbulent	21.3	6.7	189	53.3
Quasi-Steady Bernoulli	13.6	0.9	117	0.5
All pressures normalized by $1/2(\rho V_e^2) = 75.1$ Pa				

model severely underpredicts the pressure loss between the piston region and expansion

exit Υ for both restrictions. The cause of this may be attributed to flow separation and

cross-stream velocity profile differences.

7.4 COMPARISON OF QUASI-STEADY COMPUTATIONAL MODEL WITH UNSTEADY LABORATORY MODEL

The stroke normalized pressure differences for the computational turbulent and

laminar flow models are shown along with the unsteady laboratory model pressure

differences in Figure 7.6. The pressure difference between the piston region (point p) and
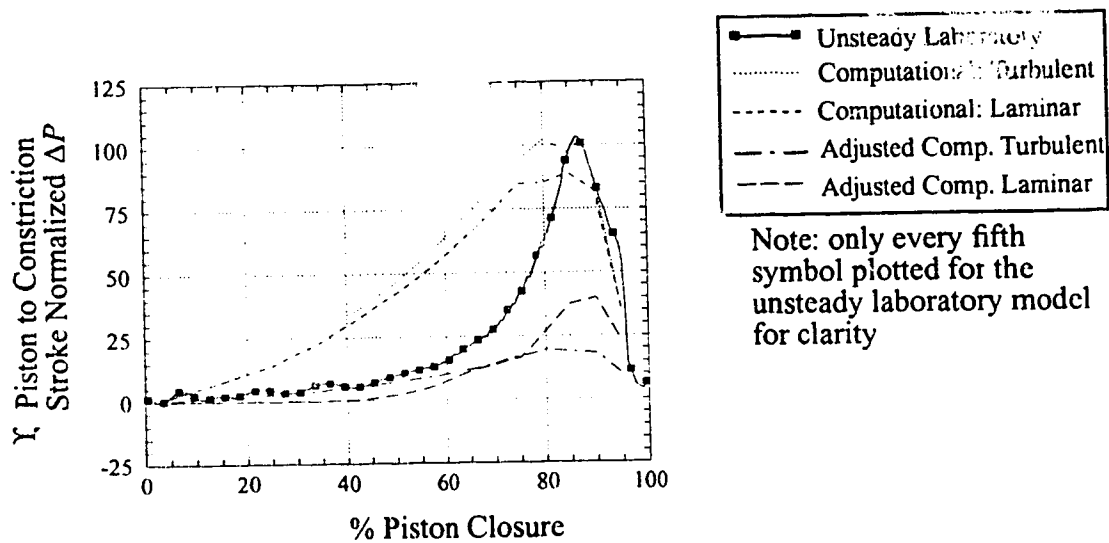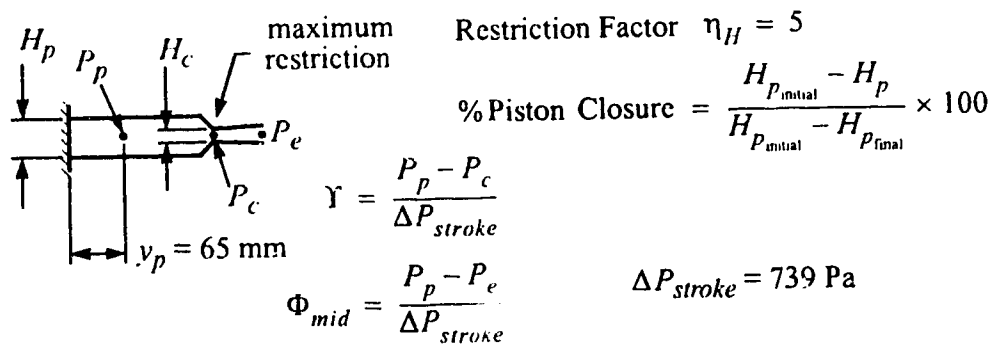
$$\text{Restriction Factor } \eta_H = 5$$

$$\%\,\text{Piston Closure} = \frac{H_{p_{initial}} - H_p}{H_{p_{initial}} - H_{p_{final}}} \times 100$$

$$\Upsilon = \frac{P_p - P_c}{\Delta P_{stroke}}$$

$$v_p = 65 \text{ mm}$$

$$\Phi_{mid} = \frac{P_p - P_e}{\Delta P_{stroke}}$$

$$\Delta P_{stroke} = 739 \text{ Pa}$$

Unsteady Laboratory
Computational: Turbulent
Computational: Laminar
Adjusted Comp. Turbulent
Adjusted Comp. Laminar

Note: only every fifth symbol plotted for the unsteady laboratory model for clarity

(a) Normalized Piston to Constriction Exit Pressure Difference

Unsteady Laboratory
Computational: Turbulent
Computational: Laminar

Note: only every fifth symbol plotted for the unsteady laboratory model for clarity
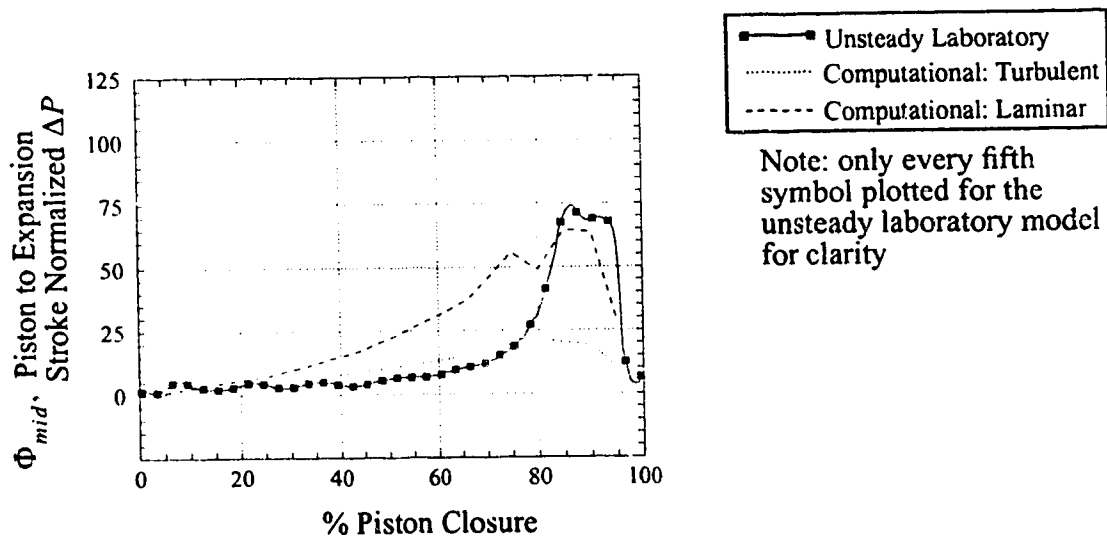
(b) Normalized Piston to Expansion Exit Pressure Difference

Figure 7.6: Computational Solutions Compared to Unsteady Laboratory Model (progressive restriction configuration)

the maximum constriction (point c) is shown in (a), and between the piston region and the expansion exit (point e) in (b). The two-dimensional FLOW3D calculations appear to overpredict the pressure loss at the constriction, but as with the Bernoulli model this may be a pressure averaging problem. When the average pressure over the pressure tap region is used, the commercial code matches much better during the first 80% of piston closure, but fails to predict the peak pressure loss at 85%.

The downstream pressure loss, $P_p - P_e$, shown in Figure 7.6(b) is quite interesting. The FLOW3D turbulent computational solution does a much better job predicting the pressure loss for the first 75% of piston closure. When the unsteady laboratory model flow separates around 80% of piston closure, the laminar solution which had separation does a much better job of predicting the pressure loss. Recall that the laminar solution was unconverged for piston closures between 55% and 85%, so one must avoid putting too much weight on these results.

7.5 EFFECT OF WALL CLOSURE RATE

It has been shown with HCM patients who have little or no pressure difference (P_p $-P_e$) when resting that a pressure difference occurs when systole is provoked, see Grose, Maskin, Spindola-Franco & Yipintsoi (1981). In other words, if the ejection occurs more vigorously over a shorter period of time, the resulting pressure difference between the left ventricle and aorta becomes higher in patients with a resting gradient, and noticeable in patients with no resting gradient. This observation was confirmed by the unsteady laboratory model: if the closure (ejection) rate was increased, the resulting pressure differences between the piston and points downstream also increased.

The "non-obstructionists" argue that this increase in the left ventricular-to-aortic pressure difference is purely an inertial effect: accelerate the fluid at a higher rate and the

time dependant inertial forces will increase. This argument is then extended to all cases of HCM, by the hypothesis that the larger pressure gradients in severe HCM is due to inertial effects alone. The "obstructionists" suggest that the faster contraction results in higher velocities through the progressive obstruction; the increase in the pressure difference is caused by increased viscous forces as well as the inertial forces. This debate is really one of geometry: unobstructed vs. progressively obstructed. If the pressure curves are properly non-dimensionalized using a parameter that accounts for the rate of ejection, the resulting pressure curves for a particular left ventricular anatomy at different rates of ejection should be similar. It will be shown that the previously derived stroke pressure difference is a reasonable choice for non-dimensionalizing the pressure differences for both the unsteady laboratory model and an *in vivo* HCM case.

It should be pointed out that most cardiologists still plot the *in vivo* pressure relationships in terms of pressure at a single point (rather than the difference between left ventricle and aorta) as a function of time. This is unfortunate, because it tends to obscure the important aspects of the ejection pressure differences. Presenting the data in terms of a dimensionless pressure difference as a function of the percentage of fluid ejected gives a more consistent result. Differences between mild HCM, severe HCM and severe aortic valvular stenosis cases become readily apparent when presented in this manner.

7.5.1 Non-Dimensional Unsteady Laboratory Model Pressure Differences

In Section 3.4.1, the stroke pressure difference was used to arrive at a non-dimensional pressure difference. Recall that the stroke pressure difference was defined in equation 3.22 as

$$\Delta P_{stroke} = \frac{\rho V_{stroke}^2}{2}$$

where

$$V_{stroke} = \frac{(90\% \text{ of stroke volume})}{(\text{exit area}) (\text{time for } 90\% \text{ of volume ejected})}$$

If ΔP_{stroke} is used to normalize the pressure differences in the unsteady laboratory model, stroke normalized pressure differences for different closure rates become very similar. This is shown in Figures 7.7, 7.8 and 7.9. In each figure, three different closure rates are shown: slow, moderate and fast. For a 300% change in closure rate, the stroke normalized pressure differences show only about a 20% variation for each of the three geometrical configurations. This indicates that the stroke pressure is a suitable normalizing parameter for the unsteady laboratory model. Unsteady inertial effects are removed when the pressure differences are normalized in this manner; pressure differences caused by a restriction or flow separation then remain and are easily discernible.

7.5.2 Non-Dimensional *In Vivo* Pressure Differences

There is little published data showing simultaneous stroke volume, left ventricular pressure, and aortic or left ventricular outflow tract (LVOT) pressure. While the pressures are often available, it is the stroke volume that is difficult to quantify. Techniques do exist to estimate the stroke volume, such as the frame by frame cine angiocardiogram methods developed by Kaser and Kennedy (1969) and Kennedy, Trenholme and Kaser (1970). An alternative to measuring the stroke volume would be to measure aortic flow rate or velocity directly. Electromagnetic flow velocity probes are commercially available for medical applications and may be mounted in a catheter to make aortic flow velocity measurements. These probes have been evaluated by Murgo and Millar (1972), Millar and Baker (1973), and Nichols, Pepine, Conti, Christie and Feldman (1980). If the aortic flow velocity is measured directly, the calculation of V_{stroke} based on ejection time, stroke volume and exit area (equation 7.2) is avoided; V_{stroke} is the average aortic flow velocity.

Murgo *et al* (1980) used a multi-sensor catheter equipped with two solid state
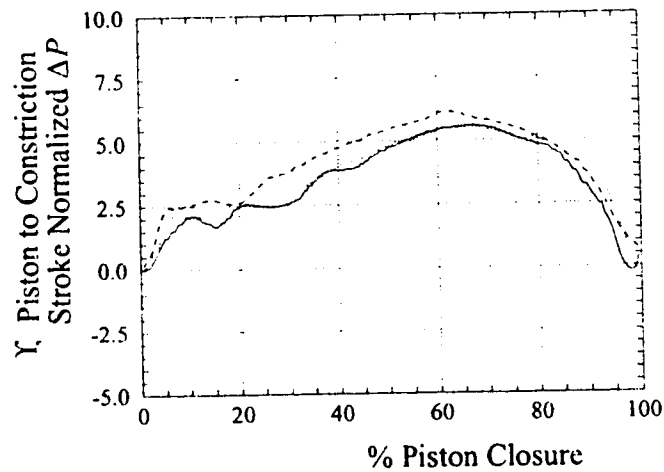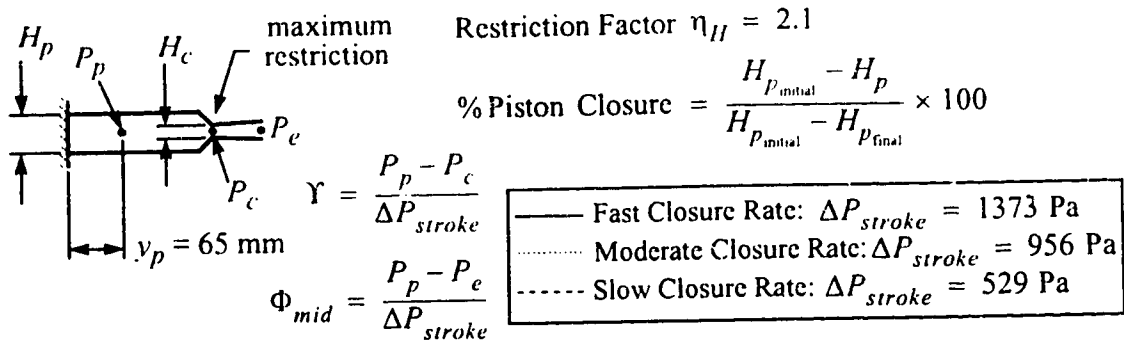
maximum restriction

Restriction Factor $\eta_{II} = 2.1$

$$\% \, \text{Piston Closure} = \frac{H_{p_{initial}} - H_p}{H_{p_{initial}} - H_{p_{final}}} \times 100$$

$$\Upsilon = \frac{P_p - P_c}{\Delta P_{stroke}}$$

$y_p = 65 \, \text{mm}$

$$\Phi_{mid} = \frac{P_p - P_e}{\Delta P_{stroke}}$$

——— Fast Closure Rate: $\Delta P_{stroke} = 1373 \, \text{Pa}$
············· Moderate Closure Rate: $\Delta P_{stroke} = 956 \, \text{Pa}$
- - - - - Slow Closure Rate: $\Delta P_{stroke} = 529 \, \text{Pa}$

(a) Normalized Piston to Constriction Exit Pressure Difference
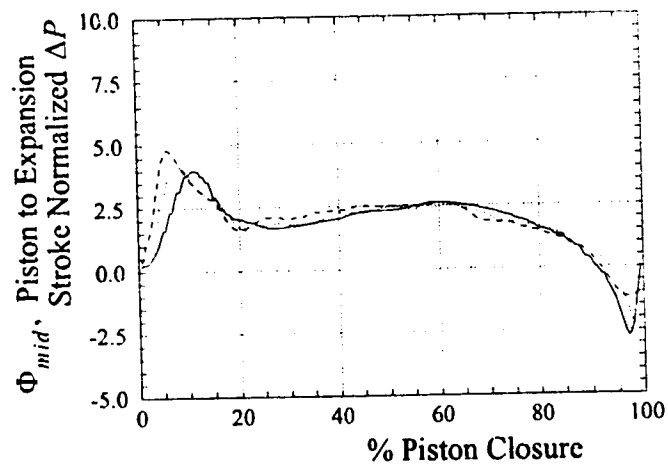
(b) Normalized Piston to Expansion Exit Pressure Difference

Figure 7.7: Removing the Effect of Wall Closure Rate by Normalization of Pressure Differences With the Stroke Pressure: Mild Fixed Restriction (unsteady laboratory model)

H_p P_p H_c maximum restriction   Restriction Factor η_{H} = 16.7

P_e

%Piston Closure $= \dfrac{H_{P_{initial}} - H_p}{H_{P_{initial}} - H_{P_{final}}} \times 100$

P_c

$\Upsilon = \dfrac{P_p - P_c}{\Delta P_{stroke}}$

y_p = 65 mm

$\Phi_{mid} = \dfrac{P_p - P_e}{\Delta P_{stroke}}$

——— Fast Closure Rate: ΔP_{stroke} = 479 Pa
·········· Moderate Closure Rate: ΔP_{stroke} = 281 Pa
- - - - - Slow Closure Rate: ΔP_{stroke} = 159 Pa

(a) Normalized Piston to Constriction Exit Pressure Difference
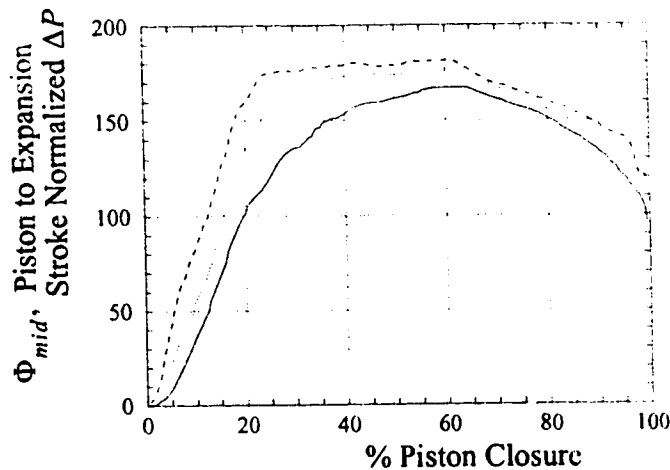
(b) Normalized Piston to Expansion Exit Pressure Difference

Figure 7.8: Removing the Effect of Wall Closure Rate by Normalization of Pressure Differences With the Stroke Pressure: Severe Fixed Restriction (unsteady laboratory model)
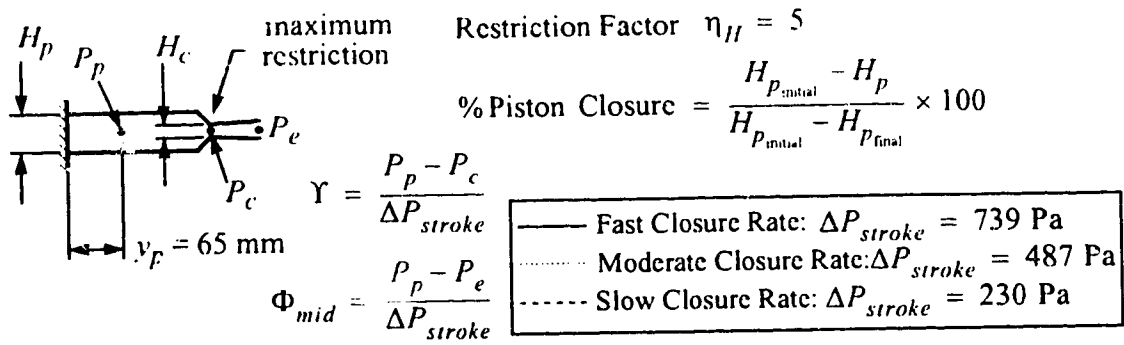
H_p P_p H_c maximum restriction

Restriction Factor $\eta_{II} = 5$

$$\% \text{Piston Closure} = \frac{H_{p_{initial}} - H_p}{H_{p_{initial}} - H_{p_{final}}} \times 100$$

$v_c = 65$ mm

$$\Upsilon = \frac{P_p - P_c}{\Delta P_{stroke}}$$

$$\Phi_{mid} = \frac{P_p - P_e}{\Delta P_{stroke}}$$

—— Fast Closure Rate: $\Delta P_{stroke} = 739$ Pa
········ Moderate Closure Rate: $\Delta P_{stroke} = 487$ Pa
----- Slow Closure Rate: $\Delta P_{stroke} = 230$ Pa

(a) Normalized Piston to Constriction Exit Pressure Difference
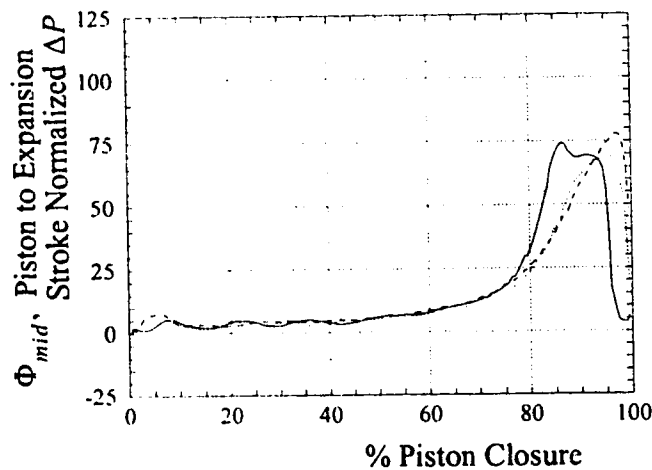
(b) Normalized Piston to Expansion Exit Pressure Difference

Figure 7.9: Removing the Effect of Wall Closure Rate by Normalization of Pressure Differences With the Stroke Pressure: Progressively Restricted (unsteady laboratory model)

pressure sensors and an electromagnetic aortic flow velocity probe to make measurements *in vivo* in HCM and normal patients. This allowed simultaneous measurement of left ventricular and aortic pressures along with the aortic flow velocity. One of the patients analyzed was an HCM case with a minor resting apical left ventricular - left ventricular outflow tract pressure difference of 900 Pa (mild HCM). The pressure and velocity curves were plotted for a resting heartbeat and a heartbeat following a premature ventricular contraction (post-PVC). A post-PVC ejection is usually more vigorous, ejecting the fluid in a shorter period of time. In this case, the post-PVC ejection occurred in approximately 30% less time but ejected about 7% less blood. The apical left ventricular - left ventricular outflow tract pressure difference rose to 1260 Pa.

The stroke normalized pressure difference for Φ_{mid} for the mild HCM patient is plotted in Figure 7.10. The non-dimensional post-PVC pressure difference does not match the corresponding resting pressure difference as well as anticipated: the post-PVC values range from 5 to 50% lower than the resting values. This may be due in part to experimental error, as only single pressure-volume curves were used. However, as will be seen in the following section when compared with patients experiencing severe HCM, the magnitude and shape of the normalized pressure difference curve is significantly different.

7.6 EFFECT OF EXIT CONFIGURATION

The role of the hypertrophy involved in HCM has been the source of much controversy: is there an obstruction or not? Does an obstruction play a crucial role in the intraventricular pressure differences or are the differences inertial in character? Through the use of the mildly restricted (unobstructed theory) and progressively restricted (SAM theory) models, it will be shown that

- mild HCM pressure differences are inertially dominated;
- severe HCM pressure differences exhibit a progressively restricted behavior.

$$\% \text{ Ejection } = \frac{\text{Volume of Blood Ejected}}{\text{Total Stroke Volume}} \times 100$$

$$\Phi_{mid} = \frac{P_{\text{Left Ventricle}} - P_{\text{Aorta}}}{\Delta P_{stroke}}$$

•········• Fast Closure Rate: $\Delta P_{stroke} = 703$ Pa

▪——▪ Slow Closure Rate: $\Delta P_{stroke} = 298$ Pa
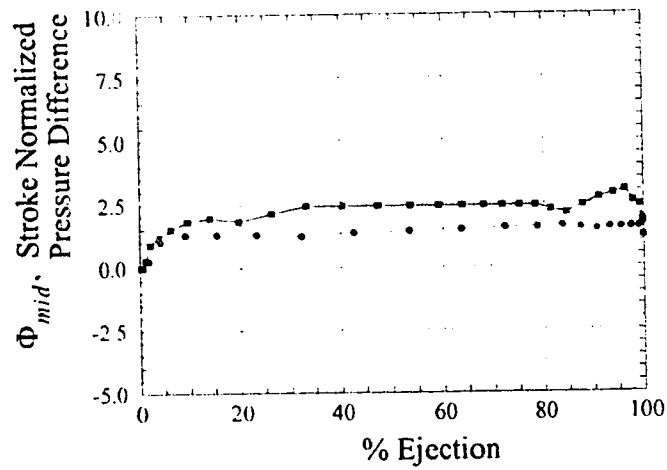
Figure 7.10: *In Vivo* **Mild HCM: Resting and Provoked Ejection. Data from Murgo** *et al* **(1980).**

The different configurations of mild HCM, progressively restricted HCM and severe aortic valvular stenosis will be shown to give distinctly different non-dimensional pressure difference curves, both for the *in vivo* situation and the unsteady laboratory model.

The stroke normalized pressure differences generated by each of the three configurations in the unsteady laboratory model are shown in Figure 7.11. It is clear that each configuration gives a decidedly different curve. The pressure difference caused by the severe restriction (aortic valvular stenosis) is the largest, exceeding Φ_{mid} of 150. This curve rises sharply during the first 30% of piston closure (ejection), peaks around 60% and falls sharply at the end of the ejection period.

The mildly restricted case is capable of generating only small pressure differences and has a significantly different pressure difference curve shape (refer also to Figure 7.5(b)). There is a sudden initial rise in the pressure difference curve, which then falls and levels off throughout much of the ejection at Φ_{mid} of about 2. During the final 20% of the ejection period, the pressure difference falls rapidly and becomes negative before returning to zero.

The progressive restriction shows a very different characteristic curve. The pressure difference remains fairly low throughout the first 60% of the ejection, then rises to a peak value of Φ_{mid} of 75 between 85% and 95% of the ejection. This late pressure rise is due to the restriction becoming increasingly severe.

The corresponding *in vivo* configurations are plotted in Figure 7.12. The severe aortic valvular stenosis (a severe restriction caused by an abnormal aortic valve) values were determined using the data of Clark and Shultz (1973), who measured left ventricular and aortic pressure, and used a catheter mounted thin film velocity probe to measure the aortic velocity. The severe and mild HCM values were determined from the data of Murgo
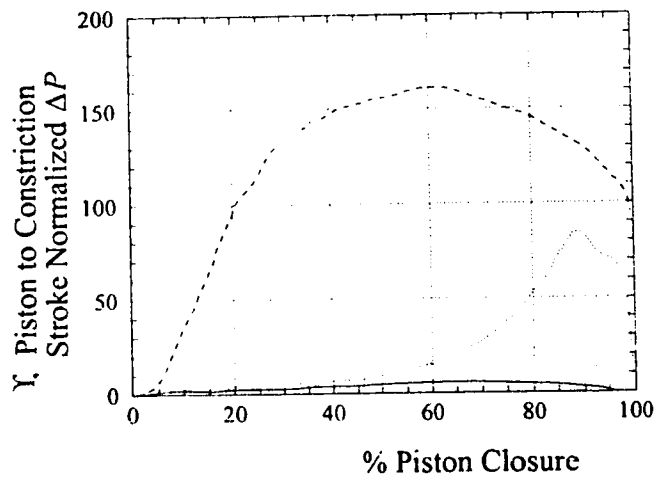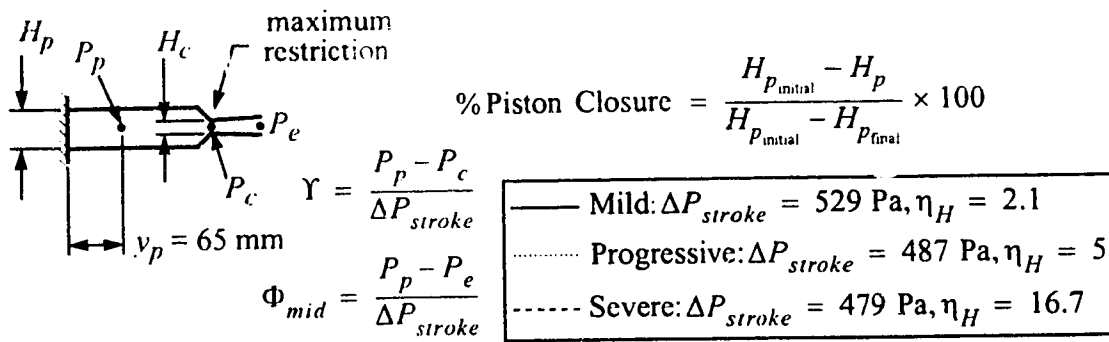
maximum
restriction

$$\%\text{Piston Closure} = \frac{H_{P_{initial}} - H_p}{H_{P_{initial}} - H_{P_{final}}} \times 100$$

H_p P_p H_c

P_e

P_c

$$\Upsilon = \frac{P_p - P_c}{\Delta P_{stroke}}$$

$v_p = 65$ mm

$$\Phi_{mid} = \frac{P_p - P_e}{\Delta P_{stroke}}$$

—— Mild: $\Delta P_{stroke} = 529$ Pa, $\eta_H = 2.1$	
·········· Progressive: $\Delta P_{stroke} = 487$ Pa, $\eta_H = 5$	
- - - - Severe: $\Delta P_{stroke} = 479$ Pa, $\eta_H = 16.7$	

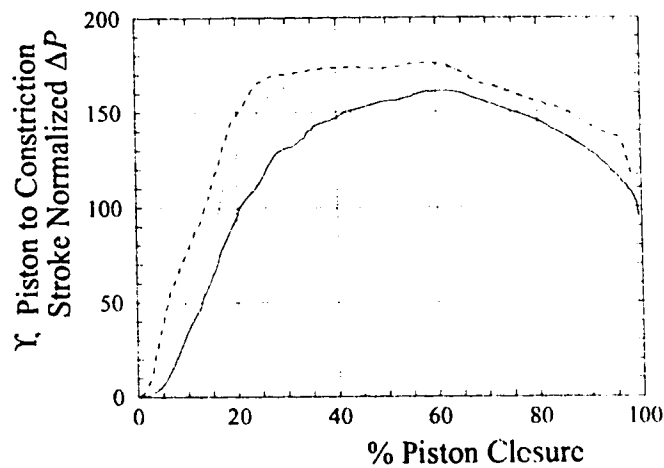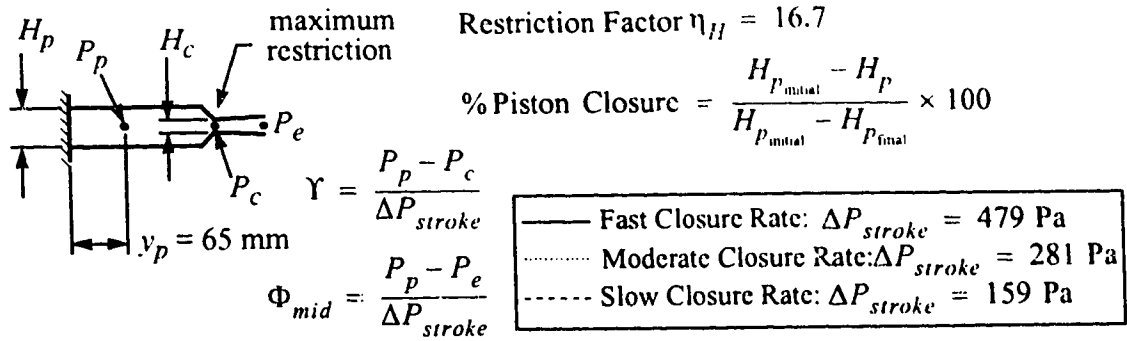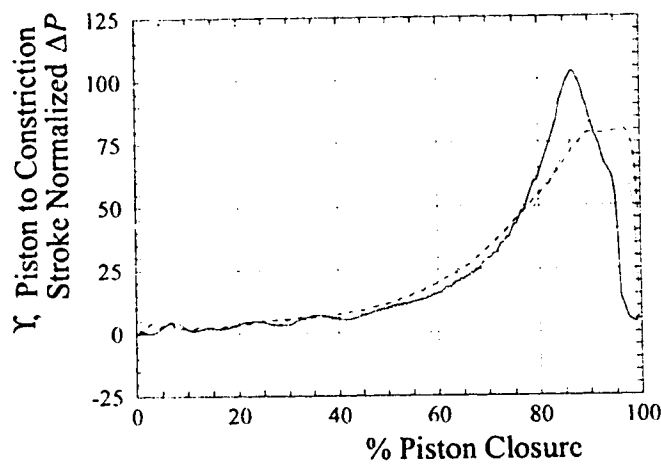(a) Normalized Piston to Constriction Exit Pressure Difference
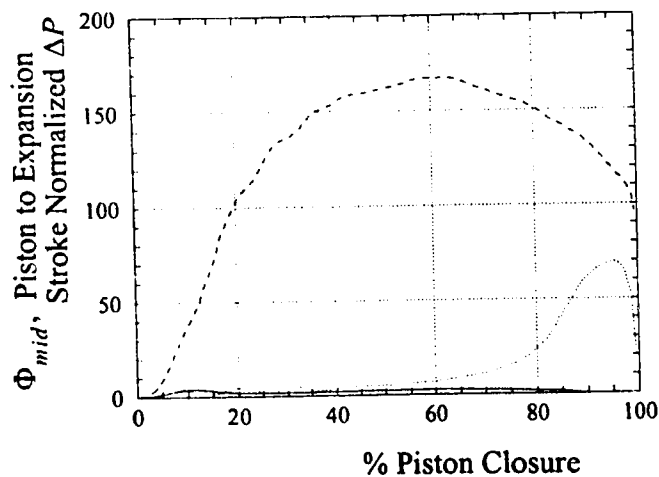
(b) Normalized Piston to Expansion Exit Pressure Difference
Figure 7.11: Comparison of Normalized Pressures for Unsteady Laboratory Model
for Different Geometric Configurations

$$\% \text{Ejection} = \frac{\text{Volume of Blood Ejected}}{\text{Total Stroke Volume}} \times 100$$

$$\Phi_{mid} = \frac{P_{\text{Left Ventricle}} - P_{\text{Aorta}}}{\Delta P_{stroke}}$$

▪——▪	Normal: $\Delta P_{stroke} = 203$ Pa
x········x	Mild HCM: $\Delta P_{stroke} = 298$ Pa
●---●	Severe HCM: $\Delta P_{stroke} = 358$ Pa
▲—·—▲	Severe Aortic Valvular Stenosis: $\Delta P_{stroke} = 267$ Pa

Figure 7.12: *In Vivo* **Ejection Comparison**
Normal, mild HCM and severe HCM based on data from Murgo, Alter, Dorethy, Altobelli, & M'Granahan (1980); Severe aortic valvular stenosis based on data from Clark (1976)

et al (1980).

As with the unsteady laboratory model, the *in vivo* configurations produce characteristic shapes for their pressure difference curves. The pressure difference caused by the severe aortic valvular stenosis is the largest, reaching nearly Φ_{mid} = 250. This curve rises sharply during the first 40% of ejection, peaks around 65% and falls sharply at the end of the ejection period. The shape of this curve is very similar to that obtained from the unsteady laboratory model.

The mild HCM pressure difference curve shows only a small pressure difference, maintaining Φ_{mid} of about 1.5 throughout much of the ejection. The shape of this curve most closely resembles the mildly restricted configuration of the unsteady laboratory model.

The severe HCM pressure difference curve slowly rises during the ejection period, reaching a peak value of Φ_{mid} of 22 when 90% of the fluid has been ejected. It will be shown in the next section that this shape is similar to the progressively restricted case if flow separation does not occur.

7.7 COMPARISON OF MODELS WITH *IN VIVO* DATA

Having determined that there are different characteristic pressure difference curves for the various configurations, the *in vivo* situation will now be compared to the models developed. The mild HCM case is most similar to the mild fixed restriction results from the unsteady laboratory model. Further, the case of a severe aortic stenosis has the same characteristics as the severe fixed restriction of the unsteady laboratory model. Another interesting result is that the severe HCM case matches quite well with the turbulent computational solution for the progressive restriction.

7.7.1 Mild Restriction (*in vivo*)

The mild HCM case stroke normalized pressure difference is shown in Figure 7.13, along with the unsteady laboratory model, and unsteady Bernoulli model. The pressure difference plotted for the models is taken between the piston region and expansion exit. The Bernoulli model pressures look quite similar to the unsteady flow laboratory model, as the input velocities were based on the unsteady flow laboratory model. The unsteady laboratory model matches the *in vivo* situation better than the unsteady Bernoulli models. The *in vivo* pressure did not fall off at the point where aortic flow ceased for this case, indicating that the left ventricle had reached an isovolumic state. The Bernoulli and laboratory models were incapable of reaching this state and thus have pressures that fall off at this point. While the pressure difference does not match particularly well during the first and last 20% of ejection, the magnitude of the pressure difference is consistent. Thus the conclusion of Murgo *et al* (1980) seems correct: the patient with mild HCM had no obstruction to outflow during systole.

7.7.2 Severe Aortic Valvular Stenosis (*in vivo*)

Stroke normalized pressure differences for the *in vivo* case of severe aortic valvular stenosis is shown in Figure 7.14. Pressure differences for the unsteady laboratory model and unsteady Bernoulli models in the severe fixed restriction configuration are also shown. As previously mentioned, comparisons should not be made to the unsteady Bernoulli model during the first 20% of the ejection, due to the unreliable piston velocities obtained from the unsteady flow laboratory model for this case. It is clear that the unsteady Bernoulli model with sudden expansion and the unsteady laboratory model give a reasonable estimate of the *in vivo* pressure difference. The unsteady laboratory model had a separated flow, as previously shown in Section 5.6. Clark (1976a) indicated that the *in vivo* flow separates with a severe aortic stenosis, so these results are consistent.

$$\% \, \text{Ejection} \; = \; \frac{\text{Volume of Blood Ejected}}{\text{Total Stroke Volume}} \times 100$$

$$\Phi_{mid} = \frac{P_{\text{Left Ventricle}} - P_{\text{Aorta}}}{\Delta P_{stroke}}$$

■——■ *in vivo*: ΔP_{stroke} = 703 Pa

●·······● Unsteady Laboratory: ΔP_{stroke} = 529 Pa

······ Unsteady Bernoulli
(No Separation): ΔP_{stroke} = 529 Pa

— — — Unsteady Bernoulli
(Sudden Expansion): ΔP_{stroke} = 529 Pa
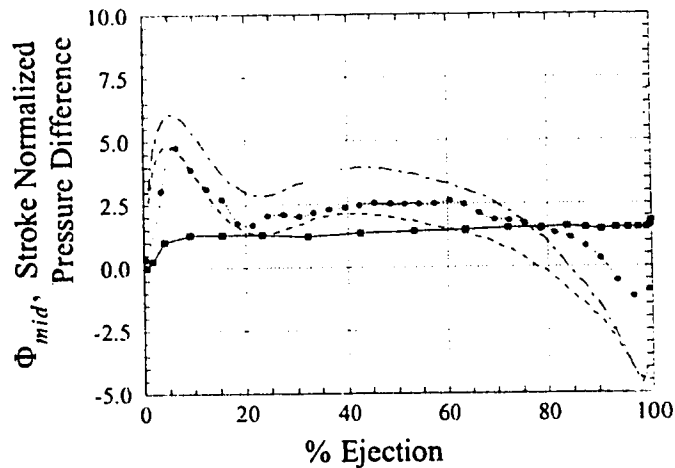
Note: only every fifth
symbol plotted for the
unsteady laboratory model
for clarity

Figure 7.13: Comparison of Mild HCM *in vivo* Normalized Pressure Differences With Unsteady Laboratory and Mathematical Models. Mild HCM *in vivo* pressures based on data from Murgo, Alter, Dorethy, Altobelli, & McGranahan (1980).

$$\% \text{Ejection} = \frac{\text{Volume of Blood Ejected}}{\text{Total Stroke Volume}} \times 100$$

$$\Phi_{mid} = \frac{P_{\text{Left Ventricle}} - P_{\text{Aorta}}}{\Delta P_{stroke}}$$

■——■ *in vivo*: $\Delta P_{stroke} = 267$ Pa

●········● Unsteady Laboratory: $\Delta P_{stroke} = 159$ Pa

------ Unsteady Bernoulli
(No Separation): $\Delta P_{stroke} = 159$ Pa

— — — Unsteady Bernoulli
(Sudden Expansion): $\Delta P_{stroke} = 159$ Pa
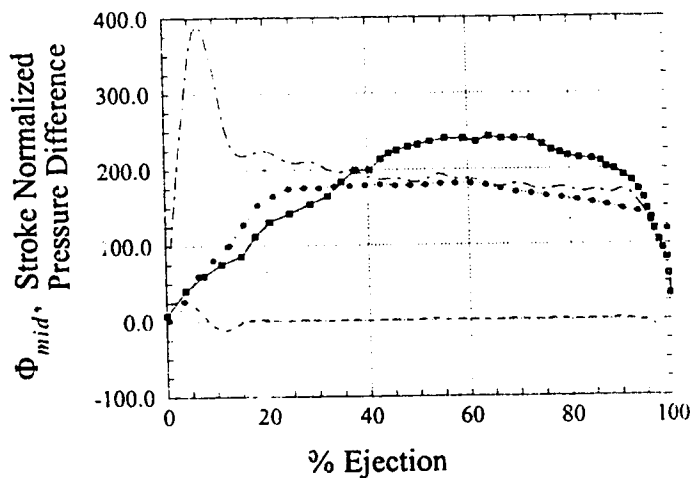
Note: only every fifth symbol plotted for the unsteady laboratory model for clarity

Figure 7.14: Comparison of Severe Aortic Valvular Stenosis *in vivo* Normalized Pressure Differences With Unsteady Laboratory and Mathematical Models. Severe Aortic Valvular Stenosis *in vivo* pressures based on data from Clark (1976).

7.7.3 Progressive Restriction (SAM) (in vivo)

The stroke normalized pressure differences for the *in vivo* case of severe HCM is shown in Figure 7.15. The corresponding pressure differences for the unsteady laboratory model, unsteady Bernoulli models (sudden expansion and no separation), and turbulent computational model are also plotted, based on the progressive restriction configuration. It is apparent that the solutions which had flow separation (unsteady Bernoulli model with a sudden expansion, and the unsteady laboratory model) do not match the *in vivo* case very well. However, the turbulent computational solution, which had no flow separation for the progressive restriction, matches the *in vivo* situation very well.

Turbulence is often observed in HCM, indicated by the presence of heart murmurs. However, flow separation has not been noted by those who have investigated the velocity in the aorta downstream of the aortic valve, see Murgo *et al* (1980). This is not to say that flow separation does not exist; rather, it has not been detected. An *in vivo* study to investigate signs of flow separation would be useful.

While it may be coincidental that the non-separated turbulent computational solution matches the severe *in vivo* HCM case, there can be no doubt that the pressure curve for severe HCM is significantly different than the unobstructed cases. Indeed, although the laboratory model was tested with ejection rates far exceeding those possible by a human heart, it was incapable of producing the magnitude of stroke normalized pressure noted for the severe HCM case. However, when operated in the progressive restriction mode, the laboratory model easily produced large stroke normalized pressures. These pressures were clearly a function of both restriction and flow separation. As the turbulent computational analysis indicates, these stroke normalized pressures were similar in magnitude to the severe HCM case when flow separation did not occur. This is an important finding, as it suggests that severe cases of HCM are progressively restricted

$$\% \text{Ejection} = \frac{\text{Volume of Blood Ejected}}{\text{Total Stroke Volume}} \times 100$$

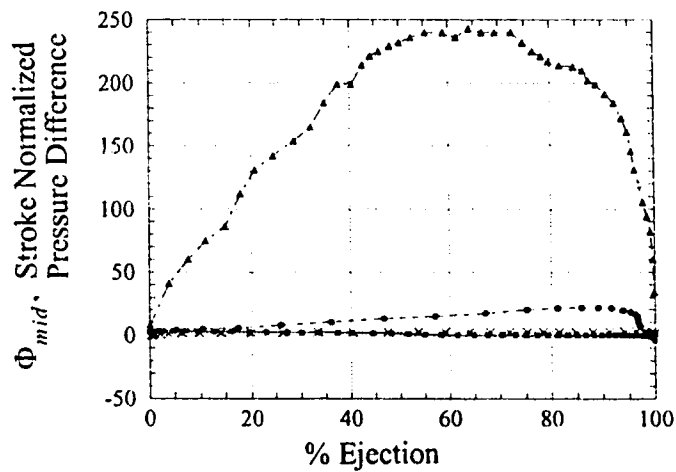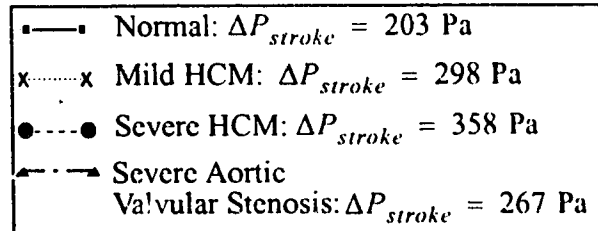$$\Phi_{mid} = \frac{P_{\text{Left Ventricle}} - P_{\text{Aorta}}}{\Delta P_{stroke}}$$

■——■ *in vivo*: $\Delta P_{stroke} = 358$ Pa

●········● Unsteady Laboratory: $\Delta P_{stroke} = 739$ Pa

— — — Turbulent CFD: $\Delta P_{stroke} = 739$ Pa

······ Unsteady Bernoulli
(No Separation): $\Delta P_{stroke} = 739$ Pa

— · — Unsteady Bernoulli
(Sudden Expansion): $\Delta P_{stroke} = 739$ Pa
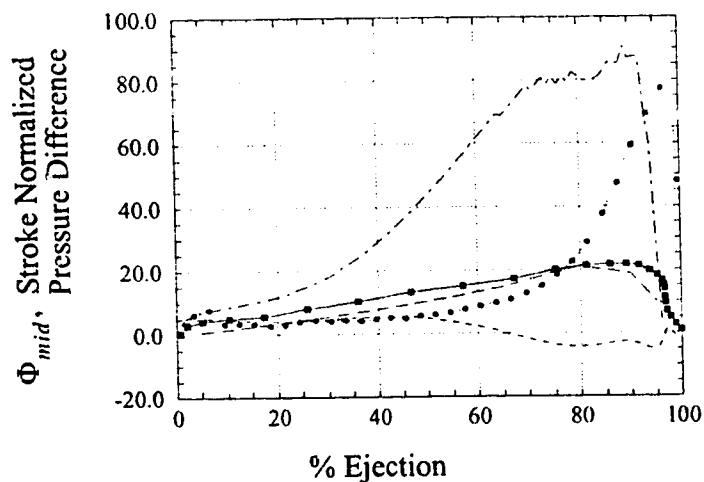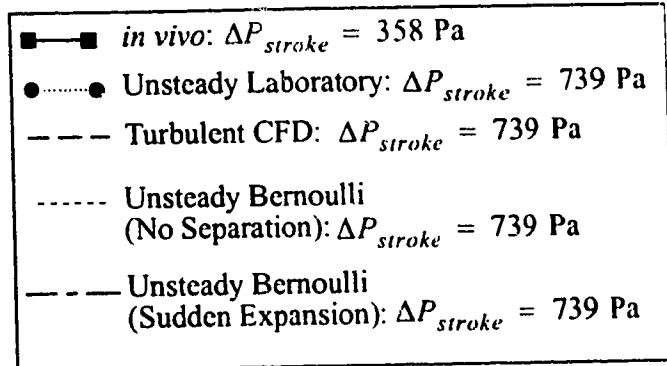
Note: only every fifth symbol plotted for the unsteady laboratory model for clarity

Figure 7.15: Comparison of Severe HCM (Progressive Restriction) (*in vivo*) Normalized Pressure Differences With Unsteady Laboratory, CFD and Mathematical Models. Severe HCM *in vivo* pressures based on data from Murgo, Alter, Dorethy, Altobelli, & McGranahan (1980).

(SAM theory) in nature. If there was no obstruction, the stroke normalized pressure would be a factor of about 4 times smaller, and the characteristic shape of the pressure curve would match that of mild HCM in Figure 7.13.

It should be noted that the stroke normalized pressure difference did not become significant until more than 75% of the contents of the piston region had been ejected. While the high pressures did retard piston motion, the pistons were already decelerating at this point, and progressive restriction did not impose a significant impediment to emptying of the piston chamber. This is consistent with the ejection in severe HCM, where most of the left ventricular contents have been ejected before the pressure difference between the left ventricle and aorta becomes significant.

7.8 EFFECT OF COMPLIANCE: EXPLORATORY TESTS

As discussed in Chapter 5, the unsteady laboratory model was used to make some exploratory tests with wall compliance. The model was tested without any added compliance, with compliance added to the piston walls, and with a compliant constriction. All results were normalized with the non-compliant test stroke pressure to allow direct comparison between the different cases. The resulting normalized pressure curves are shown in Figure 7.16. As usual, the pressure difference between the piston region (point p) and constriction region (point c) is plotted in (a), and the pressure difference between the piston region and expansion exit (point e) is plotted in (b). All tests plotted were for the same force applied to the pistons.

Three observations can be made. First, the compliant exit configuration does not have the large pressure difference shown by the non-compliant exit configurations. This is expected, as the compliant exit flexes in response to the flow pressure, effectively reducing the restriction factor. The second observation is that compliance in the piston region does

H_p P_p H_c maximum restriction

Restriction Factor $\eta_H = 5$

P_e

% Piston Closure $= \dfrac{H_{P_{initial}} - H_P}{H_{P_{initial}} - H_{P_{final}}} \times 100$

P_c

$\Upsilon = \dfrac{P_p - P_c}{P_{stroke}}$

$y_p = 65$ mm

——— Non-Compliant

·········· Compliant Piston

- - - - - Compliant Exit

$\Phi_{mid} = \dfrac{P_p - P_e}{P_{stroke}}$
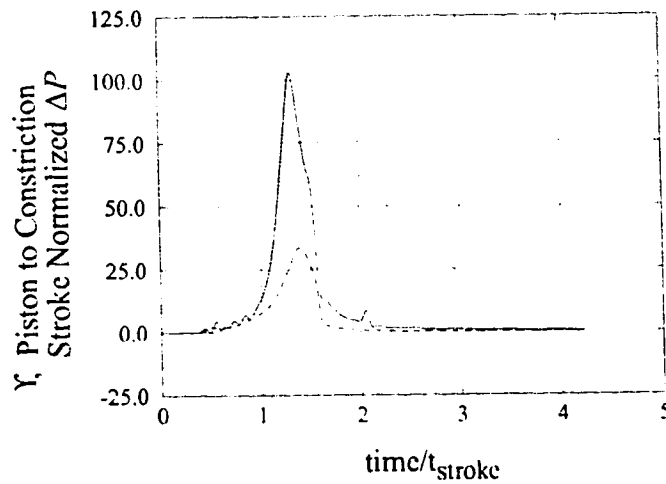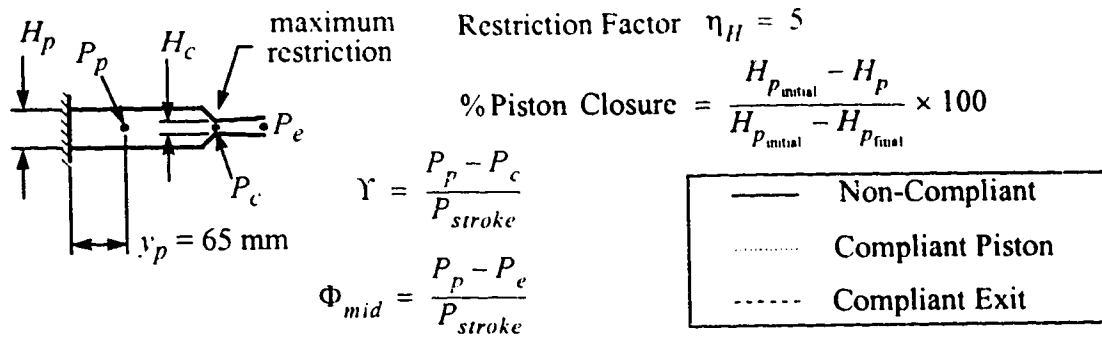
(a) Constriction Exit Pressure Difference
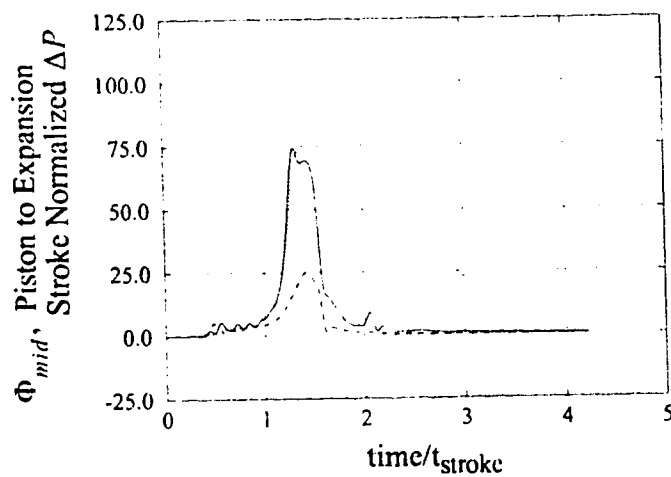
(b) Expansion Exit Pressure Difference

Figure 7.16: Comparison of Compliance Effects

not affect the rate at which the pressure difference increases. However, the compliant piston pressure difference falls at a much slower rate than the non-compliant case. This is due to the energy stored in the compliant walls slowly being released against the restriction, now at its most severe condition. Third, the peak pressure difference for the piston region with and without compliance is not significantly different.

7.9 SUMMARY

The comparison between the unsteady laboratory model and the unsteady Bernoulli models showed the following:

- the pressure differences between the piston and expansion regions for the unsteady laboratory model fall between the unsteady Bernoulli models limits of separated and unseparated flow in expansion region;

- when the spatial averaging of pressure in the constriction region of the laboratory model was considered, the pressure differences were simi... when compared to the unsteady Bernoulli model.

When comparing the quasi-steady models, it was found that:

- the quasi-steady Bernoulli model underpredicted the quasi-steady laboratory model pressure differences, especially when flow separation occurred in the expansion region of the laboratory model;

- the turbulent quasi-steady CFD analysis predicted the unsteady laboratory model pressure difference reasonably well until flow separation occurred in the unsteady laboratory model;

- the laminar separated CFD analysis predicted the unsteady laboratory model pressure difference better than the turbulent unseparated CFD analysis when flow separation occurred in the unsteady laboratory model.

The analysis of the unsteady laboratory model revealed the following:

- the effect of wall closure rate for a particular exit configuration of the unsteady laboratory model can be removed from the pressure differences by normalizing with the stroke pressure difference. This normalized pressure difference allows the effect

of flow restriction and flow separation to be easily discerned;

- the mild fixed restriction showed pressure differences that were inertial in nature;

- the progressive restriction gave pressure differences that were initially inertial, but became dominated by spatial effects and flow separation as the restriction became severe;

- the severe fixed restriction showed pressure differences that were dominated by spatial acceleration and flow separation from the onset of wall closure.

By comparing the unsteady laboratory model with *in vivo* data, it is apparent that:

- mild HCM is similar to a mild fixed restriction;

- severe HCM is most similar to a progressive restriction;

- severe aortic valvular stenosis is similar to a severe fixed restriction;

- there can be no doubt that the pressure curve for severe HCM is significantly different than the unobstructed cases. Although the laboratory model was tested with ejection rates far exceeding those possible by a human heart, it was incapable of producing the magnitude of stroke normalized pressure noted for the severe HCM case. When operated in the progressive restriction mode, the laboratory model easily produced large stroke normalized pressures.

The effect of compliance was examined and showed that:

- compliance in the piston region does not affect the rate at which the pressure difference increases;

- the peak pressure difference with and without compliance in the piston region is not significantly different;

- a compliant exit significantly reduces the pressure difference between the piston and expansion region.

CHAPTER 8 • SUMMARY AND CONCLUSIONS

8.1 MODEL DEVELOPMENT

The prime objective of this research was to look for a fluid mechanical explanation of the abnormal pressure - flow patterns seen in HCM. Two conflicting theories exist; one which proposes that the high pressure difference between the left ventricle and aorta is due to an obstruction, and another which suggests that this pressure difference is caused by inertial acceleration due to the unusually vigorous contraction of the left ventricle. The supporters of the obstructive theory point to evidence of contact between the intraventricular septum (heart wall separating the left and right ventricles) and the anterior leaflet of the mitral valve, commonly termed SAM (systolic anterior motion). This evidence suggests that the flow is progressively obstructed during the ejection period (systole). The proponents of the unobstructed theory use the faster and more complete emptying of the left ventricle during systole as proof that there can be no obstruction to the flow.

To evaluate these different theories, the analysis proceeded in two directions: theoretical flow modelling and laboratory modelling. The theoretical flow analysis allowed quantification of the geometry and flow rate components contributing to the pressure differences, while laboratory models gave valuable insight into the nature of the flow.

The one-dimensional inviscid mathematical analysis utilized the unsteady Bernoulli equation with moving walls. This included provisions for estimating the pressure loss with and without flow separation effects. This analysis was simplified to a quasi-steady case, to see the significance of the unsteady acceleration on the resulting pressure differences. This quasi-steady simplification was then applied to the two-dimensional case using a commercial computational code (FLOW3D) which was capable of predicting flow separation as well as viscous effects. A quasi-steady laboratory model

was also constructed to allow an evaluation of the commercial code results, both in terms of the two-dimensional assumption and predicted flow separation.

A simple two-dimensional transient planar piston laboratory model was developed to simulate mildly obstructed ejection, progressively obstructed ejection and severely obstructed ejection. This model featured well controlled wall motion and allowed simultaneous measurements of both wall position and pressures. The effect of the rate of ejection and degree of restriction was examined. Compliance effects in the left ventricle were evaluated by adding compliance in the model. Flow visualization was performed to determine if flow separation was occurring. Parameters were determined which allowed matching between the laboratory model and the *in vivo* situation, making comparisons between the model and real life situations meaningful.

Based on this research, the following conclusions were reached:

- the stroke pressure difference $\Delta P_{stroke} \propto V_{stroke}^2$, where $V_{stroke} \propto \dfrac{(volume)}{(time)\,(area)}$ is an appropriate parameter for normalizing the left ventricular to aortic pressure difference. This was successful in collapsing the large variability of *in vivo* data onto single curves with characteristic shapes depending on the degree of obstruction;

- the pressure difference between the left ventricle and aorta seen in HCM can be separated into unobstructed and progressively obstructed cases. Only the progressively restricted unsteady flow laboratory model was able to produce a similar stroke normalized pressure difference to the severe *in vivo* HCM case;

- initial studies of the effect of compliance on the HCM pressure differences indicate that compliance in the piston region may not play a significant role. The maximum stroke normalized pressure difference generated by the unsteady flow laboratory model was very similar for both the uncompliant and compliant pistons;

- the quasi-steady approach may work well for predicting the pressure loss at the point of maximum restriction when the spatial acceleration forces are dominant, such as in a severe restriction. The pressure difference between the piston region and constriction predicted by the quasi-steady approach matched the results from the

unsteady laboratory model only when the restriction was severe.

8.2 NORMALIZING TECHNIQUE FOR LEFT VENTRICULAR - AORTIC PRESSURES

For the most part, the measurements made by cardiologists of the left ventricular and aortic pressures are presented in their raw form: pressure in mm Hg plotted as a function of time, as shown in Figure 8.1. This is useful for the trained eye of a cardiologist, who can quickly spot abnormalities in the pulse forms. However, presenting the data in this form tends to obscure an important feature: the pressure difference between the left ventricle and aorta. An improvement would be to plot the pressure difference between the left ventricle and aorta in real time, but this also may be somewhat hard to interpret, as the magnitude of the pressure difference becomes the focal point of the analysis.

The one-dimensional order of magnitude analysis showed the forces acting on the fluid to be dominated by inertial and spatial acceleration effects, with negligible viscous drag effects. Viscous effects are only important in causing flow separation in the expansion following the restriction. This was confirmed by the unsteady Bernoulli model and the unsteady laboratory model. Based on these observations, an appropriate normalizing variable would be one that could differentiate between inertial and spatial acceleration effects. The variable used was the stroke pressure difference, ΔP_{stroke}. This was shown in Chapter 7 to reveal distinctive pressure difference curves, depending on the type of restriction. For example, the pressures plotted in Figure 8.1 are replotted in the normalized fashion in Figure 8.2, and reveal this to be a severe HCM case (stroke normalized pressure greater than 5), with the degree of restriction increasing with the ejection period. The pressure loss is dominated by spatial acceleration effects, not inertial effects, suggesting that a significant restriction to the flow exists.
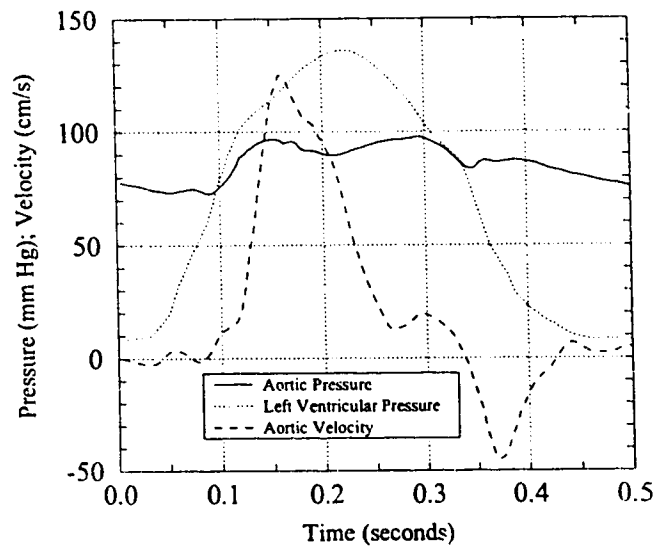
Figure 8.1: Left Ventricular Pressure, Aortic Pressure and Aortic Flow Velocity for a Severe HCM Case Based on Data of Murgo *et al* (1980), see also Figure 1.3(b).
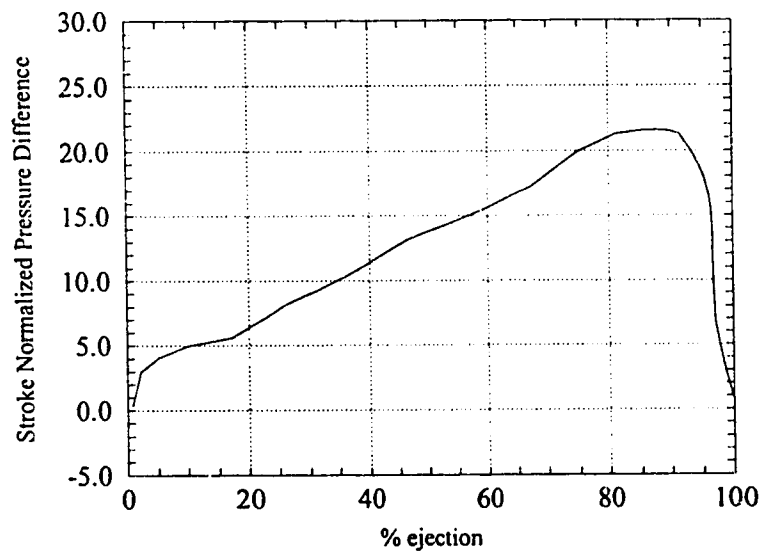
Figure 8.2: Normalized Severe HCM Pressure Difference (Left Ventricular Pressure - Aortic Pressure)/ΔP_{stroke} for Data of Figure 8.1 (see also Figure 7.15).

The cases evaluated in this thesis include a normal heart, mild HCM, severe HCM, and severe aortic valvular stenosis. When normalized by a characteristic stroke pressure difference, the various types of ejections become readily discernible. There appear to be three distinct classes:

- unrestricted flows, such as a normal heart or mild HCM, where inertial effects are predominant;

- progressively restricted flows, such as severe HCM, where spatial effects increase as the ejection proceeds;

- severely restricted flows, such as severe aortic valvular stenosis, where spatial effects dominate the pressure loss from the onset of ejection.

The magnitude of the normalized pressure difference for these three classes is so significant, as was shown by Figure 7.12, that there can be little doubt as to the classification.

This method of normalization is a significant finding, as it may give cardiologists a method to distinguish between different classes of left ventricular ejection. More importantly, it divides HCM cases into two separate classes: unobstructed and progressively obstructed.

8.3 CAUSE OF THE HCM PRESSURE GRADIENT

The question this research has attempted to answer is whether the cause of the HCM pressure gradient is caused by an obstruction which becomes progressively more severe as the ejection proceeds (systolic anterior motion of the mitral valve or SAM) or is simply an inertial acceleration effect. Based on the results from the modelling, it would appear that mild HCM cases are essentially unobstructed while severe HCM cases are progressively restricted. The assertion that inertial acceleration is the cause of the high pressure difference found in a provoked mild HCM left ventricle is plausible. However, the extension of this fluid inertia theory to explain all HCM high pressure differences, including severe cases, is not plausible. While part of the pressure difference may be

attributed to the inertial acceleration, this cannot account for the magnitude of the *in vivo* pressure difference. This was clearly demonstrated with the unsteady laboratory model, the unsteady Bernoulli model, as well as with the computational analysis. Regardless of the rate of ejection the unsteady laboratory model, when operated in the mild obstruction mode, could not produce the *in vivo* characteristic pressure difference curve of severe HCM.

Proponents of the unobstructed theory claim that a severe HCM left ventricle cannot be obstructed because it is able to eject more blood in a shorter period of time. This argument, while incorrect, is most likely due to comparing severe valvular aortic stenosis cases to normal hearts. With a severe valvular aortic stenosis, the left ventricle is restricted throughout the entire ejection period. As a result, the left ventricle empties its contents more slowly than a normal heart and also has a smaller ejection fraction. However, this is decidedly different than a progressive restriction. Since the pressure loss through a restriction becomes significant when the flow area is very small, it takes a significant restriction before an effect becomes noticeable. With a progressive restriction, this occurs late in the ejection period. By this time, most of the blood has been ejected. Thus as the restriction further increases, the pressure difference also increases and the fluid velocity decreases. This does not become significant in terms of the ejection fraction, as the left ventricle has ejected most of its contents by the time the obstruction becomes extreme.

The unsteady laboratory model using the progressive restriction configuration, as well as the normalized *in vivo* results for severe HCM, showed that flow only becomes significantly restricted late in the ejection period. By this time a high ejection fraction has already been attained. The systolic anterior motion of the mitral valve (SAM) theory, in which the mitral valve progressively obstructs the flow, is plausible in terms of explaining the pressure gradient which occurs during the forward flow portion of systole in severe

HCM cases. In the absence of a significant restriction, the magnitude of the pressure difference between the left ventricle and aorta seen in HCM cannot be produced.

8.4 COMPLIANCE EFFECTS

It was shown that compliance had little effect on the piston to expansion exit pressure difference during the ejection period of the unsteady laboratory model until the pair of pistons neared the end of their stroke. However, as the motion of the pistons was controlled by the force supplied by the drive system, the increased drag of the expanded plastic foam against the surrounding walls slowed the pistons, causing a much slower fall of the pressure difference. This effect was undesirable and illustrates the difficulties involved in properly modelling compliance. In spite of this effect, the initial study of compliance suggests that compliance upstream of the constriction does not play a significant role in the development of the pressure difference seen in HCM.

When the constriction was made of compliant material, the pressures differences became much less severe. Because of the deformation of the compliant constriction itself, the effective restriction was reduced. This result indicates that compliance at the constriction may play a significant role in HCM and warrants further investigation.

8.5 MODELLING AN UNSTEADY FLOW WITH A QUASI-STEADY APPROXIMATION

This thesis attempted to use a quasi-steady analysis for some of the modelling. It was shown in Section 2.3 that this approach could be used only if the unsteady inertial acceleration forces were small compared to the spatial acceleration forces and viscous drag forces. This was shown to be valid in Section 3.4 for the pressure differences between the piston region and the point of maximum restriction, i.e. where results using the quasi-steady approach matched the unsteady results quite well for the severe restriction, where spatial (rather than inertial) acceleration forces were dominant. The quasi-steady approach

did not match the unsteady results for the unrestricted configuration, since the inertial forces were much more significant. The quasi-steady approach should only be used where there is a severe restriction, and should be avoided in areas of flow separation.

8.6 RECOMMENDATIONS FOR FURTHER RESEARCH

Further analysis should be undertaken using *in vivo* data for a variety of heart conditions, using the normalization techniques discussed in Section 7.2. This may determine if there is a large family of characteristic non-dimensional pressure difference curves for normal and diseased left ventricles. A study should be made with normal, mild HCM, moderate HCM and severe HCM to see if the characteristic pressure difference curves vary significantly for different individuals and disease classification. A study utilizing pressure and velocity probes of the type used by Murgo *et al* (1980) would be most useful, as these probes allowed simultaneous measurement of the left ventricular pressure, aortic or left ventricular outflow tract pressure, and aortic flow velocity.

A correction to the quasi-steady results could be made using the force ratios such as equations 2.62 or 2.63. This may account to some degree for the inertial acceleration effects of the unsteady flow. This may allow the use of a quasi-steady approach for making predictions of the pressure for unsteady flow cases with moving boundaries. The ratios would have to be evaluated on an instantaneous basis and applied to each quasi-steady solution in turn. While this may give better results for comparison to unsteady flows, it will still be limited in that the quasi-steady solutions will not include the time history of the flow. This time history may be especially significant in situations where flow separation is occurring.

BIBLIOGRAPHY

Ahmed, S.A., Giddens, D.P., (1983), "Velocity Measurements in Steady Flow Through Axisymmetric Stenoses at Moderate Reynolds Numbers", *Journal of Biomechanics*, **16**, pp. 505-516.

Ahmed, S.A., Giddens, D.P., (1984), "Pulsatile Poststenotic Flow Studies With Laser Doppler Anemometry", *Journal of Biomechanics*, **17**, pp. 695-705.

Agonafer, D., Watkins, C. B., Cannon, J. N., (1985), "Computation of Steady Flow in a Two-Dimensional Arterial Model", *Journal of Biomechanics*, **18**, pp. 695-701.

Arndt, J. O., Stegall, H. F., Wicke, H. J., (1971), "Mechanics of the Aorta *In Vivo*", *Circulation Research*, **28**, pp. 693-704.

Arts, T., Reneman, R.S., Veenstra, P.C., (1979), "A Model of the Mechanics of the Left Ventricle", *Annals of Biomedical Engineering*, **7**, pp. 299-318.

Bellhouse, B. J., (1972), "Fluid Mechanics of a Model Mitral Valve and Left Ventricle", *Cardiovascular Research*, **6**, pp. 199-210.

Bellhouse, B., Bellhouse, F., (1969), "Fluid Mechanics of Model Normal and Stenoses Aortic Valves", *Circulation Research*, **25**, pp. 693-704.

Bellhouse, B.J., Talbot, L., (1969), "The Fluid Mechanics of the Aortic Valve", *Journal of Fluid Mechanics*, **35**, pp. 721-735.

Benckey, J. E. W., (1972), "Some Computer Models in Cardiovascular Research", *Cardiovascular Fluid Dynamics*, Bergel, D. H., ed., Academic Press, London, England.

Bird, J. J., Murgo, J. P., Pasipoularides, A., (1982), "Fluid Dynamics of Aortic Stenosis: Subvalvular Gradients Without Subvalvular Obstruction", *Circulation*, **66**, pp. 835-840.

Blinks, J. R., Jewell, B. R., (1972), "The Meaning and Measurement of Myocardial Contractility", *Cardiovascular Fluid Dynamics*, Bergel, D. H., ed., Academic Press, London, England.

Bonow, R. O., Rosing, D. R., Bacharach, S. L., Green, M. V., Kent, K. M., Lipson, L. C., Maron, B. J., Leon, M. B. Epstein, S. E., (1981), "Effects of Verapamil on Left Ventricular Systolic Function and Diastolic Filling in Patients with Hypertrophic Cardiomyopathy", *Circulation*, **64**, pp. 787-796.

Berer, J. S., Bacharach, S. L., Green, M. V., Kent, K. M., Rosing, D. R., Seides, S. F., Morrow, A. G., Epstein, S. E., (1979), "Effect of Septal Myotomy and Myectomy on Left Ventricular Systolic Function at Rest and During Exercise in Patients with IHSS", *Circulation*, 60, pp. 182-187.

Borgas, M. S., Pedley, T. J., (1990), "Non-uniqueness and Bifurcation in Annular and Planar Channel Flows", *Journal of Fluid Mechanics*, 214, pp. 229-250.

Braunwald, E., Morrow, A. G., Cornell, W. P., Aygen, M. M., Hilbish, T. F., (1960), "Idiopathic Hypertrophic Subaortic Stenosis", *American Journal of Medicine*, 29, pp. 924-945.

Brech, R., Bellhouse. B. J., (1973), "Flow in Branching Vessels", *Cardiovascular Research*, 7, pp. 593-600.

Bristow, J. D., (1965), "Recognition of Left Ventricular Outflow Obstruction", *Circulation*, 31, pp. 600-611.

Brock, R., (1957), "Functional Obstruction of the Left Ventricle (Acquired Aortic Subvalvular Stenosis)", *Guy's Hospital Reports*, 106, pp. 221-238.

Brock, R., (1959), "Functional Obstruction of the Left Ventricle (Acquired Aortic Subvalvular Stenosis)", *Guy's Hospital Reports*, 108, pp. 126-143.

Brockenbrough, E. C., Braunwald, E., Morrow, A. G.(1961), "A Hemodynamic Technic for the Detection of Hypertrophic Subaortic Stenosis", *Circulation*, 23, pp. 189-194.

Brooks, D. E., Goodwin, J. W., Seaman, G. V. F., (1970), "Interactions Among Erythrocytes Under Shear", *Journal of Applied Physiology*, 28, pp. 172-177.

Bulkey, B. H., (1977), "Idiopathic Hypertrophic Subaortic Stenosis Afflicted: Idols of the Cave and the Marketplace", *The American Journal of Cardiology*, 40, pp. 476-479.

Campbell, R. P., (1991), "Image Processing Techniques for Analysis of Full Color Turbulent Jet Images", M.Sc. Thesis, University of Alberta, Edmonton, Canada.

Canedo, M. I., Frank, M. J., (1981), "Therapy of Hypertrophic Cardiomyopathy: Medical or Surgical? Clinical and Pathophysiologic Considerations", *The American Journal of Cardiology*, 48, pp. 383-387.

Carabello, B. A., Green. L. H., Grossman, W., Cohn, L. H., Koster, J. K, Collins, J., (1980), "Hemodynamic Determinants of Prognosis of Aortic Valve Replacement in Critical Aortic Stenosis and Advanced Congestive Heart Failure", *Circulation* 62, pp. 42-48.

Chapra, S. C., Canale, R. P., (1988), *Numerical Methods for Engineers*, McGraw-Hill, Inc., New York, 1988.

Charm, S. E., Kurland, G. S., (1974), *Blood Flow and Microcirculation*, John Wiley and Sons, Inc., New York.

Charm, S. E., Kurland, G. S., Schwartz, M., (1969), "Absence of Transition in Viscosity of Human Blood between Shear Rates of 20 and 100 /sec", *Journal of Applied Physiology*, 26, pp. 389-392.

Chaturani, P., Pralhad, R. N., (1985), "Blood Flow in Tapered Tubes with Biorheological Applications", *Biorheology*, 22, pp. 303-314,.

Chow, J. C. F., Soda, K., (1972), "Laminar Flow in Tubes With Constriction", *The Physics of Fluids*, 15, pp. 1700-1706.

Christiansen, E. B., Kelsey, S. J., Carter, T. R., (1972), "Laminar Tube Flow Through an Abrupt Contraction", *AIChE Journal*, 18, pp. 372-380.

Clark, C., (1976a), "The Mechanics of Aortic Stenosis - I. Theory and Steady Flow Experiments", *Journal of Biomechanics*, 9, pp. 521-528.

Clark, C., (1976b), "The Mechanics of Aortic Stenosis - II. Unsteady Flow Experiments", *Journal of Biomechanics*, 9, pp. 567-573.

Clark, C., (1980), "The Propagation of Turbulence Produced by a Stenosis", *Journal of Biomechanics*, 13, pp. 591-604.

Clark, C., Schultz, D. L., (1973), "Velocity Distribution in Aortic Flow", *Cardiovascular Research*, 7, pp. 601-613.

Clark, M. E., Robertson, J. M., (1983), "Stenosis Severity Effects for Unbalanced Simple-Pulsatile Bifurcation Flow", *Journal of Biomechanics*, 16, pp. 895-906.

Coles, D. E., Hirst, E. A., (1969), "Computation of Turbulent Boundary Layers", *AFOSR - IFP - Stanford Conference*, II, Stanford University, CA.

Cooney, D. O., (1976), *Biomedical Engineering Principles*, Marcel Dekker, Inc., New York.

Cooney, D. A., Leachman, R. D., Wukasch, D. C., (1973), "Diffuse Muscular Subaortic Stenosis: Surgical Treatment", *The American Journal of Cardiology*, 31, pp. 1-6.

Criley, J. M., (1979), "The Bottom Line Syndrome Hypertrophic Cardiomyopathy Revisited", *West Journal of Medicine*, 130, pp. 350-353.

Criley, J. M., Lewis, K. B., White, R. I., Ross, R. S., (1965), "Pressure Gradients Without Obstruction", *Circulation*, 32, pp. 881-887.

Criley, J. M., Siegel, R. J., (1985a), *A Non-obstructive View of Hypertrophic Cardiomyopathy Heart Muscle Disease*, Goodwin, J. ed., MTP Press Ltd., Boston.

Criley, J. M., Siegel, R. J., (1985b), "Has 'Obstruction' Hindered Our Understanding of Hypertrophic Cardiomyopathy?", *Circulation*, **72**, pp. 1148-1154.

Criley, J. M., Siegel, R. J., (1986), "Obstruction is Unimportant in the Pathophysiology of Hypertrophic Cardiomyopathy", *Postgraduate Medical Journal*, **62**, pp. 515-529.

Criley, J. M., Siegel, R. J., (1993), "Subaortic Stenosis Revisited: The Importance of the Dynamic Pressure Gradient", *Classics in Medicine*, pp. 412-436.

Cross, C. E., Salisbury, P. F., (1963), "Functional Subaortic Stenosis Produced in Animals", *The American Journal of Cardiology*, pp. 394-398.

Daly, B. J., (1974), "A Numerical Study of Pulsatile Flow Through Constricted Arteries", Proc. 4th Intl. Conf. on Numerical Methods in Fluid Dynamics (Richtmeyer, R. D., ed.), *Lecture Notes in Physics*, **35**, pp. 117-124, Springer.

Dellagi, F., (1990), "Numerical Stability Study of Finite Difference Schemes for the Resolution of Three-dimensional Time-dependent Navier-Stokes Equations", *Applied Mathematical Modelling*, **14**, pp. 14-18.

Demiray, H., Vito, R., (1983), "On Large Periodic Motions of Arteries", *Journal of Biomechanics*, **16**, pp. 643-648.

Dinsmore, R. E., Sanders, C. A., Harthorne, J. W., (1966), "Mitral Regurgitation in Idiopathic Hypertrophic Subaortic Stenosis", *New England Journal of Medicine*, **275**, pp. 1225-1228.

Ditenfass, L., (1980), "Internal Viscosity (Rigidity) of the Red Cell and Blood Viscosity Equation: Counteraction of Errors due to Flow Instability of Plasma", *Biofluid Mechanics*, pp. 401-416, Schneck, Ed., Plenum Press, N.Y.

Doebelin, E. O., (1990), *Measurement Systems - Application and Design*, McGraw-Hill Publishing Company, New York, N.Y.

Dutta, A., Tarbell, J. M., (1989), "Numerical Simulation of Sinusoidal Flow in a Straight Elastic Tube: Effects of Phase Angles", *Biorheology*, **26**, pp. 1-22.

Enden, G., Israeli, M., Dinnar, U., (1985), "A Numerical Simulation of the Flow of a T-Type Bifurcation and Its Application to an "End to Side" Fistula", *Journal of Biomechanical Engineering*, **107**, pp. 321-326.

Ehrlich, L. W., (1979), "The Numerical Solution of a Navier-Stokes Problem in a Stenosed Tube: A Danger in Boundary Approximations of Implicit Marching Schemes", *Computers and Fluids*, **7**, pp. 247-256.

Ehrlich, L. W., Friedman, M. H., (1985), "Computational Aspects of Aortic Bifurcation Flows", *Computers and Fluids*, **13**, pp. 177-183.

Elad, D., Katz, D., Kimmel, E., Einav, S., (1991), "Numerical Schemes for Unsteady Fluid Flow Through Collapsible Tubes", *Journal of Biomedical Engineering*, 13.

Fananapazir, L., Cannon, R., Tripodi, D., Panza, J., (1992),"Impact of Dual-Chamber Permanent Pacing in Patients With Obstructive Hypertrophic Cardiomyopathy With Symptoms Refractory to Verapamil and β-Adrenergic Blocker Therapy", *Circulation*, 85, pp. 2149-2161.

Fletcher, C. A., (1988), *Computational Techniques for Fluid Dynamics*, Springer-Verlag, New York.

Floryan, J. M., Rasmussen, H., (1989), "Numerical Methods for Viscous flows With Moving Boundaries", *Applied Mechanics Reviews*, 42, pp. 323-340.

FLOW3D Release 3.2 User Manual, (1992), AEA Industrial Technology, Oxfordshire, U.K.

Frank, S., Braunwald, E., (1968), "Idiopathic Hypertrophic Subaortic Stenosis", *Circulation*, 37, pp. 759-788.

Gabr, M. H., (1983),"Flow Visualization in the Intake Process of an Internal Combustion Engine", *Proceedings of the Third International Symposium on Flow Visualization*, pp. 792-796.

Goldstein, R. J., (1983), *Fluid Mechanics Measurements*, Hemisphere Publishing Corporation, Springer-Verlag.

Goodwin, J. F., (1980), "Hypertrophic Cardiomyopathy: A Disease in Search of Its Own Identity", *The American Journal of Cardiology*, 45, pp. 177-180.

Goodwin, J. F., (1982), "The Frontiers of Cardiomyopathy", *British Heart Journal*, 48, pp. 1-18.

Goodwin, J. F., Hollman, A., Cleland, W. P., Teare, D., (1960), "Obstructive Cardiomyopathy Simulating Aortic Stenosis", *British Heart Journal*, 22, pp. 403-414.

Gotsman, M. S., Lewis, B. S., (1974), "Left Ventricular Volumes and Compliance in Hypertrophic Cardiomyopathy", *Chest*, 66, pp. 498-505.

Grose, R., Maskin, C., Spindola-Franco, H., Yipintsoi, T., (1981), "Production of Left Ventricular Cavity Obliteration in Normal Man", *Circulation*, 64, pp. 448-455.

Gunther, S., Grossman, W., (1979), "Determinants of Ventricular Function in Pressure-Overload Hypertrophy in Man", *Circulation*, 59, pp. 679-688.

Guyton, A. C., (1971), *Textbook of Medical Physiology*, W. B. Sunders Company, Philadelphia.

Harris, A., Donmoyer, T., Leatham, A., (1969), "Physical Signs of Differential Diagnosis of Left Ventricular Obstructive Cardiomyopathy", *British Heart Journal*, **31**, pp. 501-510.

Hatle, L., (1981), "Noninvasive Assessment and Differentiation of Left Ventricular Outflow Obstruction with Doppler Ultrasound", *Circulation*, **64**, pp. 381-387.

Hay, A. S., Mioduchowski, A., Faulkner, M. G., (1993), "Development of an Experimental Apparatus to Study Hypertrophic Cardiomyopathy (HCM)", *Transactions of the CSME*, **17**, pp. 435-447.

Henry, W. L., Clark, C. E., Glancy, L., Epstein, S. E., (1973), "Echocardiographic Measurement of the Left Ventricular Outflow Gradient in Idiopathic Hypertrophic Subaortic Stenosis", *New England Journal of Medicine*, **288**, pp. 989-993.

Henry, W. L., Clark, C. E., Griffith, J. M., Epstein, S. E., (1975), "Mechanism of Left Ventricular Outflow Obstruction in Patients with Obstructive Asymmetric Septal Hypertrophy (Idiopathic Hypertrophic Subaortic Stenosis)", *The American Journal of Cardiology*, **35**, pp. 337-345.

Hernandez, R. R., Greenfield, J. C., McCall, B. W., (1964), "Pressure-Flow Studies in Hypertrophic Subaortic Stenosis", *Journal of Clinical Investigation*, **43**, pp. 401-407.

Hogan, H. A., Henriksen, M., (1989), "An Evaluation of a Micropolar Model for Blood Flow Through an Idealized Stenosis", *Journal of Biomechanics*, **22**, pp. 211-218.

Holmes, J. D., Lewis, R. E., (1987), "Optimization of Dynamic-Pressure-Measurement Systems. 1. Single Point Measurements", *Journal of Wind Engineering and Industrial Aerodynamics*, **25**, pp. 249-273.

How, T. V., Black, R. A., (1987), "Pressure Losses in Non-Newtonian Flow Through Rigid Wall Tapered Tubes", *Biorheology*, **24**, pp. 337-351.

Huber, D., Grimm, J., Koch, R., Krayenbuehl, H. P., (1981), "Determinants of Ejection Performance in Aortic Stenosis", *Circulation*, **64**, pp. 126-134.

Hung, T.K., Schuessler, B. B., (1977), "An Analysis of the Hemodynamics of the Opening of Aortic Valves", *Journal of Biomechanics*, **10**, pp. 597-606.

Huxley, A. F., (1957), "Muscle Structure and Theories of Contraction", *Progr. Biophys.*, **7**, pp. 255-318.

James, M. L., Smith, G. M., Wolford, J. C., (1977), *Applied Numerical Methods for Digital Computation*, Harper & Row, Publishers, New York.

Jones, R. T., (1969), "Blood Flow", *Annual Review of Fluid Mechanics*, **1**, pp. 223-244.

Julian, O. C., Dye, W. S., Javid, H., Hunter, J. A., Muenster, J. J., Najafi, H., (1965), "Apical Left Ventriculotomy in Subaortic Stenosis due to a Fibromuscular Hypertrophy", *Supplement I to Circulation*, 31, pp. 144-154.

Kao, T. W., Park, C., (1970), "Experimental Investigations of the Stability of Channel Flows. Part I: Flow of a Single Liquid in a Rectangular Channel", *Journal of Fluid Mechanics*, 43, pp. 145-164.

Kaser, I. S., Kennedy, J. W., (1969), "Measurement of Left Ventricular Volumes in Man by Single-Plane Cineangiography", *Invest. Radiol.*, 4, pg. 83.

Kennedy, J. W., Trenholme, S. E., Kaser, I. S., (1970), "Left Ventricular Volume and Mass From Single-Plane Cine Angiocardiogram. A Comparison of Antero-Posterior and Right Anterior Oblique Methods", *American Heart Journal*, 80, pp. 343-352.

Kiris, C., Rogers, S., Kwak, D., Chang, I., (1993), "Computation of Incompressible Viscous Flows Though Artificial Heart Devices With Moving Boundaries", *Contemporary Mathematics*, 141, pp. 237-259.

Koga, D. J., Abrahamson, S. D., Eaton, J. K., (1987), "Development of a Portable Laser Sheet", *Experiments in Fluids*, 5, pp. 215-216.

Krinkler, D. M., Davies, M. J., Rowlan, E., Goodwin, J. F., Evans, R. C., Shaw, D., (1980), "Sudden Death in Hypertrophic Cardiomyopathy: Associated Accessory Atrioventricular Pathways", *British Heart Journal*, 43, pp. 245-251.

Kunz, A. B., Coulter, N. A., (1967), "Non-Newtonian Behavior of Blood in Oscillatory Flow", *Biophysical Journal*, 7, pp. 25-36.

Laniado, S., Yellin, E., Kotler, M., Levy, L., Stadler, J., Terdiman, R., (1975), "A Study of the Dynamic Relations Between the Mitral Valve Echogram and Phasic Mitral Flow", *Circulation*, 51, pp. 104-113.

Launder, B. E., Spalding, D. B., (1974), "Numerical Computations of Turbulent Flows", *Computational Methods in Applied Mechanics and Engineering*, 3, pp. 269-289.

Lewis, R. P., Sandler, H., (1971), "Relationship Between Changes in Left Ventricular Dimensions and the Ejection Fraction in Man", *Circulation*, 64, pp. 548-557.

Lieberstein, H. M., (1973), *Blood Flow and Electrically Active Cells*, American Elsevier Publishing Company, Inc., New York.

Liepsch, D. W., (1986), "Flow in Tubes and Arteries - A Comparison", *Biorheology*, 23, pp. 395-433.

Lorell, B. H., Paulus, W. J., Grossman, W., Wynne, J., Cohn, P. F., (1982), "Modification of Abnormal Left Ventricular Diastolic Properties by Nifedipine in Patients With Hypertrophic Cardiomyopathy", *Circulation*, 65, pp. 499-597.

Lutz, R. J., Hsu, L., Menawat, A., Zrubek, J., Edwards, K., (1983), "Comparison of Steady and Pulsatile Flow in a Double Branching Arterial Model", *Journal of Biomechanics*, 16, pp. 753-766.

Lynch, P. R., Bove, A. A., (1969), "Geometry of the Left Ventricle as Studied by a High-speed Cineradiographic Technique", *Federation Proceedings*, 28, pp. 1330-1333.

Mann, K. A., Deutsch, S., Tarbell, J. M., Geselowitz, D., Rosenberg, G., Pierce, W., (1987), "An Experimental Study of Newtonian and Non-Newtonian Flow Dynamics in a Ventricular Assist Device", *Journal of Biomechanical Engineering*, 109, pp. 139-147.

Maron, B. J., Gottdiener, J. S., Arce, J., Rosing, D, R., Wesley, Y. E., Epstein, S. E., (1985), "Dynamic Subaortic Obstruction in Hypertrophic Cardiomyopathy: Analysis by Pulsed Doppler Echocardiography", *Journal of the American College of Cardiology*, 6, pp. 1-15.

Maron, B. J., Harding, A. M., Spirito, P., Roberts, W. C., Waller, B. F., (1982), "A Newly Recognized Cause of Dynamic Sub-Aortic Obstruction in Hypertrophic Cardiomyopathy: Systolic Anterior Motion of the Posterior Mitral Leaflet", *Circulation*, 65-66, pp. II-267.

Maron, B. J., Savage, D. D., Wolfson, J. K., Epstein, S. E., (1981), "Prognostic Significance of 24 Hour Ambulatory Electrocardiographic Monitoring in Patients With Hypertrophic Cardiomyopathy: A Prospective Study", *The American Journal of Cardiology*, 48, pp. 252-257.

Mason, D. T., Cohn, L. H., Ross, J., Braunwald, E., (1967), "Idiopathic Hypertrophic Subaortic Stenosis: Effects of Changes in Heart Rate on the Severity of Obstruction to Left Ventricular Outflow", *The American Journal of Cardiology*, 19, pp. 797-805.

McDonald, D. A., (1974), *Blood Flow in Arteries*, Edward Arnold Ltd., London, England.

McKenna, W. J., England, D., Doi, Y. L., Deanfield, J. E., Oakley, C., Goodwin, J. F., (1981), "Arrhythmia in Hypertrophic Cardiomyopathy I: Influence on Prognosis", *British Heart Journal*, 46, pp. 168-172.

McKenna, W. J., Harris, L., Perez, G., Krikler, D. M., Oakley, C., Goodwin, J. F., (1981), "Arrhythmia in Hypertrophic Cardiomyopathy II: Comparison of Amiodarone and Verapamil in Treatment", *British Heart Journal*, 46, pp. 173-178.

McKenna, W. J., Oakley, C. M., Krikler, D. M., Goodwin, J. F., (1985), "Improved Survival With Amiodarone in Patients With Hypertrophic Cardiomyopathy and Ventricular Tachycardia", *British Heart Journal*, 53, pp. 412-416.

Merrill, E. W., Pelletier, G. A., (1967), "Viscosity of Human Blood: Transition From Newtonian to Non-Newtonian", *Journal of Applied Physiology*, 23, pp. 178-182.

Merzkirch, W., (1983), "Streaming Birefringence and Its Application to the Simulation of Problems in Blood Flow", *Proceedings of the 3rd International Symposium on Flow Visualization*, Yang, W. J., Ed., Hemisphere Publications, N.Y.

Millar, H. D., Baker, L. E., (1973),"A Stable Ultraminiature Catheter-tip Pressure Transducer", *Med. Biol. Eng.*, 11, pp. 86-89.

Mills, C. J., (1972), "Measurement of Pulsatile Flow and Flow Velocity", *Cardiovascular Fluid Dynamics*, Bergel, D. H., Ed., Academic Press, London.

Misra, J. C., Chakravarty, S., (1986), "Flow in Arteries in the Presence of Stenosis", *Journal of Biomechanics*, 19, pp. 907-918.

Mirsky, I., Pasipoularides, A., (1980), "Elastic Properties of Normal and Hypertrophied Cardiac Muscle", *Federation Proc.*, 39, pp. 156-161.

Moffat, H. K., (1963), "Viscous and Resistive Eddies Near a Sharp Corner", *Fluid Mechanics*, 18, pp. 1-18.

Moravec, S., Liepsch, D., (1983), "Flow Investigations in a Model of a Three-Dimensional Human Artery With Newtonian and Non-Newtonian Fluids. Part I", *Biorheology*, 20, pp. 745-759.

Morrow, A. G., Reitz, B. A., Epstein, S. E., Henry, W. L., Conkle, D. M., Itscoitz, S. B., Redwood, D. R., (1975), "Operative Treatment in Hypertrophic Subaortic Stenosis: Techniques, and the Results of Pre and Postoperative Assessments in 83 Patients", *Circulation*, 52, pp. 88-102.

Morrow, A. G., Vasko, J. S., Henney, R. P., Brawley, R. K., (1965), "Can Outflow Obstruction be Induced Within the Normal Left Ventricle?", *The American Journal of Cardiology*, 16, pp 540-546.

Murgo, J. P., (1982), "Does Outflow Obstruction Exist in Hypertrophic Cardiomyopathy?", *The New England Journal of Medicine*, 307, pp. 1008-1009.

Murgo, J. P., Alter, B. R., Dorethy, J. F., Altobelli, S. A., McGranahan, G. M., Dunne, T. E., (1980), "Dynamics of Left Ventricular Ejection in Obstructive and Nonobstructive Hypertrophic Cardiomyopathy", *Journal of Clinical Investigation*, 66, pp. 1369-1382.

Murgo, J. P., Millar, H. D., (1972), "A New Cardiac Catheter for High Fidelity Differential Recordings", *15th Annual Conference on Engineering in Medicine and Biology*, Bal Harbour, Fla., pg. 303.

Nerem, R. M., Seed, W. A., (1972), "An *In Vivo* Study of Aortic Flow Disturbances", *Cardiovascular Research*, 6, pp. 1-14.

Nerem, R. M., Seed, W. A., Wood, N. B., (1972), "An Experimental Study of the Velocity Distribution and Transition to Turbulence in the Aorta", *Journal of Fluid Mechanics*, 52, pp. 137-150.

Nichols, W. W., Pepin, C. J., Conti, C. R., Christie, L. G., Feldman, R. L., (1980), "Evaluation of a New Catheter-Mounted Electromagnetic Velocity Sensor During Cardiac Catheterization", *Catheterization and Cardiovascular Diagnosis*, 6, pp. 97-113.

Nichols, W. W., Pepin, C. J., Conti, C. R., Christie, L. G., Feldman, R. L., (1981), "Quantization of Aortic Insufficiency Using a Catheter-tip Velocity Transducer", *Circulation*, 64, pp. 375-380.

Nichols, W. W., Pepin, C. J., Millar, H. D., Christie, L. G., Conti, C. R., (1978), "Percutaneous Left Ventricular Catheterization With an Ultraminiature Catheter - tip Pressure Transducer", *Cardiovascular Research*, 12, pp. 566-568.

Ower, E., Pankhurst, R. C., (1966), *The Measurement of Air Flow*, Permagon Press, N.Y.

Pasipoularides, A., Murgo, J. P., Bird, J. J., Craig, W. E., (1984), "Fluid Dynamics of Aortic Stenosis: Mechanisms for the Presence of Subvalvular Pressure Gradients", *American Journal of Physiology*, 246, pp H542-H550.

Patil, M. K., Subbaraj, K., (1988), "Finite Element Analysis of Two-Dimensional Steady Flow in Model Arterial Bifurcation", *Journal of Biomechanics*, 21, pp. 219-233.

Peskin, C. S., (1972), "Flow Patterns Around Heart Valves: A Numerical Method", *Journal of Computational Physics*, 10, pp. 252-271.

Peskin, C. S., (1977), "Numerical Analysis of Blood Flow in the Heart", *Journal of Computational Physics*, 25, pp. 220-252.

Peskin, C. S., (1982), "The Fluid Dynamics of Heart Valves: Experimental, Theoretical, and Computational Methods", *Annual Review of Fluid Mechanics*, 14, pp. 235-259.

Peskin, C. S., McQueen, D. M., Greenburg, S., (1986), "Three-Dimensional Fluid Dynamics in a Two-Dimensional Amount of Central Memory", *Proceedings of Wave Motion: Theory, Modelling and Computation*.

Peskin, C. S., McQueen, D. M., (1989), "A Three-Dimensional Computational Method for the Blood Flow in the Heart", *Journal of Computational Physics*, 81, pp. 372-405.

Peterson, K. L., Uther, J. B., Shabetai, R., Braunwald, E., (1973), "Assessment of Left Ventricular Performance in Man: Instantaneous Tension -Velocity-Length Relations Obtained With the Aid of an Electromagnetic Velocity Catheter in the Ascending Aorta", *Circulation*, 67, pp. 924-935.

Pierce, G. E., Morrow, A. G., Braunwald, E., (1964), "Idiopathic Hypertrophic Subaortic Stenosis: III. Intraoperative Studies of the Mechanism of Obstruction and Its Hemodynamic Consequences", *Circulation*, **30**, pp. IV152-IV175.

Pollick, C., Morgan, C., Gilbert, B., Rakowski, H., Wigle, E., (1982), "Muscular Subaortic Stenosis - The Temporal Relationship Between Systolic Anterior Motion of the Mitral Leaflet and the Pressure Gradient", *Circulation*, **66**, pp. 1087-1094.

Pollick, C., Rakowski, H., Wigle, E. D., (1984), "Muscular Subaortic Stenosis: The Quantitative Relationship Between Systolic Anterior Motion and the Pressure Gradient", *Circulation*, **69**, pp. 43-49.

Popp, R. L., Harrison, D. C., (1969), "Ultrasound in the Diagnosis and Evaluation of Therapy of Idiopathic Hypertrophic Subaortic Stenosis", *Circulation*, **40**, pp. 905-914.

Powell, W. J., Whiting, R. B., Dinsmore, R. E., Sanders, C. A., (1973), "Symptomatic Prognosis in Patients With Idiopathic Hypertrophic Subaortic Stenosis (IHSS)", *The American Journal of Medicine*, **55**, pp. 15-24.

Press, W. H., Flannery, B. P. Teukolsky, S. A., Vetterling, W. T., (1988), *Numerical Recipes in C*, Cambridge University Press.

Rackley, C. W., Whalen, R. E., McIntosh, H. D., (1966), "Ventricular Volume Studies in a Patient With Hypertrophic Subaortic Stenosis", *Circulation*, **34**, pp. 579-584.

Ralph, M. E., Pedley, T. J., (1988), "Flow in a Channel with a Moving Indentation", *Journal of Fluid Mechanics*, **190**, pp. 87-112.

Ralph, M. E., Pedley. T. J., (1989), "Viscous and Inviscid Flows in a Channel With a Moving Indentation", *Journal of Fluid Mechanics*, **209**, pp. 543-566.

Reis, R. L., Hannah, H., Carley, J. E., Pugh, D. M., (1977), "Surgical Treatment of Idiopathic Hypertrophic Subaortic Stenosis (IHSS)", *Circulation*, **55**, pp. II128-II132.

Roache, P. J., (1972), *Computational Fluid Dynamics*, Hermosa Publishers, Albuquerque, N.M.

Robertson, J. M., Clark, M. E., Cheng, L. C., (1982), "A Study of the Effects of a Transversely Moving Boundary on Plane Poiseuille Flow", *Journal of Biomechanical Engineering*, **104**, pp. 314-323.

Rodkewiez, C. M., (1975), "Localization of Early Atherosclerotic Lesions in the Aortic Arch in the Light of Fluid Flow", *Journal of Biomechanics*, **8**, pp. 149-156.

Ross, J., Braunwald, E., Gault, J. H., Mason, D. T., Morrow, A. G., (1966), "The Mechanism of the Intraventricular Pressure Gradient in Idiopathic Hypertrophic Subaortic Stenosis", *Circulation*, 34, pp. 558-578.

Rushmer, R. F., Crystal, D. K., Wagner, C., (1953), "The Functional Anatomy of Ventricular Contraction", *Circulation Research*, 1, pp. 162-170.

Sanderson, J. E., Gibson, D. G., Brown, D. J., Goodwin, J. F., (1977), "Left Ventricular Filling in Hypertrophic Cardiomyopathy", *British Heart Journal*, 39, pp. 661-670.

Savage, D. D, Seides, S. F., Maron, B. J., Myc s, D. J., Epstein, S. E., (1989), "Prevalence of Arrhythmias During 24-Hour Electrocardiographic Monitoring and Exercise Testing in Patients with Obstructive and Nonobstructive Hypertrophic Cardiomyopathy", *Circulation*, 59, pp. 866-875.

Schlichting, H., (1979), *Boundary-Layer Theory*, McGraw-Hill Book Company, New York, N.Y.

Schultz, D. L., Tunstall-Pedoe, D. S., Lee, G. J., Gunning, A. J., Bellhouse, B. J., (1969), "Velocity Distribution and Transition in the Arterial System" *Circulatory and Respiratory Mass Transport*, Wolstenholme, G. E., Knight, J., Eds., J. & A. Churchill, Ltd., London, pp. 172-202.

Schmidt, R. C., Patankar, S. V., (1991), "Simulating Boundary Layer Transition with Low Reynold's Number $k-\varepsilon$ Models, Part 1: An Evaluation of Prediction Characteristics", *Transactions of the ASME, Journal of Turbomachinery*, 113, pp. 10-17.

Seed, W. A., Wood, N. B., (1971), "Velocity Patterns in the Aorta", *Cardiovascular Research*, 5, pp. 319-330.

Shah, P. M., Gramiak, R., Kramer, D. H., (1969), "Ultrasound Localization of Left Ventricular Outflow Obstruction in Hypertrophic Obstructive Cardiomyopathy", *Circulation*, 40, pp. 3-11.

Siegel, R. J., Criley, J. M., (1985), "Comparison of Ventricular Emptying With and Without a Pressure Gradient in Patients with Hypertrophic Cardiomyopathy", *British Heart Journal*, 53, pp. 283-291.

Siegel, R. J., Fishbein, M. C., Criley, J. M., (1986), "Functional Anatomy of the Mitral Valve in Health and Disease: Emphasis on Rheumatologic Disorders: Part I", *Cardiovascular Reviews and Reports*, 7, pp. 331-354.

Siegel, R. J., Fishbein, M. C., Criley, J. M., (1986), "Functional Anatomy of the Mitral Valve in Health and Disease: Emphasis on Rheumatologic Disorders: Part II", *Cardiovascular Reviews and Reports*, 7, pp. 431-455.

Singh, M. P., Sinha, P. C., Aggarwal, M., (1987), "Flow in the Entrance of the Aorta", *Journal of Fluid Mechanics*, **89**, pp. 97-120.

Siouffi, M., Pelissier, R., Farahifar, D., Rieu, R., (1984), "The Effect of Unsteadiness on the Flow Through Stenoses and Bifurcations", *Journal of Biomechanics*, **17**, pp. 299-315.

Spencer, M. P., Greiss, F. C., (1962), "Dynamics of Ventricular Ejection", *Circulation Research*, **10**, pp. 274-279.

Stein, P. D., Sabbah, H. N., (1976), "Turbulent Blood Flow in the Ascending Aorta of Humans with Normal and Diseased Aortic Valves", *Circulation Research*, **39**, pp. 58-65.

Sugrue, D. D., McKenna, W. J., Dickie, S., Myers, M. J., Lavender, J. P., Oakley, C. M., Goodwin, J. F., (1984), "Relation Between Left Ventricular Gradient and Relative Stroke Volume Ejected in Early and Late Systole in Hypertrophic Cardiomyopathy", *British Heart Journal*, **52**, pp. 602-609.

Tarbel, J. M., Gunshinan, J. P., Geselowitz, D. B., (1986), "Pulse Ultrasonic Doppler Velocity Measurements Inside a Left Ventricular Assist Device", *Journal of Biomech. Trans. ASME*, **108**, pp. 232-238.

Tarbel, J. M., Gunshinan, J. P., Geselowitz, D. B., Rosenburg, G., Shung, K. K., Pierce, W. S., (1986), "Pulse Ultrasonic Doppler Velocity Measurements Inside a Left Ventricular Assist Device", *J. Biomech. Eng., Trans. ASME*, **108**, pp. 232-238.

Taylor, D. E. M., Wade, J. D., (1973), "Patterns of Blood Flow Within the Heart: A Stable System", *Cardiovascular Research*, **7**, pp. 14-21.

Teare, D., (1958), "Asymmetrical Hypertrophy of the Heart in Young Adults", *British Heart Journal*, **20**, pp. 1-8.

Teichholz, L. E., Kreulen, T., Herman, M. V., Gorlin, R., (1976), "Problems in Echocardiographic Volume Determinations: Echocardiographic - Angiographic Correlations in the Presence or Absence of Asynergy", *The American Journal of Cardiology*, **37**, pp. 7-11.

Thompson, J. F., (1984), "Grid Generation Techniques in Computational Fluid Dynamics", *AIAA Journal*, **22**, pp. 1505-1523.

Thompson, J. F., Thames, F. C. Mastin, C. W., (1977), "Boundary-Fitted Curvilinear Coordinate Systems For Solution of Partial Differential Equations on Fields Containing Any Number of Arbitrary Two -Dimensional Bodies", *NASA CR-2729*, Washington, D.C.

Tortora, G. J., Evans, R. L., Anagnostakos, N. P., (1982), *Principles of Human Physiology*, Harper & Row, Publishers, Inc., New York, N.Y.

Tutty, O. R., (1988), "Flow in a Tube With a Small Side Branch", *Journal of Fluid Mechanics*, **191**, pp. 79-109.

Viecelli, J. A., (1971), "A Computing Method for Incompressible Flows Bounded by Moving Walls", *Journal of Computational Physics*, **8**, pp. 119-143.

Walbum, F. J., Stein, P. D., (1981), "Velocity Profiles in Symmetrically Branched Tubes Simulating the Aortic Bifurcation", *Journal of Biomechanics*, **14**, pp. 601-611.

Wells, R. E., Merrill, E. W., (1962), "Influence of Flow Properties of Blood Upon Viscosity-Hematocrit Relationships", *Journal of Clinical Investigation*, **41**, pp. 1591-1598.

White, F. M., (1974), *Viscous Fluid Flow*, McGraw-Hill Book Company, New York, N.Y.

White, F. M., (1986), *Fluid Mechanics*, McGraw-Hill Book Company, New York, N.Y.

White, R. I., Criley, J. M., Lewis, K. B., Ross, R. S., (1967), "Experimental Production of Intracavity Pressure Differences", *The American Journal of Cardiology*, **19**, pp. 806-817.

Whitmore, R. L., (1967), "Slip of Blood at a Wall", *Biorheology*, **4**, pp. 121-122.

Wigle, E. D., Sasson, Z., Henderson, M. A., Ruddy, T. D., Fulop, J., Rakowski, H., Williams, W. G., (1985), "Hypertrophic Cardiomyopathy. The Importance of the Site and the Extent of Hypertrophy. A Review", *Progress in Cardiovascular Diseases*, **XXVIII**, pp. 1-83.

Wilcox, D. C., (1993), *Turbulence Modeling for CFD*, DCW Industries, Inc.

Wigle, E. D., Auger, P., Marquis, Y., (1966), "Muscular Subaortic Stenosis: The Initial Left Ventricular Inflow Tract Pressure as Evidence of Outflow Tract Obstruction", *The Canadian Medical Association Journal*, **95**, pp. 793-797.

Wigle, E. D., Marquis, Y., Auger, P., (1967), "Muscular Subaortic Stenosis: Initial Left Ventricular Inflow Tract Pressure in Assessment of Intraventricular Pressure Differences in Man", *Circulation*, **35**, pp. 1100-1117.

Wilson, W. S., Criley, J. M., Ross, R. S., (1967), "Dynamics of Left Ventricular Emptying in Hypertrophic Subaortic Stenosis", *American Heart Journal*, **73**, pp. 4-16.

Winslow, A. J., (1966), "Numerical Solution of the Quasi-Linear Poisson Equation in a Non-Uniform Triangular Mesh", *J. of Computational Physics*, **2**, p. 149.

Womersley, J. R., (1955), "Oscillatory Flow in Ateries. II: The Reflection of the Pulse Wave at Junctions and Rigid Inserts in the Arterial System", *Phys. Med. Bi.*, **46**, pp. 313-323.

APPENDIX A: PLANAR MODEL

A.1 ORDER OF MAGNITUDE ANALYSIS: PLANAR HEART MODEL

The following analysis parallels that of Section 2.2 where an axisymmetric heart model was analyzed. In the case developed here, a one-dimensional planar model is considered, as shown by the following geometry:
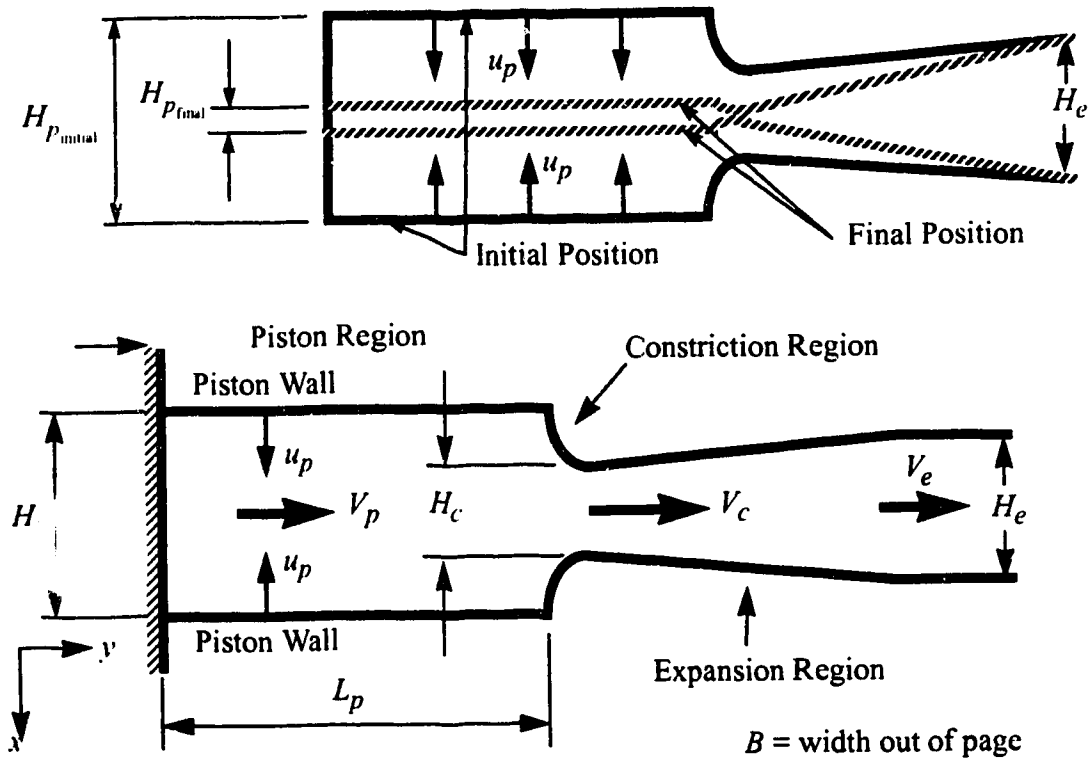
Figure A.1: Planar Heart Geometry

L_p = length of piston region (in y-direction);

H_p = width of duct in piston region - varies with time;

H_e = width of duct downstream of constriction (in x-direction);

H_c = constriction width;

B = width of duct (out of page);

u_p = piston wall velocity;

V_p = fluid velocity in piston region;

V_c = fluid velocity through constriction;

V_e = fluid velocity in exit region.

In this model, a channel with a constriction is used to represent the left ventricle and aorta.

The constriction may be used to represent a stenosis in the exit region of the left ventricle.

The two piston walls drive the fluid through the exit, starting from stationary positions and

accelerating towards each other. This shape is the rectangular coordinate analogue of the

axisymmetric model used in Chapter 2.

To determine the pressure forces involved, the following assumptions were made:

- There is a period of constant flow acceleration, followed by a period of constant

    deceleration, as shown in Figure A.2(a). This gives the exit velocity variation

    shown in Figure A.2(b), which approximates the *in vivo* situation (refer to Figure

    2.3).

- Flow separation may occur downstream of the restriction.

- The flow is uniform, with a flat cross-stream velocity profile.

- The force required to drive the pistons must overcome (i) the **inertial** force to

    accelerate the fluid, (ii) the **viscous** shear force along the walls and (iii) the flow

    resistance due to **spatial** acceleration, caused by of the constriction.
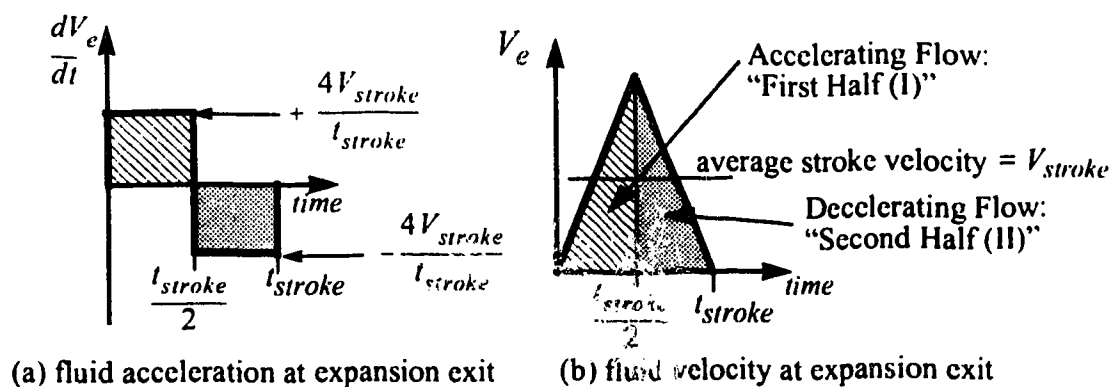

(a) fluid acceleration at expansion exit   (b) fluid velocity at expansion exit

Figure A.2: Idealized Fluid Acceleration and Velocity

Before determining the actual force values, some general flow parameters will be deter-

mined. These include the stroke volume and stroke velocity. The stroke volume is given by

$$\text{stroke volume} = [H_{P_{initial}} - H_{P_{final}}] BL_p,$$

where

$H_{P_{initial}}$ is the initial width between the piston walls;

$H_{P_{final}}$ is the final width between the piston walls.

If the length L_p of the ventricle is approximated as $2H_{P_{initial}}$, the stroke volume becomes

$$\text{stroke volume} = 2BH_{P_{initial}} [H_{P_{initial}} - H_{P_{final}}]. \tag{A.1}$$

As with the axisymmetric analysis, the ejection period is divided into two equal periods of $\frac{t_{stroke}}{2}$. These correspond to the acceleration and deceleration periods shown in Figure A.2.

The average velocity exiting the expansion region, shown in Figure 2.2, may be estimated as

$$V_{stroke} = \frac{\text{stroke volume}}{(\text{expansion exit area})(\text{ejection time})}. \tag{A.2}$$

The ejection time t_{stroke} is the time during which blood is flowing out of the left ventricle, and may be less than the systolic period. For *in vivo* situations, this average velocity will be is estimated as

$$V_{stroke} = \frac{(90\% \text{ of stroke volume})}{(\text{exit area})(90\% \text{ of } t_{stroke})}. \tag{A.3}$$

In terms of the geometry of Figure A.1,

$$V_{stroke} = \frac{2H_{P_{initial}} [H_{P_{initial}} - H_{P_{final}}]}{H_e t_{stroke}}.$$

In HCM, the stroke volume is large compared to the end systolic volume, so that $H_{P_{initial}} \gg H_{P_{final}}$. In this case, $H_{P_{final}}$ may be neglected, so that

$$V_{stroke} \approx \frac{2H_{P_{initial}}^2}{H_e t_{stroke}}. \tag{A.4}$$

$$\text{stroke volume} = 2BH^2_{P_{initial}} \qquad (A.5)$$

Alternatively, the stroke volume may be expressed in terms of the stroke velocity and the stroke time

$$\text{stroke volume} = BH_e V_{stroke} t_{stroke}. \qquad (A.6)$$

Having defined V_{stroke} and t_{stroke} and determined the stroke volume, the average inertial, viscous and spatial forces during the first half (acceleration) and second half (deceleration) of the stroke period will be determined. This will allow the calculation of the average inertial to viscous force ratio, and the average spatial to inertial force ratio.

A.1.1 Unsteady Inertial Acceleration Force, $F_{inertial}$

The unsteady inertial acceleration force $F_{inertial}$ required to accelerate the fluid volume is given by the mass of the fluid times its acceleration. Referring to Figure A.2(a), the acceleration during each period of ejection is constant and is given by

$$\frac{4V_{stroke}}{t_{stroke}} \qquad (A.7)$$

in the first half of the ejection period (acceleration) and

$$-\frac{4V_{stroke}}{t_{stroke}} \qquad (A.8)$$

in the second half of the ejection period (deceleration). The mass being considered is that contained within the piston region; the mass contained within the constriction and expansion regions is neglected. The mass flow rate through the expansion exit will increase and decrease linearly as shown in Figure A.3(b). The mass flow rate is

$$\dot{m} = \rho V_e H_e B \qquad (A.9)$$

where V_e varies with time as shown in Figure A.2(b). During the first half of the ejection period (acceleration), this velocity is
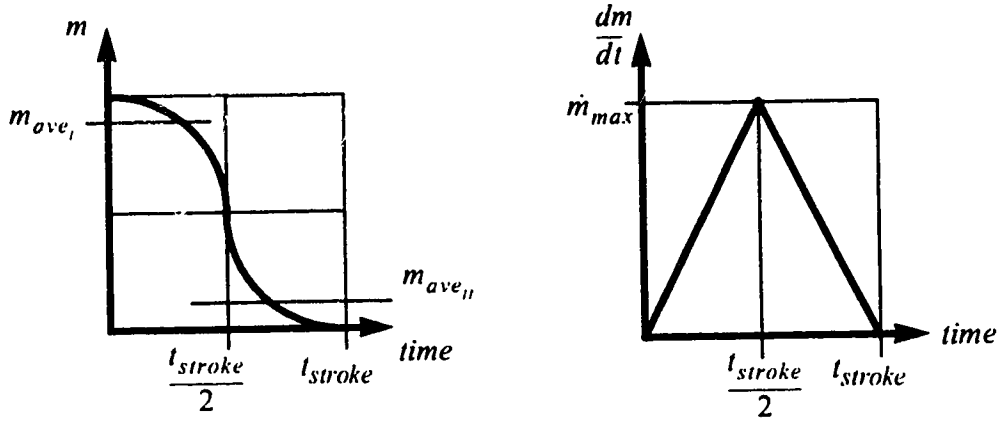
Figure A.3: Fluid Mass Variation in Planar Heart Model

$$V_{e_I} = 4V_{stroke}\left[\frac{t}{t_{stroke}}\right],$$

(A.10)

during the first half (acceleration) of the ejection period and

$$V_{e_{II}} = 2V_{stroke}\left[1 - 2\left[\frac{t - \dfrac{t_{stroke}}{2}}{t_{stroke}}\right]\right]$$

(A.11)

during the second half (deceleration) of the ejection period. The subscripts I and II will be used to denote the first and second halves of the ejection period. The mass being accelerated at any time may be determined from the mass flow rate $\dot{m}$:

$$m(t) = m_{initial} - \int \dot{m}dt.$$

(A.12)

where $m_{initial}$ is the initial mass. The average mass being accelerated in each period will then be determined from

$$m_{ave} = \frac{1}{t_2 - t_1}\int_{t_1}^{t_2} m(t)\, dt.$$

(A.13)

For the first half (acceleration) of the ejection period, this becomes

$$m_{ave_I} = \frac{5BH_e\rho\, V_{stroke}t_{stroke}}{6}.$$

(A.14)

Rather than take the average value for the second half, the instantaneous value will be used. This is to avoid subsequent problems when taking the ratio with the viscous force, as will be explained later.

$$m_{II}(t) = \frac{\rho BH_e V_{stroke} t_{stroke}}{2} \left[1 - 4\left[\frac{t - \frac{t_{stroke}}{2}}{t_{stroke}}\right] + 4\left[\frac{t - \frac{t_{stroke}}{2}}{t_{stroke}}\right]^2 \right]$$ (A.15)

The average inertial force for ι half (acceleration) of the ejection period will be

$$F_{inertial_I} \approx \frac{10}{3}\rho BH_e V_{stroke}^2$$ (A.16)

while the instantaneous value during deceleration will be

$$F_{inertial_{II}}(t) \approx 2\rho V_{stroke}^2 BH_e \left[1 - 4\left[\frac{t - \frac{t_{stroke}}{2}}{t_{stroke}}\right] + 4\left[\frac{t - \frac{t_{stroke}}{2}}{t_{stroke}}\right]^2 \right].$$ (A.17)

A.1.2 Viscous Drag Force, $F_{viscous}$

The viscous force acting on the fluid during the ejection period (systole) may be estimated from the wall shear stress τ_w as

$$F_{viscous} = \tau_w (\text{shear surface area}).$$ (A.18)

The average wall shear stress may be estimated as

$$\tau_w = \frac{\mu V_{stroke}}{\delta_{ave}},$$ (A.19)

where δ_{ave} is the average boundary layer thickness. The boundary layer thickness estimate of Section 2.2 will also be used here·

$$\delta \approx 4\sqrt{\nu t}$$ (A.20)

where t is the time from the onset of motion. As shown previously (equations 2.22 and 2.23),

$$\delta_{ave_i} \approx 2 \, [v \, t_{stroke}]^{1/2} \tag{A.21}$$

$$\delta_{ave_{II}} \approx 2\sqrt{3} \, [v \, t_{stroke}]^{1/2}. \tag{A.22}$$

The velocity V_p in the piston region increases linearly along the piston length, as shown in Figure A.4. This velocity will vary with time and position, so that
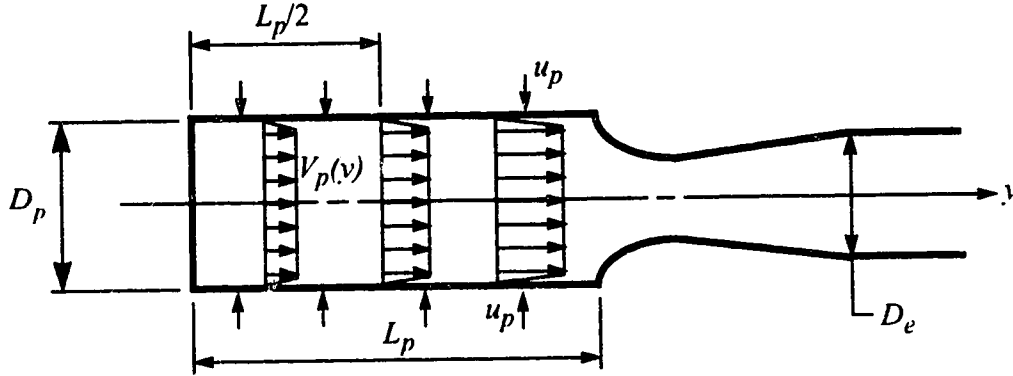
Figure A.4: Variation in Piston Region Velocity

$$V_p = \frac{\left[\dfrac{dA_p}{dt}\right] y}{A_p} \tag{A.23}$$

where A_p is the cross-sectional area of the piston region at any time t. The average velocity within the piston region will be the velocity at $y = L_p/2$, since the velocity varies linearly between $y=0$ and $y=L_p$. For the two periods being considered,

$$V_{P_i}(y=\frac{L_p}{2}) = \frac{4H_{P_{initial}} \, t}{\left[1 - 2\left(\dfrac{t}{t_{stroke}}\right)^2\right] t_{stroke}^2} \tag{A.24}$$

$$V_{P_{II}}(y=\frac{L_p}{2}) = \frac{\dfrac{4H_{P_{initial}} B}{t_{stroke}}\left[2\left[\dfrac{t - \dfrac{t_{stroke}}{2}}{t_{stroke}}\right] - 1\right]}{1 - 4\left[\dfrac{t - \dfrac{t_{stroke}}{2}}{t_{stroke}}\right] + 4\left[\dfrac{t - \dfrac{t_{stroke}}{2}}{t_{stroke}}\right]^2} \tag{A.25}$$

The shear surface area is given by:

$$A_{surf} \approx 4H_{p_{initial}}B.$$

(A.26)

For this model, the surface area is constant throughout the ejection period. This is quite different from the cylindrical model, where the surface area grows smaller with time.

Substituting these expressions for the boundary layer thicknesses (equations A.21 and A.22), velocities (A.24 and A.25) and surface area (A.26) into the viscous force equation (A.18), the instantaneous viscous forces become

$$F_{viscous_I} \approx 8\rho \sqrt{\frac{\nu}{t_{stroke}} \frac{H_{p_{initial}}^2 B}{t_{stroke}^2}} \left[\frac{t}{1 - 2\left[\frac{t}{t_{stroke}}\right]^2} \right]$$

(A.27)

during the first half (acceleration) period of the ejection, and

$$F_{viscous_{II}} \approx \frac{8}{\sqrt{3}}\rho \sqrt{\frac{\nu}{t_{stroke}}} \left[\frac{H_{p_{initial}}^2 B}{t_{stroke}}\right] \frac{1}{1 - 2\left[\frac{t - \dfrac{t_{stroke}}{2}}{t_{stroke}}\right]}$$

(A.28)

during the second half (deceleration) period.

The average viscous force during the first half of the ejection period is

$$F_{viscous_{I_{ave}}} \approx 3.9\rho \left[\frac{\nu}{t_{stroke}}\right]^{1/2} \frac{H_{p_{initial}}^2 B}{t_{stroke}}.$$

(A.29)

However, $F_{viscous_{II}} \rightarrow \infty$ as $t \rightarrow t_{stroke}$, so taking an average value of the viscous force will not work. Fortunately, if the average of the ratio of the instantaneous $F_{inertial_{II}}$ to the instantaneous $F_{viscous_{II}}$ is used, this problem is avoided.

A.1.3 Constriction Spatial Acceleration Force, $F_{spatial}$

The spatial acceleration force required to push the fluid through the constriction is modelled two different ways. The first is to model the downstream side of the constriction as a sudden expansion, shown in Figure A.5. This simulates a separated flow which gives
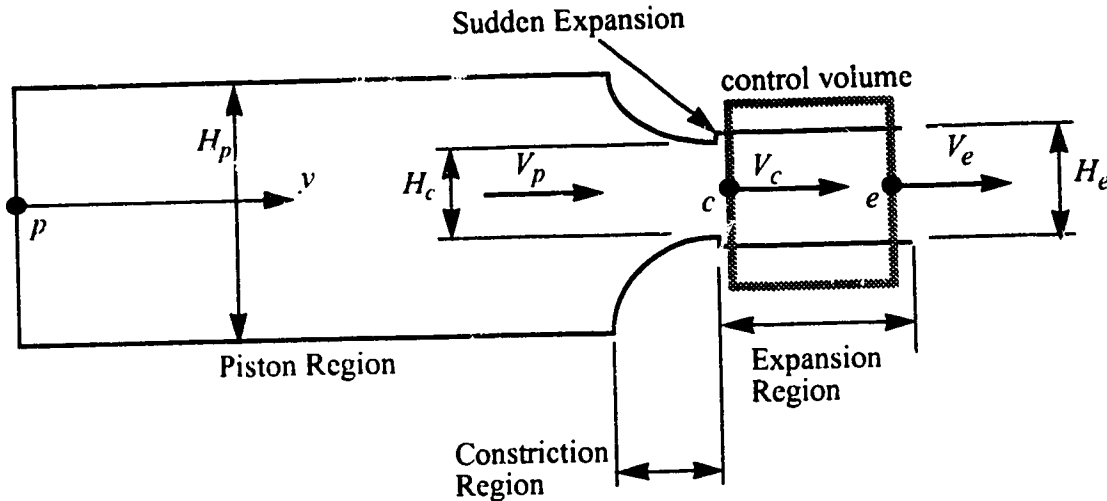
Figure A.5: Constriction Geometry With Sudden Expansion

the least amount of pressure recovery in the expansion. The second method assumes no separation and uses the Bernoulli equation to estimate the pressure difference between p and e. The geometry for the second case is shown in Figure A.6. As noted in Chapter 2, two methods were used to determine the limits of pressure loss: separated flow (sudden expansion) where the pressure loss is large, and fully attached flow (unseparated expansion) where the pressure loss will be smaller. Both methods will determine the pressure drop between p and e, then determine the spatial acceleration force $F_{spatial}$ by multiplying the pressure drop by the appropriate area.

A.1.3.1 First Case: Sudden Expansion

For the first case, the pressure differences will be determined using the Bernoulli equation between p and c, and a linear momentum analysis for the sudden expansion between c and e. The velocities that appear in the resulting equations will be averaged and

specified in terms of V_{stroke}. The steady form of the Bernoulli equation is used to avoid
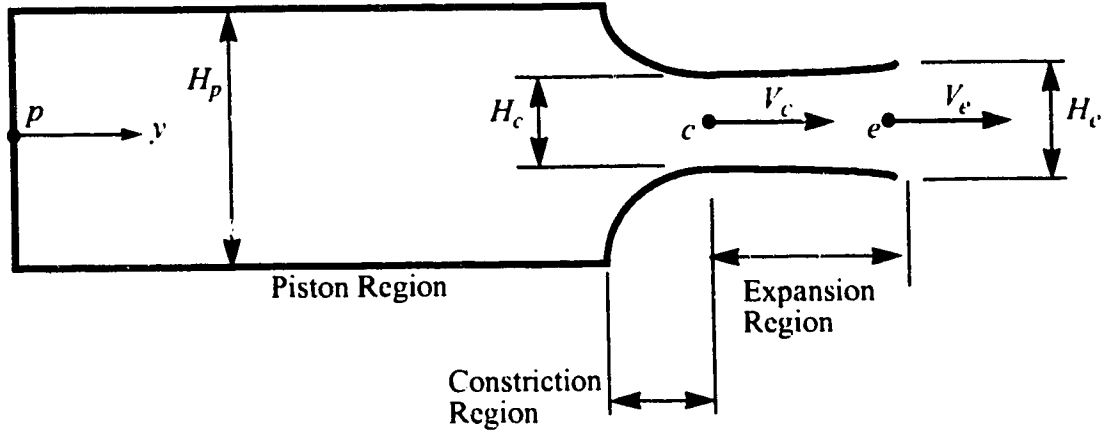
Figure A.6: Constriction Geometry Without Sudden Expansion

including the inertia terms, as these are accounted for in $F_{inertial}$.

Noting that the velocity at p is zero (p is located against a fixed wall), the instantaneous pressure drop between p and c will be

$$p_p - p_c = \frac{1}{2}\rho\, V_c^2.$$

Using continuity to relate V_c to V_e,

$$p_c - p_e = \frac{\rho\, V_e^2}{2}\left[\frac{H_e}{H_c}\right]^2. \tag{A.30}$$

Note that H_c may vary with time, depending on the situation being modelled. For the normal heart, fixed stenosis and unobstructed HCM case, H_c will be a constant value, while for the progressive restriction HCM cases, H_c will become smaller during the ejection period.

Now consider the control volume shown in Figure A.5. This control volume is situated just downstream of the constriction. It is assumed that the pressure across the

control volume at c is uniform and equal to p_c. Using a linear momentum balance across the control volume from c to e, the instantaneous pressure difference is

$$p_c H_e B - p_e H_e B = \rho V_e^2 H_e B - \rho V_c^2 H_c B \qquad \text{(A.31)}$$

Relating V_c to V_e through continuity, equation A.31 becomes

$$p_c - p_e = \rho V_e^2 \left[1 - \frac{H_e}{H_c} \right]. \qquad \text{(A.3?)}$$

Equating the two pressure equations A.30 and A.32, the instantaneous pressure difference is

$$p_p - p_e = (\rho V_e^2) \left[1 - \frac{H_e}{H_c} + \frac{1}{2} \left[\frac{H_e}{H_c} \right]^2 \right]. \qquad \text{(A.33)}$$

The instantaneous spatial force required to overcome this pressure loss is

$$F_{spatial} \approx (\rho H_p B V_{stroke}^2) \left[1 - \frac{H_e}{H_c} + \frac{1}{2} \left[\frac{H_e}{H_c} \right]^2 \right]. \qquad \text{(A.34)}$$

The minimum constriction width H_c may vary with time and its average value for the ejection period is denoted as $H_{c_{ave}}$. The average spatial acceleration force is determined from

$$F_{spatial_{ave}} = \frac{1}{t} \int_0^t F_{spatial} dt \qquad \text{(A.35)}$$

During the first half (acceleration) of the ejection period,

$$F_{spatial_{I_{ave}}} = 0.933 \rho H_{p_{initial}} B V_{stroke}^2 \left[1 - \frac{H_e}{H_{c_{ave}}} + \frac{1}{2} \left[\frac{H_e}{H_{c_{ave}}} \right]^2 \right] \qquad \text{(A.36)}$$

while during the second half (deceleration) of the ejection period

$$F_{spatial_{II_{ave}}} = 0.400 \rho H_{p_{initial}} B V_{stroke}^2 \left[1 - \frac{H_e}{H_{c_{ave}}} + \frac{1}{2} \left[\frac{H_e}{H_{c_{ave}}} \right]^2 \right]. \qquad \text{(A.37)}$$

A.1.3.2 Second Case: No Separation

For the case of no flow separation, the Bernoulli equation may be applied from p to e (Figure A.6):

$$P_p - P_e = \frac{1}{2}\rho \left[V_e^2 - V_p^2 \right]$$

As before, $V_p = 0$ and the average value of V_e is V_{stroke}, so that

$$P_p - P_e = \frac{1}{2}\rho V_{stroke}^2 \cdot \tag{A.38}$$

Thus the average full pressure recovery spatial force during the first half (acceleration) of the ejection period is

$$F_{spatial_{I_{ave}}} \approx 0.466\rho H_{P_{initial}} B V_{stroke}^2 \cdot \tag{A.39}$$

while during the second half (deceleration) of the ejection period

$$F_{spatial_{II_{ave}}} \approx 0.200\rho H_{P_{initial}} B V_{stroke}^2 \cdot \tag{A.40}$$

A.1.4 Dimensionless Parameters

A dimensionless parameter which may be used to describe the flow from the left ventricle into the aorta is obtained from the ratio of the acceleration force $F_{inertial}$ (equations A.16 and A.17) to the viscous force $F_{viscous}$ (equations A.27 and A.29). For the acceleration period,

$$\left. \frac{F_{inertial}}{F_{viscous}} \right|_I \approx 3.4 \left[\frac{H_{P_{initial}}}{H_e} \right]^2 (Re_H)^{0.5} (St_H)^{0.5} \tag{A.41}$$

while for the deceleration period

$$\left. \frac{F_{inertial}}{F_{viscous}} \right|_{II} \approx 0.4 \left[\frac{H_{P_{initial}}}{H_e} \right]^2 (Re_H)^{0.5} (St_H)^{0.5} \tag{A.42}$$

where

$$St_H = \text{Strouhal Number} = \frac{H_e}{V_{stroke} t_{stroke}} = \frac{\text{unsteady acceleration force}}{\text{dynamic pressure force}},$$

$$Re_H = \text{Reynolds Number} = \frac{V_{stroke} H_e}{\nu} = \frac{\text{inertia force}}{\text{viscous force}},$$

The "H" subscripts are used to differentiate these parameters from the axisymmetric versions, as the axisymmetric parameters were based on diameter. The product $(Re_H)^{0.5}(St_H)^{0.5}$ is the Womersley parameter α_H. Replacing $[Re_H St_H]^{0.5}$ with α_H in the force ratio in equations A.41 and A.42, and taking the average value of the two ratios,

$$\frac{F_{inertial}}{F_{viscous}} \approx 1.9 \beta_H^2 \alpha_H . \tag{A.43}$$

where

$$\beta_H = \text{geometry factor} = \frac{H_{p_{initial}}}{H_e} .$$

Thus the characteristic dimensionless parameter is a combination of the Womersley parameter and a geometry factor, as it was for the axisymmetric configuration.

The second dimensionless parameter is determined from the ratio of the time averaged spatial forces for the sudden expansion (equations A.36 and A.37) to inertial forces (equations A.16 and A.17). During the first half (acceleration) of the ejection period,

$$\left. \frac{F_{spatial}}{F_{inertial}} \right|_I \approx 0.28 \left[\frac{H_{p_{initial}}}{H_e} \right] \left[1 - \left(\frac{H_e}{H_{c_{ave}}} \right) + \frac{1}{2} \left(\frac{H_e}{H_{c_{ave}}} \right)^2 \right], \tag{A.44}$$

while during the second half (deceleration)

$$\left. \frac{F_{spatial}}{F_{inertial}} \right|_{II} \approx 0.60 \left[\frac{H_{p_{initial}}}{H_e} \right] \left[1 - \left(\frac{H_e}{H_{c_{ave}}} \right) + \frac{1}{2} \left(\frac{H_e}{H_{c_{ave}}} \right) \right]. \tag{A.45}$$

The overall average is

$$\frac{F_{spatial}}{F_{inertial}} \approx 0.44 \left[\frac{H_{p_{initial}}}{H_e} \right] \left[1 - \left(\frac{H_e}{H_{c_{ave}}} \right) + \frac{1}{2} \left(\frac{H_e}{H_{c_{ave}}} \right)^2 \right] \tag{A.46}$$

This may be expressed using a geometry factor and a restriction factor:

$$\frac{F_{spatial}}{F_{inertia}} = 0.44 \beta_H \left[1 - \eta_H + \frac{1}{2} \eta_H^2 \right] \tag{A.47}$$

where

$$\eta_H = \text{restriction factor} = \frac{H_e}{H_{c_{a,r}}}$$

If the full pressure recovery spatial forces (equations A.39 and A.40) are used in the spatial/inertial force ratio,

$$\frac{F_{spatial_{\substack{unseparated \\ expansion}}}}{F_{inertial}} = 0.22\beta_H.$$

(A.48)

A.2 QUASI-STEADY APPROXIMATION FOR PLANAR HEART MODEL

This analysis is analogous to the quasi-steady analysis of section 2.3, where an axisymmetric config. was considered. The configuration considered is the same rectangular configuration used in A.1. Once again, the ratio of the time averaged total force to the quasi-steady force will be taken.

A.2.1 Total Force

The time averaged total force F_{total} is given by the sum of $F_{inertial} + F_{viscous} + F_{spatial}$:

$$F_{total}\bigg|_{\substack{sudden \\ expansion}} \approx 2.7\rho\,V_{stroke}^2 H_e B + \frac{5.7\rho H_{p_{initial}}^2 B}{t_{stroke}}\left[\frac{v}{t_{stroke}}\right]^{1/2}$$

$$+ 0.67\rho H_{p_{initial}} B V_{stroke}^2\left[1 - \frac{H_e}{H_{c_{a,r}}} + \frac{1}{2}\left[\frac{H_e}{H_{c_{a,r}}}\right]^2\right]$$

(A.49)

using $F_{spatial}$ for the sudden expansion, while for the unseparated expansion

$$F_{total}\bigg|_{\substack{sudden \\ expansion}} \approx 2.7\rho\,V_{stroke}^2 H_e B + \frac{5.7\rho H_{p_{initial}}^2 B}{t_{stroke}}\left[\frac{v}{t_{stroke}}\right]^{1/2}$$

$$+ 0.33\rho H_{p_{initial}} B V_{stroke}^2$$

(A.50)

A.2.2 Quasi-Steady Limit

Using the quasi-steady approach, the force required to move the fluid will not include the inertial force, so that for the sudden expansion

$$
F_{quasi-steady}\bigg|_{\substack{sudden \\ expansion}} \approx \frac{5.7\rho H_{P_{initial}} B}{t^2_{stroke}} \left[\frac{v}{t_{stroke}}\right]^{1/2}
$$

$$
+ 0.67\rho H_{P_{initial}} B V^2_{stroke}\left[1 - \frac{H_e}{H_{c_{avr}}} + \frac{1}{2}\left[\frac{H_e}{H_{c_{avr}}}\right]^2\right] \tag{A.51}
$$

while for the unseparated expansion

$$
F_{quasi-steady}\bigg|_{\substack{unseparated \\ expansion}} \approx \frac{5.7\rho H_{P_{initial}} B}{t^2_{stroke}} \left[\frac{v}{t_{stroke}}\right]^{1/2}
$$

$$
+ 0.33\rho H_{P_{initial}} B V^2_{stroke}\left[1 - \frac{H_e}{H_{c_{avr}}} + \frac{1}{2}\left[\frac{H_e}{H_{c_{avr}}}\right]^2\right] \tag{A.52}
$$

The average ratio of the total force to the quasi-steady force for the sudden expansion is

$$
\frac{F_{total}}{F_{quasi-steady}}\bigg|_{\substack{sudden \\ expansion}} \approx 1 + \frac{1}{\dfrac{0.53}{\beta^2_H \alpha_H} + 0.44\beta_H\left[1 - \eta_H + \frac{1}{2}\eta^2_H\right]} \tag{A.53}
$$

where the dimensionless parameters have the same definition as in Section A.1.

The time averaged force ratio may also be determined using the full pressure recovery spatial force:

$$
\frac{F_{total}}{F_{quasi-steady}}\bigg|_{\substack{unseparated \\ expansion}} \approx 1 + \frac{1}{\dfrac{0.53}{\beta^2_H \alpha_H} + 0.22\beta_H}. \tag{A.54}
$$

APPENDIX B: DEVELOPMENT OF THE UNSTEADY BERNOULLI EQUATION

Consider the general case, as shown in Figure B.1. The velocity along the mid-line, V, is in the y-direction only, and may vary with time (t) and position (y). This velocity was uniform across the entire flow cross-section.

Cross-Sectional Area: at inlet, $A_{in} = H_{in}B$
at outlet, $A_{out} = H_{out}B$

Figure B.1: Moving Wall Control Volume
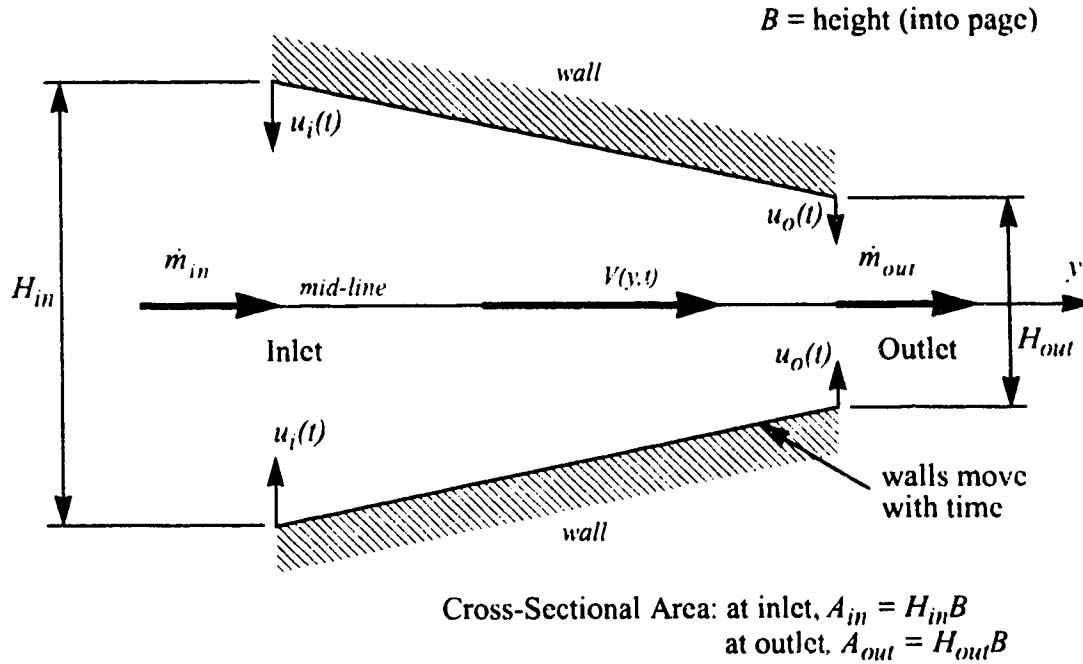
For an incompressible fluid, the conservation of mass for this control volume is

$$\frac{\partial}{\partial t}\int \rho A \, dy + \dot{m}_{out} - \dot{m}_{in} = 0$$

or

$$\rho \frac{\partial A}{\partial t} dy + d\dot{m} = 0,$$

$$d\dot{m} = -\rho \frac{\partial A}{\partial t} dy. \tag{B.1}$$

Note that the flow cross-sectional area (A) varies with both time and position. Applying

the conservation of momentum along the streamwise (v) direction, with no change in elevation along v.

$$\sum \text{Surface Forces} + \sum \text{Body Forces} = \frac{\partial}{\partial t} \begin{bmatrix} \text{momentum in} \\ \text{control volume} \end{bmatrix} + \begin{bmatrix} \text{net rate of} \\ \text{flow of momentum} \\ \text{across boundaries} \end{bmatrix}$$

$$\sum F_S + \sum F_B = \frac{\partial}{\partial t} (\iint_{CV} \int V dm) + \iint_{CS} V d\dot{m} \qquad (B.2)$$

Evaluating each term separately, the surfaces forces at any time t are

$$\sum F_S \approx \frac{1}{2} dp dA - dp (A + dA)$$

$$= -A dp - \frac{1}{2} dp dA.$$

Neglecting $dpdA$ as small compared to Adp,

$$\sum F_S = -A dp. \qquad (B.3)$$

There are no body forces acting in the v-direction, so

$$\sum F_B = 0. \qquad (B.4)$$

The first term on the right side (rate of change of momentum in the control volume) becomes

$$\frac{\partial}{\partial t} (\iint_{CV} \int V dm) = \frac{\partial}{\partial t} (\rho V A dv)$$

$$= \rho A \frac{\partial V}{\partial t} + \rho V \frac{\partial A}{\partial t} dv. \qquad (B.5)$$

This differs from the usual development of the unsteady Bernoulli equation, see for example White (1986, page 147), in that here $\frac{\partial A}{\partial t} \neq 0$. The second term on the right side (net rate of flow of momentum across the control volume boundaries) becomes

$$\iint_{CV} V d\dot{m} = (V + dV)(\dot{m} + d\dot{m}) - V\dot{m}$$

$$= \dot{m} dV + V d\dot{m} + dV d\dot{m}$$

Neglecting second order terms like $dVdm$ as small compared to the other terms.

$$\int\int_{CV} Vdm = (mdV + Vdm).$$

(B.6)

Substituting equations (B.3) - (B.6) into the conservation of momentum equation (B.2) gives

$$-Adp = \rho A\frac{\partial V}{\partial t}dy + \rho V\frac{\partial A}{\partial t}dy + mdV + Vdm.$$

(B.7)

Now at any time t, and at any cross-section along the mid-line, the mass flow rate is given by $m = \rho AV$. Substituting this into equation (B.7) yields the unsteady kinetic energy equation for moving walls

$$-Adp = \rho A\frac{\partial V}{\partial t}dy + \rho V\frac{\partial A}{\partial t}dy + \rho A VdV - \rho V\frac{\partial A}{\partial t}dy.$$

$$-Adp = \rho A\frac{\partial V}{\partial t}dy + \rho A VdV.$$

It is interesting to note that the $\frac{\partial A}{\partial t}$ terms have cancelled because they appear in both mass conservation and momentum conservation equations. The equation may be rearranged to give

$$\frac{\partial V}{\partial t}dy + \frac{dp}{\rho} + VdV = 0.$$

(B.8)

This equation relates the mid-line pressure to the fluid velocities. Even though it was developed for a case for a flow bounded by moving walls ($\frac{\partial A}{\partial t} \neq 0$), it has the same form as the unsteady Bernoulli equation with stationary walls ($\frac{\partial A}{\partial t} = 0$). The effect of the wall movement is determined entirely by the $\frac{\partial V}{\partial t}$ term.

The unsteady Bernoulli equation may be integrated along the streamwise direction (y) to give

$$p(y) - p_{inlet} = \rho\left\{-\int_{inlet}^{y} \frac{\partial V}{\partial t}dy - \frac{1}{2}[V(y)^2 - V_{inlet}^2]\right\}.$$

(B.9)

If the velocity V is constant with time, equation (3.9) reduces to the familiar steady form

of the Bernoulli equation (with no change in elevation):

$$p(y) - p_{inlet} = -\frac{\rho}{2}[V(y)^2 - V_{inlet}^2] \tag{B.10}$$

B.2 Development of Velocity and Acceleration Terms for Moving Walls

All that remains to be determined, to calculate the pressure along the mid-line of the flow, are expressions for the velocity V and the acceleration $\frac{\partial V}{\partial t}$ at any point y along the mid-line. Since the velocity profile at any cross-section is assumed to be uniform, the mid-line velocity will be equal to the volume flow rate divided by the cross-sectional area. The acceleration will the derivative of this expression.

Consider the general case of a linear wall, as shown in Figure B.2. Both u_i and u_0
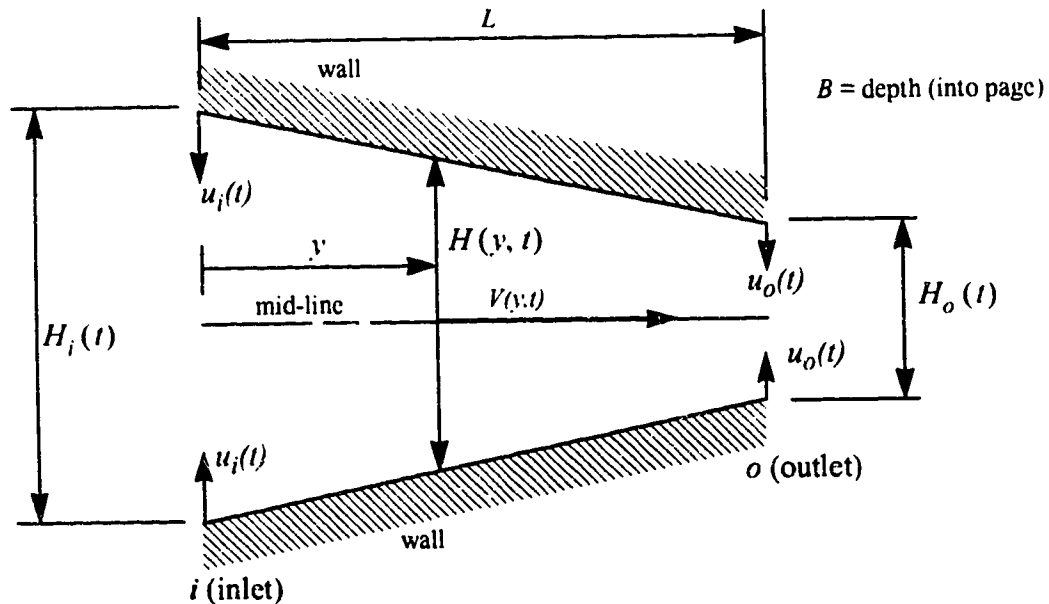

Figure B.2: General Moving Wall Geometry

are wall velocities, based on experimental data obtained from the unsteady laboratory model. In order to develop an equation for the velocity $V(y,t)$ at any point along the mid-line, expressions for cross-sectional area and volume flow rate at any location y must first be derived.

The time dependent inlet and exit widths may be expressed as

$$H_i(t) = H_i\big|_{t_0} - 2\int_0^t u_i(t)\,dt \tag{B.11}$$

$$H_o(t) = H_o\big|_t - 2\int_0^t u_o(t)\,dt. \tag{B.12}$$

The cross-section width at any point y is defined in terms of these values as

$$H(y,t) = H_i(t) - [H_i(t) - H_o(t)]\frac{y}{L}. \tag{B.13}$$

In a similar manner, the wall velocity at any distance along the mid-line will be

$$u(y,t) = u_i(t) - [u_i(t) - u_o(t)]\frac{y}{L} \tag{B.14}$$

If the depth of the flow section into the page is B, then the cross-sectional area at any point y is given by

$$A(y,t) = H(y,t)B. \tag{B.15}$$

The volume flow rate at any cross-section will be given by the sum of the inlet volume flow rate and the change in volume from the inlet to y due to the motion of the walls. The inlet volume flow rate is given by

$$\dot{Q}_{inlet} = V_i A_i = V_i H_i B \tag{B.16}$$

while the change in volume due to wall motion in time dt is

$$dQ = B\int_i^y [2u(y,t)\,dt]\,dy. \tag{B.17}$$

Substituting for $u(y,t)$ (equation (B.14)) and integrating gives

$$\frac{dQ}{dt} = B\left[2u_i(t)y - (u_i(t) - u_o(t))\frac{y^2}{2}\right]. \tag{B.18}$$

The velocity, $V(y,t)$, may now be determined by substituting equations (B.15), (B.17) and

(B.18) into the mass conservation equation:

$$V(y,t) = \frac{\dot{Q}_{inlet} + \frac{dQ}{dt}}{A(y,t)}$$

(B.19)

$$V(y,t) = \frac{V_i H_i(y,t) + 2u_i(t)y - (u_i(t) - u_o(t))\frac{y^2}{L}}{H_i(t) - (H_i(t) - H_o(t))\frac{y}{L}}.$$

(B.20)

Differentiating equation (B.18) with respect to time gives the fluid acceleration at any

position y

$$\frac{\partial V}{\partial t} = \frac{\frac{\partial V_i}{\partial t}H_i - 2V_i u_i + 2y\frac{\partial u_i}{\partial t} - \frac{y^2}{L}\left[\frac{\partial u_i}{\partial t} - \frac{\partial u_o}{\partial t}\right]}{H_i - (H_i - H_o)\frac{y}{L}}$$

$$- \frac{\left[V_i H_i + 2u_i y - (u_i - u_o)\frac{y^2}{L}\right]\left[-2u_i + \frac{2y}{L}(u_i - u_o)\right]}{\left[H_i - (H_i - H_o)\frac{y}{L}\right]^2}$$

(B.21)

APPENDIX C: EQUIPMENT SPECIFICATIONS

C.1 PRESSURE TRANSDUCER SPECIFICATIONS

C.1.1 Entran EPX-10101W-10
Miniature Threaded Pressure Transducer

Manufacturer's Specifications:

Operating Pressure:	10 psig (normal); 50 psig (max)
Sensitivity:	2.46 mV/psig
Combined Linearity and Hysteresis:	1%FS
Useful Frequency Range:	10 KHz

C.1.2 Validyne DP15-20
Variable Reluctance Differential Pressure Transducer
Manufacturer's Specifications:

Operating Pressure:	10 psig (normal); 20 psig (max)
Sensitivity:	2.5 mV/psig
Linearity:	2% F.S.
Hysteresis:	2% F.S.

C.2 DISPLACEMENT TRANSDUCER SPECIFICATIONS

C.2.1 Schaevitz 1" Linear Variable Differential Transformer
Displacement: ±1 inch

Linearity: 0.5% F.S.

C.2.2 Schaevitz 0.5" Linear Variable Differential Transformer
Displacement: ±1 inch

Linearity: 0.5% F.S.

C.3 DATA ACQUISITION SYSTEM SPECIFICATIONS

C.3.1 MetraByte Corporation DASH-8

8 Channel High Speed A/D Converter and Timer Counter Interface

Manufacturer's Specifications:

Full Scale:	5 Volts
Resolution:	12 bits
Accuracy:	0.01% of reading 1 bit
A/D Type:	Successive approximation

C.3.2 Low-pass Filter

Two stage continuously variable (clock tunable) circuit that approximates a fifth order Butterworth polynomial. Attenuation at a frequency of twice the clock frequency is 60 db. Filter is tunable from 20 to 100 Hz (set to 60 Hz for tests reported in this thesis).

APPENDIX D: INSTRUMENT CALIBRATION

D.1 L.V.D.T. CALIBRATION

The L.V.D.T.s were calibrated over the full range using a standard L.V.D.T. calibrator. Both transducers were linear as expected (correlation coefficient of 0.99996 for the 1"; 0.99995 for the 0.5"), and the repeatability was also superb (0.25% full scale; 0.16% full scale). The sensitivity of the 1" L.V.D.T. was 78.4 bits/mm, while the 0.5" L.V.D.T. showed a sensitivity of 142 bits/mm. Thus the resolution was 0.013 mm for the 1" L.V.D.T., and 0.007 mm for the 0.5" L.V.D.T.

D.2 PRESSURE TRANSDUCER CALIBRATION

The Entran and Validyne pressure transducers were calibrated statically using an Omega Digital Pressure Calibrator (Model PCL601) over a range of -8 psig to +10 psig in 1 psig increments. The transducers were calibrated both before and after each test sequence (a test sequence being defined as a series of 175 individual tests for a given model configuration). The results indicated that the calibration was consistent: no significant changes occurred in the calibration.

The Validyne transducers were highly linear, with correlation coefficients ranging from 0.999407 to 0.999999. Their sensitivity ranged from 162 bits/psig to 173 psig/bit (0.0235 bit/Pa to 0.0251 bit/Pa), with a repeatability of 0.66% full scale. The resolution based on the sensitivity ranged from 0.040 kPa to 0.043 kPa. No dynamic calibration of these transducers was performed; the comparison with the fast response Entran transducer indicated the dynamic response to be adequate for the pressure transients being measured.

The Entran EPX transducer was highly linear, with a correlation coefficient of 0.99987. Its sensitivity was 140 bits/psig (0.0203 bit/Pa), with a repeatability of 0.42% full scale. The resolution based on the sensitivity was 0.049 kPa. No dynamic calibration of this transducer was performed; the manufacturer's specifications were taken at face value. The listed frequency response was 10,000 Hertz.